

DUBLIN CITY UNIVERSITY

INTERACTIONS OF INTENSE OPTICAL AND  
EXTREME-ULTRAVIOLET LASERS WITH ATOMS AND SOLIDS

*A thesis submitted for the degree of:*

DOCTOR *of* PHILOSOPHY

*Presented to:*

*The School of Physical Sciences*

*Submitted by:*

JOHN DARDIS

*Research Supervisor:*

PROF. JOHN T COSTELLO

*August 2009*

# Declaration

I hereby certify that this material which I now submit for assessment on the programme of study leading to the award of Doctor of Philosophy is entirely my own work and has not been taken from others save and to the extent that it has been cited and acknowledged within the text of my work.

---

John Dardis, 6<sup>th</sup> August, 2009

Student Number: 50363138

*To Mum and Dad.*

# Contents

<b>List of Figures</b>	<b>vii</b>
<b>List of Tables</b>	<b>xiv</b>
<b>Acknowledgements</b>	<b>xv</b>
<b>Abstract</b>	<b>xvii</b>
<b>I Intense Laser Interactions with Solids</b>	<b>1</b>
<b>1 Laser-Produced Plasmas</b>	<b>2</b>
1.1 Plasma Definition . . . . .	4
1.2 Plasma Evolution . . . . .	5
1.3 Plasma Expansion . . . . .	9
1.4 Atomic Processes in Plasmas . . . . .	11
1.4.1 Bound-Bound Pathways . . . . .	11
1.4.2 Bound-Free Pathways . . . . .	13
1.4.3 Free-Free Pathways . . . . .	14
1.5 Equilibrium in Plasmas . . . . .	15
1.5.1 Local Thermodynamic Equilibrium . . . . .	17
1.5.2 Coronal Equilibrium . . . . .	18
1.5.3 Collisional Radiative Equilibrium . . . . .	19
1.6 Colliding Plasma Systems . . . . .	21
1.6.1 Orientation . . . . .	21
1.6.2 Basic Theory of Colliding Laser-Produced Plasmas . . . . .	23
<b>2 Experimental Systems and Procedures I</b>	<b>33</b>
2.1 The EKSPLA™ 312p Laser System . . . . .	35
2.2 Experimental Setup . . . . .	42

2.3	Optical Setup for Colliding Plasma Systems . . . . .	44
2.4	Target Configurations . . . . .	45
2.5	Photon Diagnostics . . . . .	46
2.5.1	X-ray Imaging . . . . .	47
2.5.2	X-ray Spectroscopy Setup . . . . .	50
2.5.3	Visible Emission Imaging . . . . .	56
2.5.4	Visible Emission Spectroscopy . . . . .	58
2.6	Summary . . . . .	62
<b>3</b>	<b>Soft X-ray Emission Studies</b>	<b>68</b>
3.1	Overview of Soft X-Ray Measurements . . . . .	68
3.2	Initial Characterization of Laser-Produced Plasmas . . . . .	69
3.2.1	Surface Cratering . . . . .	71
3.2.2	Plasma Temperature . . . . .	72
3.2.3	Plasma Dimensions . . . . .	74
3.3	Colliding Plasma Systems . . . . .	78
3.3.1	Soft X-ray Spectroscopy . . . . .	80
3.3.2	Pinhole Imaging . . . . .	82
3.4	Conclusions . . . . .	86
<b>4</b>	<b>Emission Imaging and Spectroscopic Studies</b>	<b>91</b>
4.1	Overview of Visible Emission Experiments . . . . .	91
4.2	Single Plasma Studies . . . . .	92
4.2.1	Emission Imaging of Single Plasmas . . . . .	93
4.2.2	Spectroscopy of Single Plasmas . . . . .	97
4.2.2.1	Electron Density . . . . .	98
4.2.2.2	Electron Temperature . . . . .	118
4.2.3	Summary . . . . .	121
4.3	Colliding Plasma Systems . . . . .	123
4.3.1	Colliding Plasmas on Flat Targets . . . . .	127
4.3.1.1	Imaging of Colliding Point Plasmas . . . . .	127
4.3.1.2	Spectroscopy of Colliding Point Plasmas . . . . .	137
4.3.1.3	Imaging of Colliding Line Plasmas . . . . .	143
4.3.2	Colliding Plasmas on Wedge-Shaped Targets . . . . .	152
4.3.2.1	Emission Imaging of Colliding Point Plasmas . . . . .	153
4.3.2.2	Emission Imaging of Colliding Line Plasmas . . . . .	157
4.4	Conclusions . . . . .	162

<b>II</b>	<b>Intense EUV Laser Interactions with Atoms</b>	<b>167</b>
<b>5</b>	<b>Photoionization of Atoms</b>	<b>168</b>
5.1	Single-Ionization Mechanisms . . . . .	169
5.1.1	Multiphoton Ionization . . . . .	170
5.1.2	Above-Threshold Ionization . . . . .	171
5.1.3	Tunneling ionization . . . . .	174
5.1.4	The Keldysh Parameter . . . . .	175
5.2	Double-Ionization Mechanisms . . . . .	176
5.2.1	Case I: Low-Energy Photons . . . . .	177
5.2.1.1	The Recollision Model . . . . .	179
5.2.1.2	The Electron Shake-Off Model . . . . .	180
5.2.2	Case II: High-Energy Photons . . . . .	181
5.3	Two-Color Above-Threshold Ionization . . . . .	183
<b>6</b>	<b>Experimental Systems and Procedures II</b>	<b>193</b>
6.1	The Free Electron Laser in Hamburg . . . . .	195
6.1.1	The Photoinjector . . . . .	196
6.1.2	Electron Acceleration & Bunch Compression . . . . .	196
6.1.3	The Undulator . . . . .	197
6.1.4	FEL Radiation . . . . .	197
6.1.5	The Experimental Hall . . . . .	200
6.2	The Experimental Chamber . . . . .	201
6.2.1	Pump-Probe Synchronization . . . . .	205
6.3	Summary . . . . .	209
<b>7</b>	<b>Two-Color Photoionization Experiments at FLASH</b>	<b>213</b>
7.1	Characterization of Pump-Probe Setup . . . . .	214
7.1.1	Temporal Overlap using the Cross-Correlation Method . . . . .	215
7.1.2	Recording the Spectral Content of FLASH . . . . .	217
7.2	Two-Color Above-Threshold Photoionization Studies . . . . .	221
7.2.1	Orientation . . . . .	221
7.2.2	The Soft Photon Approximation . . . . .	222
7.2.3	Dependence of Photoelectron Sideband Intensity . . . . .	230
7.2.3.1	Electron Kinetic Energy . . . . .	230
7.2.3.2	Atomic Number of Element . . . . .	237
7.2.3.3	Optical Laser Wavelength . . . . .	242
7.2.4	Polarization Control in Two-color Above-Threshold Ionization . . . . .	246

7.2.4.1 Helium . . . . .	247
7.2.4.2 Neon, Krypton & Xenon . . . . .	257
7.3 Conclusions . . . . .	264
<b>Conclusions &amp; Perspectives</b>	<b>272</b>
<b>A Appendix</b>	<b>281</b>
A.1 World Record at FLASH in Hamburg . . . . .	281
A.2 List of Publications . . . . .	284

# List of Figures

1.1	Simplified illustration of the bound-bound collisional and radiative processes which occur in laser-produced plasmas. . . . .	12
1.2	Simplified illustration of the bound-free collisional and radiative processes which occur in laser-produced plasmas. . . . .	14
1.3	Simplified illustration of Bremsstrahlung and inverse-Bremsstrahlung processes in a laser produced plasmas. . . . .	15
1.4	Criteria for applicability of different ionization models . . . . .	17
1.5	ionization balance of an aluminium plasma as a function of temperature assuming a state of collisional radiative equilibrium and an electron density of $10^{17} \text{ cm}^{-3}$ . . . . .	20
1.6	Computer simulated spatial distribution of the electron and ion densities for the two colliding lithium plasmas as a function of time after the laser pulse has terminated . . . . .	26
2.1	Schematic diagram of an EKSPLA™ SL312p laser system . . . . .	35
2.2	Schematic of the master oscillator in an EKSPLA™ SL312p laser system . . . . .	36
2.3	Pulse compression by stimulated Brillouin scattering in a tapered waveguide . . . . .	39
2.4	Experimental setup for the study of intense laser interactions with solids . . . . .	43
2.5	Optical system incorporating a wedge-prism and plano-convex lens which is used to split the laser beam into two parts, which are subsequently used to generate two point-plasmas on metal targets . . . . .	45
2.6	Target configurations used in studies on colliding plasma systems . . . . .	45
2.7	Photograph of the X-ray pinhole camera setup . . . . .	48
2.8	Diagram of the X-ray pinhole camera setup . . . . .	49
2.9	Schematic diagram of the X-ray crystal spectrometer . . . . .	51

2.10	Transmission of 3 $\mu\text{m}$ thick aluminium and 25 $\mu\text{m}$ beryllium filters used to isolate plasma emission in the EUV and soft X-ray spectral regions . . . . .	51
2.11	Simplified diagrams illustrating the operation of a Bragg crystal spectrometer . . . . .	52
2.12	Soft X-ray spectra of a single copper plasma . . . . .	53
2.13	Schematic diagram showing the metal target and the moveable aluminium bar which was used to block either one of the portion of the two laser beams generating the individual seed plasmas . . . . .	54
2.14	Photograph of the X-ray crystal spectrometer . . . . .	55
2.15	Photograph showing the visible emission imaging setup . . . . .	57
2.16	Magnification of visible emission imaging system . . . . .	57
2.17	Schematic representation of the position of the entrance slit of the spectrometer in relation to the position of the plasma . . . . .	59
2.18	Schematic diagram of the target chamber and the Chromex™ 0.5 m visible spectrometer used in the study of colliding laser-produced plasmas in the visible spectral region . . . . .	60
3.1	Total soft X-ray flux from the plasma obtained as a function of the number of consecutive laser shots and the on-target energy . . . . .	71
3.2	Electron temperature of a copper plasma as a function of on-target laser irradiance . . . . .	73
3.3	Soft X-ray emission spectrum of a magnesium plasma produced by picosecond laser irradiation of a flat metal target and ionization balance within a laser-produced magnesium plasma assuming a state of collisional-radiative equilibrium . . . . .	74
3.4	Soft X-ray emission images of laser-produced plasmas generated on flat targets of various metals . . . . .	76
3.5	Soft X-ray spectra of colliding plasma systems . . . . .	81
3.6	Soft X-ray emission images of two laterally colliding copper plasmas produced on a flat target recorded using a pinhole camera. . . . .	85
4.1	Spectrally filtered time-resolved image array of an expanding aluminium plasma . . . . .	95
4.2	Broadband image of an aluminium plasma and plume front positions of aluminium and calcium plasmas as a function of time . . . . .	96
4.3	Spectral image of a single aluminium plasma generated on the surface of a flat metal target . . . . .	99

4.4	Temporally-resolved electron density distributions along the expansion axis of a laser produced aluminium plasma plume obtained using Stark broadened line profile analysis . . . . .	104
4.5	$1/e$ width of laser-produced aluminium plasmas for different distances from the target surface at three time delays . . . . .	114
4.6	Emission spectra from a laser-produced aluminium plasma for different distances from the target surface at time delays of 130 ns and 250 ns . . . . .	116
4.7	Electron density distribution across the length of the plasma obtained using the self-absorption computer model . . . . .	117
4.8	Spectral image of an aluminium plasma centered at 460 nm used in the determination of the plasma electron temperature . . . . .	120
4.9	Spatially and temporally resolved electron temperature distribution along the expansion axis of a single aluminium plasma produced on a flat metal target . . . . .	121
4.10	Spectrally filtered time-resolved image array of two colliding aluminum plasmas produced on a flat metal target by a point focus of the laser beam . . . . .	128
4.11	Full-width half-maximum along the length and width of a stagnation layer generated by the collision of two aluminium seed plasmas as a function of time delay . . . . .	130
4.12	Spatial and temporal luminosity distribution of colliding plasmas . . . . .	131
4.13	Time-resolved filtered emission images of colliding plasmas produced on flat calcium targets in the visible spectral region . . . . .	134
4.14	Plume intensity (full-width half maximum) as a function of time delay for broadband emission from a calcium stagnation layer . . . . .	136
4.15	Images of the colliding plasma system indicating the position of the spectrometer slit . . . . .	138
4.16	Spatial distributions of the electron density and temperature along the length of an aluminium stagnation layer . . . . .	139
4.17	Emission spectra from a calcium stagnation layer taken at different distances from the target surface . . . . .	141
4.18	Spatial distribution of the electron density across the length of a stagnation layer created by the collision of two calcium plasmas . . . . .	142
4.19	Spectrally filtered and time-resolved image array of two colliding aluminum plasmas produced on a flat metal target using a line focus of the laser beam . . . . .	147

4.20 Plume-front position of the stagnation layer as a function of time delay for an aluminum plasma produced on a flat target using a line focus of the laser beam . . . . .	148
4.21 Electron density and temperature plots for the interaction region at the collision plane between two aluminium line plasmas . . . . .	148
4.22 Spectrally filtered and time-resolved image array of two colliding calcium plasmas produced on a flat metal target by a line focus of the laser beam . . . . .	149
4.23 Plume front position as a function of time delay for broadband plume emission of the stagnation layer created by the collision of two calcium line plasmas . . . . .	150
4.24 Electron density calculated using both the radiation transport computer model for the early time delays close to the target and conventional Stark broadening analysis for later time delays . . . . .	150
4.25 Spectrally filtered and time-resolved emission images of colliding plasmas produced on wedge-shaped aluminium targets in the visible spectral region . . . . .	154
4.26 Time-resolved spectrally-filtered emission images of colliding plasmas produced on wedge-shaped calcium targets in the visible spectral region . . . . .	155
4.27 Full width half maximum length of the stagnation layers produced by the collision of two aluminium and calcium seed plasmas . . . . .	156
4.28 Spectrally filtered and time-resolved image array of two colliding aluminium plasmas produced on a wedge-shaped metal target by a line focus of each laser beam . . . . .	159
4.29 Spectrally filtered and time-resolved image montage of two colliding calcium plasmas produced on a wedge-shaped metal target by a line focus of each laser beam . . . . .	160
4.30 Full-width half-maximum along the length of a stagnation layer generated by the collision of two line-like aluminium and calcium seed plasmas on a wedge-shaped target as a function of time delay . . . . .	162
5.1 Simplified energy level diagram showing the processes of multiphoton ionization, resonantly-enhanced multiphoton ionization and above-threshold ionization . . . . .	171
5.2 Electron spectra from the multiphoton ionization of xenon using a Nd:YAG laser system operating at the fundamental wavelength of 1064 nm . . . . .	173

5.3	Schematic diagram showing the three possible mechanisms for ionization by an intense laser fields . . . . .	174
5.4	Measured ion yields from the ionization of atomic helium using an intense laser operating at a wavelength of 780 nm . . . . .	178
5.5	Schematic diagram showing the Corkum rescattering proposal when an intense laser interacts with an atom or ion . . . . .	180
5.6	Simplified energy level diagram showing the dominant channels involved in the ionization of neon atoms by 50 eV ( $\sim 25$ nm) photons .	182
5.7	Simplified energy level diagram illustrating the two-color above-threshold ionization (ATI) of the helium 1s electron using a combination of 13.7 nm and 800 nm photons from the FEL and optical laser . . . . .	186
6.1	Peak brilliance of EUV and X-ray FELs versus 3rd generation synchrotron light sources . . . . .	194
6.2	Schematic diagram of the layout of the EUV-FEL beamline at the FLASH facility . . . . .	195
6.3	Density modulation induced in the electron bunch by the FEL instability	198
6.4	Pulse structure of the FEL radiation operating at a macropulse repetition rate of 5 Hz . . . . .	199
6.5	Layout of the FLASH experimental hall . . . . .	200
6.6	Schematic diagram of the pump-probe experimental chamber showing the main components of the experimental system . . . . .	202
6.7	Transmission of the 3 $\mu\text{m}$ thick polypropylene ( $\text{C}_3\text{H}_6$ ) and the 1.5 $\mu\text{m}$ thick aluminium filters used in the experiments to determine the spectral content of the FLASH beam . . . . .	204
6.8	Components of the photodiode-based temporal overlap system . . . . .	207
6.9	Output from fast photodiodes in temporal the overlap experiment . . . . .	208
7.1	Single-shot two-color ATI spectra and cross-correlation curve of Xe . . . . .	217
7.2	EUV photon spectra of the FEL beam in the vicinity of 13.5 nm using a two optical filters which select either the emission of the fundamental or of the higher-order harmonics . . . . .	220
7.3	Helium photoelectron spectra simulated using the soft-photon approximation model for low- and high-intensity of optical dressing field	228
7.4	Diameter and radial intensity of the optical laser along the length of the interaction region . . . . .	229

7.5	Summation of the intensity of all sidebands (both low- and high-energy) in helium as a function of the wavelength of the FEL, calculated using the using the soft-photon approximation model . . . . .	233
7.6	Two-color photoionization spectra of neon and xenon taken with different wavelengths of the FEL . . . . .	236
7.7	Total sideband intensity and photoelectron spectra predicted by the soft-photon approximation for a selection of the rare gas elements . . . . .	238
7.8	Waterfall plot presentation of photoelectron spectra taken during a temporal scan between the pump and probe beams for a selection of rare gas elements . . . . .	239
7.9	Photoelectron spectra for a selection of the rare-gas elements for zero delay between the FEL (pump) and the optical laser (probe) beams . . . . .	240
7.10	Ratio between the magnitude of the first and second high-energy sidebands for a selection of rare gas atoms . . . . .	241
7.11	Simulated photoelectron spectra and total sideband yield for helium as a function of the wavelength of the optical dressing field, calculated using the soft-photon approximation . . . . .	243
7.12	Temporally resolved photoelectron spectra of the two-color above-threshold ionization of xenon using a combination of 13.9 nm radiation from the FEL and 400 nm or 800 nm radiation from the optical laser . . . . .	244
7.13	Two-color photoelectron spectra of xenon taken for an optical laser operating at wavelengths of 400 nm and 800 nm . . . . .	245
7.14	Simplified energy level diagram illustrating the two-color above-threshold ionization (ATI) of a helium 1s electron using a combination of 13.7 nm and 800 nm beams from the FEL and optical laser . . . . .	248
7.15	Photoelectron spectra showing the He 1s photoline and the high energy sidebands for low intensity of the optical dressing field ( $\sim 8 \times 10^{10}$ W/cm <sup>2</sup> ) . . . . .	250
7.16	Magnitude of the first photoelectron sideband in helium as a function of the relative angle between the linear polarization vectors of the FEL and optical laser for a low-intensity optical dressing field . . . . .	251
7.17	Photoelectron spectra showing the He 1s photoline and the high energy sidebands for high intensity of the optical laser . . . . .	255

7.18 Magnitude of the first and second high-energy sidebands as a function of the polarization angle in the case of helium for an optical dressing field of $\sim 6 \times 10^{11}$ W/cm <sup>2</sup> . . . . .	255
7.19 Simplified energy level diagram of the two-color above-threshold ionization scheme for the rare-gas group elements . . . . .	258
7.20 Photoelectron spectra showing the Ne photoline at approximately 68.8 eV corresponding to the one-photon ionization of the Ne 2p valence electron by an FEL photon . . . . .	259
7.21 Series of photoelectron spectra of krypton plotted as a function of the relative polarization angle between the FEL and optical laser . . .	261
7.22 Magnitude of photoelectron sidebands of the Kr 4s and 4p photolines as a function of the relative polarization angle between the FEL and optical laser . . . . .	262
7.23 Simulated photoelectron spectra from the soft-photon approximation computer model for the 5p ( $^2P_{3/2,1/2}$ ) levels in xenon . . . . .	262
7.24 Experimental photoelectron spectra showing the Xe 5p photoline and the high energy sidebands for low and high intensity of the optical laser . . . . .	263
7.25 Magnitude of the first sideband for both low- and high-intensity of the optical dressing field in xenon . . . . .	264

# List of Tables

1.1	Classification of the main atomic processes in laser-produced plasmas.	11
2.1	Specifications of the EKSPLA™ SL312p Nd:YAG laser. . . . .	41
2.2	Specifications of the Chromex-Bruker Optics™ 500 visible spectrometer. . . . .	59
3.1	Dimensions (FWHM) of the X-ray emitting core of a laser-produced plasma in the directions parallel and perpendicular to the surface of the target . . . . .	77
4.1	Stark parameters for the Al <sup>0</sup> doublet $3s^23p(^2P_{3/2,1/2}) - 3s^24s(^2S_{1/2})$ at 394.4 nm and 396.15 nm respectively. . . . .	104
4.2	Parameters used in the self-absorption computer model for the simulation of the self-reversed Al <sup>0</sup> doublet $3s^23p(^2P_{3/2,1/2}) - 3s^24s(^2S_{1/2})$ at 394.4 nm and 396.15 nm respectively. . . . .	113
6.1	Operational parameters of the the EUV-FEL at FLASH . . . . .	199
6.2	High-speed EUV-sensitive photodiodes used to obtain the coarse temporal overlap of the pump and probe beams at FLASH . . . . .	207
7.1	Experimental $a_n$ and $b_n$ parameters extracted from the polarization dependence of the sidebands on the He 1s photoline. . . . .	253

# Acknowledgements

First and foremost, I would like to thank my research supervisor, Prof. John Costello, who has been a source of knowledge, guidance and inspiration over the course of this work. I sincerely thank John for all his friendship and support during this time.

I would also like to extend my gratitude to the other members of the laser-plasma group, both past and present, who have made my experience in DCU enjoyable. From the golden years, I would like to thank: Eoin O’Leary, Pat Yeates, Kevin Kavanagh, Hugo de Luna, Mark Stapleton, Jofre Pedregosa Gutierrez, Domenico Doria, and Jean-Rene Duclère; the present post-graduate students: Pdraig, Conor McL., Ricky, Mossy, Mairead, Vincent, Jiang Xi, Colm, and Conor C.; the solitary post-doc: Paddy Hayden; and lastly: Jean-Paul Mosnier, Paul van Kampen and Eugene Kennedy.

Thanks are also extended to all the support staff, both academic and technical, in the physics department on a whole, and in the NCPST in particular. Many thanks go to Lisa Peyton, Sheila Boughton and Samantha Fahy, who form the administrative backbone of the department and the NCPST. The research work presented in this thesis would not have been possible without the help from the technical staff, Des Lavelle, Pat Wogan, Alan Hughes and Ray Murphy.

A proportion of my time was spent at the Deutsches Elektronen-Synchrotron (DESY) facility in Hamburg. While there I had the pleasure of working in a collaboration with some of the best minds in my field of research. A very special thanks must go to Michael Meyer for all his help and assistance during my time at FLASH. I’d also like to thank Denis Cubaynes, Stefan Düsterer, Paul Radcliffe, Wenbin Li, Armin Azima and Harold Redlin. The first few months of my work in DCU also involved a collaboration with Queen’s University Belfast and accordingly I would like to thank: Philip Orr, Alice Delserieys, Colm McKenna, Jason Greenwood and Ciaran Lewis.

A very special mention is required for Caroline and Phil. Through rational thinking (Caroline) and exuberant energy (Phil) they both managed to keep my feet securely rooted to the ground while providing a very enjoyable and often raucous working atmosphere in the office. I would also like to extend my thanks to my non-DCU buddies who have been very supportive over the last few years: Mike, Ciaran, Francesca, Tara, Tine, Niamh and Steve Chaney.

I would like to acknowledge financial support from the Irish Government’s National

Development Plan which includes the Basic Research Grants Scheme (Frontiers Programme) of Science Foundation Ireland/Enterprise Ireland and the Higher Education Authority Programme for Research in Third Level Institutions and North-South Scheme.

And finally, I would like to thank my family: Clive, Lee, Paul and Suzanne for their support during my Ph.D. and beforehand; and my wonderful parents, who have always been there for me during the good-times and especially in the bad-times. Their lack of knowledge in physics was more than compensated for by their wisdom and love. It gives me great pleasure to dedicate this thesis to them.

# Abstract

This thesis describes the interaction of intense optical and extreme-ultraviolet laser pulses with atoms and solids. The work was divided into two main parts: The first part describes studies on laser-produced plasmas done at the National Centre for Plasma Science and Technology in Dublin City University using an intense optical laser system. The second part describes the interaction of intense EUV radiation with atoms, performed at the free-electron laser in Hamburg.

When an intense optical laser impinges on a solid metal surface a high density, high temperature plasma is produced. If two such plasmas are produced within close proximity on flat (or wedge-shaped) targets, as they expand into vacuum they will collide. The collision of these two expanding plumes will eventually lead to a region in space where the counter-streaming plumes begin to stagnate. As plasma expansion continues the temperature and density of material at this interface increases significantly, a dense stagnation layer is formed and begins to glow. Plasma diagnostics, more specifically the extraction of plasma electron temperatures and densities and also plume expansion dynamics have been performed on this stagnation layer and the seed plasmas which feed it. The primary goal in the first part of this work was the study of colliding laser produced plasmas using an EKSPLA™ 312p picosecond laser system. We study the evolution of the stagnation layer under different experimental conditions and discuss the suitability of this system for current and future applications, e.g., pulsed-laser deposition.

The second part of this thesis deals specifically with the interaction of an intense extreme-ultraviolet free electron laser with gas jets. The primary goal in this study was the understanding of two-color above-threshold ionization in rare gases. The intense extreme-ultraviolet (EUV) radiation from FLASH was combined with an intense synchronized optical laser (800 nm, 4 ps). The photoelectron spectrum revealed one strong photoline attributed to the one-photon direct ionization of helium by FLASH pulses accompanied on either side by smaller sidebands originating from the two-color (FEL and optical laser) above-threshold ionization. These sidebands show strong variations of their amplitudes as a function of both the intensity of the optical dressing field and the relative orientation of the linear polarization vectors of the two fields. We exploit this polarization dependence to (i) make the first interference-free study of the dynamics of the two-color above-threshold ionization process in rare gases, and (ii) to directly probe the branching ratios for continuum-continuum transitions in helium.

**Part I**

**Intense Laser Interactions  
with Solids**

# Chapter 1

## Laser-Produced Plasmas

Pulse durations of compact laboratory scale laser systems have decreased substantially over the years. In the early 1980s the term 'intense laser system' would be used to describe any picosecond duration laser system which was capable of a focussed irradiance in the region of  $10^{14}$  W/cm<sup>2</sup>. Nowadays, pulse durations of 100 fs are standard and sub 10 fs pulses are routinely achievable. In this case the on-target irradiance can easily exceed  $10^{15}$  W/cm<sup>2</sup>. The progress in this field and specifically in the development of the titanium-sapphire (Ti:Sapphire) laser system (arguably the most common of all short-pulse systems in use today) would not have been possible without the development of techniques like passive mode-locking [1], self-mode-locking [2] and chirped-pulse amplification [3].

This first part of this thesis describes work on the interaction of sub-nanosecond infrared pulses from an intense table-top laser system with solid metal targets. The laser system used exclusively for this work had a pulse duration of  $170 \pm 20$  ps and when tightly focused was able to deliver an intense beam ( $\leq 10^{13}$  W/cm<sup>2</sup>) onto the surface of the target. This pulse duration positions the laser system in the region between the two temporal regimes for normal Q-switched lasers (nanoseconds) and ultra-fast mode-locked lasers (femtoseconds). On one side is the nanosecond regime, where a laser-produced plasma is generated via an initial process of heating and melting of the target surface followed by rapid ionization to form a so-called thermal-plasma. And on the other side is the sub-picosecond temporal regime where a laser plasma is generated by the direct photoionization of the surface atoms with a minimum of energy transfer into the bulk via thermal effects. Plasmas formed by the EKSPLA™ 312p picosecond laser system are still classed as thermal plasmas, though they share some traits which are characteristic of plasmas produced via femtosecond laser irradiation of solid targets. Most of the other

studies to date into plasmas generated by lasers operating in the 10 – 200 ps range have been with petawatt ( $10^{15}$  W/cm<sup>2</sup>) laser systems, like that of the 12 ps (268 nm) SPRITE laser at the Rutherford Appleton Laboratory in the UK [4]. With the advent of compact (table-top) systems offering multi GW peak intensities, such studies are not just worthwhile, but also become easily accessible. Our main motivation in this sense was the study of collisions between two counter-propagating laser-produced plasmas. Both X-ray and visible emission imaging and spectroscopy was performed on the two seed plasmas and on the interaction region between them. The work was done at the National Centre for Plasma Science and Technology (NCPST) in Dublin City University.

Plasma formation depends on the pulse duration and wavelength of the laser and also on the optical properties of the solid. When an intense nanosecond laser is focused onto a metal surface, the radiation will penetrate the surface to a depth known as the skin depth, while the majority of the energy will be conducted into the solid to a depth known as the heat-conduction depth. The extent of this heat-conduction region depends on the duration of the laser pulse and so laser ablation using picosecond or femtosecond lasers will yield in a smaller heat-conduction depth compared to the nanosecond laser case. In effect, the collateral damage to the surrounding metal surface caused by heat diffusion (and consequently material melting) is greatly reduced when using ultra-short laser pulses ( $\tau_L \ll 1$  ns). Hence femtosecond lasers have been exploited in processes such as nano-patterning and micro-machining [5]. However, while the laser ablation process is much more precise when using short-pulse lasers, the long-pulse laser systems ( $\tau_L \geq 1$  ns) are generally more efficient at creating plasmas because over the period of the pulse duration a larger percentage of the laser radiation is absorbed by the expanding plasma through a process known as inverse-Bremsstrahlung (see section 1.4). Notwithstanding the ever-decreasing pulse durations of table-top femtosecond laser systems, long-pulse laser systems still remain an essential tool in field of laser-plasma physics.

The focusing geometry also plays an important role in plasma production. The focal spot shape and size will determine (to some extent) the overall shape of the plume. When a small focal spot is used, e.g. the tight focus of a laser beam onto target using a high-quality spherical lens, the plasma evolves into spherical shape. If a large spot diameter is used, typically a few hundred microns, then the plasma will evolve into a more elliptical shape as it expands away from the target surface [6]. This can be explained with the aid of the adiabatic expansion model of Singh

and Narayan [7], whereby the smallest initial dimension (typically in the direction normal to the target surface) yields a higher value of the pressure gradient which acts to drive the plume outwards at a faster velocity than in the orthogonal direction. Also, the use of a large focal spot diameter will mean that the irregularities in the radial profile of the laser beam will introduce hot-spots which are characteristic of the laser beam. As one reduces the focal spot diameter, the radial profile of the beam becomes more uniform and so these localized hot-spots play less of a role. If a cylindrical lens is used, then the plasma will form a plasma sheath which will have a length determined by the length of the line focus (usually the width of the laser beam).

All these parameters play a significant role in plasma formation. In the following section the interaction of intense table-top lasers with solids will be discussed. The laser system used exclusively for the work presented in this thesis had a pulse duration of  $170 \pm 20$  ps and as such was positioned in the region between the two temporal regimes for normal Q-switched lasers (nanoseconds) and ultra-fast mode-locked lasers (femtoseconds).

## 1.1 Plasma Definition

The term plasma can be used to describe matter in either a state of partial or complete ionization. Laser-produced plasmas are formed when a high-power laser is focused onto a target surface. In this case, atoms are ionized upon the absorption of photons and the resultant assembly of electrons and ions can be called a plasma when certain criteria are met. The first important criterion stipulates that the bulk plasma is overall electrically neutral for the duration of its life, such that

$$n_e = \sum_z n_z z \quad (1.1)$$

where  $n_e$  is the electron density and  $n_z$  is the density of ions in charge state  $z$  [8].

Unlike gases, where the neutral particles interact weakly with each other within short range, the Coulombic forces between the charged particles in a plasma are both strong and relatively long ranged. The distance over which a charged particle has influence over its neighbouring particles is known as the Debye length ( $\lambda_D$ ),

$$\lambda_D = \left( \frac{\epsilon_0 k_B T}{n_e e^2} \right)^{1/2} \quad (1.2)$$

where  $\epsilon_0$  is the permittivity of free space,  $k_B$  is the Boltzmann constant,  $T$  is the plasma temperature (in Kelvin) and  $e$  is the electron charge. This produces a sphere of radius  $\lambda_D$  beyond which the field effects on a charge are screened by oppositely charged particles within the plasma [8]. In dense plasma regions, charge screening can be significant, leading to a small  $\lambda_D$  and a plasma which is said to be '*strongly coupled*' [9].

A perturbation on any one ion will immediately influence its neighbouring charges. A charged particle may influence neighbouring particles to such an extent that any external perturbation on the plasma will result in a response from a considerable number of particles. This collective response of the particles is an important criterion in the definition of a plasma and is only significant when the geometrical size of the plume is substantially larger than the Debye length,  $L \gg \lambda_D$  [8]. Furthermore the number of particles within this sphere must be greater than unity which distinguishes a true plasma from a highly energetic medium and is described by,

$$N_D = \frac{4\pi n_e}{3} \lambda_D^3 \gg 1 \quad (1.3)$$

The collective response of the particles in the plasma will manifest itself as wave-like motions which are superimposed onto the random motions of the individual particles. Collective electron oscillations (waves) play a more significant role than the relatively slow oscillations of the heavier ions in plasma-laser interactions. The electron wave oscillates at the so-called plasma frequency  $\omega_p$  given by

$$\omega_p = \left( \frac{n_e e^2}{m_e \epsilon_0} \right)^{1/2} \quad (1.4)$$

where  $m_e$  is the mass of the electron.

## 1.2 Plasma Evolution

The laser system operated at the Nd:YAG fundamental wavelength of 1064 nm and had a pulse duration of 170 ps. As this laser operates just beyond the characteristic relaxation time of the phonons in most metals (typically < 100 ps) the discussion will be limited to plasma formation using relatively long pulse duration laser systems, i.e., the 'thermal' plasma regime. However, where necessary this discussion will examine the contrasting processes which are characteristic of short-pulse laser ablation.

When an intense laser is focused to a point on a metal surface a bright, hot and rapidly evolving plasma will be formed. The formation of this plasma depends critically on the duration, intensity and wavelength of the laser pulse and also on the thermal and optical properties of the target. The formation and evolution of a laser-produced plasma can be divided into two main phases: (i) the period during the laser pulse phase, and (ii) the period after the termination of the laser pulse.

When a laser impinges on a surface the radiation will penetrate into the material to a depth known as the optical skin depth (or radiation penetration depth) which is a fraction of the wavelength of the radiation and is given by [10],

$$\delta = \sqrt{\frac{2}{\omega\mu\sigma}} \quad (1.5)$$

where  $\omega$  is the angular frequency of the radiation [ $\text{s}^{-1}$ ],  $\mu$  is the magnetic permeability [ $\text{kg}\cdot\text{m}\cdot\text{s}^{-2}\cdot\text{A}^{-2}$ ] and  $\sigma$  is the conductivity [ $\text{kg}^{-1}\cdot\text{m}^{-3}\cdot\text{s}^3\cdot\text{A}^2$ ]. As it turns out, the optical skin depth is typically only a small fraction of the laser wavelength and for the case of aluminium (where  $\mu = 1.257 \times 10^{-6}$  H/m and  $\sigma = 37.8 \times 10^6$  S/m) the optical skin depth is approximately 5 nm.

Radiation is absorbed by electrons within this skin depth through a variety of photo-processes, (e.g., photoexcitation, direct photoionization and multi-photon ionization), most of which result in the liberation of a significant quantity of electrons. Furthermore, energetic electrons that still remain in the metal lattice (having been raised to the conduction band in the metal) can transfer their energy deep into the bulk material up to a depth known as the heat penetration depth, given by [10],

$$L_{th} \approx \sqrt{2D\tau_L} \quad (1.6)$$

where  $D = k/\rho C$  (where  $k$  is the thermal conductivity [ $\text{W}/(\text{m}\cdot\text{K})$ ],  $\rho$  is the mass density [ $\text{kg}/\text{m}^3$ ] and  $C$  is the specific heat capacity [ $\text{J}/(\text{kg}\cdot\text{K})$ ]) is the thermal diffusivity and  $\tau_L$  is the pulse duration of the laser. For a typical nanosecond laser system ( $\tau_L = 15$  ns) the heat penetration depth is 1.6  $\mu\text{m}$ , while for the EKSPLA™ 312p laser system used here ( $\tau_L = 170$  ps) it is 0.17  $\mu\text{m}$ , calculated for an aluminium target. In the nanosecond case, one may see that the heat penetration depth is many times larger than the optical skin depth, meaning that the energy delivered by the laser pulse will be transferred via heat conduction deep into the bulk metal, resulting in the creation of a relatively large layer of molten metal. Over the duration of the laser pulse localized heating yields in the vaporization of the surface. The target is said

to undergo a solid – liquid – vapour transition. As metals need much more energy to vaporize than to melt this effect reduces the efficiency of the ablation process [11]. For sub-picosecond laser pulses, the heat penetration depth becomes small (i.e., comparable to the optical skin depth). Because the characteristic timescale for lattice heating is in the 1 – 10 ps range, larger than the pulse duration of the laser ( $\tau_L \approx 100$  fs, for a typical Ti:Sapphire laser system), there is insufficient time for the laser energy to be transferred deep to the lattice, resulting in a reduction in the degree of surface melting. In this case, the target is said to undergo a direct solid – vapour (or plasma) transition [11]. The reduction in the degree of melting means that there is less collateral damage to the surrounding substrate [10] and the craters which form have very sharp edges which makes femtosecond laser systems suitable for nano-patterning applications [5].

As stated earlier, the pulse duration of the laser system used in this work is above the characteristic relaxation time of the phonons in most metals (typically < 100 ps). So in this case, plasma formation remains within the thermal regime and evaporation of the target surface occurs when the energy absorbed by this molten layer is greater than the latent heat for vaporization. The depth of ablation can be calculated from [10]:

$$\delta z \approx \frac{A_s(F_L - F_{th})}{\rho L_v} \quad (1.7)$$

where  $A_s$  is the surface absorbance,  $F_L$  is the laser fluence in J/cm<sup>2</sup>,  $F_{th}$  is the threshold fluence at which vaporization occurs and  $L_v$  is the latent heat of vaporization. The vast quantity of liberated electrons and ions are unable to expand much beyond a few nanometers from the target surface, forming what is known as the *deflagration layer*. The free electrons within this layer interact with the laser pulse through the process of inverse-Bremsstrahlung (IB) (see section 1.4), gaining further kinetic energy. Over the duration of the laser pulse collisional excitation and ionization processes will create an influx of electrons and ions leading to the enhancement of this process [12]. The absorption of photons via the process of inverse-Bremsstrahlung is highly dependent on the electron and ion densities and on the laser wavelength. The IB absorption coefficient is given by [10]

$$\alpha_{IB} = \sigma_{IB} N_e = \frac{4}{3} \left( \frac{2\pi}{3k_B T_e} \right)^{1/2} \frac{z^2 e^6}{h c m_e^{3/2} \nu^3} N_i g_{ff} \left( 1 - \exp \left( \frac{-h\nu}{k_B T_e} \right) \right) N_e \quad (1.8)$$

where  $\sigma_{IB}$ ,  $z$ ,  $m_e$ ,  $g_{ff}$  are the IB cross section, the atomic number of the target and the Gaunt factor [13] respectively. The value of the latter factor can in most cases be taken as unity. One will notice that the IB process is less efficient in the ultraviolet

(UV) and visible spectral regions than in the infrared (IR) part of the spectrum which makes short-wavelength lasers ideal for the probing of the most dense regions of plasma which are opaque to IR radiation.

An electromagnetic (EM) wave propagating through the plasma will be subjected to dispersion, the magnitude of which will vary with the plasma electron density. The dispersion relation describes the propagation of an EM wave within a plasma plume and is given by,

$$\omega^2 = \omega_p^2 + c^2 k_p^2 \quad (1.9)$$

where  $\omega_p$  is the plasma frequency and  $k_p = 2\pi/\lambda$  is the propagation constant of the wave. When  $\omega_p < \omega$  one can see from equation 1.9 that the value of  $k_p$  is real and the wave will propagate. However, if  $\omega_p > \omega$  then  $k$  becomes negative and the wave does not propagate in the plasma. By setting  $\omega_p = \omega$  and using equation 1.4 one can determine the electron density of the plasma at which the EM wave is reflected. That value is given by,

$$n_c = \frac{\epsilon_0 m_e \omega^2}{e^2} \quad (1.10)$$

which is known as the critical density. For a CO<sub>2</sub> laser ( $\lambda = 10.6 \mu\text{m}$ ) the critical density is  $10^{19} \text{ cm}^{-3}$ , while for a Nd:YAG laser ( $\lambda = 1064\text{nm}$ ) it is  $10^{21} \text{ cm}^{-3}$ .

The point in space where the density of the deflagration layer reaches the value of this critical density ( $n_c$ ) is known as the critical density layer. It is at this point that the majority of the laser radiation is reflected backwards from either the critical layer or via a Brillouin scattering process (caused by the creation of acoustic waves in the plasma) [14]. In this case, the laser radiation is momentarily blocked from reaching the target surface and the ablation process ceases [15]. During this time however, the plasma will expand slightly, leading to a reduction in the density at this layer. The laser can propagate through the entire plume once again and resume the ablation process. This dynamic self-regulation of the ablation process will continue for the duration of the laser pulse from which point heating and energy transfer within the plume will be caused by atomic process (to be discussed in section 1.4). This stage of the plasma's life-cycle can be considered isothermal as the rate of heating far exceeds the expansion time which dictates the rate at which cooling of plasma species takes place, i.e., the temperature of the plasma remains constant even though the volume of the plume is increasing.

### 1.3 Plasma Expansion

During the very short time when the laser is on (within the first few hundred picoseconds) the plasma can be defined as being isothermal, i.e., the rate of thermal generation via IB and collisional excitation is greater than or equal to the rate at which heat is being lost to its surroundings (radiative processes). In other words, the time-scale of heat propagation within the plasma plume at this early stage is fast compared to the rate of growth of the plume dimensions and so the temperature is relatively uniform (isothermal) across the plasma. Assuming this hypothesis is correct, the change in the dimension of the plasma plume in this early stage is well described by the equation for isothermal expansion [7],

$$X(t) \left( \frac{1}{t} \frac{dX}{dt} + \frac{d^2X}{dt^2} \right) = Y(t) \left( \frac{1}{t} \frac{dY}{dt} + \frac{d^2Y}{dt^2} \right) = Z(t) \left( \frac{1}{t} \frac{dZ}{dt} + \frac{d^2Z}{dt^2} \right) = \frac{k_B T}{m} \quad (1.11)$$

where  $T$  is the plasma temperature,  $k_B$  is the Boltzmann's constant,  $m$  is the mass of the particle, and  $X(t)$ ,  $Y(t)$ ,  $Z(t)$  are the plume dimensions as a function of time.

When the laser pulse has terminated, ablation from the surface (which supplies material to the plasma) and heating of the plasma via inverse-Bremsstrahlung terminates. The plasma plume expands into the vacuum and cools. In this case the plume can be described by the adiabatic expansion model of Singh and Narayan [7]. In this model the laser-produced plasma is treated as an ideal gas at a high pressure and temperature which is initially confined to small dimensions and is suddenly allowed to expand into vacuum. The expansion velocities of the plasma are related to its initial dimensions, the initial temperature, and the atomic weight of the species and can be described by the following equation of motion [7],

$$X(t) \frac{d^2X}{dt^2} = Y(t) \frac{d^2Y}{dt^2} = Z(t) \frac{d^2Z}{dt^2} = \frac{k_B T_0}{m} \left[ \frac{X_0 Y_0 Z_0}{X(t) Y(t) Z(t)} \right]^{\gamma-1} \quad (1.12)$$

where  $X_0$ ,  $Y_0$ ,  $Z_0$  are the initial values of  $X$ ,  $Y$  and  $Z$  which are the plume dimensions at time  $t$ ;  $T_0$  is the temperature after the isothermal expansion phase and  $\gamma$  is the ratio of the specific heat capacities at constant pressure and constant volume, the so-called adiabaticity parameter. This parameter is assumed to remain constant throughout the expansion and has been assigned a value of 1.24 in view of the increased number of degrees of freedom than just translational in the plasma [16]. An adiabatic process is one that occurs so rapidly that there is no transfer of heat between the plasma and its surroundings (i.e., no work done on the system), a process which fits nicely to the free-expansion of laser-produced plasmas

in vacuum.

The plasma expands rapidly into vacuum over the first few tens of nanoseconds after which the shape and size of the bulk plasma plume<sup>1</sup> can be described using the adiabatic expansion model. This expansion model predicts that the largest acceleration will occur along the plane of smallest initial dimension, and consequently the largest pressure gradient [16]. At the end of the laser-ablation phase when the laser has terminated ( $t_d \approx 200\text{ps}$ ) the plasma has a lateral (parallel to the surface) dimension of between a few hundred microns and  $\sim 1\text{ mm}$ , while the orthogonal plume dimension (normal to the target surface) is typically only a few microns. Therefore the adiabatic expansion model predicts that the forward expansion velocity (normal to target) will be substantially larger (owing to the smaller initial length) than the lateral expansion velocity. This leads to a plasma plume which resembles an elliptical shape [17]. It is worth noting that if the focal spot diameter can be decreased<sup>2</sup> to  $10\ \mu\text{m} - 20\ \mu\text{m}$  then one might expect the two orthogonal expansion velocities to be of similar magnitudes which would yield a more spherically-shaped plasma plume (according to the adiabatic expansion model). Variations in the dynamics and dimensions of the plasma plume as a function of focal spot shapes and sizes was investigated by Harilal *et al.* in 2003 [17].

As the plasma begins to expand into vacuum the velocity of the electrons far exceeds that of the ions, due to the relative mass difference. The electrons, which have the highest velocity, travel at the front of the plume and begin to accelerate away from the bulk of the plasma - leaving the ions behind. This causes a strong electric potential to be created between the two species fronts, affecting both constituents oppositely. The Coulombic force due to the fast-electrons acting on the ions will help to accelerate the heavy ions away from the target, while the ions will tend to slow down the expansion of the electrons. This can result in a plasma plume in which charge-separation [19] has occurred and usually takes place within the early expansion stages.

In the next section the atomic processes which govern the transport of radiation within and the emission from a laser-produced plasma will be discussed.

---

<sup>1</sup>This expansion model is based on a simple gas dynamics law which does not discriminate between the plasma species (electrons, ions and neutrals), whose velocity profiles can be quite different.

<sup>2</sup>Achromatic doublets can achieve a spot diameter which can be up to an order of magnitude smaller than that obtained using conventional (BK-7 glass) single-element optics [18].

## 1.4 Atomic Processes in Plasmas

As the plasma expands into vacuum, many radiative processes occur which mediate the emission, absorption and transfer of laser radiation throughout the plume; and collisional processes which control the transfer of energy between the species within the plasma. When a laser impinges on a plasma plume the laser radiation can be: (i) absorbed by atoms and ions, causing an increase in the excitation balance throughout the plasma (photoabsorption), (ii) absorbed by atoms/ions and cause electrons to be liberated into the free-electron continuum (photoionization), and lastly, (iii) absorbed by free-electrons in the vicinity of ions resulting in an increase in kinetic energy of the electrons (inverse-Bremsstrahlung). Collisional processes between electrons, ions and neutral atoms within the plasma plume occur throughout the life-cycle of the plasma and will dominate energy transfer both internally and externally (emission) during the expansion stage, when the laser is off. All these atomic processes are in some way inter-linked, whereby collisional processes lead to an increase in the rate at which radiative processes occur, and *vice-versa*.

The main excitation/de-excitation processes involving electrons, ions and photons in the plasma are summarized in table 1.1. They can be divided into three main groups, namely bound – bound, bound – free and free – free processes. They can be further subdivided into either, collisional or radiative processes, depending on whether the process was induced or mediated by collisions with electrons/ions or through the interaction with laser photons.

Process	Excitation	De-excitation	Type
B – B	Impact Excitation	Impact De-excitation	Collisional
B – B	Photoabsorption	Spontaneous Decay	Radiative
B – F	Impact Ionization	3-Body Recombination	Collisional
B – F	Photoionization	Radiative Recombination	Radiative
F – F	Bremsstrahlung	—	Collisional
F – F	—	Inverse Bremsstrahlung	Radiative

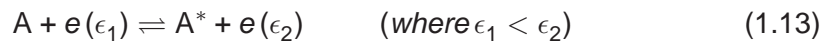
Table 1.1: Classification of the main atomic processes in laser-produced plasmas: (B–B) Bound-Bound, (B–F) Bound-Free, (F–F) Free-Free.

### 1.4.1 Bound-Bound Pathways

**Collisional Processes** A bound electron can be excited to a higher energy level or state through the collision of a free-electron with the atom. The kinetic energy

of the free-electron is transferred to the bound electron, promoting it to a higher discrete state within the atom in a process known as *electron-impact excitation*. Conversely, an electron in an excited state within an atom may be demoted to a lower state upon collision of the atom with another electron. The kinetic energy of the second electron in this case will increase by an amount equal to the energy difference between the initial (i) and final (f) states of the first electron. This inverse process is referred to as *electron-impact de-excitation*.

These collisional processes are described by the following balance equation [9],



where A is the element under consideration and  $\epsilon_1$  and  $\epsilon_2$  are the electron kinetic energies before and after the collision. Reading equation 1.13 from the left-hand side to the right-hand side describes the process of electron-impact excitation, and *vice-versa* for the case of electron-impact de-excitation (right-to-left). A simplified diagram which illustrates the process is shown in figure 1.1 (a). The right-to-left process results in the emission of a photon when  $A^*$  relaxes back to A.

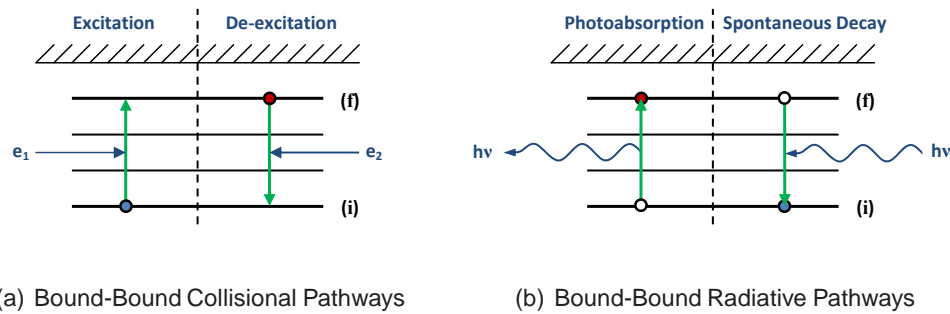


Figure 1.1: Simplified illustration of the bound-bound collisional (a) and radiative (b) processes which occur in laser-produced plasmas [9].

**Radiative Processes** *Photoabsorption* is the process by which an electron in a bound state is promoted to a higher energy state following the absorption of a photon. The inverse process is known as *spontaneous decay*, which occurs when an electron drops from a high energy state to one of lower energy with the excess energy being emitted as a photon. Both processes can be described by the following balance equation,

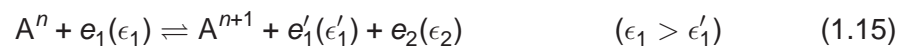


An illustration of this process is presented in figure 1.1 (b). These bound-bound collisional and radiative processes are of significant importance in the area of laser-plasma physics. In typical laser-produced plasmas ( $n_e \geq 10^{16} \text{ cm}^{-3}$ ) the collisional pathways described above become the key processes involved in the transfer of energy within the plasma plume. The competition between the rate of collision excitation/de-excitation with that of radiative excitation/de-excitation is a very important factor in the plasma equilibrium models (specifically, the collisional-radiative equilibrium model [20]) which are presented in section 1.5.

### 1.4.2 Bound-Free Pathways

Bound – free transitions occur between discrete states and continuum states in an atom. In these processes, the electron originates (or terminates) in a bound state of the atom and terminates (or originates) in the continuum. In other words these processes describe ionization or recombination.

**Collisional Processes** When a free electron collides with a bound electron it may impart enough energy to enable it to escape the nuclear Coulombic field of the core. When this occurs, the electron is promoted into a continuum state and the atom is said to be ionized. This process is known as *electron-impact ionization* and is shown (reading from left-to-right) in equation 1.15 and is illustrated in figure 1.2 (a). The inverse process is known as *3-body recombination*. In relatively high density plasmas the probability of two electrons entering the Debye sphere<sup>3</sup> of an ion can become quite high. If one of these electrons is captured into one of the outer-most bound levels of the ion, the ionization stage will be reduced by one, while the other electron will absorb the surplus energy and gain kinetic energy. The first electron can then cascade down into a lower vacant bound state of the atom/ion. This process is represented by the following balance equation (reading from the right),



where  $\epsilon_1$  is the energy of the incoming electron,  $\epsilon'_1$  denotes its energy after the interaction and  $\epsilon_2$  is the energy of the liberated free-electron.

---

<sup>3</sup>A sphere surrounding an ion the size of which is determined by the Debye length (see equation 1.2 on page 4) beyond which collective influences dominate over the Coulombic force due to the individual ions.

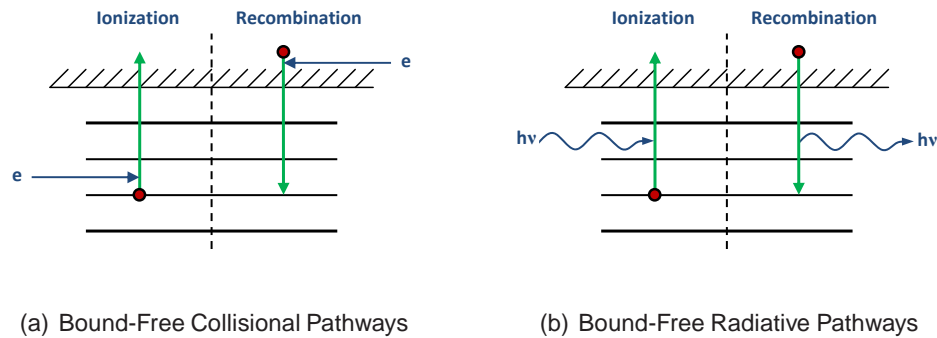


Figure 1.2: Simplified illustration of the bound-free collisional (a) and radiative (b) processes which occur in laser-produced plasmas [9].

**Radiative Processes** When a bound electron absorbs a photon of energy greater than the binding energy of the atom, the electron will gain enough energy to be promoted to the continuum and the parent atom is then left in a state of ionization, so-called *photoionization*. The inverse case is called *radiative recombination* and occurs when a free electron in the continuum is captured by an ion, emits a photon and falls into a discrete energy level of an atom or ion. Both processes are illustrated in figure 1.2 (b) and can be described by the following balance equation,



Bound-free radiative pathways are a very important process in low density laser-produced plasmas, when the rate of competing processes such as collisional excitation/ionization (and their inverse processes) are less significant in comparison.

### 1.4.3 Free-Free Pathways

There are only two processes in this category, namely *Bremsstrahlung* which can be classified as collisional and *inverse-Bremsstrahlung* which can be considered radiative. Both processes occur when a free electron scatters off an ion. As discussed previously (see section 1.2) free-free transitions are of major importance in laser-plasma physics. Inverse-Bremsstrahlung is the primary process through which a plasma absorbs laser radiation and is heated, “because energy-absorbing encounters dominate energy-emitting encounters” [21]; and Bremsstrahlung is the process which generates the bright continuum emission emitted from a hot plasma during the early stages of its lifetime.

**Collisional Processes** When an electron passes through the Coulombic field of an ion, it may be accelerated in this field and thereby emit a photon. This radiation is incoherent and forms the background continuum or white-light emission seen at the early stages of laser-produced plasma expansion. The following equation (reading left-to-right) and figure 1.3 (left-hand side) represents this process.

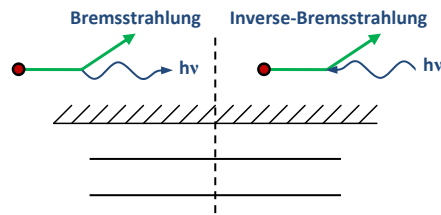


Figure 1.3: Simplified illustration of Bremsstrahlung and inverse-Bremsstrahlung processes which occur in laser-produced plasmas [9].

**Radiative Processes** Inverse-Bremsstrahlung occurs when a free electron absorbs a photon in the vicinity of an ion and increases in kinetic energy. This process can only proceed when the electron is in the presence of an ion in order to obey the law of conservation of momentum. This process is illustrated in figure 1.3 and can be represented by equation 1.17 (reading right-to-left). The work on two-color above-threshold ionization mentioned in section 5.3 along with the experimental results presented in Chapter 7 are based on a very similar concept to inverse-Bremsstrahlung.

## 1.5 Equilibrium in Plasmas

Laser produced plasmas are transient in nature and theoretical models of the ionization balance within a plasma is quite challenging to simulate. In an ideal case, a plasma would behave as an ideal black body radiator where the emissivity is equal to unity and hence all radiation falling on the plasma is absorbed. When this is the case the following criteria are satisfied [8]:

- The intensity distribution of the radiation emission is described by the Planck distribution function.

- The velocity distribution of all particles in the plasma (neutrals, ions, electrons) is described by the Maxwell velocity distribution.
- The population of all states of an atom or ion is described by the Boltzmann distribution.
- The ionization balance between two successive charge states is described by Saha equation.

In this ideal case a single temperature appears in all of the above equations and the plasma is said to exist in a state of complete thermal equilibrium (CT).

This ideal case rarely exists, considering that the majority of plasmas are continuously emitting radiation throughout their lifetime and hence continuously losing energy to their surroundings. The failure of a single model to accurately describe the full range of plasma conditions (from low density to high density) has given rise to an easing of the above criteria for plasmas residing in specific locations on the density-temperature phase diagram 1.4.

The following list gives three of the most commonly used thermodynamic models applicable to plasmas produced in the laboratory and which place less stringent conditions on particles and radiation distributions than complete thermodynamic equilibrium (CTE).

1. Local Thermodynamic Equilibrium (LTE)
2. Coronal Equilibrium (CE)
3. Collisional Radiative Equilibrium (CRE)

The applicability of each model is determined mainly by the electron density ( $n_e$ ) of the plasma. The collisional de-excitation rate must be smaller than the radiative decay rate for the CE model to apply, and *vice-versa* for the LTE model; both of which depend critically on the electron density.

Figure 1.4 (after Colombant and Tonon (1973) [20]) shows the regions of applicability of each model for a range of electron densities and temperatures. One will immediately observe that the *Collisional Radiative* model is widely applicable for typical laboratory-scale laser-produced plasmas (covering two orders of magnitude below the critical density limits of both a CO<sub>2</sub> and Nd:YAG laser-produced plasma).

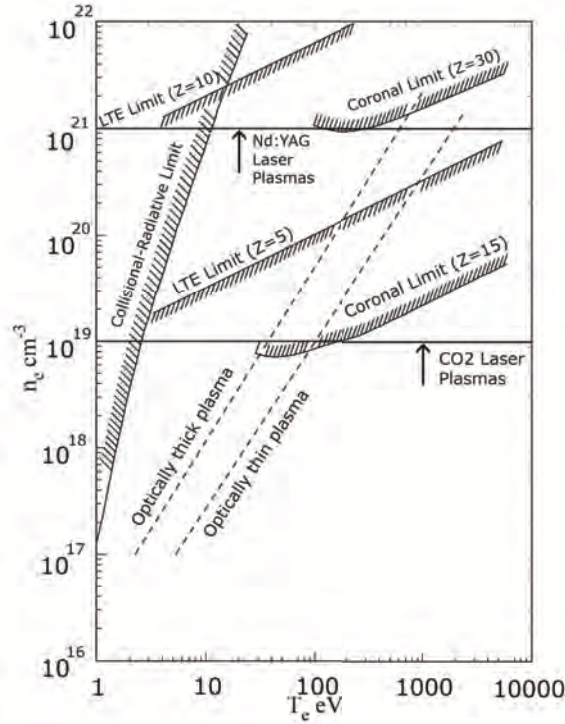


Figure 1.4: Criteria for applicability of different ionization models (after Colombant and Tonon 1973 [20]).

### 1.5.1 Local Thermodynamic Equilibrium

The first model to be discussed is the *Local Thermodynamic Equilibrium* model which best describes plasmas which are hot and of high density. At densities greater than  $10^{21} \text{ cm}^{-3}$  the electron collision frequency becomes high resulting in collisional excitation/ionization processes dominating radiative processes. The plasma is considered to be in equilibrium when the rate of collisional excitation and collisional ionization are balanced with their inverse processes, namely collisional de-excitation and three-body recombination[20]. In LTE plasmas, radiation is being continuously emitted, so in order for LTE to remain valid the rate of collisional de-excitation must be at least an order of magnitude larger than that of radiative decay for all transitions. This puts a lower limit on the electron density of such plasmas, given by [22]

$$n_e \geq 1.6 \times 10^{12} T_e^{\frac{1}{2}} (\chi)_{max}^3 \quad (1.18)$$

where  $n_e$  is in  $\text{cm}^{-3}$ ,  $T_e$  is the electron temperature in electron volts and  $\chi_{max}$  is the transition energy of interest (usually taken as the ionization potential). This relation is valid for plasmas which are said to be optically thick, where radiation emitted within the core of the plasma is re-absorbed in the cooler periphery regions of the plume<sup>4</sup>. In the case of optically thin plasmas, where radiation is not (or not significantly) re-absorbed as it travels through the plasma, the electron density threshold in the above equation must be increased to compensate for the loss of radiation to its surroundings. These limits of validity are shown on figure 1.4.

While the temperature is not considered to be uniform throughout the entire plasma, it is assumed that a specific temperature exists that satisfies the Maxwell, Boltzmann and Saha distributions locally, i.e., so that both the electrons and ions are in a state of equilibrium. In LTE plasmas the radiation spectrum can no longer be described by Planck's law because the typical mean free path (or mfp) of the photons is smaller than the plasma dimensions which results in the radiative processes being unbalanced with respect to their inverse (photoabsorption) processes.

### 1.5.2 Coronal Equilibrium

We now look at the Coronal Equilibrium model, the second plasma equilibrium model which is used to describe low density plasmas such as those found in nebulae or in the outer-regions of a star (the corona). At low densities (typically  $n_e < 10^{12} \text{ cm}^{-3}$ ) the probability of radiative de-excitation transitions occurring now becomes comparable to (or even greater than) that of collisional de-excitation processes.

The rate of collisional excitation is low in CE plasmas because the collision rates scale with electron density, meaning that electrons in excited states will have sufficient time in which to decay (radiatively) to their ground state before another collisional excitation event occurs. As a consequence most of the ions in the plasma are in their ground state. In CE plasmas, the mean free path of the photons is large and so the plasma is said to be optically thin. Because the radiation emitted within the volume of the plasma is not significantly re-absorbed as it travels through the plasma to the periphery region, photoexcitation and photoionization rates are negligible. Therefore one may assume that collisional processes (namely electron-impact excitation and electron-impact ionization) excite the atoms/ions but rarely de-excite them, de-excitation being dominated by radiative processes.

---

<sup>4</sup>This scenario introduces complications in the spectroscopic analysis of the emission from the plasma plume, discussed in section 4.2.2.

### 1.5.3 Collisional Radiative Equilibrium

The final model described here is *collisional radiative equilibrium* or CRE. This model is best suited to describe plasmas which have intermediate electron densities (typically  $10^{19} - 10^{21} \text{ cm}^{-3}$ ), a range which matches the critical densities of common laser-produced plasmas produced from  $\text{CO}_2$  and Nd:YAG lasers ( $\lambda = 10.6$  and  $1.06 \mu\text{m}$  respectively).

This model is somewhat akin to the CE model but it adds collisional de-excitation and three-body recombination terms which are important in transitions involving the higher energy levels. In a collisional radiative plasma, electron collisions compete with photon emission in de-exciting levels, i.e. a level may be collisionally de-excited before it can radiate.

In order for CRE to remain valid, Colomant and Tonon [20] defined certain criteria that must be satisfied:

- The velocity distribution of electrons must be Maxwellian.
- The population density of ions of charge  $(Z+1)$  must not change significantly during the period when the quasisteady-state population distribution is being established among ions of charge  $z$ .
- The plasma must be optically thin to its own radiation.

Under these assumptions Colombant and Tonon [20] have shown that the steady-state ionization balance between successive ion stages is given by

$$\frac{n_{z+1}}{n_z} = \frac{S(z, T_e)}{[\alpha_r(z+1, T_e) + n_e \alpha_{3B}(z+1, T_e)]} \quad (1.19)$$

where  $S$  (the collisional ionization rate),  $\alpha_r$  (the radiative recombination rate) and  $\alpha_{3B}$  (the three-body recombination rate) are given by

$$S = \frac{9 \times 10^{-6} \xi (T_e / \chi_z)^{1/2}}{\chi_z^{3/2} (4.88 + T_e / \chi_z)} \exp(-\chi_z / T_e) \quad (1.20)$$

where  $\chi_z$  is the ionization potential in electron volts.

$$\alpha_r = 5.2 \times 10^{-14} (\chi_z / T_e)^{1/2} z \left[ 0.429 + \frac{1}{2} \log \left( \frac{\chi_z}{T_e} \right) + 0.469 \left( \frac{T_e}{\chi_z} \right)^{1/2} \right] \quad (1.21)$$

and,

$$\alpha_{3B} = 2.97 \times 10^{-27} \xi_z / T_e \chi^2 (4.88 + T_e / \chi_z) \quad (1.22)$$

where  $\xi_z$  is the number of electrons occupying the outer shell of an ion of charge state  $z$ .

By removing the three-body recombination term (and hence the dependence on the electron density) from equation 1.19 one can approximate the average ionic charge state  $z$  in terms of  $T_e$ , such that

$$z \approx \frac{2}{3}[A T_e]^{1/3} \quad (1.23)$$

where  $A$  is the atomic number of the element under consideration. The assumption that the three-body recombination term is significantly smaller than the radiative recombination term ( $n_e \alpha_{3B} \ll \alpha_r$ ) only holds if  $T_e \geq 30$  eV [20].

Equation 1.19 can be used to calculate the ratio of each individual charge state population ( $n_z$ ) to the total population  $n_T$  of all charge stages using the simple relationship:

$$\frac{n_z}{n_T} = n_z / \sum_{i=1}^Z n_i \quad (1.24)$$

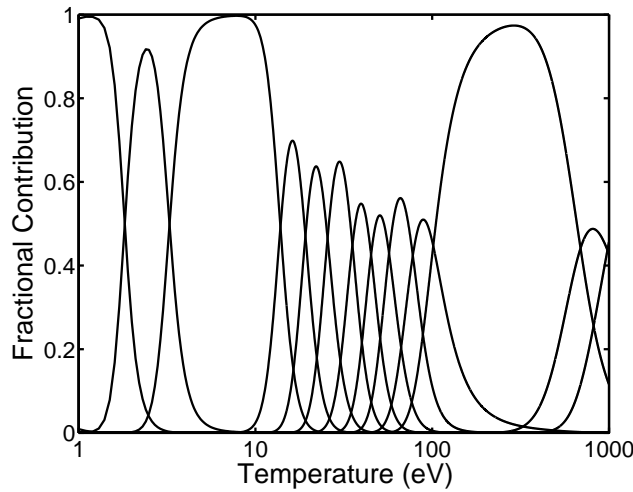


Figure 1.5: ionization balance of an aluminium plasma as a function of temperature assuming a state of collisional radiative equilibrium [20] and an average electron density of  $10^{17} \text{ cm}^{-3}$  [23]. Each trace represents the fractional contribution of the charge state within the plasma. Beginning on the left-hand side of the figure, neutral species appears to be the dominant constituent of the plasma of 1 eV. As the electron temperature of the plasma increases the percentage of neutral species decreases while the contribution from the succeeding charge state increases. This trend continues in sequence as the temperature increases and the model shows that at approximately 1 keV  $\text{Al}^{11+}$  becomes the dominant charge state within the plasma.

Figure 1.5 shows the ionization balance for an aluminium plasma in collisional radiative equilibrium, calculated using equation 1.19 by McGuigan [23]. The model shows that at low temperature, the dominant atomic species in the plasma is atomic aluminium. The dominant charge state in the plasma depends on the electron temperature. At approximately 1 keV the model shows that the  $\text{Al}^{11+}$  becomes the dominant charge state. The work in the soft X-ray spectral region in Chapter 3 employed this model in order to determine an approximate value of the electron temperature within our laser-produced plasmas. The value of the highest charge state observed in the X-ray spectra was compared to the output from the model in figure 1.5 and by knowing the on-target laser irradiance, a value of the plasma temperature was deduced.

## 1.6 Colliding Plasma Systems

Colliding plasmas occur predominantly in the astrophysical regime, however the last 15 years have seen the emergence of several very interesting applications which are based on the novel use of colliding laser-produced plasmas. In this section the discussion of laser-produced plasmas is extended into the realm of colliding plasma systems where some of the wide variety of applications and uses of colliding plasmas are discussed.

### 1.6.1 Orientation

Naturally occurring phenomena such as the collision between astrophysical objects like stars, galaxies and nebulae have evoked interest in laboratory-based simulations with the long term aim of understanding the processes involved in these phenomena [24, 25, 26, 27, 28]. Woolsey *et al.* [29] used laser-produced plasmas to replicate the mutual collision between some of the densest of interstellar objects, namely the collision of stars and the formation of supernovae<sup>5</sup> (SNe) and supernovae remnants<sup>6</sup> (SNR). Laser-produced plasmas proved to be an ideal candidate for this study because key dimensionless parameters which define the level of interaction between the two stellar objects (and hence the two laser-plasma plumes) could be finely-controlled within the laboratory. By changing parameters such as laser irradiance, laser wavelength, target composition and target geometry

---

<sup>5</sup>The death of a super-massive star occurs when fusion processes cease in the core and the star collapses inwards accompanied by a supernova explosion which expels surface material outwards into space.

<sup>6</sup>The hot material ejected from a supernova.

it was possible to tailor the laboratory-based experiments to suit a wide variety of astrophysical phenomena, from interpenetrating nebulae to colliding stars.

Colliding plasma systems have also emerged in inertial confinement fusion or ICF [30, 31]. Briefly, ICF is a technique where a high-power (e.g., 1.8 MJ and 500 TW, at the National Ignition Facility [32]) laser is used to initiate a fusion process through the heating and compression of a deuterium-tritium (DT) fusion pellet [30]. Compression of the fuel pellet can occur through either, (i) inverse-bremsstrahlung (and a variety of other plasma collective processes) when the intense laser beam is focused directly onto the DT fuel pellet, in so-called 'direct-drive' ICF; or (ii) through the absorption of intense X-rays emitted from the many plasmas which are created when multiple beams from the high-power laser system are focused onto the inside surface of a hohlraum<sup>7</sup> which contains the DT fuel pellet, so-called 'indirect-drive' ICF. The indirect-drive arrangement has been the focus of most of the research into ICF since the earliest experiments in the mid 1970s [33], because of the relaxed requirements on laser beam uniformity and reduced sensitivity to hydrodynamic instabilities. Each focused laser beam generates a high-density high-temperature plasma inside the hohlraum that emits intense X-rays which impinge on the DT fuel pellet from all angles. The surface (or shell) of the fuel pellet heats up rapidly due to the absorption of this radiation and it expands (or explodes) away from the center of the pellet. As it expands outwards the rest of the shell implodes inwards, initiating a fusion process in the dense core of the pellet. A thermonuclear burn-front propagates radially outward into the rest of the remaining fuel which prolongs the fusion process [34]. If one ignore the effects of laser-beam non-uniformity, the collisions and subsequent instabilities between the plasmas plumes generated inside the hohlraum can lead to asymmetric compression and other unpredictable effects which will make the fusion process less efficient. A significant portion of the research in this field has been carried out with the Nova laser at the National Ignition Facility of the Lawrence Livermore National Laboratory in California, and it was here that some of the first computer modeling [35] of the ICF process and of colliding plasma plumes in general was developed.

Colliding plasmas can also be applied to other purposes, namely, pulsed laser deposition (PLD). In conventional PLD, a laser-produced plasma is generated in close proximity to a silicon wafer and material from the plasma is deposited onto the surface. Depending on the plasma conditions this thin-film layer may have a large variation in thickness over the entire surface of the wafer. The plasma plume

---

<sup>7</sup>A cylindrical-shaped hollow gold enclosure which contains the DT fuel pellet.

may also contain large aggregate particles, like clusters, which can cause surface damage (known as splashing [36]) and non-uniformity in the electrical properties of the layer. To avoid this negative side-effect of single plasma PLD, Camps *et al.* [37] developed a new method for thin-film deposition, known as cross-beam pulsed laser deposition or CBPLD, whereby the interaction between two colliding laser-produced plasmas is capable of producing an aggregate-free source of dopant [37, 38].

Previous work on colliding plasmas have been performed in the visible spectral region [39], the vacuum-ultraviolet (VUV) [40] using table-top nanosecond laser systems. Extensive work has also been done in the soft X-ray spectral region [41, 42, 43] using intense petawatt ( $10^{15}$  W/cm<sup>2</sup>) laser systems. The motivation behind this present work was to extend the study of colliding plasma systems using table-top laser systems into the soft X-ray spectral region (*leq* 1 nm).

### **1.6.2 Basic Theory of Colliding Laser-Produced Plasmas**

When two counter propagating laser-produced plasmas (known henceforth as ‘seed’ plasmas) collide there are two extremes of behavior. If the two seed plasmas have a large relative velocity (and modest density at the collision plane) with respect to each other, then the plasma plumes will pass through each other to a certain degree. This is called interpenetration, and the two plumes will behave more like dilute gas jets. However, when the relative collision velocity between the two seed plasmas is small then the interaction between the plumes will take place only at a narrow interface between the two plasmas. The interpenetration distance will be quite small and so the material from the two seed plasmas will tend to collide and decelerate abruptly at this midplane region. As the seed plasmas continue to expand more and more plasma material will reach this boundary which fuels the collision process and compression will begin to occur. Over time, compression of the material within this region will occur yielding a significant increase in the temperature and density and the formation of what is known as a stagnation layer. The kinetic energy of the colliding material is converted into thermal energy and the material within the stagnation layer will begin to emit brightly in the visible and vacuum-ultraviolet spectral regions.

To summarize, interpenetration will occur between the two seed plasmas when the ion-ion mean-free path or *mfp* is larger than the typical dimensions of the system [44], usually taken to be the separation of the seed plasma plumes. The interaction between the two plumes can be considered collisionless and collective plasma

effects dominate. In this case the heating process is mainly driven by the internal collisions between ionic species in each of the individual seed plasmas. Stagnation occurs when the ion-ion mfp is small in comparison with the distance separating the two seed plasmas. In this case the two plumes decelerate rapidly and little or no interpenetration occurs. Furthermore, the interaction is dominated by collisions between ionic species between each of the opposing seed plasmas. The collisionality parameter [41, 35], is used to help determine which collision scenario to expect, and is defined as,

$$\xi = D/\lambda_{ii} \quad (1.25)$$

where  $D$  is the separation between the two seed plasmas and  $\lambda_{ii}$  is the ion-ion mean free path which is given by [41],

$$\lambda_{ii}(1 \rightarrow 1) = \frac{(k_B T_e)^2}{4\pi e^4 Z^4 n_i \ln \Lambda_{1 \rightarrow 1}} \quad (1.26)$$

$$\lambda_{ii}(1 \rightarrow 2) = \frac{m_i^2 v_{12}^4}{4\pi e^4 Z^4 n_i \ln \Lambda_{1 \rightarrow 2}} \quad (1.27)$$

where  $T_e$  is the temperature,  $n_i$  is the average plasma ion density at the collision plane,  $v_{12}$  is the relative collision velocity,  $z$  is the average ionization state of the plasma,  $m_i$  is the ion mass,  $e$  is the charge of the electron and  $\ln \Lambda_{1 \rightarrow 1, 1 \rightarrow 2}$  is the so-called Coulomb logarithm<sup>8</sup> for collisions between seed plasma 1 and seed plasma 2. Equation 1.26 represents the mfp of the ionic species within each of the seed plasmas, while equation 1.27 represents the mean free path between counter-streaming ionic species; both of which are given in *cgs* units. The contribution from ion-electron collisions has been ignored because the ion-electron mfp is usually much larger than ion-ion mfp for medium  $Z$  plasmas, especially for laser-produced plasmas in the density range of  $10^{16} - 10^{19} \text{ cm}^{-3}$ , as is the case in stagnation layers of interest in this thesis.

From equation 1.27 one can see that the collisionality of the system is highly dependent on  $v$  the relative velocity of the colliding plume pair and to a lesser extent on  $n_e$ , the electron density of the plasma plumes. Therefore, it is possible to engineer the experiment in such a way as to control the collisionality of the system. By changing either (i) the separation between the two seed plasmas ( $D$ ), or (ii) the on-target laser irradiance and hence the expansion velocity of the seed plasmas ( $v$ ), in principle the level of plume interpenetration can be controlled.

---

<sup>8</sup>The value of the Coulomb logarithm is typically in the range of 10 – 30 for most laboratory plasmas [45]. The value decreases as the plasma density ( $n_e$ ) increases, a consequence of a reduction in the Debye length of the plasma [46].

Early attempts to model the collision of two counter-streaming plasmas were mainly focused on fusion codes based on the single fluid model. But there is a fundamental difficulty in simulating the collision of two plasmas using these models. These codes do not allow for plume interpenetration and so when the two seed plasmas collided, they simply merged into a single fluid and always stagnated, resulting in an unphysical temperature spike at the interface and the formation of excessively strong shockwaves [35].

A one-dimensional multi-fluid code was developed by Rambo and Denavit [44, 35] at the Lawrence Livermore National Laboratory which was able to simulate both interpenetration and stagnation in colliding plasmas. The kinetic model makes use of a particle-in-cell (PIC) [47] representation of the ions augmented by Coulomb collisions. The versatility of this particular multi-fluid code meant that Rambo and Denavit were able to simulate ion separation during the initial expansion of the seed plasmas. They concentrated on laser-ablated polypropylene ( $C_3H_6$ ) foils and used separate fluids for hydrogen and carbon. They were able to track the dynamics of each elemental species independently, hence the term 'multi-fluid'.

A preliminary computer model based on this code was developed by Stapleton [48] in Dublin City University which was capable of simulating both interpenetration and stagnation between two counter-propagating seed plasmas. Sample outputs from an early version of the code are shown in figure 1.6.

The plasmas were initially separated by  $162 \mu\text{m}$  and the spatial distributions of the electron and ion densities were approximated by half-Gaussian functions. The model tracks three fluids within each seed plasma, namely electrons, ions and neutrals; hence this was a multi-fluid code. In the case of a system with low collisionality, figure 1.6 (top row), the two seed plasmas show clear signs of significant plume interpenetration. At approximately 33 ns after the laser pulse has terminated each plasma plume appears to have interpenetrated up to  $75 \mu\text{m}$  into the opposing plume. The model shows that the penetrating seed plasma induces a recession in the advancement of the oncoming plasma, an effect that is much greater in the case of the ions than the electrons.

In the high collisionality case where the ion-ion mfp is comparable to (or smaller than) the separation between the two seed plasmas, figure 1.6 (bottom row), it is clear that the expanding Li plumes stagnate upon impact, illustrated by the onset of a sharp spike in the local electron/ion densities. As more ablated material enters the interaction region, this high density spike grows at the mid-plane region since

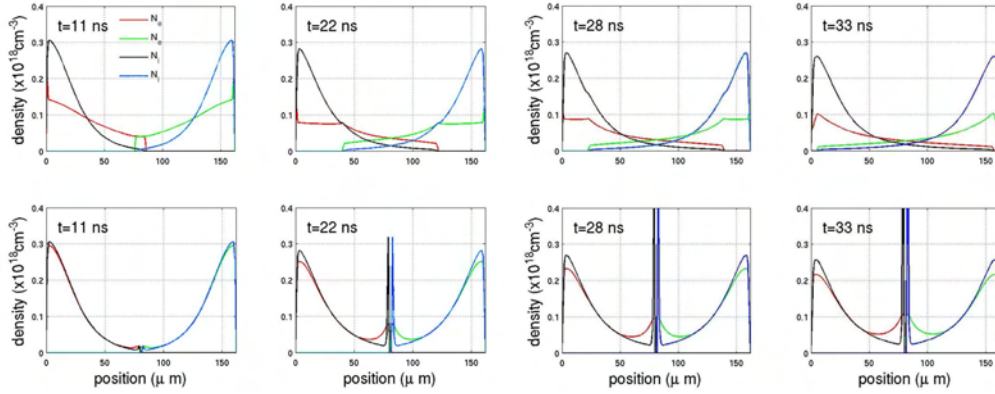


Figure 1.6: Computer simulated spatial distribution of the electron and ion densities for the two colliding lithium plasmas as a function of time after the laser pulse has terminated. An initial half-Gaussian spatial distribution of the electron and ion densities was assumed. Results from both low and high collisionality systems are presented in the top and bottom halves of the figure respectively. In the low collisionality case (top row), significant plume interpenetration is observed. In the high collisionality case (bottom row), the formation of a high density region between the two seed plasmas, a stagnation layer, is seen. The two seed plasmas had an initial separation of  $162 \mu\text{m}$ . After [49].

this material cannot penetrate into the opposing plume. The mid-distance plane (collision-front) between the two seed plasmas adds significant complexity to the calculations, as each of the variables, such as density, temperature, momentum and electric field strength for each species and in both plasmas plumes must be accounted for.

Appropriate engineering of experiments can be achieved with relative ease using colliding plasma systems, thereby they offer a flexible platform for the study of many complex physical systems. Previous plasma diagnostic experiments in this field have either concentrated on the collision of relatively cold plasmas ( $T_e \approx 1 \text{ eV}$ ) generated from nanosecond laser irradiation of targets [40, 50, 39], or at the opposite extreme of high temperature plasmas ( $T_e \approx 500 \text{ eV}$ ) produced from ultra-intense petawatt laser systems [51, 41].

In this work, a novel compact system for the study of the collision between two relatively high temperature plasmas generated by an intense picosecond table-top laser system is described. Using a variety of target geometries, specifically flat and orthogonal-shaped metal targets, as well as different optical focusing configurations, namely point and line focus, the extent over which the two seed plasmas interact has been controlled. Both X-ray and visible emission imaging and spectroscopy was performed on the interaction between the counter-streaming seed

plasmas. Significant self-absorption was observed during the course of our spectroscopic work and so a computational model based on the solution of the one-dimensional equation of radiative transfer was implemented in order to extract the plasma electron density.

# Bibliography

- [1] H. A. Haus. Theory of mode locking with a fast saturable absorber. *Journal of Applied Physics*, 46:3049–3058, 1975.
- [2] D. E. Spence, P. N. Kean, and W. Sibbett. 60-fsec pulse generation from a self-mode-locked Ti:sapphire laser. *Optics Letters*, 16(1):42–44, 1991.
- [3] D. Strickland and G. Mourou. Compression of amplified chirped optical pulses. *Optics Communications*, 55:447–449, 1985.
- [4] L. A. Gizzi, A. Giulietti, O. Willi, and D. Riley. Soft-x-ray emission dynamics in picosecond laser-produced plasmas. *Physical Review E*, 62(2):2721–2727, 2000.
- [5] F. Korte, J. Serbin, J. Koch, A. Egbert, C. Fallnich, A. Ostendorf, and B. N. Chichkov. Towards nanostructuring with femtosecond laser pulses. *Applied Physics A: Materials Science & Processing*, 77(2):229–235, 2003.
- [6] S. S. Harilal. Influence of spot size on propagation dynamics of laser-produced tin plasma. *Journal of Applied Physics*, 102(12):123306, 2007.
- [7] R. K. Singh and J. Narayan. Pulsed-laser evaporation technique for deposition of thin films: Physics and theoretical model. *Physical Review B*, 41(13):8843–8859, 1990.
- [8] P. K. Carroll and E. T. Kennedy. Laser-produced plasmas. *Contemporary Physics*, 22(1):61 – 96, 1981.
- [9] D. Salzmann. *Atomic Physics in Hot Plasmas*. Oxford University Press, New York, 1998.
- [10] S. Amoruso, R. Bruzzese, N. Spinelli, and R. Velotta. Characterization of laser-ablation plasmas. *Journal of Physics B: Atomic, Molecular and Optical Physics*, 32(14):R131–R172, 1999.

- [11] B. N. Chichkov, C. Momma, S. Nolte, F. von Alvensleben, and A. Tünnermann. Femtosecond, picosecond and nanosecond laser ablation of solids. *Applied Physics A: Materials Science & Processing*, 63(2):109–115, 1996.
- [12] D. A. Cremers L. J. Radziemski. *Laser-induced plasmas and applications*. Marcel Dekker, New York, 1989.
- [13] J. A. Gaunt. Continuous absorption. *Philosophical Transactions of the Royal Society of London. Series A: Mathematical and Physical Sciences*, 229:163–204, 1930.
- [14] M. H. Key and C. Yamanaka. Some topical issues in research on short-pulse laser-produced plasmas (and discussion). *Philosophical Transactions of the Royal Society of London. Series A: Mathematical and Physical Sciences*, 298(1439):351–364, 1980.
- [15] J. F. Ready. *Effects of high-power laser radiation*. Academic Press, 1971.
- [16] M. Stapleton. *Modelling Study of the Hydrodynamic Expansion of a Laser Ablation Plume of Lithium in Vacuum*. Ph.D. Thesis, Dublin City University, 2003.
- [17] S. S. Harilal, C. V. Bindhu, M. S. Tillack, F. Najmabadi, and A. C. Gaeris. Internal structure and expansion dynamics of laser ablation plumes into ambient gases. *Journal of Applied Physics*, 93(5):2380–2388, 2003.
- [18] CVI - Melles Griot. Manufacturer's Website. <http://www.mellesgriot.com/>.
- [19] Y. Okano, Y. Hironaka, K. G. Nakamura, and K. Kondo. Time-resolved electron shadowgraphy for 300 ps laser ablation of a copper film. *Applied Physics Letters*, 83(8):1536–1538, 2003.
- [20] D. Colombant and G. F. Tonon. X-ray emission in laser-produced plasmas. *Journal of Applied Physics*, 44(8):3524–3537, 1973.
- [21] N. M. Kroll and K. M. Watson. Charged-particle scattering in the presence of a strong electromagnetic wave. *Physical Review A*, 8(2):804–809, 1973.
- [22] R. W. P. McWhirter. *Plasma diagnostic techniques*. Academic Press Inc., 1965.
- [23] C. McGuigan. *Computing Ionization Balance within Laser-Produced Plasmas*. B.Sc. Thesis, Dublin City University, 2007.

- [24] A. R. Bell, P. Choi, A. E. Dangor, O. Willi, D. A. Bassett, and C. J. Hooker. *Physical Review A*, 38:1363, 1988.
- [25] A. Levinson and R. Blandford. *Mon.Not.R.Astron.Soc.*, 274:717, 1995.
- [26] A. Remington, R. P. Drake, H. Takabe, and D. Arnett. *Physics of Plasmas*, 7:1641, 2000.
- [27] T. S. Perry, R. I. Klein, D. R. Bach, K. S. Budil, R. Cauble, H. N. Kornblum, R. J. Wallace, and R. W. Lee. Temperature and density measurements of the collision of two plasmas. *Astrophysical Journal Supplement Series*, 127(2):437–443, 2000.
- [28] R. I. Klein, K. S. Budil, T. S. Perry, and D. R. Bach. The interaction of supernova remnants with interstellar clouds: Experiments on the Nova laser. *Astrophysical Journal*, 583:245–259, 2003.
- [29] N. C. Woolsey, Y. Abou Ali, R. G. Evans, R. A. D. Grundy, S. J. Pestehe, P. G. Carolan, N. J. Conway, R. O. Dendy, P. Helander, K. G. McClements, J. G. Kirk, P. A. Norreys, M. M. Notley, and S. J. Rose. Collisionless shock and supernova remnant simulations on VULCAN. *Physics of Plasmas*, 8(5):2439–2445, 2001.
- [30] Brueckne K. A. and S. Jorna. Laser-driven fusion. *Reviews of Modern Physics*, 46(2):325–367, 1974.
- [31] T. R. Dittrich, S. W. Haan, M. M. Marinak, S. M. Pollaine, D. E. Hinkel, D. H. Munro, C. P. Verdon, G. L. Strobel, R. McEachern, R. C. Cook, C. C. Roberts, D. C. Wilson, P. A. Bradley, L. R. Foreman, and W. S. Varnum. Review of indirect-drive ignition design options for the National Ignition Facility. *Physics of Plasmas*, 6(5):2164–2170, 1999.
- [32] A new age for science? *Nature Photonics*, 2:3–5, 2008.
- [33] J. Lindl. Development of the indirect-drive approach to inertial confinement fusion and the target physics basis for ignition and gain. *Physics of Plasmas*, 2(11):3933–4024, 1995.
- [34] E. M. Campbell and W. J. Hogan. The National Ignition Facility - applications for inertial fusion energy and high-energy-density science. *Plasma Physics and Controlled Fusion*, 41(12B):B39–B56, 1999.

- [35] P. W. Rambo and J. Denavit. Time-implicit fluid simulation of collisional plasmas. *Journal of Computational Physics*, 98(2):317–331, 1992.
- [36] S. Witanachchi, K. Ahmed, P. Sakthivel, and P. Mukherjee. Dual-laser ablation for particulate-free film growth. *Applied Physics Letters*, 66(12):1469–1471, 1995.
- [37] E. Camps, L. Escobar-Alarcón, E. Haro-Poniatowski, and M. Fernández-Guasti. Spectroscopic studies of two perpendicularly interacting carbon plasmas generated by laser ablation. *Applied Surface Science*, 9(197-198):239–245, 2002.
- [38] E. Irissou, F. Vidal, T. Johnston, M. Chaker, D. Guay, and A. N. Ryabinin. Influence of an inert background gas on bimetallic cross-beam pulsed laser deposition. *Journal of Applied Physics*, 99(3), 2006.
- [39] H. Luna, K. D. Kavanagh, and J. T. Costello. Study of a colliding laser-produced plasma by analysis of time and space-resolved image spectra. *Journal of Applied Physics*, 101(1):1–6, 2007.
- [40] S. S. Harilal, C. V. Bindhu, and H.-J. Kunze. Time evolution of colliding laser produced magnesium plasmas investigated using a pinhole camera. *Journal of Applied Physics*, 89(9):4737–4740, 2001.
- [41] C. Chenais-Popovics, P. Renaudin, O. Rancu, F. Gilleron, J.-C. Gauthier, O. Larroche, O. Peyrusse, M. Dirksmüller, P. Sondhaus, T. Missalla, I. Uschmann, E. Förster, O. Renner, and E. Krousky. Kinetic to thermal energy transfer and interpenetration in the collision of laser-produced plasmas. *Physics of Plasmas*, 4:190–208, 1997.
- [42] O. Rancu, P. Renaudin, C. Chenais-Popovics, H. Kawagashi, J. C. Gauthier, M. Dirksmüller, T. Missalla, I. Uschmann, E. Förster, O. Larroche, O. Peyrusse, O. Renner, E. Krouský, H. Pépin, and T. Shepard. Experimental evidence of interpenetration and high ion temperature in colliding plasmas. *Physical Review Letters*, 75(21):3854–3857, 1995.
- [43] R. Fabbro, B. Faral, J. C. Gauthier, C. Chenais-Popovics, J. P. Geindre, and H. Pepin. Study of the emissivity of the rear face of a shocked foil with temporal and x-uv spectral resolution in single and colliding foil experiments. *Laser and particle beams*, 8(1-2):73–79, 1990.

- [44] P. W. Rambo and J. Denavit. Interpenetration and ion separation in colliding plasmas. *Physics of Plasmas*, 1(12):4050–4060, 1994.
- [45] J. D. Huba. Naval Reseach Laboratory: Plasma Formulary. <http://www.ppd.nrl.navy.mil/nrlformulary/>, Naval Research Laboratory, Washington, DC 20375, 2004. Revised Edition.
- [46] R. J. Goldston and P. H. Rutherford. *Introduction to Plasma Physics*. Taylor & Francis, 1995.
- [47] M. M. Turner. Kinetic properties of particle-in-cell simulations compromised by Monte Carlo collisions. *Physics of Plasmas*, 13(3), 2006.
- [48] M. Stapleton. Private communication, 2005.
- [49] M. W. Stapleton and J. T. Costello. Multi-fluid simulations of colliding plasmas. In *37<sup>th</sup> Conference of the European Group for Atomic Systems*, volume 291, page 159, 2005.
- [50] P. T. Rumsby, J. W. M. Paul, and M. M. Masoud. Interactions between two colliding laser produced plasmas. *Plasma Physics*, 16(10):969–975, 1974.
- [51] S. M. Pollaine, J. R. Albritton, R. Kauffman, C. J. Keane, R. L. Berger, R. Bosch, N. D. Delameter, and B. H. Failor. Stagnation and interpenetration of laser-created colliding plasmas. *APS Meeting Abstracts*, pages 12–16, 1990.

## Chapter 2

# Experimental Systems and Procedures I

Over the past four decades, studies of plasmas generated by the interaction of compact and intense laser systems have been many and wide ranging (see for example the review article [1]). The early table-top lasers developed in the period between the mid 1960s and 1970s were mainly limited to the nanosecond pulse duration region with the exception of dye lasers based on passive mode locking [2, 3]. But since the appearance of the first Ti:Sapphire laser in the late 70s [4], optical pulse durations have steadily decreased reaching the few femtosecond region [5] more than 16 years ago. The ever shortening pulse durations has brought concomitantly increasing peak pulse intensities. These intense table-top laser systems have now come to dominate much of the new science being reported in the field of laser-solid interactions.

In Chapter 1 the processes involved in the generation and evolution of the laser-produced plasmas were discussed, noting in particular that the pulse duration of the laser system plays a critical role. Nanosecond laser systems deliver relatively long pulses to the target surface. This means that the heat energy gained by the absorption of the laser pulse in the top layer of the target will have enough time to be transferred deep into the metal via phonon excitation. Plasmas generated in this way, where the transfer of heat energy into the target adds to the molten metal created by the initial laser pulse (before the eventual evaporation of the molten material) are known as 'thermal plasmas'. On the other hand, a femtosecond laser system can deliver a short duration and extremely intense pulse onto the target surface. In this case the heat-diffusion depth is significantly smaller than in the nanosecond regime as the pulse duration of the laser is typically smaller than the

lifetime of phonons in the metal, i.e., the laser pulse has terminated before an acoustic phonon in the lattice has grown to acquire a significant amplitude. There is little or no transfer of heat below the optical penetration depth (typically a few nanometers) into the bulk metal and so the intermediate melting stage is foreshortened. Plasmas generated in this way are said to undergo a direct solid-to-vapour transition.

The laser system used exclusively in the work presented here had a pulse duration of approximately  $170 \pm 20$  ps [6]. In this region, the heat-transfer depth is considerably (but not entirely) reduced. This means that plasmas generated using this laser system will share some of the characteristics inherent to both of the regimes mentioned previously, although surface melting and vaporization still remains the dominant ablation process. Plasma formation by pulses on the 100 ps timescale, explored in this thesis, were studied extensively in the late 1970s and the beginning of the 1980s because of the connection with the explosive laser compression of spherical microballoons in studies of laser-driven fusion [7, 8, 9]. However, with the emergence of femtosecond laser systems (e.g.: Ti:Sapphire) in the mid 1980s, there has been a shift in focus of these studies, leading to the picosecond regime being somewhat neglected in the literature.

Plasmas generated by picosecond laser irradiation of solid metal targets are generally hotter, significantly more dense and tend expand away from the target surface at a greater velocity than those produced in nanosecond laser ablation experiments [10]. These plasmas are also usually smaller in size, which may be due in part to the reduction in the amount of material ablated from the surface (due in turn to a reduction in the heat-diffusion depth brought about by the shorter pulse duration). The result is that picosecond laser ablation becomes very efficient at converting the laser energy into plasma [11].

The initial expansion velocity of these plasmas is extremely fast (typically  $10^6 - 10^7$  cm/s) so that the birth, expansion and demise of a laser produced plasma can take place in little over  $1 \mu\text{s}$ . The rapid initial heating of the critical layer of the plume to  $> 100$  eV leads to a burst of X-rays [12] which can be used as a diagnostic tool (see Dardis *et al.* [13]) of dense media like other plasmas.

In this chapter the operation of the experimental systems used to generate and characterize laser-produced plasmas will be presented. Particular attention will be paid to the table-top picosecond laser system which is capable of producing gigawatt (GW) level laser pulses. Our discussion will then move to a description of

the experimental apparatus, examining in detail the optical and target geometries for the production of both single plasmas and colliding plasma systems. In the final section the optical diagnostic systems used to characterize the plasmas generated by this intense picosecond laser system, in both the soft X-ray and visible spectral regions will be presented.

## 2.1 The EKSPLA™ 312p Laser System

The key component of the experimental setup was the EKSPLA™ 312p Nd:YAG (Neodymium:Yttrium Aluminium Garnet) laser system. A schematic diagram of the laser is shown in figure 2.1. The laser system is divided into three main parts, the oscillator, the pulse compression stage and the amplifier stage.

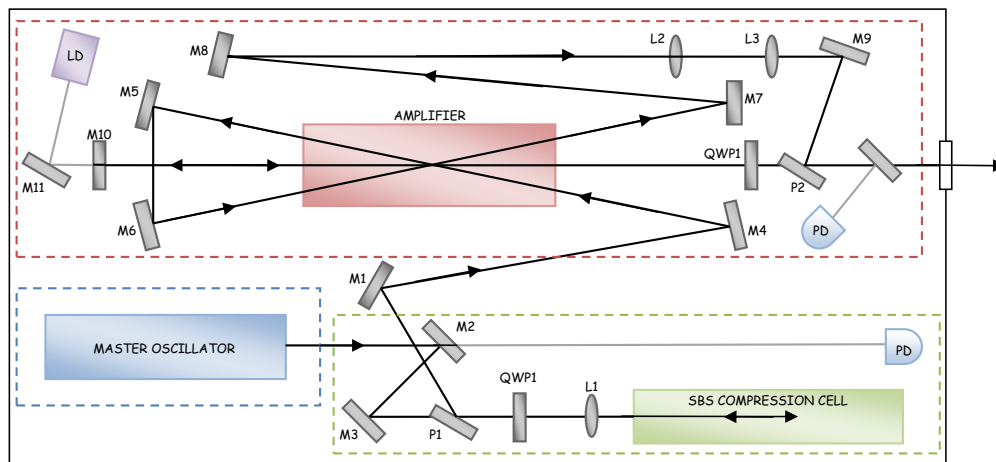


Figure 2.1: Schematic diagram of an EKSPLA™ SL312p laser system [6] with the three main stages (the oscillator, compression chamber and amplifier) highlighted by blue, green and red dashed boxes respectively. Abbreviations used in diagram, M: mirror, P: polarizer, QWP: quarter-wave plate, L: lens, PD: photodiode, LD: laser diode.

### Oscillator

The master oscillator consists of a module of rigid design which is mounted on invar<sup>1</sup> rods ensuring mechanical and thermal stability. A separate module containing the Nd:YAG rod (4 mm diameter, 5 cm long) and a xenon flashlamp (Verre et

<sup>1</sup>A nickel-steel alloy which has a low coefficient of thermal expansion [14].

Quartz Flashlamps, Bondy, France [15]) is positioned onto the first module using dowels and fixed in place using screws. The single flashlamp operating at 5 Hz is located above the rod inside this module which is water-cooled in order to remove the excess heat generated during optical-pumping of the laser rod. The optical cavity is formed by a 100% reflectivity mirror (M1) and an un-coated glass Fabry-Pérot etalon. The main components which form the optical cavity are illustrated in figure 2.2. The etalon ensures that the cavity is operating with a single longitudinal mode (SLM) or single frequency which is a strict requirement for the pulse compression stage. The Pockels cell is divided into two sections. The first part (between electrodes *a* and *b*) is used as a classical Q-switch, while the second part (between electrodes *b* and *c*) together with the polarizing beam-splitter (P1) and photodiode (PD1) form part of the negative feedback system.

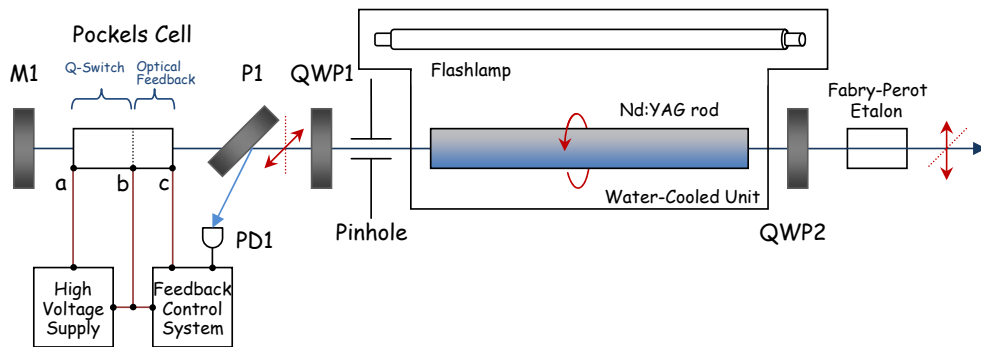


Figure 2.2: Schematic of the master oscillator in an EKSPLA™ SL312p laser system [6]. Abbreviations used in diagram, M: mirror, P: polarizing beam-splitter, QWP: quarter-wave plate, PD: photodiode. The red arrows indicate the direction of the polarization vector of the laser beam, circularly polarized light within the laser-rod, and linearly polarized elsewhere. Both the flashlamp and the laser-rod are housed in a removable module which is water-cooled.

When the process of optical pumping of the laser rod is initiated emission in the region between 700 nm – 1000 nm is produced which overlaps with strong absorption lines in Nd. The Nd ions in the YAG host are excited (pumped) to an upper energy level from where they undergo a rapid non-radiative decay into a metastable state. The lifetime of this level is relatively long in comparison to the other participating levels and so population inversion is achieved. Spontaneous emission leading to lasing occurs when the atoms relax back to an intermediate (lower) level. Hence Nd:YAG is a four level system [16]. In a Nd:YAG oscillator the strongest laser transition occurs at a wavelength of 1064 nm, however other laser transitions occur at

wavelengths of 946 nm, 1123 nm, and 1319 nm. Coinciding with the optical pumping, a high voltage is applied to the Pockels cell, which when energized acts as a quarter-wave plate. Light generated in the laser rod will pass through the Pockels cell twice on its journey through the optical cavity and therefore the net effect of the Pockels cell is to rotate the polarization vector of the light by a full  $180^\circ$  - similar to the operation of a half-wave plate. When the light reaches the end of the cavity it is reflected by the Fabry-Pérot etalon where the parallel reflecting surfaces serve to enhance a single frequency. The radiation continues to bounce from either end of the cavity. As the intensity of light in the cavity grows in the regime known as free-running, a small proportion of it will be reflected onto the photodiode (labeled PD1 in figure 2.2). The diode forms part of the optical feedback system and the signal is used to control the duration of free-running operation. The voltage applied to the second part of the Pockels cell (between nodes b and c) is proportional to the light intensity falling on this photodiode. This negative feedback system enables the oscillator to continue lasing for up to a few microseconds. This signal will increase as the intensity within the cavity grows. When the voltage reaches a threshold value, predefined by the user, the high-voltage on the Pockels cell is switched to ground. On its final journey through the cavity the Pockels cell is off and so the polarization of the light remains unchanged. The light passes through the Fabry-Perót etalon and leaves the cavity. This process of dumping the energy stored in the cavity using a Pockels cell is known as active Q-switching and gives rise to output pulses of nanosecond duration, in this case a 4 ns pulse is formed.

A pinhole aperture with a diameter of 3 mm is also located in the optical cavity (labeled in figure 2.2). The pinhole acts as a spatial filter to reject the higher-order modes from the beam and ensures TEM<sub>00</sub> (transverse electromagnetic) or single transverse mode operation. When the two counter propagating light waves combine within the laser rod they become superimposed and a standing wave will be formed. This standing wave will act to distort the distribution of the gain along the length of the crystal, and hence the optical intensity will also vary along its length. This will give rise to the effect known as spatial hole burning [17] which acts to disrupt the single-frequency operation of the cavity. By installing two quarter-wave plates (QWP) on either side of the laser rod, in what is known as the 'twisted-mode' technique [18] this effect can be eliminated. As linearly polarized light passes through the first quarter-wave plate it becomes circularly polarized. Then passing through the second quarter-wave plate it will revert to linear polarization but having gained a rotation of  $90^\circ$  with respect to the initial linear polarization vector. On reflection from the output coupler (in our case the Fabry-Perót etalon) the light

passes through the QWP series for a second time on its return journey and is converted back to circularly polarized light. Because the polarization handedness of the outward and return light waves propagating within the laser rod are opposite in direction an interference pattern will not be generated<sup>2</sup>. In this way the optical intensity is constant along the length of the laser rod and the effects of hole burning are suppressed. This enables single-frequency operation to be achieved much more easily which is a critical mode of operation for the compression process to follow.

Optical pumping of a laser rod using flashlamps is a fairly low-efficiency scheme. Photons are produced not only at the absorption wavelength(s) of the crystal but over a broad wavelength band. This low efficiency results in excessive heating of the laser rod. To ameliorate this effect the oscillator module is temperature stabilized using water cooling, connected via pipes to a tank of de-ionized water. The flashlamps operate at a repetition rate of 5 Hz. The output from the oscillator consists of a 3 mJ pulse of 4 ns duration which is linearly polarized in the vertical direction. The output energy of the oscillator was monitored by a calibrated photodiode (PD1 in figure 2.2) and was displayed on a remote control pad.

## Pulse Compression

The nanosecond duration pulse generated within the oscillator is directed towards the second stage of the laser, the pulse compression system. The laser pulse initially passes through a quarter-wave plate (QWP1 in figure 2.1) which changes the state of its polarization from linear to circular before being focused into a cell (SBS compression cell in figure 2.1) containing carbon-tetrachloride ( $\text{CCl}_4$ ) at high pressure<sup>3</sup>. Through a process known as stimulated Brillouin scattering (SBS) [19] the 4 ns pulse from the oscillator is compressed to a duration of  $\sim 170$  ps. The temporal compression of the nanosecond pulse to picosecond duration occurs in the following sequence: The laser beam generates an acoustic wave in the solvent at the point of focus through the process of electrostriction, which is the tendency of materials to become more dense in regions of high optical intensity [20]. This acoustic wave created by the density modulation within the solvent leads to a localized region of high refractive index. When the laser pulse impinges upon this mirror-like region (phase conjugate mirror [19]) a percentage of its intensity will be

---

<sup>2</sup>An interference pattern does in fact occur for each of the linear polarization components but they are out of phase with each other and so patterns do not form over the full length of the rod.

<sup>3</sup>The pressure within the SBS cell is typically several hundred bar, but in this case it has not been disclosed by the manufacturer.

reflected. This backscattered radiation is known as the Stokes pulse and it propagates in the opposite direction to the laser, back towards the entrance window of the cell. If the length of the SBS cell is chosen such that the backscattered Stokes pulse overlaps perfectly with the incident beam then as the Stokes pulse propagates it begins to beat with the counter-propagating laser pulse [21]. The point of high intensity and concomitantly, the point of reflection travels backwards leading to exponential growth of the intensity of the Stokes radiation.

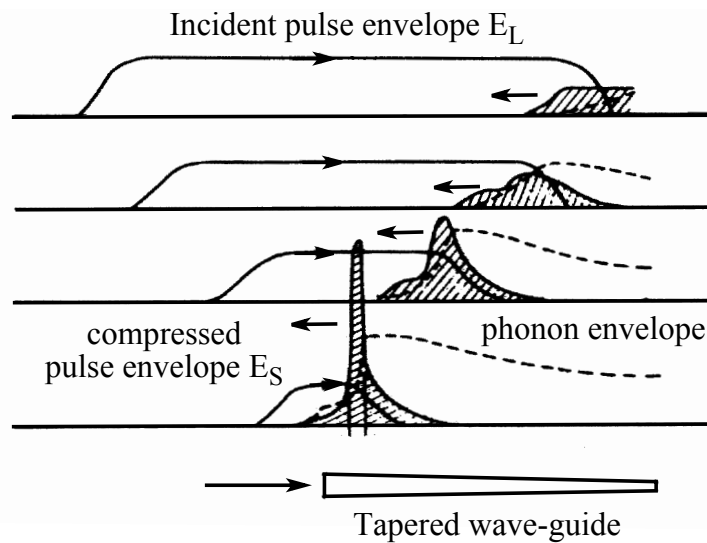


Figure 2.3: Pulse compression by stimulated Brillouin scattering in a tapered waveguide (after [21]).

The physical key to the compression process can be explained with the aid of figure 2.3 where the time sequences of the three interacting fields, the laser (approximated by a square wave), the Stokes pulse and the acoustic wave are shown (after Hon (1980) [21]). In the first sequence a small acoustic wave is generated at the end of the taper where the intensity of the laser is highest. The next time-sequence shows that the acoustic wave has grown in strength, due to the beating of the backward Stokes pulse with the incident laser. The leading edge of this wave forms the position of the mirror and as this front propagates backwards one will see from the last two time-sequences that the Stokes pulse grows in amplitude. The majority of the intensity is localized into a very narrow temporal window which results in the reflected beam having a pulse duration significantly less than the incident pulse [21].

Both the intensity and the mode structure of the laser are critical factors in efficient SBS compression. If the intensity of the laser is below the Brillouin threshold of the medium then electrostriction will not occur and the laser beam will propagate through the cell. Similarly, if the laser oscillator is not operating in single longitudinal mode, the backscattered Stokes pulse will not overlap with the laser beam, beating will not occur and there will be no further amplification of the Stokes pulse leading to compression [22]. Pulse compression based on SBS was first demonstrated in 1980 by Hon [21] in solid-state media (quartz, sapphire) but liquid and gaseous media soon became favored for use over solid-state media because of the reduced risk of bulk damage (i.e., crystal fracture), caused by the high optical intensities needed to drive the process. The pulse compression ratio [23] is proportional to the phonon lifetime in the medium and the pulse duration of the input pulse ( $K = \tau_L/\tau_S$ ). The highest compression ratios are achieved with SBS media that possess short phonon lifetimes.  $\text{CCl}_4$ , which is used in the EKSPLA™ 312p laser system, is an ideal candidate for an SBS medium because it has one of the shortest phonon lifetimes of most tetrachlorides, resulting in a very high compression ratio [19].

The backward propagating Stokes pulse is phase conjugated with the input pulse and as such will exit the cell with the same circular polarization. The duration of the output pulse is  $\sim 170$  ps, implying a compression ratio of ca. 24. Passing through QWP1 the compressed pulse is converted to linear polarization and is reflected by the polarizing beam splitter (P1) into the amplification stage. The strict prerequisite of the SBS process on the mode structure of the input laser ensures that the output laser pulse is always of excellent quality. Furthermore, the fact that the Stokes pulse is the phase-conjugate of the input pulse means that wavefront distortions in the beam are corrected [24]. This gives the EKSPLA™ 312p laser system a superior advantage over laser systems incorporating other forms of compression systems [25].

## Amplification

After the compression stage, the pulse is directed to a multi-pass power amplifier. Here the beam passes through another Nd:YAG rod (12 mm diameter, 100 mm long) with Brewster-angled<sup>4</sup> end-faces, that is optically pumped via two xenon flashlamps. The beam passes through the amplifier rod twice (bouncing between mirrors M4 and M7 in figure 2.1) before being expanded up to a diameter of  $\sim$

---

<sup>4</sup>The angle at which the reflection losses at the air-glass interface are significantly reduced for light with polarization parallel to the surface (p-polarized).

12 mm by a telescope assembly (L2 and L3 in 2.1) and passing through the rod a further two times (M9 and M10 in 2.1). The pulse exits the laser system with a maximum energy of  $\sim 500$  mJ. By varying the power supplied to the amplifier flash-lamps one can control the overall power of the output pulse, without affecting the duration of the pulse. This control function is available on an external and portable key-pad. The pulse duration is approximately 170 ps (FWHM) and so the peak power can reach a maximum of  $\sim 3$  GW.

Parameter	Value
Pulse Duration	$170 \pm 20$ ps
Peak Energy	500 mJ
Wavelength	1064 nm
Repetition Rate	5 Hz
Mode	TEM <sub>00</sub>
Polarization	Linear (Vertical)
Beam Diameter	$\sim 12$ mm

Table 2.1: Specifications of the EKSPLA™ SL312p Nd:YAG laser. [6]

The specifications of the laser system are given in table 2.1. Whilst this laser can operate via an external trigger pulse, in practice it was found that the shot-to-shot pulse energy (*in particular when operated in single shot mode*) became very unstable. Therefore the laser was operated in internal trigger mode<sup>5</sup> and the output from the Pockels cell was used as the master trigger for synchronization with the rest of the experimental apparatus.

Although very compact in size (250 mm  $\times$  190 mm  $\times$  775 mm) the output of the EKSPLA™ 312p laser system is both powerful (up to the gigawatt peak power level) and of high beam quality. The laser operates in TEM<sub>00</sub> mode and has a near-Gaussian beam profile which means that the beam can be focused down to extremely small spot sizes with diameters in the region of 20  $\mu$ m [26]. With its 0.5 J output and 170 ps pulse duration, the EKSPLA™ 312p laser system bridges the gap between laboratory-scale nanosecond and femtosecond lasers permitting laser plasma studies in a relatively unexplored laser parameter regime.

In the following section the overall experimental setup used to diagnose these plasmas is introduced. These diagnostics included soft X-ray spectroscopy and pinhole imaging for single plasma plumes (used later in plasma-plasma collision experi-

---

<sup>5</sup>By allowing the laser to fire a number of times before each required shot, the negative-feedback system was able to stabilize the output energy.

ments), as well as optical imaging and spectroscopy of the collision plane between the two colliding plasmas.

## 2.2 Experimental Setup

The experimental layout for the study of intense laser interactions with solids is shown in figure 2.4. The main components are the laser system, the optical isolator and the vacuum chamber which contains the focusing optics and the target holder. Both the wedge prism and the target holder were mounted on computer controlled translation stages while the the focusing optics are secured to manually controlled stages. The optical diagnostic systems are also shown in the figure highlighted by the four boxes (dashed blue lines). The two X-ray diagnostics, namely the pinhole camera and the Bragg crystal spectrometer were located inside the vacuum chamber, with only one system available for use at any one time. The two optical diagnostic systems were positioned outside the vacuum chamber. The Chromex™ visible spectrometer was mounted on an optical table which had micrometer controlled height and position adjustment and is shown at the bottom of figure 2.4. The visible emission imaging setup is shown at the top of the figure.

The reflected infrared radiation ( $\lambda = 1064 \text{ nm}$ ) from mirrors, lenses or windows can in some instances be as much as 4% of the total pulse energy per reflection [27]. This reflected power can reach significant values when using picosecond laser pulses. If this reflected laser light re-enters the laser it may be re-focused inside the amplification stage and cause severe damage to the amplifier rod. To avoid this hazard, back-reflections can be directed away from the exit aperture of the laser by aligning the laser slightly off-axis with respect to the optics in the vacuum chamber. This method, while proving successful at eliminating the dangers associated with back-reflections, distorts the focal spot shape on the target surface (astigmatism), making it a more oval in shape and thereby reducing the on-target irradiance. Another solution, and one which was adopted here, was to place an optical isolator or Faraday rotator (Electro-Optics Technology, HP-15-I-1064-090) between the laser and the target chamber. This device allows all optical components to be collinear, ensuring a small focal spot diameter, while preventing any damage to the optical elements inside the laser system.

The optical isolator consisted of a Faraday rotator encased in a strong magnet, which was in turn located between two crossed polarizers. The unit was aligned so the the input polarizer was parallel with the polarization of the laser. The isolator

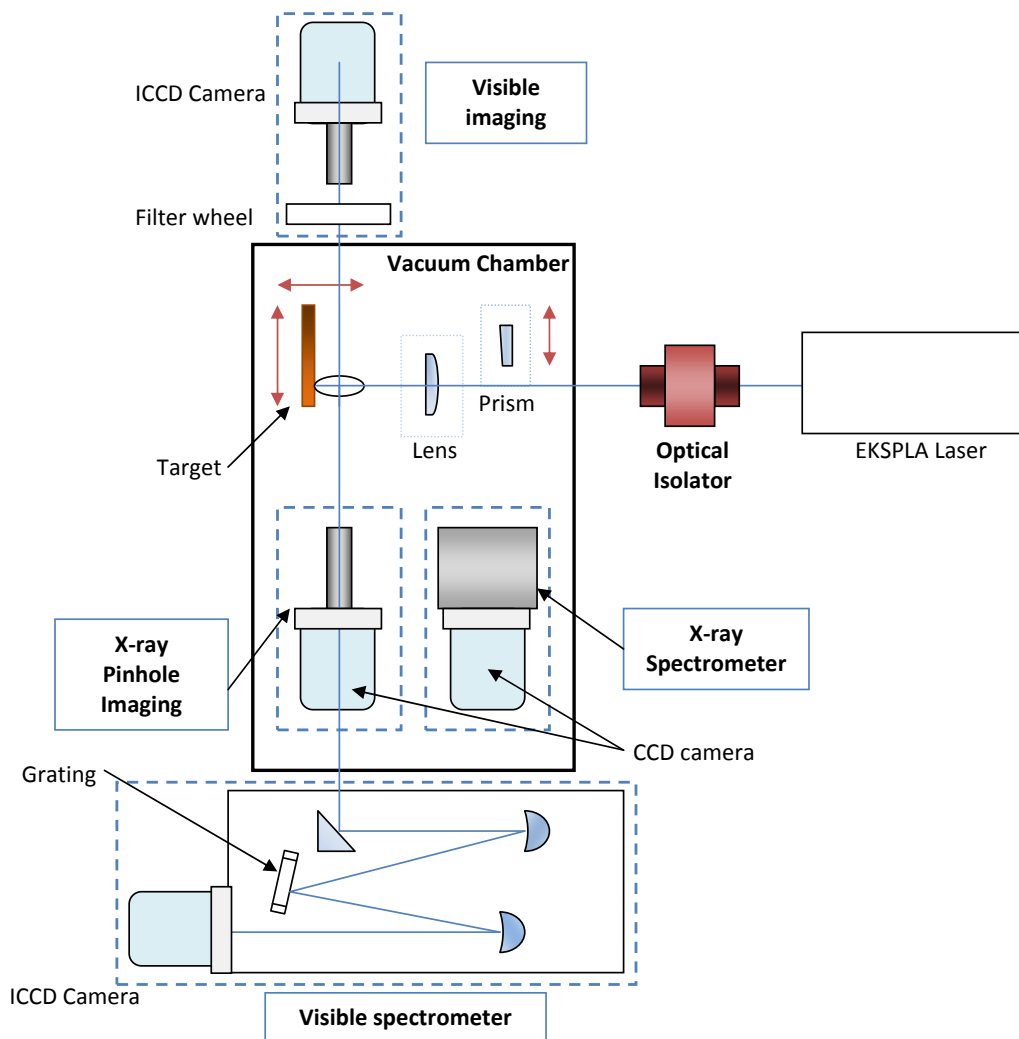


Figure 2.4: Experimental setup for the study of intense laser interactions with solids. Highlighted in blue dashed boxes are the four diagnostic systems used during this study. Located inside the vacuum chamber are the two X-ray diagnostics, namely the pinhole camera and the Bragg crystal spectrometer, while the two optical diagnostic tools, namely the 0.5 m Chromex™ visible spectrometer and the visible emission imaging setup are located outside the chamber, at the bottom and top of the diagram respectively. Also shown is the EKSPLA™ 312p laser system, the optical isolator, the wedge prism and the focusing optics. The red arrows indicate the direction of translation (motorized) of the target and the wedge prism respectively.

rotates the plane polarized light of the laser by  $45^\circ$  which was then passed by the second polarizer. Any back-reflected light is rotated a further  $45^\circ$  and so it is blocked/absorbed by the input polarizer. This setup eliminates the danger posed by

back reflections, but unfortunately reduced the power of the laser beam reaching the target surface by up to 10%

Figure 2.4 shows the location of each component in the experimental setup. The laser beam was steered into the vacuum chamber via a periscope and brought to a focus on a metal target by an anti-reflection coated plano-convex lens which had an effective focal length (*eff.*) of approximately 100 mm or less. The EKSPLA™ 312p laser system operates in TEM<sub>00</sub> [6] mode and the smallest focal spot diameter achievable with this type of laser system was reported by the Michette group in King's College London to be ca. 20 μm [26].

## 2.3 Optical Setup for Colliding Plasma Systems

All experiments on the collision of laser produced plasmas require the simultaneous production of two or more plumes. In the course of this work a simple setup described by Harilal *et al.* in 2001 [28] was adopted which uses a wedge prism to deviate a defined portion of the laser beam.

Wedge prisms are normally used in beam steering applications, where the entire laser beam goes through the center of the optic. As the prism is rotated the path of the laser beam will trace out a circle, the radius of which is proportional to the acute-angle of the wedge prism. However, if one bisects a laser beam using a wedge prism as is illustrated in figure 2.5, then only the portion going through the prism will be deflected. By placing a focussing optic after the prism, the two (*diverging*) beams will be focused to two different points on the focal plane. This was the method by which two laser-produced plasmas were generated within close proximity, and is illustrated in figure 2.5

The distance between the two foci  $d$  and hence the distance between the two plasmas can be determined by [28]

$$d = \gamma f(n - 1) \quad (2.1)$$

where  $\gamma$  is the wedge angle in radians,  $f$  is the focal length of the lens in mm and  $n$  is the refractive index of the optics (here  $n = 1.5$ ). By changing either  $\gamma$  or  $f$  the separation between the two foci and thus the separation between the plasmas can be controlled. The ratio of the flux in each of the two focal spots can also be adjusted by changing the vertical position of the prism in the beam (Y-translation in 2.5). The individual point plasmas are referred to as 'seed' plasmas from this point

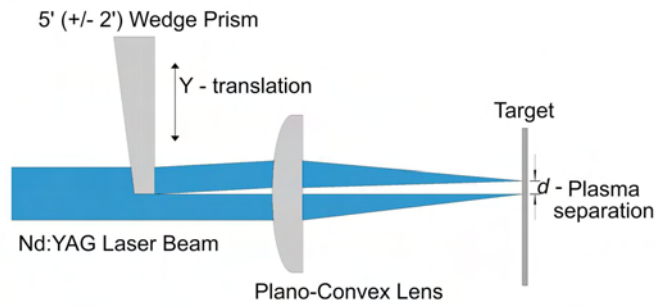


Figure 2.5: Optical system incorporating a wedge-prism and plano-convex lens which is used to split the laser beam into two parts, which are subsequently used to generate two point-plasmas on metal targets (after Harilal [28]). The wedge prism was mounted onto an in-vacuum motorized translation stage which allowed control of the height and hence the energy sharing between the two laser beams.

onwards in order to distinguish them from plasmas in the vicinity of the collision front (e.g., a stagnation layer).

## 2.4 Target Configurations

Single plasmas were formed on flat metal targets in vacuum ( $p < 10^{-4}$  mbar) with the laser at normal incidence and the various detectors positioned perpendicular to the plasma expansion plane. The targets were placed on computer-controlled motorized translation stages giving full X-Y-Z movement. The target was translated after a user-defined number of consecutive laser shots which prevented the formation of craters could have occluded the emission from the micron-scale X-ray emitting core of the plasma.

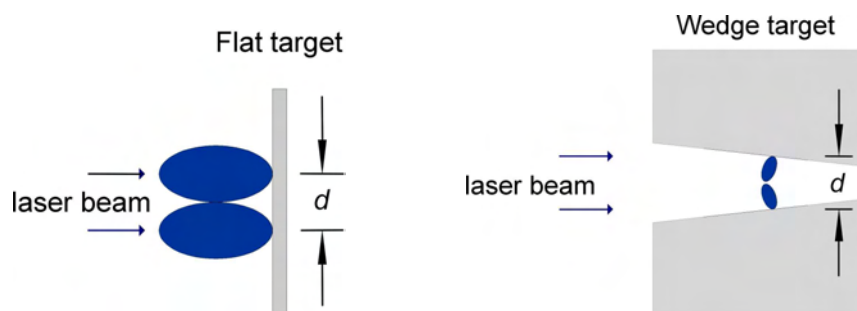


Figure 2.6: Target configurations used in studies on colliding plasma systems. Left: flat target used for studies on laterally colliding plasmas, right: wedge-shaped targets used for studies on orthogonally colliding plasmas.

Two different target configurations were used during the study of colliding plasma systems. In figure 2.6 one can see both configurations; on the left-hand side is a flat target while on the right-hand side is the wedge-shaped target. The orientation of the seed plasmas with respect to each other will in large measure determine the collisionality of the system and to what extent the two plasmas will interact. The primary study was done by generating two seed plasmas on flat metal targets and allowing them to expand into vacuum. As they expanded they collided along their lateral expansion plane. By controlling  $d$ , the separation between the two plasmas, it is possible to vary the collisionality parameter of the system [29]. When  $d$  is large, one can expect the collisionality parameter to be low and so 'soft stagnation' [30, 31] would be expected to occur. However, when  $d$  is small, on the order of the size of the plasma, then one would expect to observe the formation of a well defined stagnation layer [28].

Plasma expansion velocities normal to the target surface are typically an order of magnitude larger than parallel to the surface (lateral expansion plane) as has been documented in the literature [32, 33]. Therefore the collisionality of the system can be significantly decreased by the use of wedge-shaped targets. In this case the two plasmas are now forced to counter propagate in an almost opposed fashion so they will expand and subsequently collide with a larger component of forward expansion velocity. As the relative collision velocity is high, one can see from equation 1.27 on page 24 that the ion-ion mean free path will be large, and so one might expect to observe a higher degree of plume interpenetration occurring than in the flat-target case.

## 2.5 Photon Diagnostics

Plasma parameters such as electron temperature and density, along with plume expansion velocity were obtained via imaging and spectroscopy in the soft X-ray and visible spectral regions. Using a gigawatt laser, relatively hot seed plasmas which would emit predominantly in the extreme-ultraviolet (EUV) and soft X-ray spectral regions are expected to be generated. Imaging of these plasmas in the soft X-ray region was done using a pinhole camera incorporating a pinhole and a back-illuminated CCD (charge-coupled device) camera. This setup gave time-integrated images of the expanding plasma plumes. A Bragg crystal spectrometer was used to obtain time-integrated spectra of the hot plasma. The photon diagnostics in the visible spectral region comprised of a gated CCD camera with a

micro-channel plate (MCP) image intensifier which provided time-resolved images. The operation of this system has been described in detail in Kavanagh (2006) [34]. Visible emission images of the colliding plasma system tracked the expansion and collision of the seed plasmas in successive time windows of 5 ns duration. Emission from individual ion stages was selected using spectral filters which isolated particular emission lines originating from a single ion species. Plume expansion velocities, as well as the formation/evolution of the stagnation layer could be extracted using this spectrally resolved visible emission imaging technique. Visible emission spectroscopy was used to determine plasma electron temperatures and densities and is described in section 2.5.4.

Previous work on colliding plasma systems has been done on plasmas generated using laser systems with output pulses in the few nanoseconds to few tens of nanoseconds range [35, 36, 37, 38]. Using the EKSPLA 312p picosecond laser system we had the opportunity to extend this research into the picosecond domain, where the plasmas would be much hotter and would be expected to evolve on a faster time-scale than in previous studies. Analysis in both the soft X-ray and visible spectral regions was performed using the same equipment described above.

As the plasmas generated using this laser system are expected to emit predominantly in the soft X-ray spectral region the first plasma diagnostic tool used was X-ray imaging with the aid of a pinhole camera enabling the extraction of the dimension of the hot, X-ray emitting, core of the plasma. Time-integrated spectroscopy of the plasma core was performed in the soft X-ray spectral region using a Bragg crystal spectrometer. Emission from various ionic charge states were identified in these spectra leading to an estimation of the local electron temperature within the hottest regions of the plasma. Once diagnostics in the soft X-ray spectral region were complete attention shifted to the visible spectral region to determine the electron density and temperature of the bulk plasma with spectroscopy in the UV – visible region of the electromagnetic spectrum. What follows is an overview of the apparatus used for each diagnostic tool.

### **2.5.1 X-ray Imaging**

X-ray imaging of laser-produced plasmas using a pinhole camera is a simple and versatile method to determine plume dimensions and estimate the expansion velocity of the plasma. The pinhole camera illustrated in figure 2.7, consisted of a 5  $\mu\text{m}$  pinhole and an in-vacuum back-illuminated X-ray sensitive CCD (Andor Technology™ DX420BN) which had 1024  $\times$  256 detector array with 26  $\mu\text{m}$  pixel

pitch. A schematic diagram (figure 2.8) and a photograph (figure 2.7) of the layout are shown on the following page. The schematic shows the target and pinhole both mounted on computerized translation stages. The pinhole views the plasma plume normal to its expansion direction. As with any pinhole aperture, diffraction effects can contaminate the image and must be estimated. A rough criterion for the determination of the minimum aperture size before the onset of appreciable diffraction effects can be obtained from the following equation [39],

$$F = \pi a^2 / 4 \lambda d \quad (2.2)$$

where  $a$  is the radius of the pinhole,  $d$  is the target to pinhole distance and  $\lambda$  is the wavelength of the radiation in meters. Equation 2.2 reveals two distinct regions where the extent of diffraction in the imaging system is either strong or negligible: When  $F > 1$ , the imaging system is firmly within the region where diffraction effects are negligible, while for  $F < 1$ , the images acquired by the pinhole camera will be distorted by significant diffraction caused by the micron-scale circular aperture. In the imaging system presented here, where  $d \approx 3$  cm and  $\lambda \approx 1$  nm, a minimum pinhole diameter of  $2 \mu\text{m}$  was calculated (by setting  $F = 1$ ), which implies that diffraction was not an immediate concern with this setup.

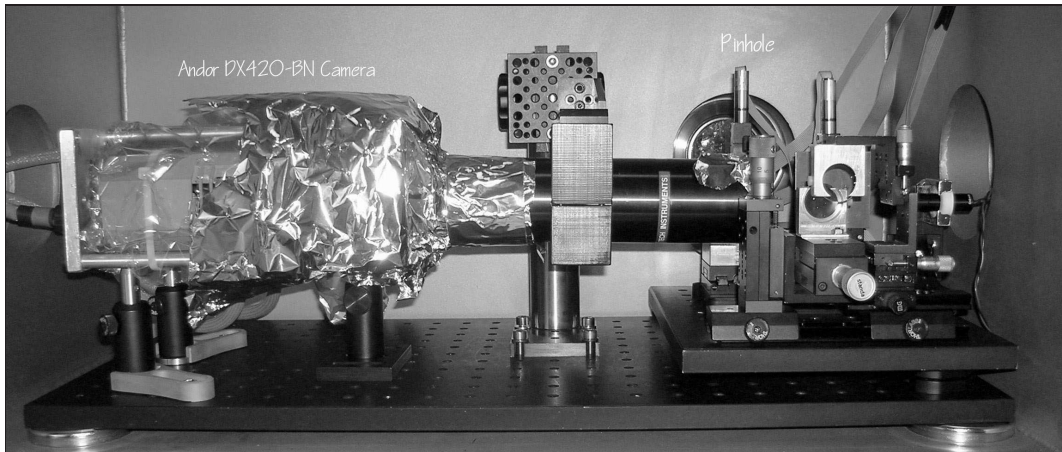


Figure 2.7: Photograph of the X-ray pinhole camera setup used for X-ray emission imaging showing the CCD camera encased in aluminium foil on the left, the 300 mm long extension tube in the middle with the pinhole attached to the end and the target holder on the right.

A  $3 \mu\text{m}$  thick aluminum filter was placed in front of the CCD camera in order to select only soft X-ray wavelengths below  $\sim 1$  nm. The X-ray transmission of this filter was obtained from the CXRO (Center for X-Ray Optics) website [40] and is

shown in figure 2.10 on page 51. The pinhole was positioned  $\sim 30$  mm from the focal spot position (the object distance) and a 300 mm long aluminium tube was placed between the pinhole and the camera in order to shield it from stray laser light which was present in the chamber. The ratio between the object distance and the image distance yielded a magnification of  $10\times$ .

In the photograph of the X-ray pinhole setup (figure 2.7) one can see the camera on the left-hand side of the picture with the coupling tube in the middle and the pinhole, target mount and focusing optics on the right of the photograph. It was necessary to encase both ends of the 300 mm long tube in aluminium foil in order to prevent any scattered laser light reaching the CCD chip.

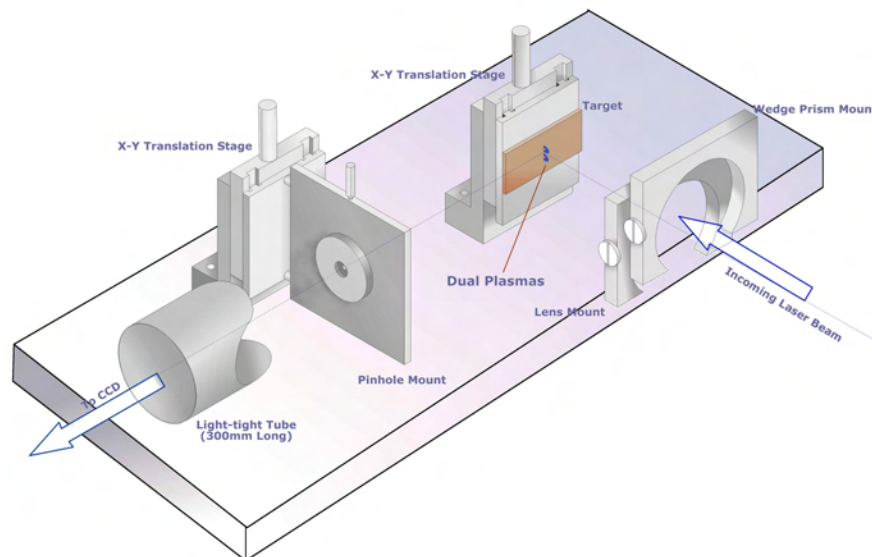


Figure 2.8: Schematic diagram of the X-ray pinhole camera setup used for X-ray emission imaging. Both the target and the pinhole are fixed to computer controlled translation stages which give accurate position control down to a fraction of a millimeter.

A plasma was created on the surface of the target and an image of the plasma projected onto the CCD chip. The X-ray sensitive camera was not gateable and had a minimum integration time of 30 ms. It was set to integrate over a  $\sim 1$  s period. The magnification ( $M$ ) of the system was determined using the equation  $M = v/u$ , where  $v$  is the image distance ( $\sim 300$  mm) and  $u$  is the object distance (30 mm). Hence the pinhole camera operated with a magnification of  $10\times$  and therefore each pixel on the CCD chip represented an effective dimension of 2.6

$\mu\text{m}$  in the object plane, sufficient to determine the plasma emitting size, which was expected to be on the order of 10 microns.

## 2.5.2 X-ray Spectroscopy Setup

A Bragg crystal spectrometer was used to obtain spectra of the hot seed plasmas. The spectrometer incorporated a flat KAP (potassium acid phthalate) crystal, which had a  $2d = 2.66 \text{ nm}$  (*lattice constant*), as the dispersing element. The crystal (dimensions:  $25 \text{ mm} \times 40 \text{ mm}$ ) was positioned on a rotational mount which was located in the centre of the circular-shaped casing of the spectrometer (see figures 2.9 and 2.14). The detector system was the same in-vacuum back-illuminated CCD camera as used in the soft X-ray imaging experiments. The camera was fitted to the outside of the spectrometer by an adaptor which coupled the flat edge of the camera to the curved edge of the spectrometer. The entrance slit of the spectrometer consisted of metal plate to which transmission filters could be fixed.

The operating range of the spectrometer was determined using the Bragg equation;

$$n\lambda = 2d\sin(\theta) \quad (2.3)$$

where  $d$  is the lattice spacing of the crystal,  $\theta$  is the angle of the crystal with respect to the plane normal to the entrance slit and  $n$  is the diffraction order number (here equal to unity). The flat KAP crystal used as the dispersing element during the work presented here can operate comfortably within the range  $0.23 - 1.88 \text{ nm}$  corresponding to crystal angles of  $5^\circ$  and  $\sim 45^\circ$  respectively. The lower-limit on the operational angle of the crystal is due to the fact that, at more shallow angles, radiation from the plasma can enter the spectrometer and bypass the crystal. Some of this radiation may fall upon on the CCD chip without being reflected resulting in a portion of the chip being saturated from white-light (within the X-ray spectral region) from the plasma. By using a different dispersing crystal, for example pentaerythritol ammonium dihydrogen phosphate (ADP) which has a  $2d = 1.0648 \text{ nm}$  the operating range of the spectrometer can be further extended into the X-ray spectral region.

A schematic diagram of the Bragg crystal spectrometer is illustrated in figure 2.9. The centre wavelength ( $\lambda_c$ ) of the spectrometer was selected by rotating the angle of the crystal. This angle was set before the entire spectrometer (including the CCD camera) was fixed to the optical base-plate and located inside the vacuum chamber, hence the wavelength range captured by the  $26 \text{ mm}$  long CCD was fixed

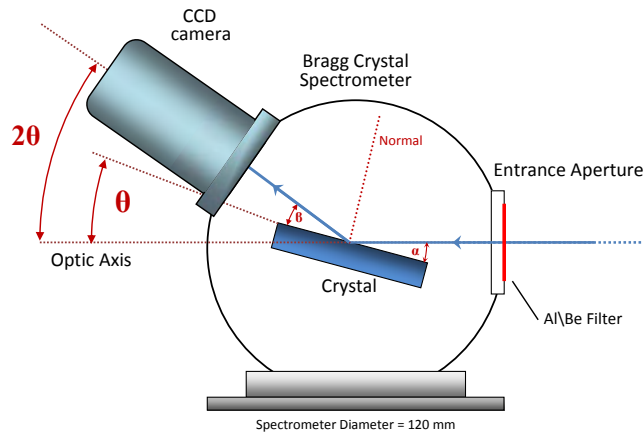


Figure 2.9: Schematic diagram of the soft X-ray crystal spectrometer. Radiation from a point-like plasma passes through an entrance slit and impinges on the dispersing crystal which is set at an angle  $\theta$  with respect to the optic axis, and is subsequently Bragg reflected onto the CCD chip positioned at an angle  $2\theta$ .

for the duration of the experiment. The expanding X-ray beam from the hot plasma was incident on the KAP crystal and each incident ray was Bragg reflected at twice its angle of incidence. The CCD camera was fitted to the spectrometer with the centre of the CCD chip positioned at twice the angle of incidence for the central ray. The spectrometer was supplied with a scale engraved onto the side of the spectrometer body (see inset in figure 2.14) which aided the angular alignment of both the crystal and the CCD camera; each division on the angular scale corresponds to  $2^\circ$ .

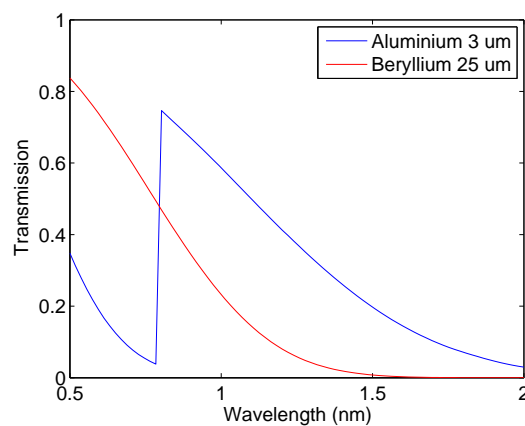


Figure 2.10: Transmission of  $3 \mu\text{m}$  thick aluminium and  $25 \mu\text{m}$  beryllium filters used to isolate plasma emission to the EUV and soft X-ray spectral regions [40].

A 3  $\mu\text{m}$  thick aluminium metal filter (or 25  $\mu\text{m}$  thick beryllium filter) can be placed across the entrance aperture of the spectrometer to protect the dispersing crystal from plasma debris and limit radiation incident on the crystal to the X-ray range. The X-ray transmissions of each filter, obtained from the Berkeley CXRO website [40] are shown in figure 2.10. It is clear from figure 2.10 that beryllium is best for wavelength measurements below 0.8 nm while aluminium works well in the 0.8 – 1.5 nm spectral range. In order to shield the camera from scattered laser light a second Al or Be X-ray filter is placed directly in front of the CCD sensor.

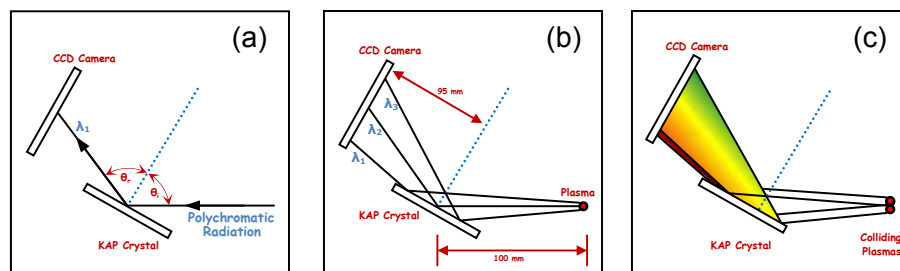


Figure 2.11: Simplified diagrams illustrating the operation of a Bragg crystal spectrometer. (a) In the simple case, a single polychromatic ray enters the spectrometer and impinges on the KAP crystal at an angle of  $\theta_i$ . The Bragg equation is satisfied only for one single wavelength ( $\lambda_1$ ) determined by the Bragg criterion  $\theta_i = \theta_r = \theta_B$ , where  $\theta_B$  is the Bragg angle, resulting in constructive interference. (b) When the spectrometer is used in conjunction with a laser-produced plasma, a fan of polychromatic rays from the plasma impinge on the crystal. The Bragg equation is now satisfied for a range of different wavelengths corresponding to discrete angles lying within the opening angle set by the aperture presented by the diffracting crystals. In this case the crystal acts as a dispersing element and a spectrum is formed on the CCD chip. (c) In the special case of colliding plasma systems, X-ray emission from the two seed plasmas appears at different positions on the CCD chip.

The operation of the spectrometer can be explained with the aid of figure 2.11. In the simplest case, a single polychromatic ray enters the spectrometer and strikes the KAP crystal at an angle of  $\theta_i$ . The ray is coherently reflected only if the wavelength and incident angle values satisfy the Bragg equation. Hence only a single spectrum line corresponding to that one unique wavelength is observed on the CCD array. Illustrated in figure 2.9 (b) is the typical scenario when the spectrometer is used in conjunction with a single point-like laser-produced plasma. In this case, a fan of polychromatic rays from the plasma impinged on the surface of the crystal. The Bragg equation is again satisfied, but this time for multiple wavelengths, each one corresponding to a different angle of incidence. Therefore, constructive interference occurs for a broad range of wavelengths and a full spectrum is detected by the CCD camera. The wavelength range captured by the CCD depends on the

angular dispersion and distance between the source and CCD planes, i.e., the reciprocal linear dispersion of the spectrometer. The reciprocal linear dispersion of the spectrometer was calculated to be 0.012 nm/mm, using the expression,

$$\frac{d\lambda}{dx} = \frac{d\lambda}{d\theta} \frac{1}{x_1} \quad (2.4)$$

where  $d\lambda/d\theta = 2d\cos\theta$  is the angular dispersion in first order, equal to 2.46 nm/radian (0.043 nm/degree) for a crystal angle of  $22^\circ$  and  $x_1$  being the optical path length distance between the plasma and the CCD chip ( $x_1 = 195$  mm), see figure 2.11 (b). This value agrees with that deduced from the experimental spectra (e.g., 0.01 nm/mm in figure 2.12). The operation of the spectrometer is complicated slightly when used in conjunction with colliding plasma systems, illustrated in figure 2.9 (c). Here there are two sources of X-ray rays corresponding to each of the seed plasmas and a third source if one considers the region around the expected collision plane. While the concept is essentially the same as in figure 2.9 (b), because the two seed plasmas are in different locations, their spectra will form at slightly different positions on the CCD camera. The experiment was arranged in order to have each seed plasma lying on either side of the optical axis of the spectrometer, which resulted in emission from the interaction region being aligned with the center of the CCD chip.

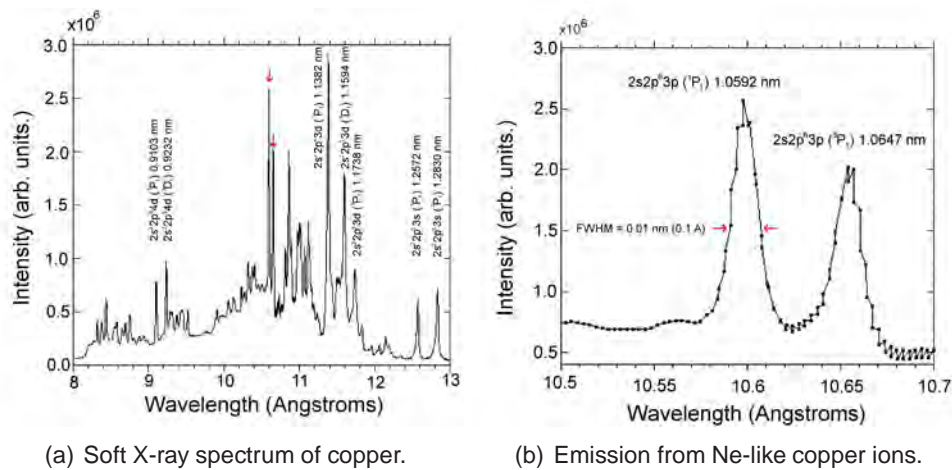


Figure 2.12: Soft X-ray spectrum of a single copper plasma in the region of 0.8 – 1.3 nm (a). The emission lines highlighted in the figure correspond to transitions in Ne-like copper (Cu XX) which involve the upper state (*quoted in figure*) and the  $2s^2 2p^6 ({}^1S_0)$  level. The right-hand panel (b) shows an expanded view of the copper spectrum in the region of the Ne-like doublet at approximately 1.06 nm (*highlighted by the red arrows*). The majority of emission lines in this spectral region are well known [41].

The resolution of the spectrometer was estimated by taking a spectrum of a single copper plasma. Figure 2.12 (a) shows a typical copper spectrum in the region of 0.8 – 1.3 nm taken using an Al filter. This spectrum is a mosaic of two overlapping CCD camera positions, necessary to acquire the 0.55 nm spectral window. All the lines in this spectrum are well known and have been classified by Hutcheon *et al.* (1980) [41]. The lines of interest used to estimate the spectral resolution were the Ne-like doublet at 1.06 nm and 1.065 nm corresponding to 19-times ionized species which are presented in an exploded view in figure 2.12 (b). This spectrum shows that the two lines are very well resolved by the instrument. Highlighted in the figure is the full width half maximum (FWHM) of the line at 1.06 nm which is  $\sim 0.01$  nm. In practice we found that one can measure the positions of spectral lines to better than 0.001 nm, however in making a full vertical bin<sup>6</sup> of each spectral image one can introduce a broadening of the spectral lines, since they often tend to lie at a small, but not insignificant angle to the CCD vertical (due to a small misalignment of the crystal with respect to the CCD).

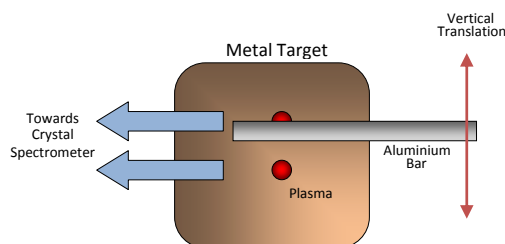


Figure 2.13: Schematic diagram showing the metal target and the moveable aluminium bar which was used to block either of the two laser beams generating the individual seed plasmas. The direction of propagation of the beams is into the page. Not shown is the lens which focuses the pair of laser beams, split by the optical wedge, onto the target.

As will be shown in the results chapter, the X-ray emitting size of plasmas generated by irradiation of aluminium targets using picosecond lasers is less than 10  $\mu\text{m}$  in diameter. Experiments on colliding plasmas in this spectral region require that the plasmas be separated by less than some hundreds of microns in order to facilitate an appreciable interaction between the two opposing plumes. Isolating emission from the seed plasmas in a manner ensuring that it did not occlude or blend with the emission which originates in the interaction region proved to be very challenging. In order to isolate and select emission from each of the three regions

<sup>6</sup>Creating a line spectrum from a two-dimensional image by summing the counts along each vertical row (column) of pixels - if the image is skewed then this summation process will broaden the resulting spectrum.

of interest, namely the two source plasmas and the interaction region between them, a 10 mm wide aluminium shield was placed between the lens and the target (see figure 2.13). By translating this shield vertically, the portion of the laser beam that generated any one of the individual seed plasmas was blocked. X-ray spectra of each of the individual plasmas could be recorded with the aid of the moveable shield. With it removed, spectra of the entire colliding plasma system, including the seed plasmas and the interaction region could be obtained. Due to the spatial separation of the two plasmas on the target surface, spectra from each seed plasma were formed at slightly different positions on the CCD chip. A comparative study could then be made between the spectra in the absence of collisions case with spectra obtained from the full colliding plasma system.

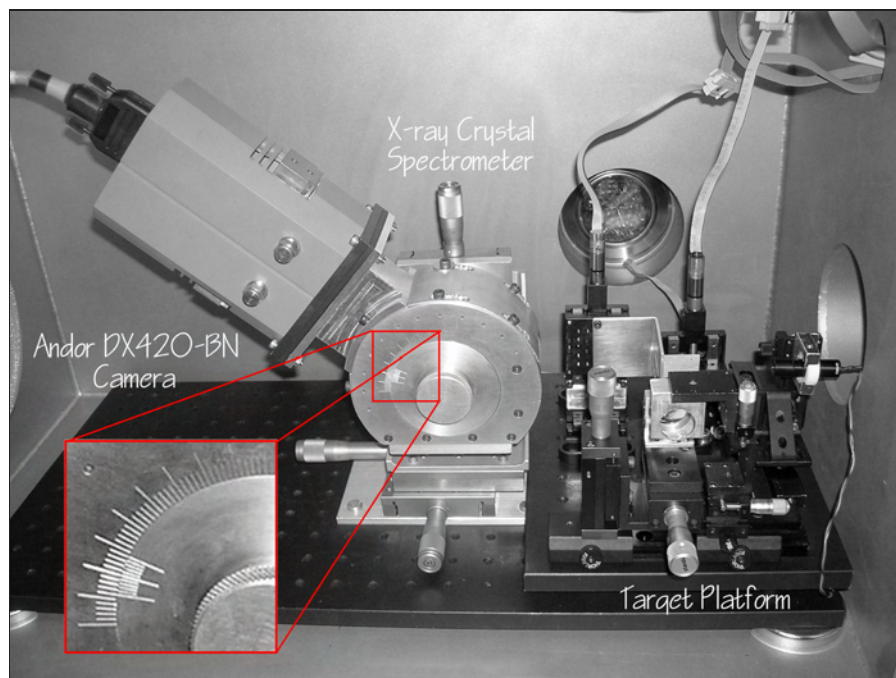


Figure 2.14: Photograph showing the target chamber, X-ray crystal spectrometer, CCD camera and target platform. The inset shows the angular scale on the spectrometer with each division corresponding to a deviation of  $2^\circ$  which was used to aid the alignment of the crystal and the CCD camera.

A photograph of the crystal spectrometer, CCD camera and target platform is shown in figure 2.14. In the interests of constructing a very flexible system we have built up the complete spectrometer system on a single large optical base plate ( $0.6 \text{ m} \times 0.3 \text{ m}$ ) fixed inside the vacuum chamber and evacuated with a turbo-molecular pump system (150 l/s) to a pressure approaching  $1 \times 10^{-4}$  mbar. The spectrometer

is mounted on a micrometer controlled X-Y-Z mount so that it can be aligned accurately with the micron-scale plasma. The target and laser beam focusing optics are mounted on motorized drives which are in turn located on a separate optical base plate for pre-alignment outside the vacuum system. This base plate is then secured on the main baseplate using kinematic breadboard seats (Thorlabs KBS98). Fine tuning of the source target position with respect to the optic axis of the spectrometer is done under vacuum using the computer controlled motorized target mounts.

The spectrum of a copper plasma, shown in figure 2.12, was used to calibrate the wavelength axis for each soft X-ray spectrum acquired by the CCD camera. Each line in the copper spectrum was identified from assignments (term designations) already published in the literature [41, 42]. From these data a calibration plot of wavelength versus pixel number was produced and a second order polynomial fitted to it. Each spectral image acquired during the experiments were full vertically binned to improve the signal-to-noise ratio (SNR) of the data and the calibration polynomial was subsequently applied to the spectrum.

### 2.5.3 Visible Emission Imaging

The first phase of the study on plasmas generated by the EKSPLA™ 312p picosecond laser system in the visible spectral region employed fast gated emission imaging. The core of the experimental setup consisted of an Andor™ intensified charge coupled device (ICCD) coupled to a Tonika™ zoom lens assembly. The Andor™ ICCD (BH5H7 series) consists of a two-dimensional CCD array of  $512 \times 512$  pixels with a pitch of  $26 \mu\text{m}$ . A micro-channel plate which is fiber-coupled to the CCD chip was gated to provide optical exposure times as short as 3 ns.

The zoom lens assembly was attached to the camera via a threaded coupling. As the lens was located outside the vacuum chamber, the distance between the plasma (object distance) and the lens was quite large ( $\sim 200$  mm). An extension tube of approximately 300 mm in length was used to increase the image distance with respect to the object distance, resulting in a magnification of ca. 1.5X. Without this extension tube the image of plasma formed on the CCD chip would be greatly de-magnified. From figure 2.15 it can be seen that the camera was placed on an optical lab-jack which was in turn mounted on a guide rail to provide both height and position control.

To determine the magnification of the system, a ruler was placed next to the target surface at the exact position of the focus of the laser beam. A broadband image was acquired and is displayed in figure 2.16 (a). A 'lineout' trace perpendicular to

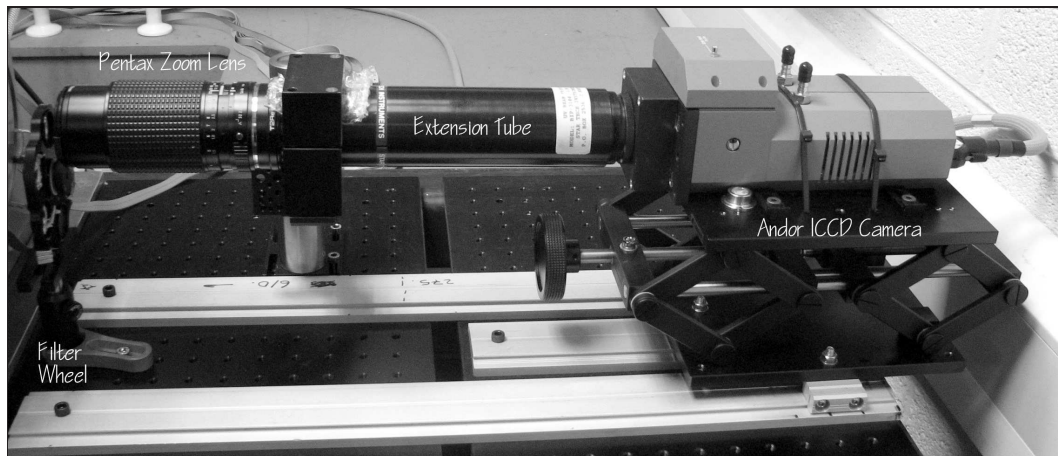


Figure 2.15: Photograph showing the visible emission imaging setup, containing the filter wheel, Tonika™ zoom lens, aluminium extension tube and Andor™ ICCD (BH5H7) camera.

the graduations was extracted and plotted (see figure 2.16 (b)). Using the fact that the spatial period is 1 mm and relating this value to the number of pixels (and hence distance since each pixel is  $26 \mu\text{m}$  in width) the ratio between the image and object dimensions, in other words the magnification was determined.

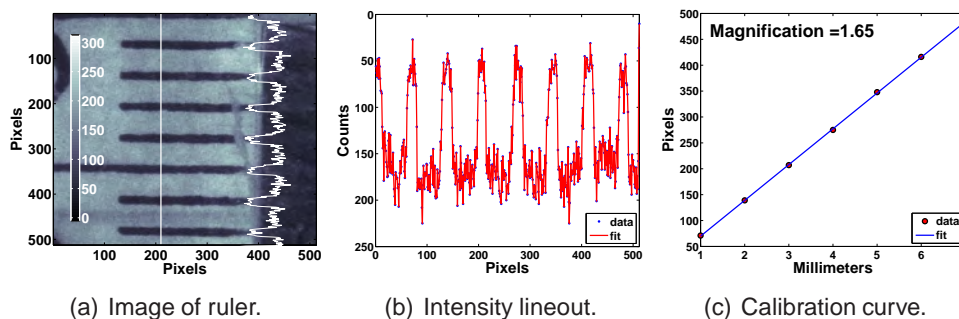


Figure 2.16: Method to determine the magnification of the visible emission imaging setup. (a) A broadband image of a precision metal ruler placed in the target surface plane at the point of focus of the laser. (b) Intensity plot obtained from an image lineout corresponding to the white vertical line in image (a). (c) Plot of pixel position of each graduation versus actual position in mm. One can determine the magnification of the imaging system by fitting a simple linear model to the data shown in (c) and using the fact that each pixel is 26 microns wide.

An important component of the imaging system was the optical filter wheel, located between the zoom lens and the vacuum chamber. Bandpass filters were used to isolate emission from neutral (395 nm for Aluminium; 420 nm for Calcium) and

from singly ionized (470 nm for Aluminium; 395 nm for Calcium) species in the seed plasma plumes and the stagnation layer. A broadband filter which transmitted radiation between 300 nm – 950 nm was used to image the bulk plume emission (while importantly rejecting the 1064 nm scattered laser light from the plume).

By spectrally resolving the emission from the plasma plume, it was possible to isolate the different ionic species. Plume expansion velocities were determined by tracking the locus of the plume front position over time. The plume front position was taken to be the position where the intensity has dropped to 10 % of the peak intensity. Forward and lateral expansion velocities of the plume were determined by extracting intensities along a line perpendicular and parallel to the target surface respectively.

Although fast gated emission imaging is a simple and effective way to determine the whole plume (or selected atomistic plume species) spatial distributions and to extract their expansion velocities, it cannot however be used to determine other important plasma parameters such as electron temperature and density. One tool that can be used for this purpose is optical spectroscopy.

#### **2.5.4 Visible Emission Spectroscopy**

A Chromex-Bruker Optics™ 0.5 m visible spectrometer was used to obtain spectra of aluminium and calcium plasmas formed on flat targets. The spectrometer slit was aligned perpendicular to the plasma expansion axis, allowing the simultaneous recording of spectra from both the seed plasmas and the stagnation layer, see figure 2.17 (b). Preliminary emission images in the visible spectral region revealed that the size of the plasma plume was up to one hundred times larger than in the soft X-ray spectral region. This allowed the mean separation between the seed plasmas (in the case of colliding plasma systems) to be increased to  $\sim 2$  mm whilst still providing a strong interaction (at least as far as generating visible emission that could be detected by the CCD cameras was concerned).

The spectrometer comprised a Czerny-Turner mount with toroidal collimating and focusing mirrors which enable aberration-corrected flat field stigmatic imaging. The spectrometer was equipped with a 1200 groove/mm diffraction grating blazed at 400 nm, which gave a reciprocal linear dispersion of 1.6 nm/mm and a resolution of 0.07 nm (FWHM) [43, 35]. The instrument function of the spectrometer was found to be 0.16 nm [43] and was determined using a method described by Kavanagh [34] which employed a narrow spectral line from a Cadmium lamp (441 nm). A CCD was

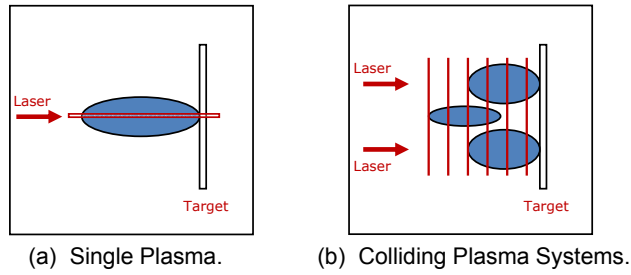


Figure 2.17: Schematic representation of the approximate position of the entrance slit of the spectrometer (red solid lines) in relation to the position of the plasma for the case of a single plasma with the dove-prism (a) and colliding plasma systems without the dove-prism installed (b).

equipped with a lens coupled MCP which provided time-resolved spectral readout with a gate width of ca. 5 ns width. The main specifications of the spectrometer are listed in table 2.2.

Parameter	Value
Focal Length	0.5 m
Optical Layout	Czerny-Turner
Aperture	f/8
Spectral range	200 – 900 nm
Slit width	10 $\mu\text{m}$ – 2 mm
Slit height	10 mm
Reciprocal linear dispersion (RLD)	1.6 nm/mm
Instrument function <sup>†</sup>	0.16 nm
Resolution (FWHM)	$\sim$ 0.08 nm

Table 2.2: Specifications of the Chromex-Bruker Optics™ 500 visible spectrometer. The parameters quoted in the table correspond to the spectrometer operating with a 1200 grooves/mm grating. <sup>†</sup> Instrument function quoted for an optimum slit width of 50  $\mu\text{m}$  [35].

In a typical stigmatic spectrometer the optical aberrations are corrected both in the spectral dispersion plane, perpendicular to the entrance slit, and in the spatial plane, parallel to the entrance slit. The optical layout of the spectrometer and plasma relay imaging system are shown in figure 2.18. When studying single laser-produced plasmas a dove-prism was installed between the relay lens system (L1 and L2 in figure 2.18) which rotated the image of the plasma by 90°. The image of the plasma was then formed along the length of the entrance slit of the spec-

trometer, as shown in figure 2.17 (a). During the studies of colliding plasmas the dove-prism was removed and the image of the expanding plasma was formed orthogonal to the entrance slit of the spectrometer. Each spectrum corresponded to the spectral distribution of a vertical slice of the colliding plasma system, containing the two seed plasmas and the interaction region between them, see figure 2.17 (b). The table, to which the spectrometer was fixed, was translated in small increments (0.5 mm) in the direction normal to the target surface (i.e., along the expansion axis of the plume). Each such incremental movement corresponded to a distance of 0.25 mm at the plasma plume as the image of the plasma, projected onto the entrance slit, was magnified by a factor of 2 by the relay imaging optics. By combining these spectra into a waterfall plot it was possible to build up a spectral image of the entire plume.

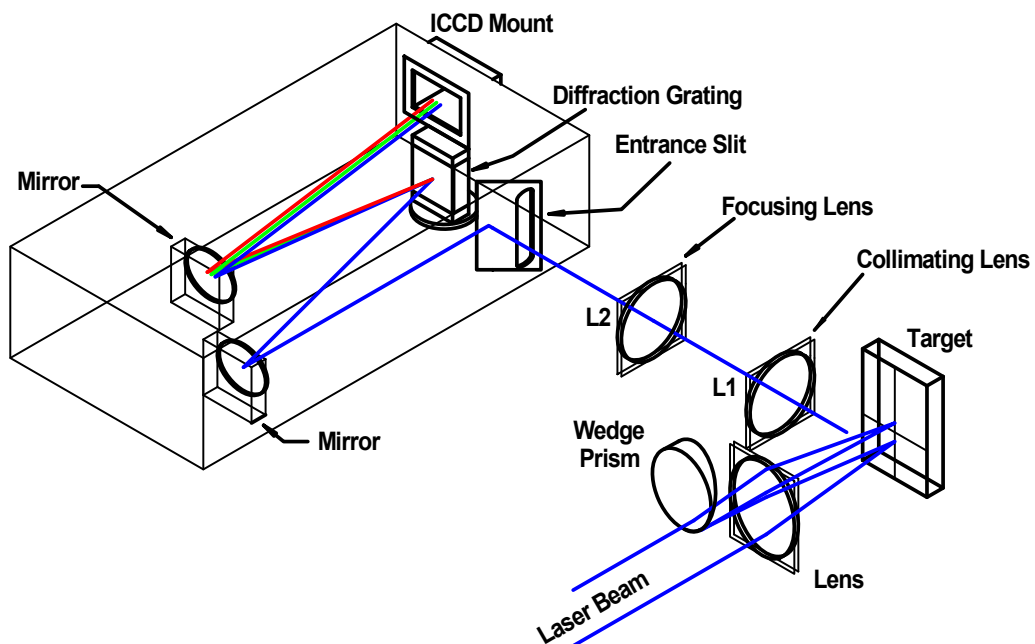


Figure 2.18: Schematic diagram of the target chamber and the Chromex™ 0.5 m visible spectrometer used in the study of colliding laser-produced plasmas in the visible spectral region. The main components include the wedge-prism which splits the laser beam, the relay lens system (L1 and L2) which forms an image of the plasma plume on the entrance slit of the spectrometer with its axis of expansion aligned perpendicular to the vertical slit of the spectrometer.

The spectrometer was fixed to a moveable optical table, which had height and position adjustment, located  $\sim 1$  m away from the interaction region. Light from the plasma was focused onto the entrance slit of the spectrometer using a pair of

achromatic-doublet lenses, ( $f_{L1} = 200$  mm and  $f_{L2} = 400$  mm) in a relay lens setup, located inside the vacuum chamber. This resulted in an image of the plasmas formed normal to the slit plane and magnified by a factor of two as mentioned above. An optional dove prism could be inserted into the space between the two achromatic lenses to rotate the image of the plasma by  $90^\circ$ . In doing so the image of the plasma plume was projected vertically so that its expansion axis lay along the entrance slit of the spectrometer. In this case, a single image could record both the dynamic spectral changes and the expansion of the plume away from the target surface.

The optical layout chosen in the study of colliding plasma systems here omitted the dove-prism so that spectra of both the seed plasmas and the stagnation layer could be captured simultaneously. By translating the spectrometer along the plasma expansion axis a series of spectra could be recorded, which when combined gave a full 2-dimensional spectrally resolved view of the colliding plasma system. Spectral readout was provided by an intensified CCD (ICCD) camera operated with a gate-width of typically 5 ns.

The widths of spectral lines in a laser produced plasma is dominated by Stark broadening and to a much lesser degree in our plasma parameter range, by (thermal) Doppler broadening. Motional Doppler broadening was not considered to be significant as all spectra and images were recorded normal to the expansion axis. The contribution from Doppler broadening was estimated to be ca. 0.001 nm for plasmas studied in this work. Stark broadening of a spectral line leads to a Lorentzian line shape, while Doppler broadening will lead to a Gaussian line shape in the spectral line. Therefore a spectral line is best fitted using a convolution of both line shapes, the so-called Voigt profile. The Voigt profile incorporates the bell-shaped centre of the Gaussian profile with the extended wings of the Lorentzian profile. A more detailed discussion on the mechanisms which contribute to the broadening of spectral lines in dense laser-produced plasmas is given in section 4.2.2. Suffice to say here that the full width half maximum (FWHM) of the Lorentzian component of a spectral line can be related to the electron density using [44],

$$\Delta\lambda_{FWHM} = 2w \left( \frac{n_e}{10^{16}} \right) \quad (2.5)$$

where  $w$  is the Stark broadening parameter and  $n_e$  is the electron density. Equation 2.5 assumes that the ion field contribution to the broadening is negligible. By extracting the FWHM of the Lorentzian component from the Voigt profile one can determine the electron density of the plasma in this region. A Matlab™ program

was written which has as input a spectral image from the CCD camera. The code divides each spectral image into three spatial sections, each fifty pixels wide containing the emission from each of the two seed plasmas and the stagnation layer respectively. Each of these sections is vertically summed (full vertical binning) which results in three one dimensional line spectra of improved signal-to-noise ratio. Voigt profiles are then fitted to the major spectral lines using a minimization routine and the local electron density, determined using equation 2.5. This procedure was repeated for the range of spectra obtained by spatially sampling the seed plasma and stagnation layer regions in each spectral image and the electron density was plotted against distance from the target surface.

The electron temperature ( $T_e$ ) was extracted by comparing the peak intensity of spectral lines which originate from consecutive charge states [45]. Assuming a Boltzmann population distribution of the charge states, the ratio of line intensities from successive charge states is described by [45],

$$\frac{I'}{I} = \frac{f'g'\lambda^3}{fg\lambda'^3} (4\pi^{3/2} a_0^3 n_e)^{-1} \frac{k_b T_e}{E_H} \exp\left(\frac{E - E' - E_\infty}{k_b T_e}\right) \quad (2.6)$$

where  $I$ ,  $\lambda$ ,  $g$  and  $f$  are: total intensity (integrated over the profile), wavelength, statistical weight of the lower state of the transition, and absorption oscillator strength, respectively.  $E$  and  $E'$  are the excitation energies of the transitions of interest in the successive ion stages, while  $E_\infty$  and  $E_H$  are the ionization energies of the lower of the two ion stages and the hydrogen atom, respectively. The subsequent ionization stage is denoted by primed quantities. The temperature distribution along the entire length of the plasma was determined by repeating these steps for each position of the spectrometer. Using these methods it was possible to build up a complete picture of both the density and temperature along the length of an expanding plasma plume or stagnation layer.

## 2.6 Summary

In this section the experimental system for the production and study of single and colliding laser produced plasmas was presented. The main component of this system was the EKSPLA™ 312p laser system which was used exclusively for the work in this thesis. Four photon diagnostics were presented, two in the soft X-ray spectral region and two in the visible spectral region. The diagnostics in the visible region in particular were used to track the evolution of the plasma and to extract plasma

parameters such as electron density and temperature.

The optical setup of the colliding plasma system was also presented in this section. The laser beam was split into two equal beams using a wedge prism which bisected the beam. A plano-convex lens was then placed after the wedge prism and the two divergent beams were brought to a focus on the target. It was shown that the separation between the two foci depended on both the acute angle of the wedge prism and the focal length of the lens. By changing either of these two parameters, the collisionality parameter defining the system could be controlled. Furthermore, by experimenting with different target geometries, namely flat and wedge-shaped targets it would also be possible to control (to some extent) the value of the collisionality parameter.

# Bibliography

- [1] S. Amoruso, R. Bruzzese, N. Spinelli, and R. Velotta. Characterization of laser-ablation plasmas. *Journal of Physics B: Atomic, Molecular and Optical Physics*, 32(14):R131–R172, 1999.
- [2] H. A. Haus. Theory of mode locking with a fast saturable absorber. *Journal of Applied Physics*, 46:3049–3058, 1975.
- [3] C. P. Ausschnitt and R. K. Jain. Pulse-width dependence on intracavity bandwidth in synchronously mode-locked cw dye lasers. *Applied Physics Letters*, 32(11):727–730, 1978.
- [4] P. F. Moulton. Spectroscopic and laser characteristics of Ti:Al<sub>2</sub>O<sub>3</sub>. *Journal of the Optical Society of America B*, 3(1):125–133, 1986.
- [5] M. T. Asaki, C. P. Huang, D. Garvey, J. P. Zhou, H. C. Kapteyn, and M. M. Murnane. Generation of 11-fs pulses from a self-mode-locked Ti-sapphire laser. *Optics Letters*, 18(12):977–979, 1993.
- [6] Lithuania EKSPLA UAB. Ekspla SL300 series brochure. Manufacturer's website. <http://www.ekspla.com/repository/catalogue/infofiles/lasers/SL312.pdf>.
- [7] J. Soures, L. M. Goldman, and M. Lubin. Short-pulse-laser-heated plasma experiments. *Nuclear Fusion*, 13(6):829–838, 1973.
- [8] B. Yaakobi and L. M. Goldman. Laser compression studies with neon-filled glass microballoons. *Physical Review Letters*, 37(14):899–902, 1976.
- [9] B. Yaakobi, S. Skupsky, R. L. McCrory, C. F. Hooper, H. Deckman, P. Bourke, and J. M. Soures. Symmetric laser compression of argon-filled glass shells to densities of 4-6 g/cm<sup>3</sup>. *Physical Review Letters*, 44(16):1072–1075, 1980.
- [10] S. Amoruso, G. Ausanio, R. Bruzzese, L. Gagnaniello, L. Lanotte, M. Vitiello, and X. Wang. Characterization of laser ablation of solid targets with near-

- infrared laser pulses of 100 fs and 1 ps duration. *Applied Surface Science*, 252(13):4863–4870, 2006.
- [11] B. LeDrogoff, J. Margot, F. Vidal, S. Laville, M. Chaker, M. Sabsabi, T. W. Johnston, and O. Barthélemy. Influence of the laser pulse duration on laser-produced plasma properties. *Plasma Sources Science and Technology*, 13(2):223–230, 2004.
- [12] M. Murnane, H. Kapteyn, M. Rosen, and R. Falcone. Ultrafast X-ray pulses from laser-produced plasmas. *Science*, 251(4993):531 – 536, 1991.
- [13] J. Dardis, A. Murphy, H. de Luna, E. T. Kennedy, A. Seugnet, P. Orr, J. Greenwood, C. McKenna, C. L. S. Lewis, and J. T. Costello. Progress report on compact system for point projection X-ray absorption spectroscopy and imaging of laser produced plasmas. volume 5826, pages 363–370, 2005.
- [14] Goodfellow Corporation. Specification sheet for Invar. <http://www.goodfellow.com/E/Invar-ControlledExpansionAlloy.html>.
- [15] Verre et Quartz Flashlamps. Bondy, france. <http://www.verre-et-quartz.com/indexuk.html>.
- [16] A. E. Siegman. *Lasers*, chapter 6, figure 6.1, pg. 244. University Science Books, 1986.
- [17] J. J. Zayhowski. Limits imposed by spatial hole burning on the single-mode operation of standing-wave laser cavities. *Optics Letters*, 15(8):431–433, 1990.
- [18] P. Polynkin, A. Polynkin, M. Mansuripur, J. Moloney, and N. Peyghambarian. Single-frequency laser oscillator with watts-level output power at 1.5 um by use of a twisted-mode technique. *Optics Letters*, 30(20):2745–2747, 2005.
- [19] R. W. Boyd. *Nonlinear Optics*. Academic Press, New York, 1993.
- [20] Y. Shen. Electrostriction optical kerr effect and self-focusing of laser beams. *Physics Letters*, 20(4):378, 1966.
- [21] David T. Hon. Pulse compression by stimulated Brillouin scattering. *Optics Letters*, 5(12):516, 1980.
- [22] 300 ps ruby laser using stimulated Brillouin scattering pulse compression. *Review of Scientific Instruments*, 65:2460–2463, 1994.

- [23] M. J. Damzen. *Stimulated brillouin scattering: fundamentals and applications*. 2003.
- [24] R. Mittra and T. M. Habashy. Theory of wave-front-distortion correction by phase conjugation. *Journal of the Optical Society of America A*, 1(11):1103–1109, 1984.
- [25] A. J. Scroggie, G. D’Alessandro, N. Langford, and G. L. Oppo. Pulse compression by slow saturable absorber action in an optical parametric oscillator. *Optics Communications*, 160(1):119–124, 1999.
- [26] A. Michette. Private communication, 2005.
- [27] CVI - Melles Griot. Manufacturer’s Website. <http://www.mellesgriot.com/>.
- [28] S. S. Harilal, C. V. Bindhu, and H.-J. Kunze. Time evolution of colliding laser produced magnesium plasmas investigated using a pinhole camera. *Journal of Applied Physics*, 89(9):4737–4740, 2001.
- [29] C. Chenais-Popovics, P. Renaudin, O. Rancu, F. Gilleron, J.-C. Gauthier, O. Larroche, O. Peyrusse, M. Dirksmüller, P. Sondhaus, T. Missalla, I. Uschmann, E. Förster, O. Renner, and E. Krousky. Kinetic to thermal energy transfer and interpenetration in the collision of laser-produced plasmas. *Physics of Plasmas*, 4:190–208, 1997.
- [30] P. W. Rambo and J. Denavit. Interpenetration and ion separation in colliding plasmas. *Physics of Plasmas*, 1(12):4050–4060, 1994.
- [31] O. Rancu, P. Renaudin, C. Chenais-Popovics, H. Kawagashi, J. C. Gauthier, M. Dirksmüller, T. Missalla, I. Uschmann, E. Förster, O. Larroche, O. Peyrusse, O. Renner, E. Krouský, H. Pépin, and T. Shepard. Experimental evidence of interpenetration and high ion temperature in colliding plasmas. *Physical Review Letters*, 75(21):3854–3857, 1995.
- [32] R. K. Singh and J. Narayan. Pulsed-laser evaporation technique for deposition of thin films: Physics and theoretical model. *Physical Review B*, 41(13):8843–8859, 1990.
- [33] S. S. Harilal. Influence of spot size on propagation dynamics of laser-produced tin plasma. *Journal of Applied Physics*, 102(12):123306, 2007.
- [34] K. Kavanagh. *Imaging and Spectroscopy of Laser-Produced Colliding Plasmas*. Ph.D. Thesis, Dublin City University, 2006.

- [35] H. Luna, K. D. Kavanagh, and J. T. Costello. Study of a colliding laser-produced plasma by analysis of time and space-resolved image spectra. *Journal of Applied Physics*, 101(1):1–6, 2007.
- [36] Atwee T. and Kunze H. J. Spectroscopic investigation of two equal colliding plasma plumes of boron nitride. *Journal of Physics D: Applied Physics*, 35:524–528, 2002.
- [37] P. T. Rumsby, J. W. M. Paul, and M. M. Masoud. Interactions between two colliding laser produced plasmas. *Plasma Physics*, 16(10):969–975, 1974.
- [38] S. S. Harilal, C. V. Bindhu, V. P. Shevelko, and H. J. Kunze. XUV diagnostics of colliding laser-produced magnesium plasmas. *Journal of Physics B: Atomic, Molecular and Optical Physics*, 34(18):3717–3726, 2001.
- [39] K. Sayanagi. Pinhole imagery. *Journal of the Optical Society of America*, 57(9):1091–1098, 1967.
- [40] Lawrence Berkeley National Laboratory Centre for X-ray Optics. X-ray transmission of solids tool. [http://henke.lbl.gov/optical\\_constants/filter2.html](http://henke.lbl.gov/optical_constants/filter2.html).
- [41] R. J. Hutcheon, L. Cooke, M. H. Key, C. L. S. Lewis, and G. E. Bromage. Neon-like and fluorine-like X-ray emission spectra for elements from Cu to Sr. *Physica Scripta*, 21(1):89–97, 1980.
- [42] I. C. E. Turcu, I. N. Ross, and G. J. Tallents. Efficient keV x-ray emission from plasmas generated with 4 ps KrF excimer laser pulses. *Applied Physics Letters*, 63(22):3046–3048, 1993.
- [43] H. Luna, J. Dardis, D. Doria, and J.T. Costello. Analysis of time-resolved laser plasma ablation using an imaging spectra technique. *Brazilian Journal of Physics*, 37:1301–1305, 2007.
- [44] H. R. Griem. *Principles of Laser Plasmas*. Cambridge University Press, Cambridge, U.K., 1997.
- [45] H. R. Griem. *Spectral Line Broadening by Plasmas*. Academic, New York, 1974.

## Chapter 3

# Soft X-ray Emission Studies

### 3.1 Overview of Soft X-Ray Measurements

In this section results obtained during the study of plasmas generated using the EKSPLA™ 312p picosecond laser system are presented. Emission from the plasma was recorded using both imaging and spectroscopy for wavelengths around 1 nm corresponding to the soft X-ray spectral region. The sequence of experiments began with a study of emission spectra from a copper plasma obtained using a Bragg crystal spectrometer. Estimates of the plasma temperature can be made from such spectra by determining the highest and average charge states present. Emission imaging using the pinhole camera setup enabled the determination of the overall size of the X-ray emitting core of the plasma. This chapter concludes with a brief description of the search for X-ray emission from colliding plasma systems.

The laser system can deliver powerful (up to 500 mJ) pulses of picosecond duration (170 ps) at 5 Hz repetition rate. When these pulses are focused down to a small spot (typically 30 – 100  $\mu\text{m}$ ), a plasma will form which is both hot and dense. Plasmas generated in this way will expand rapidly away from the target surface with emission predominantly in the extreme-ultraviolet to soft X-ray spectral regions. An intense burst of X-ray radiation accompanies the rapid expansion of the laser plasma and lasts for some hundreds of picoseconds when the plasma is at its hottest [1, 2]. X-rays penetrate deep into the densest regions of plasmas and so are an ideal diagnostic tool for the study of parts of the plasma which are close to the target surface where optical emission is unable to penetrate. Also because the X-rays are only emitted within (at most) the first few hundred picoseconds of the plasma lifetime, X-ray imaging is an important probe and record of the early stages of plasma expansion.

As stated above an EKSPLA™ 312p Nd:YAG operating at its fundamental wavelength (1064 nm) was used exclusively for the studies reported here. This laser has a pulse duration of  $\sim 170$  ps and a maximum output pulse energy of 500 mJ. Soft X-ray emission spectra of laser plasmas produced by irradiating flat metal targets were recorded using the Bragg crystal spectrometer described in section 2. Emission spectra of individual magnesium, copper and aluminium plasmas as well as many of the rare earth metals ( $Z = 60 - 68$ ) were recorded, all of which emit brightly in the soft X-ray region and contain a number of distinct lines or transition arrays arising from electric dipole transitions in highly-charged ions.

Working in the soft X-ray spectral range is experimentally challenging. Given that the burst of X-ray emission has a duration of at most a few nanoseconds, ideally optical diagnostics should have access to a fast gated detector with ideally picosecond time-resolution such as a streak camera. In our experiments an X-ray detector with such high time resolution was not available and so our studies were limited to estimation of plasma parameters using time integrated images and spectra.

### 3.2 Initial Characterization of Laser-Produced Plasmas

We begin this section with the characterization of a single laser-produced plasma generated at the focus of the EKSPLA™ 312p picosecond laser on flat metal targets. The laser was operated at a 5 Hz repetition rate at the fundamental wavelength of 1064 nm for all data reported in this thesis. Plano-convex lenses with focal lengths in the range of 50 mm – 200 mm were used to focus the laser onto the surface of flat metal targets. The spot radius at the point of focus for a Gaussian laser beam can be related to the focal length of the lens using the equation [3],

$$w_F = \frac{\lambda f}{\pi w_L} \quad (3.1)$$

where  $w_F$  is the spot radius at the focal point,  $\lambda$  is the wavelength of the laser beam,  $f$  is the focal length of the lens and  $w_L$  is the radius of the laser beam before impinging on the optic. A reduction in the focal length of the lens leads to a concomitant reduction in the radius of the focal spot, towards the diffraction limit of  $\text{XXX } \mu\text{m}$ . Previous studies into laser-produced plasmas have reported that the focal spot diameter when using a multimode nanosecond laser such as a Surelite III-10™ is typically  $\sim 60 \mu\text{m}$  (see Luna *et al.* 2007 [4]). The EKSPLA™ 312p laser system used in the current study is believed to have a far superior beam quality as the uncompressed pulse from the Q-switched oscillator must be close

to single longitudinal mode for successful compression in the SBS cell. Hence it is reasonable to assume that the focal spot diameter achieved here was less than  $50 \mu\text{m}$  leading to an on-target irradiance of up to  $\sim 10^{14} \text{ W/cm}^2$  for optimal conditions. Measurements at King's College London put the spot size for a similar EKSPLA™ laser design at  $< 25 \mu\text{m}$  [5].

When a pulse of light at this intensity impinges on a metal surface the radiation will be absorbed in a thin layer and a high temperature, high density plasma is formed. The plasma expands rapidly away from the target surface, cooling and emitting radiation from the X-ray through vacuum-ultraviolet to the infrared spectral range as it does so. The peak wavelength of this emission is related to the on-target irradiance used to produce the plasma. X-rays are produced in the hottest regions of the plasma which are typically in the core, close to the target surface [6]. Because of the transient nature of laser-produced plasmas, the temperatures and densities do not remain sufficiently high to produce prolonged X-ray emission. In the majority of laser-produced plasmas, the duration of the X-ray emission is on the order of the laser pulse duration, and rarely exceeds a few hundred picoseconds after the pulse has terminated [1].

The broadband X-ray pulse duration was measured using fast silicon diodes (Dardis *et al.* (2005) [7]) which yielded a pulse duration of below 1 ns. As this was comparable to the rise-time of the photodiode we estimate that the true pulse duration to be on the order of a few hundred picoseconds. The X-ray radiation from these plasmas originates from highly stripped atoms and three atomic processes in the plasma contribute to the radiation emitted. They are: Bremsstrahlung continuum emission due to free-free transitions, recombination continuum from free-bound transitions and line radiation from bound-bound transitions (see section 1.4.

Before beginning the study into single plasmas and also colliding plasma systems in the soft X-ray spectral region it was important to know how the X-ray emission changes with the laser power density or irradiance (in  $\text{W/cm}^2$ ). When a laser produces a plasma, a relatively small but significant crater is produced on the metal surface. The first initiative was to study the dependence of the soft X-ray flux from the plasma with respect to the number of successive laser shots on the same target position.

### 3.2.1 Surface Cratering

As the X-ray emitting core region of the plasma is on the order of a few tens of microns, cratering of the surface due to the laser can become a problem. After multiple laser shots on the target, the crater will become large enough to occlude emission coming from the X-ray core. The first experiment was established to monitor the effect of surface cratering on the X-ray emission from the plasma. The pinhole camera (incorporating the  $1.5\ \mu\text{m}$  thick aluminium filter) was used to obtain time-integrated images (which were corrected for stray background radiation) of single copper plasmas produced on flat metal targets.

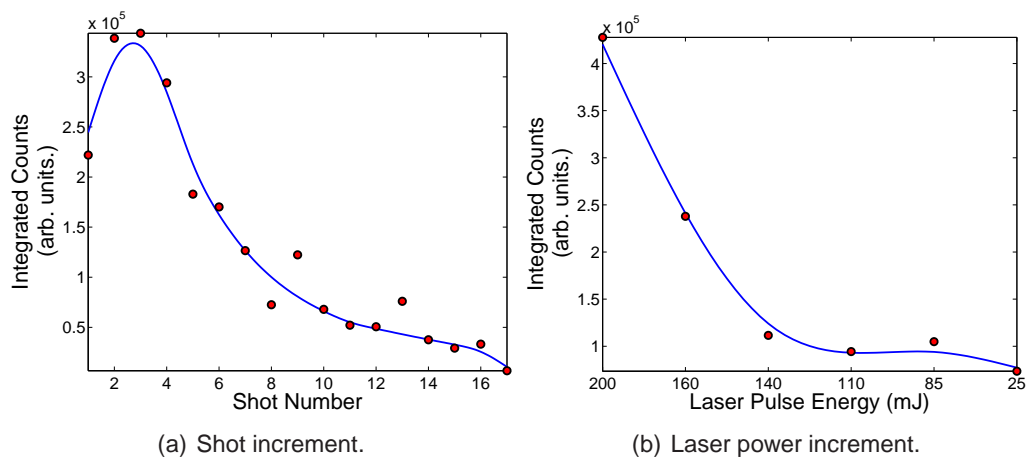


Figure 3.1: Integrated soft X-ray flux from a laser-produced copper plasma as a function of the number of consecutive laser shots (a) and the on-target laser energy (mJ) (b). The low-level background signal was automatically subtracted from each acquisition. The estimated on-target irradiance at 170 mJ was more than  $10^{13}\ \text{W}/\text{cm}^2$ .

In figure 3.1 (a) the total summed counts in each these X-ray images is plotted against the number of consecutive laser shots. Before acquiring each image, a background was obtained. One can see from the figure that the majority of the X-ray flux is generated within the first five overlapping laser pulses, with the exception of the first shot, which is generally lower in intensity as some of the laser energy acts to clean the surface of the target. Over a number of consecutive laser shots a crater forms on the target surface. The decrease in the X-ray yield can be attributed to the fact that over time, the plasma will begin to be formed on the inside surface of the crater. As the depth of the crater increases (with increasing number of consecutive laser shots) the micron-scale X-ray emitting core of the plasma will form deeper inside the crater and the emission will become highly directional normal to the target surface (i.e., rather 'jet-like'). Our detector, positioned at right-angles to

the target, will therefore see a reduction in X-ray flux.

Also shown in figure 3.1 (right) is a measure of the soft X-ray flux as a function of the laser energy. As the energy of the laser decreases the maximum number of counts detected also decreases. The trend in figure 3.1 (right) can be understood by the following simple argument. From the collisional radiative model [8] introduced in section 1.5 we find that the electron temperature of the plasma scales with the on-target laser irradiance (see next section for details). Therefore, as the energy of the laser is reduced the irradiance decreases and hence the plasma temperature. In this case the wavelength peak of the plasma emission is shifted from the SXR region to longer wavelengths, where the transmission window of the aluminium filter is greatly reduced.

### 3.2.2 Plasma Temperature

The first stage of our study was to determine the time-integrated electron temperature of the plasma which was expected to be significantly hotter than that for a nanosecond laser system formed by uncompressed Q-switched laser systems which typically deliver pulses of similar energy but in the 5 – 30 ns duration range. These systems therefore yield peak pulse intensities of one to two orders of magnitude lower than that achievable with the EKSPLA™ 312p laser system used in this work. The in-vacuum Andor™ X-ray sensitive CCD camera consisted of just a bare chip with no micro-channel plate detector attached and hence no time resolution beyond that afforded by the lowest readout time of 100 ms per 1024×256 pixel image<sup>1</sup>. Hence spatial and spectral image data acquired from this camera were time-integrated.

A simple intensity scaling law derived from the collisional radiative (CR) equilibrium model by Colombant and Tonon [8] which relates the plasma electron temperature ( $T_e$ ) in eV to the on-target irradiance ( $\phi$ ) in W/cm<sup>2</sup> is given by the equation,

$$T_e \approx 5.2 \times 10^{-6} Z^{1/5} [\lambda^2 \phi]^{3/5} \quad (3.2)$$

where  $Z$  is the atomic mass of the target material and  $\lambda$  is the wavelength of the laser radiation in microns (here 1.064  $\mu\text{m}$ ). We saw in section 1.5 where the Collisional Radiative Equilibrium model [8] is best suited to describing plasmas which have electron densities in the region of  $10^{19} - 10^{21} \text{ cm}^{-3}$ . This density range co-

---

<sup>1</sup>The readout time can be reduced to  $\sim 6$  ms when the camera is set to full vertical binning mode via the computer software, yielding approximately 166 spectra per second [9].

incides nicely with the typical density range of the most laser-produced plasmas (produced using either Nd:YAG or CO<sub>2</sub> laser systems). Equation 3.2 was evaluated for a range of laser irradiance values between 10<sup>10</sup> W/cm<sup>2</sup> and 10<sup>13</sup> W/cm<sup>2</sup> and the resulting trend is presented in figure 3.2.

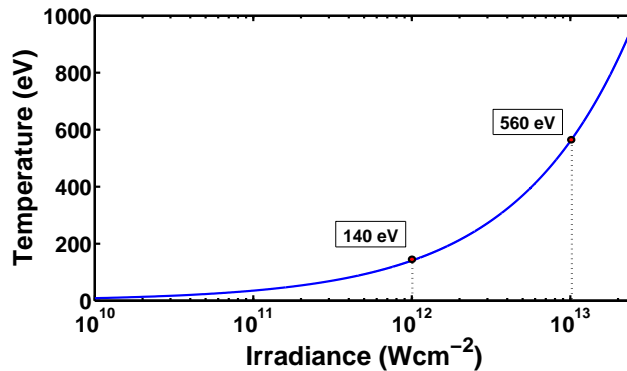
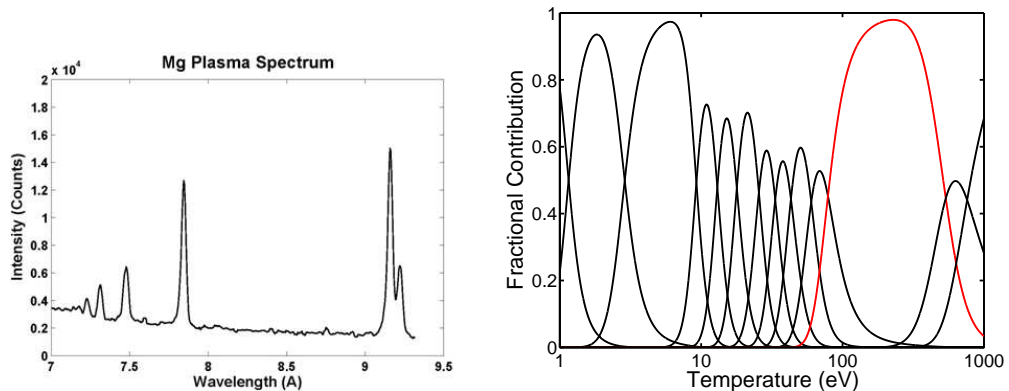


Figure 3.2: Electron temperature of a magnesium plasma as a function of on-target laser irradiance (After Colombant and Tonon [8])

If one takes a laser irradiance of  $> 10^{13}$  W/cm<sup>2</sup>, which we have seen is quite a reasonable estimate for this type of laser system, corresponding to a 300 mJ laser pulse of 170 ps duration focused to spot sizes of 50  $\mu$ m diameter, then the plasma temperature from this model (using  $A = 12$ , for magnesium) is estimated to be  $\sim 560$  eV.

This value was compared to a value determined using an alternative method in the same plasma equilibrium model which relates the electron density of the plasma to the highest charge state observed in the soft X-ray spectra. A time-integrated spectrum from a magnesium plasma produced by this intense laser system was recorded in the wavelength region of 0.7 nm – 0.95 nm (*corresponding to a crystal rotation angle of 20°*) and is shown in figure 3.3. The doublet at 0.916 nm and 0.923 nm correspond to the 1s<sup>2</sup> – 1s2p transition of He-like magnesium (Mg XI). The features on the left hand side of the figure (shorter wavelength) are the He-like 1s<sup>2</sup> – 1snp series ending at the series limit at 0.785 nm. These lines originate from highly charged ions and so one can deduce from this emission spectrum that the plasmas are relatively hot, with an estimated electron temperature of some hundreds of electron volts.

The computer model of McGuigan [10] based on the collisional-radiative equilibrium model of Colombant and Tonon [8] was used to generate the ionization balance of a



(a) Soft X-ray emission spectrum from a magnesium plasma.

(b) Ionization balance of a magnesium plasma calculated using the Collisional Radiative Equilibrium model.

Figure 3.3: (a) Soft X-ray emission spectrum from a magnesium plasma in the region of 0.8 nm produced by irradiating a flat metal target with the picosecond laser system. (b) Ionization balance of a magnesium plasma as a function of temperature assuming a state of collisional radiative equilibrium [8] which was calculated using the computer model developed by McGuigan [10] for a laser irradiance of  $10^{13}$  W/cm<sup>2</sup> and an average electron density of  $10^{19}$  cm<sup>-3</sup>. The highest charge state observed in the experimental spectrum (a) was He-like magnesium (Mg XI) which yields an upper limit of the plasma electron temperature of less than 250 eV, deduced using the output of the computer model in (b). Highlighted in red is the trace that corresponds to the Mg XI ion. The absence of emission from H-like (Mg XII) ions places an upper limit on the value of the plasma electron temperature.

magnesium laser-produced plasma which had an average electron density of  $10^{19}$  cm<sup>-3</sup>. The output from the model is shown in figure 3.3 (b). The red trace in the figure represents the fraction of Mg XI ions within the plasma. One can clearly see that these ions emerge in appreciable number densities above 100 eV. According to the model, they remain the dominant charge state up to approximately 700 eV. However, the absence of emission from H-like ions (Mg XII) places an upper limit on the electron temperature of less than 250 eV. This temperature range agrees somewhat with that predicted using the intensity scaling law described earlier.

### 3.2.3 Plasma Dimensions

Images of laser-produced plasmas in the soft X-ray spectral region can reveal the shape and size of the soft X-ray emitting core of the plasma. The same back-illuminated CCD camera was used to record time-integrated images, meaning that each image acquired by the CCD was composed of the X-ray emission from the plasma over its entire life. As such, the determination of plasma plume dimensions

and expansion dynamics were restricted to simple estimates using the bulk plume images.

Figure 3.4 shows images of four laser-produced plasmas corresponding to copper, magnesium and tungsten recorded using the pinhole camera. The color scale represents intensity but is not normalized between the images as to do so would mean that the faint emission from the magnesium plasma would not be visible. In each of the images a white line is used to represent the approximate position of the surface of the target. Each image in figure 3.4 is a summation of 15 laser shots on the same spot on the target surface. The dimensions of each plume were obtained by taking an intensity line-out across each plasma in planes normal (length of plume) and parallel (width of plume) to the target surface.

The intensity of the soft X-ray emission varies greatly between each image. Both copper and tungsten emit brightly in the soft X-ray spectral region and lead to a high number of counts recorded by the CCD. However the emission intensity recorded from the magnesium plasma is substantially less than that of copper and tungsten.

Beside each image are the intensity lineouts of each plume in two directions, i.e. parallel and perpendicular to the surface of the target. These values will be used to estimate the X-ray emission lifetime of the hot core of the plasma. Listed in table 3.1 are the full width half maximum (FWHM) values for the X-ray emitting core of each plume in microns for the two orthogonal directions. It is clear that as the atomic number of the target increases from low to high, the extent of the X-ray emitting region in the direction normal to the target surface (the plasma expansion axis) decreases. The images reveal that magnesium ( $Z = 12$ ) is not very bright but has the largest emitting size, with material extending up to  $40 \mu\text{m}$  from the target of all the metals presented here. Tungsten ( $Z = 74$ ) on the other hand has the smallest emitting dimension but produces relatively bright emission below  $\lambda = 1 \text{ nm}$ . An increase in atomic number leads to an increase in the mass of the ions. This in turn leads to a slower expansion velocity of the bulk of the plume. Tungsten has a relatively large mass compared to copper or magnesium and so it is expected to have a concomitantly smaller expansion velocity. The bulk of the plasma plume in this case would be confined to a region with an extent of a few hundred micrometers from the target surface.

From the FWHM dimensions quoted in figure 3.4 it is possible to estimate the X-ray

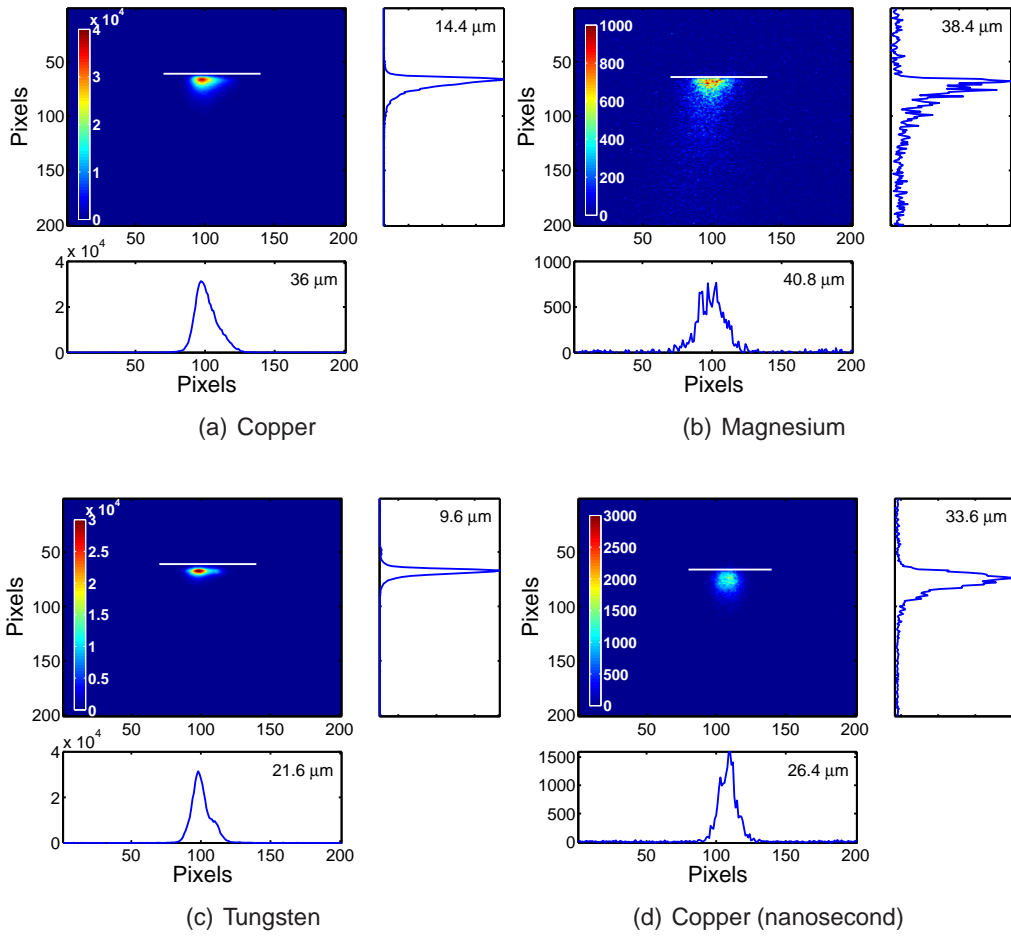


Figure 3.4: Soft X-ray emission images of laser-produced plasmas generated on flat targets of various metals. Each image is a summation of 15 laser shots (400 mJ) with the exception of magnesium. Magnesium image (b) contains 60 single shots over four spot locations in order to amplify the very faint single. The white line in each image represents the approximate position of the target surface in each case. Also shown are line-outs taken through the center of the plume in a plane normal and parallel to the target surface. The FWHM of each plume along the different planes is quoted in each figure. Plasmas were generated using the EKSPLA™ 312p picosecond laser system with the exception of (d) which was taken using a nanosecond laser (*see text for details*).

emission duration from the plasma using,

$$L = C_S \tau_X \quad (3.3)$$

where L is the length of the bulk plasma deduced from the X-ray pinhole images,

$\tau_x$  is the emission time and  $C_s$  is the ion sound speed, which is given by [11],

$$C_s = \left( \frac{\gamma z k_B T_e}{m_i} \right)^{\frac{1}{2}} \quad (3.4)$$

where  $\gamma = c_p/c_v$  is the adiabatic index (or isentropic expansion factor [12]),  $z$  is the average charge state,  $k_B$  is Boltzmann's constant,  $T_e$  is the electron temperature and  $m_i$  is the ion mass. All quantities are in *cgs* units except temperature ( $T_e$ ) which is expressed in eV. To calculate the ion sound speed an average charge ( $z$ ) of 5, an electron temperature of 250 eV and an adiabatic index of 1.24 [13] were used in the calculation, yielding an ion sound speed of  $\sim 5 \times 10^6$  cm/s for copper. The plasma dimension normal to the surface of the target (along the expansion axis of the plasma) deduced from figure 3.4 (a) was in the region of 15  $\mu\text{m}$ . Substituting this value into equation 3.3 reveals an X-ray emission duration in the region 220 ps for the copper plasma shown in figure 3.4 (a) which is in agreement of the upper limit of 1 ns obtained using fast photodiodes in section 3.2.3 above.

It should be noted however that while there is a decrease in the plume dimension in the plane normal to the target surface for increasing atomic number, the lateral (or plane parallel to the target surface) dimension is almost equal for magnesium and copper and is considerably smaller in the case of tungsten (see table 3.1). In the image in figure 3.4 (c) the tungsten plasma appears to be quite wide which may indicate that its lateral expansion velocity, along the plane parallel to the target surface, could be quite high.

<b>Metal</b>	<b>Perpendicular (<math>\mu\text{m}</math>)</b>	<b>Parallel (<math>\mu\text{m}</math>)</b>
Magnesium (12)	38.4	40.8
Copper (29)	14.4	36.0
Tungsten (74)	9.60	21.6

Table 3.1: Dimensions (FWHM) of the X-ray emitting core of a laser-produced plasma in the directions parallel and perpendicular to the surface of the target. A 3  $\mu\text{m}$  aluminium filter was used to limit the radiation reaching the CCD chip to the soft X-ray spectral region around 1 nm.

An interesting comparison was made between a plasma generated by a picosecond laser system and by a nanosecond laser system. In figure 3.4 (d) one can see a pinhole image of a copper plasma generated using a 15 ns pulse from a Spectron™ SL800 Nd:YAG laser system operating at the fundamental wavelength of 1064 nm and a peak pulse energy of  $\sim 1.2$  J. The most striking difference be-

tween figure 3.4 (a) and (d) are the plume dimensions, especially in the direction normal to the target surface. Along this forward expansion axis the copper plasma that was generated by the picosecond laser pulse has a FWHM of  $14.4 \mu\text{m}$ , while in the nanosecond case it was  $33.6 \mu\text{m}$ ; an increase of  $19.2 \mu\text{m}$  or approximately 60 % in the length of the plume. The fluence ( $\text{J}/\text{cm}^2$ ) of both laser systems was quite similar ( $\sim 2 \times 10^4 \text{ J}/\text{cm}^2$ ), the increased pulse energy (1.2 J) compensating for the larger spot size of the nanosecond laser ( $\sim 80 \mu\text{m}^2$ ) meaning that the main difference between the two are the pulse durations of the lasers. As mentioned in section 1.2, nanosecond laser systems cause substantial melting of the surface material, more than in the case of a short-pulse laser system like the EKSPLA™ 312p. This results in ablation of a larger amount of target material which as one might expect a bigger plasma than that of short-pulse laser systems. Assuming a similar expansion velocity for the nanosecond case, the soft X-ray pulse duration is approaching 2.5 times that in the picosecond laser case and so enters the 1 – 2 ns pulse width range.

### 3.3 Colliding Plasma Systems

The physics of colliding laser-produced plasmas plays a key role in areas of research such as inertial confinement fusion [15] and new forms of pulsed laser deposition [16]. This section presents results from the preliminary study on the collision of two counter-propagating plasmas studied in the soft X-ray spectral region. Recent studies into colliding plasma systems have mainly concentrated on two distinct parameter spaces, the collision of plasmas generated from table-top nanosecond laser systems [17, 18] and from irradiation with nanosecond and sub-picosecond petawatt lasers [19, 20, 21]. These experiments revealed that material from the two plasmas will accumulate in the midplane region of the colliding plasmas. As the two plasmas continue to expand, more and more material reaches this region which leads to a rise in temperature as ion kinetic energy is converted into excitation energy at the boundary.

In stark contrast to the studies made previously using nanosecond laser systems, in this section data on the collision between two relatively hot plasmas will be presented. Results from the spectroscopic study on single laser-produced plasmas presented in the previous section revealed that plasma temperatures in the hundred to few hundred electron volt range were easily achieved using the picosecond

---

<sup>2</sup>The spot diameter was assumed to be in the region of  $80 \mu\text{m}$ , as quoted in Banahan *et al.* [14].

laser. When plasmas of this temperature range collide the formation of a 'hard' well defined stagnation layer is not a given. In the case of hot colliding plasma plumes in close proximity, the ion-ion mean free path can be larger than the separation between the two seed plasmas (as it scales with the square of the temperature). Therefore, this case will tend to favor interpenetration of plasma constituents over stagnation.

Equations 1.27 and 1.25 from section 1.6 were used to calculate both the ion-ion mean free path and the collisionality parameter which characterize these hot X-ray emitting plasmas, repeated here for the reader's convenience. The ion-ion mean free path for colliding plasmas is given by [20],

$$\lambda_{ii}(1 \rightarrow 2) = \frac{m_i^2 v_{12}^4}{4\pi e^4 z^4 n_i \ln \Lambda_{1 \rightarrow 2}} \quad (3.5)$$

where  $v_{12}$  is the relative collision velocity,  $n_i$  is the average plasma ion density at the collision plane,  $z$  is the average ionization state of the plasma,  $m_i$  is the ion mass,  $e$  is the charge of the electron and  $\ln \Lambda_{1 \rightarrow 2}$  is the so-called Coulomb logarithm (assumed to be equal to 10 [11]). The collisionality of the colliding plasma system can be determined from [20]:

$$\xi = D/\lambda_{ii} \quad (3.6)$$

where  $D$  is the separation between the two seed plasmas. The ion-ion mean free path was calculated using a collision velocity ( $v$ ) of  $5 \times 10^6$  cm/s corresponding to the ion sound speed, a charge state ( $Z$ ) of 5, an ion mass ( $m_i$ ) of 63 (atomic mass units) for copper and an average electron density ( $n_e$ ) of  $10^{17}$  cm<sup>-3</sup> at the collision plane<sup>3</sup>. This yields an ion-ion mean free path of 165  $\mu$ m.

Two seed plasmas were generated on a flat copper target using the optical setup described previously. Briefly, the setup uses a wedge-prism to deflect a portion of the laser beam before the beam is focused onto the surface of the target using a spherical short focal length plano-convex lens. The distance between the two focal spots depends on the wedge angle of the prism and on the focal length of the lens. By controlling the position of the wedge prism in the beam a controllable portion of the beam can be deflected. In this way the ratio of the laser pulse energy shared between the two beams can be controlled and in turn, the ratio of the irradiance at each of the two focal spots can be varied quite precisely. In this experiment the two plasmas were initially separated by  $\sim 145$   $\mu$ m with the laser energy equally

---

<sup>3</sup>This value was chosen because the density in the periphery of the plasma plume is assumed to be significantly less than that of the core (where we estimate  $n_e = 10^{19}$  cm<sup>-3</sup>).

shared between each focal spot, i.e. the wedge prism bisected the path of the laser beam creating two equal intensity beams. The average separation between the two seed plasmas was comparable to (*or less than*)  $\lambda_{ij}$ , resulting in a low value of the collisionality parameter. This implies that very little stagnation between the two plumes will occur and any interaction which may be occurring may not be hot enough to emit in the X-ray spectral region.

Point like plasmas generated on a flat target will expand into the vacuum away from the target surface. As they expand normal to the target they will also expand along the orthogonal direction, i.e., parallel to the surface. This is the lateral expansion plane of the plasma and the expansion velocity along this plane can be up to an order of magnitude less than along the plane normal to the target surface [17]. If the two plasmas are generated close to one another, then they will expand and subsequently collide along this lateral axis. The lateral plane lying between the two plasmas defines the collision region which was investigated using imaging and spectroscopy.

### 3.3.1 Soft X-ray Spectroscopy

The KAP crystal was set to an angle of  $21^\circ$  with respect to the optic-axis, thereby setting the center wavelength of the spectrometer to  $\sim 0.955$  nm. The laser beam from the picosecond laser system was bisected using a  $10'$  wedge prism and two point plasmas were generated on a flat magnesium target with a separation of  $150 \mu\text{m}$ . Magnesium was chosen as the target metal because the intense Ne-like doublet at  $0.916$  nm and  $0.923$  nm corresponding to the  $1s^2 - 1s2p$  transition of He-like magnesium which could be used to identify emission from any stagnation layer that might be formed. The two plasmas were generated at points lying either side of the optical axis which defined the center position of the spectrometer and so spectra from each of the two plasmas were formed at slightly different positions on the CCD chip. Any emission from the interaction region between the two plasmas would then appear at the center of the CCD chip.

As described in Chapter 2, isolation of the emission from the two seed plasmas was achieved by placing a movable aluminium bar between the target and the lens. By translating this bar vertically, the beam initiating any one of the individual seed plasmas could be blocked. Hence one could take spectra of either of the seed plasmas for the no collision case and by removing the bar a spectrum of the full colliding plasma system (including the seed plasmas) could be recorded. The spectra from the two individual seed plasmas were summed and subtracted from the spectrum

of the colliding case to search for a spectral signal representing evidence of any X-ray generation at the collision front.

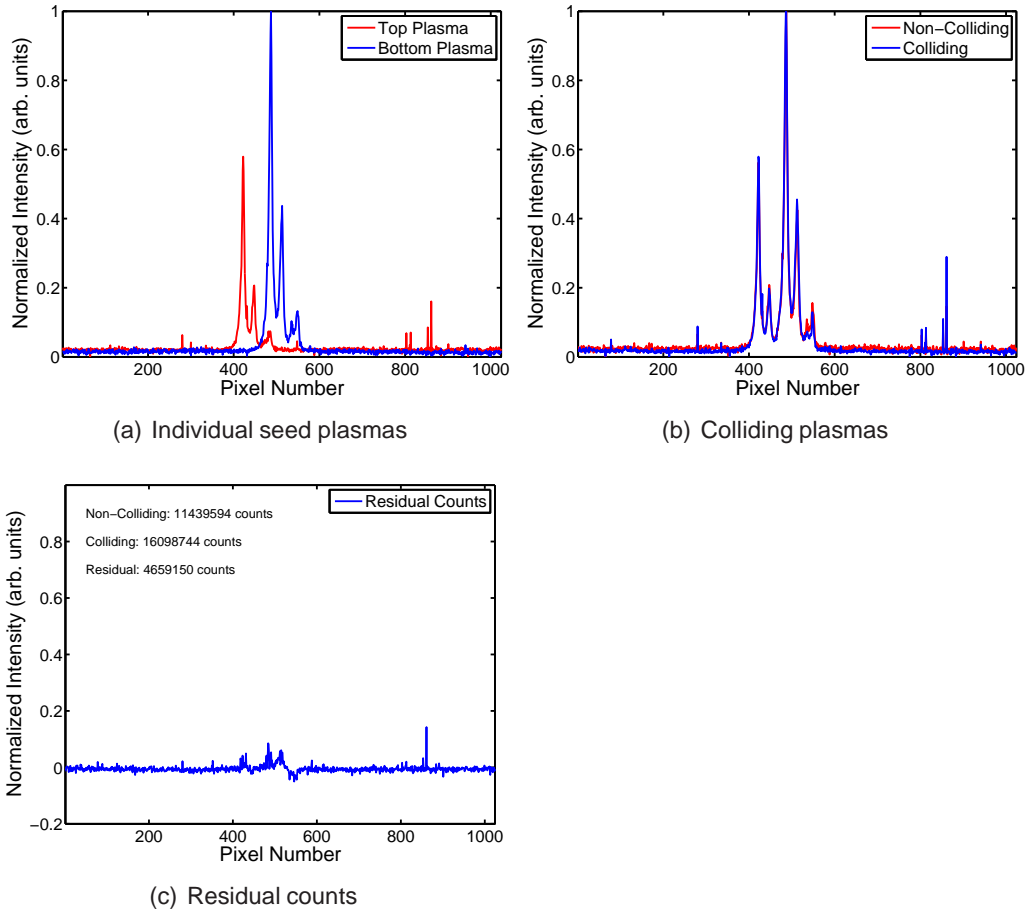


Figure 3.5: Soft X-ray spectra of two equally colliding magnesium plasmas generated using an intense table-top picosecond laser system. (a) The individual spectra from each of the seed plasmas was acquired by blocking the opposite portion of the laser beam. (b) Spectrum of the colliding plasma system (overlaid with the spectrum from the non-colliding case) obtained by removing the aluminium bar used to block the laser beams. (c) The residual counts which remain when the spectrum from the non-colliding case is subtracted from the colliding case. The integrated counts for the two cases are shown in figure. The separation between the two foci, and consequently the two plasmas was  $\sim 150 \mu\text{m}$ . A  $1.5 \mu\text{m}$  thick aluminium filter was used to select only soft X-ray wavelengths below 1 nm.

The results are shown in figure 3.5 where (a) shows the individual emission spectra of the top and bottom seed plasmas. Any emission from the interaction region would appear between these two spectra, in the region of pixel 450. The second figure (3.5 (b)) shows the spectrum of the complete colliding plasma system (including seed plasmas) after the bar was removed compared to the summation of

the individual seed plasma spectra. The final figure (3.5 (c)) shows the residual counts when the colliding and no-colliding spectra were subtracted. No significant additional emission in the difference spectrum was observed which could be attributed to the interaction/collision region. The residual counts around pixel 500 are simply the result of shot-to-shot fluctuations in the pulse energy of the laser. Labeled in figure 3.5 (c) are the integrated counts for the two cases. One can clearly see that there is an increase in the absolute value of the counts for the colliding plasmas system, but it is highly unlikely that the binary collisions which occur in plume interpenetration (which is assumed to be the predominant collision process here, at least in the very early stages of the interaction where the fastest moving ions reach the collision plane) will have sufficient frequency or energy to produce species which can emit strong radiation in the soft X-ray spectral range.

This result highlights that there appears to be no appreciable emission from the interaction region between the two plumes below the 1 nm cutoff wavelength of the aluminium filter. The observation of no additional emission does not rule out that stagnation is occurring between the two plasmas, but it does imply that there is insufficient heating of the material in the collision region to produce emission of X-ray radiation. It is difficult to conclude whether interpenetration or stagnation is occurring between the two plasmas using this setup and so in the next section we present images of the colliding plasma system obtained using an X-ray pinhole camera.

### 3.3.2 Pinhole Imaging

Spectra of the colliding plasma system, recorded using the crystal spectrometer, revealed no observable emission that could be attributed to the formation of a well-defined stagnation layer. A plasma produced using the picosecond laser was estimated to have an electron temperature in the range of one to a few hundred electron volts, depending on atomic number or mass. At this temperature, the ion-ion mean free path was calculated to be  $\sim 165 \mu\text{m}$ , which is larger than the separation between the two plasmas ( $d \leq 145 \mu\text{m}$ ), leading to a very low value of the collisionality parameter defining the system. In this case one would expect at least some interpenetration to occur, where some of the plasma species from the two plumes pass through each other with perhaps only binary collisions prevalent in this case. The absence of bright X-ray emission from the interaction region between the two plasmas does not however confirm or disprove interpenetration but it would certainly indicate that if there was any material heating and/or buildup at the collision

front, it was certainly not hot enough to emit sufficiently strongly in the 1 nm region covered by the crystal spectrometer setup. Further, if there was significant interpenetration, the resulting plasma-plasma species collisions were not sufficiently great in energy and/or number to excite weak X-ray emission and/or produce a detectable X-ray signal. To simplify the experiment and capture broadband X-ray emission with hoped for high SNR images, it was decided to invoke X-ray imaging using a pinhole camera (albeit this is not an ideal configuration for light gathering due to the micron sized pinhole aperture ).

However, at least we could confirm without ambiguity the spatial distribution of X-ray emission, normalized to a bright seed plasma. In addition, we could obtain an upper bound for the plasma temperature by making the naive assumption that collision front region is approximated by a blackbody emitter. That is to say, the absence of emission would certainly imply that the collision front region was cooler than a blackbody with a peak wavelength of 1 nm.

The Bragg crystal spectrometer was replaced by a pinhole camera setup which consisted of a 5  $\mu\text{m}$  diameter pinhole aperture and a back-illuminated X-ray sensitive CCD camera. A 300 mm long tube was fixed between the pinhole and the CCD camera to ensure that no scattered laser radiation would impinge on the CCD chip. The pinhole assembly was fixed to manual translation stages which gave full X-Y-Z movement. The size of this assembly meant that the pinhole was limited to a distance of 30 mm from the plasma. The ratio of the image distance (between the pinhole aperture and the CCD chip) to object distances (between the pinhole and the plasma) resulted in a magnification of 10. Hence each pixel (26  $\mu\text{m}$  pitch) on the CCD camera represented a dimension of 2.6  $\mu\text{m}$  at the colliding plasma object plane. Image magnification was critical in this experiment as the X-ray emitting size of the plasma was expected to be on the scale of a few to ten micrometers, the same dimensions as the pixels in the CCD chip.

From our single plasma experiments we have seen that the X-ray emitting core of a plasma produced from this laser system was typically  $\sim 10 \mu\text{m}$  in diameter. To ensure an appreciable interaction between the two plasmas we set the upper limit of the plasma separation at  $\sim 150 \mu\text{m}$ . This ensured that the two cores or the two X-ray emitting regions of the plasma would collide within their emission lifetime. Combining the 10' wedge prism with lenses which had effective focal lengths of 100, 75 and 50 mm the distance between the two plasmas was set to 145, 110 and 70  $\mu\text{m}$  respectively. The collisionality of the system was controlled by changing the focal length of the lenses and hence the distance between the plasmas. The

two plasmas were formed on flat copper targets and so as the plasmas expanded into vacuum, they collided along their lateral expansion plane. Figure 3.6 (a – c) shows time-integrated images of two copper plasmas colliding along their lateral expansion axis for different plasma separations.

The first image in the sequence was recorded with a plasma separation of 145  $\mu\text{m}$ . At this distance one can see that the two plumes are distinct and do not collide during their expansion. One flaw with the wedge prism deviation is that the deviated beam suffers astigmatism at the focus with a concomitantly lower on-target irradiance and plasma temperature. This effect is likely to be exacerbated at X-ray wavelengths where there is increased sensitivity to plasma temperature and so it proves here where one plume is clearly smaller and more asymmetric than the other. The effect is less pronounced as the focal length is shortened as can be seen in the 110  $\mu\text{m}$  and 70  $\mu\text{m}$  cases. In the 110  $\mu\text{m}$  case, figure 3.6 (b), it is clear that the individual X-ray images of the seed plasmas overlap. One has to be careful in this case as the experiment may be reaching the spatial resolution limit of the pinhole imaging system, which is limited by the pixel dimensions of the CCD camera (26  $\mu\text{m}$ ). When the separation between the two seed plasmas was reduced further, figure 3.6 (c), the periphery of each plasma came into contact. At this separation, which is comparable to the FWHM of their cores, one begins to observe evidence of interaction between the cores, notwithstanding comments made above on approaching the resolution limit of the imaging system. However, the images show little sign of a stagnation layer, which would appear as a significant increase in the intensity of the image along the midplane between the two plumes. The outer corona of both plasmas appears to have merged into one large elliptical shape and although there may be some slight evidence of a feature protruding from the mid plane beyond the main seed plasmas in this case, one cannot say with certainty that it is the progenitor of a stagnation layer.

With no convincing evidence of sufficiently hot source formation via either stagnation or interpenetration to drive X-ray imaging, it was decided that it would be preferable to move the imaging and spectroscopy programme to longer wavelengths where cooler plasma regions could be detected in emission. The results of a study in the UV - Visible spectral range are given in the next chapter.

Before concluding, it is worth noting that a similar study was undertaken on magnesium plasmas by Harilal *et al.* in 2001 [17] where they collided two plasmas which were produced using a nanosecond laser system (15 ns pulse duration). In their work they recorded emission from the plasma in the extreme-ultraviolet spectral re-

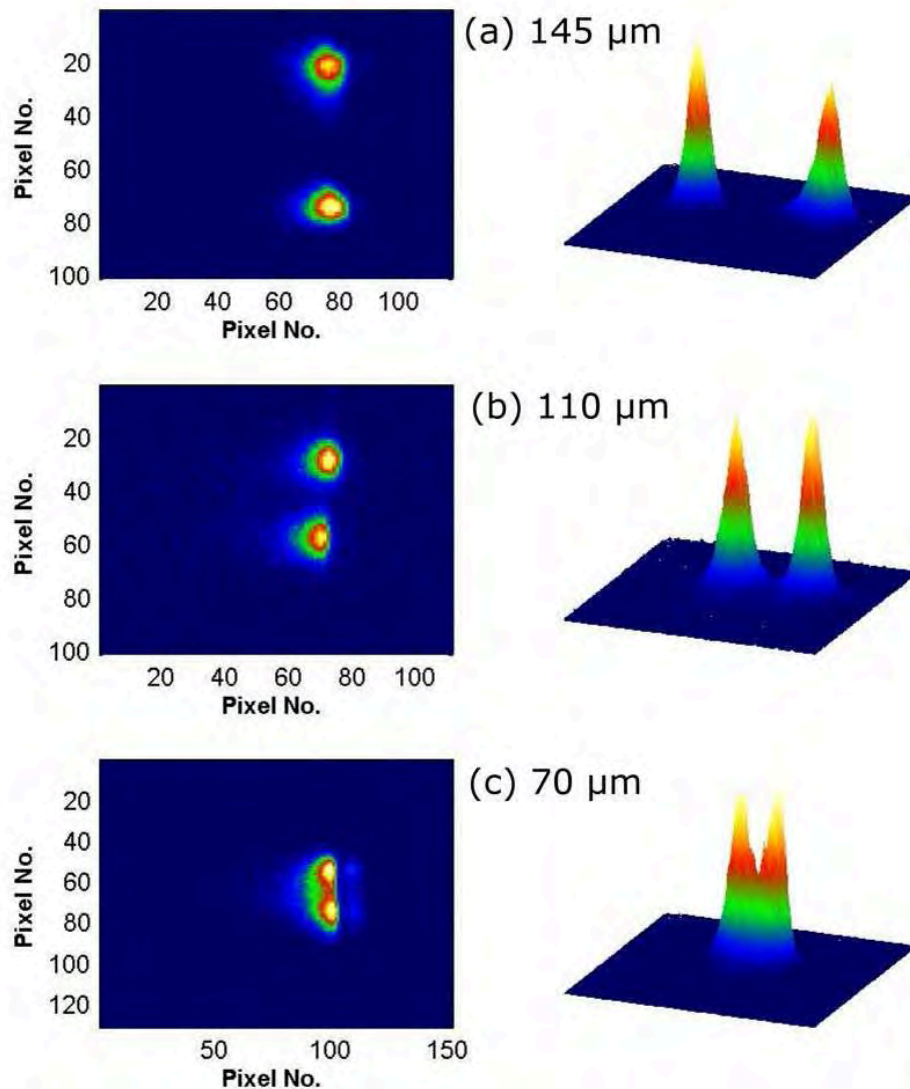


Figure 3.6: Soft X-ray emission images of two laterally colliding copper plasmas produced on a flat target recorded using a pinhole camera. The separation between the two seed plasmas was reduced by replacing the lens with a shorter focal length. By reducing the separation between the two plasmas one can control the value of the collisionality of the system. The ion-ion mean free path was calculated to be  $165 \mu\text{m}$ .

gion using a pinhole camera (which had a spectral sensitivity of  $\lambda < 80 \text{ nm}$ ). What they observed was the formation of a very bright and well-defined stagnation layer

in the region between the two colliding plumes. The minimum separation between the two plasmas was  $750 \mu\text{m}$  which is significantly larger than what was used in the work presented here. The result indicated that one should see stagnation in our hot plasmas but at longer wavelengths and it provided the motivation to pursue this line of investigation. The conclusive observation of stagnation would also give a feel for how low the collisionality parameter could go while still observing stagnation - a correlation of the phenomenological collisionality parameter with a real experimental situation.

### 3.4 Conclusions

Spectra and images in the soft X-ray spectral region of plasmas generated using the EKSPLA™ 312p picosecond laser system were presented in this chapter. Photon diagnostics in the soft X-ray spectral region examine the initial conditions of the plasma soon after it has been formed by the laser, information which is unattainable in the visible spectral region due to the density of the plasma during this time. The on-target laser irradiance in the experiment was believed to be in the region of  $10^{13}$ , or at most a few  $10^{14} \text{ W/cm}^2$ . Spectroscopy of single magnesium plasmas revealed emission lines from highly charged ions and from this we estimated a plasma temperature of one to a few hundred electron volts. A collisional radiative model described in [8] which relates the plasma temperature to the on-target irradiance was used to refine this estimate ( $T_e \approx 540 \text{ eV}$ ). An alternative estimate of the plasma temperature, (in the region  $100 - 250 \text{ eV}$ ) based on the average ionic charge state was found to best agree with our expected value range and with similar systems in the literature [17].

Time-integrated pinhole images were used to determine the dimensions of the seed plasmas. We observed that the FWHM of the X-ray emitting core of the plasma was only a few tens of microns. Images of different metals showed that as the atomic number increases, the size of this core decreases, an observation explained by the decrease in the expansion velocity of the ions in the plasma. Images showed that the hot core in a tungsten plasma was smaller and more compact than that of a magnesium plasma.

Also presented in this chapter was a preliminary study into colliding plasma systems in the soft X-ray (SXR) spectral region. The X-ray diagnostics have shown that the seed plasmas are hot enough to produce easily detected single-shot plasma images and spectra in the  $0.8$  to  $1.5 \text{ nm}$  spectral range selected by the aluminium

filter. Notably, no intense SXR emission in the spectra was observed which would be indicative of a stagnation layer between the plumes. As the collisionality depends on the ion-ion mean free path (mfp) and the plasma geometrical scale length, at these high temperatures the ion-ion mean-free-path is quite large and so theory [20] predicts plume interpenetration to be the dominant collision process. Pinhole images revealed no localized emission which could be attributed to a stagnation region. If significant interpenetration between the two plumes was occurring, it was quite possible that the binary collisions which mediate energy transfer within this type of collision were not capable of producing material that was hot enough to emit in the soft X-ray spectral range, and so the absence of a stagnation layer cannot be stated conclusively (at least for the experiments presented here which probe the early stages of the colliding plasma system where the fastest and most highly charged ions are most likely to generate X-ray emission). For later times in the interaction, where colder plasma constituents interact, UV – visible imaging and spectroscopy would seem appropriate.

Hence, in the next chapter the photon diagnostics are moved into the ultraviolet and visible bands of the spectrum where there is significant atomic data available for us to accurately measure and map in space-time all plasma parameters such as density and temperature as well as ion distributions and expansion velocities (Luna *et al.* [4]). Our preliminary study of colliding plasmas will be expanded and the evolution of the stagnation layer will be tracked using time-resolved imaging and spectroscopy. Here, the value of the collisionality parameter would be high for the part of the plasma emitting in the visible region, and so stagnation between the two colliding plumes is expected to dominate over plume interpenetration.

# Bibliography

- [1] M. Murnane, H. Kapteyn, M. Rosen, and R. Falcone. Ultrafast X-ray pulses from laser-produced plasmas. *Science*, 251(4993):531 – 536, 1991.
- [2] O. Meighan, A. Gray, J.-P. Mosnier, W. Whitty, J. T. Costello, C. L. S. Lewis, A. MacPhee, R. Allott, I. C. E. Turcu, and A. Lamb. Short-pulse, extreme-ultraviolet continuum emission from a table-top laser plasma light source. *Applied Physics Letters*, 70(12):1497–1499, 1997.
- [3] R. S. Quimby. *Photonics and Lasers: An Introduction*. Wiley-Interscience, 2006.
- [4] H. Luna, J. Dardis, D. Doria, and J.T. Costello. Analysis of time-resolved laser plasma ablation using an imaging spectra technique. *Brazilian Journal of Physics*, 37:1301–1305, 2007.
- [5] A. Michette. Private communication, 2005.
- [6] S. S. Harilal, C. V. Bindhu, V. P. Shevelko, and H. J. Kunze. XUV diagnostics of colliding laser-produced magnesium plasmas. *Journal of Physics B: Atomic, Molecular and Optical Physics*, 34(18):3717–3726, 2001.
- [7] J. Dardis, A. Murphy, H. de Luna, E. T. Kennedy, A. Seugnet, P. Orr, J. Greenwood, C. McKenna, C. L. S. Lewis, and J. T. Costello. Progress report on compact system for point projection X-ray absorption spectroscopy and imaging of laser produced plasmas. volume 5826, pages 363–370, 2005.
- [8] D. Colombant and G. F. Tonon. X-ray emission in laser-produced plasmas. *Journal of Applied Physics*, 44(8):3524–3537, 1973.
- [9] Andor Technology Inc. Manufacturers website. [http://www.andor.com/pdfs/spec\\_sheets/DX420.pdf](http://www.andor.com/pdfs/spec_sheets/DX420.pdf).
- [10] C. McGuigan. *Computing Ionization Balance within Laser-Produced Plasmas*. B.Sc. Thesis, Dublin City University, 2007.

- [11] J. D. Huba. Naval Research Laboratory: Plasma Formulary. <http://www.ppd.nrl.navy.mil/nrlformulary/>, Naval Research Laboratory, Washington, DC 20375, 2004. Revised Edition.
- [12] S. I. Anisimov, B. S. Lukyanchuk, and A. Luches. An analytical model for three-dimensional laser plume expansion into vacuum in hydrodynamic regime. *Applied Surface Science*, 96-8:24–32, 1996.
- [13] M. Stapleton. *Modelling Study of the Hydrodynamic Expansion of a Laser Ablation Plume of Lithium in Vacuum*. Ph.D. Thesis, Dublin City University, 2003.
- [14] C. Banahan. *One and Two Photon Absorption of Atoms and Ions*. Ph.D. Thesis, Dublin City University, 2009.
- [15] T. R. Dittrich, S. W. Haan, M. M. Marinak, S. M. Pollaine, D. E. Hinkel, D. H. Munro, C. P. Verdon, G. L. Strobel, R. McEachern, R. C. Cook, C. C. Roberts, D. C. Wilson, P. A. Bradley, L. R. Foreman, and W. S. Varnum. Review of indirect-drive ignition design options for the National Ignition Facility. *Physics of Plasmas*, 6(5):2164–2170, 1999.
- [16] E. Camps, L. Escobar-Alarcón, E. Haro-Poniatowski, and M. Fernández-Guasti. Spectroscopic studies of two perpendicularly interacting carbon plasmas generated by laser ablation. *Applied Surface Science*, 9(197-198):239–245, 2002.
- [17] S. S. Harilal, C. V. Bindhu, and H. J. Kunze. Space- and time-resolved soft X-ray emission from laser-produced magnesium plasma. *Journal of Physics D: Applied Physics*, 34(4):560–566, 2001.
- [18] H. Luna, K. D. Kavanagh, and J. T. Costello. Study of a colliding laser-produced plasma by analysis of time and space-resolved image spectra. *Journal of Applied Physics*, 101(1):1–6, 2007.
- [19] S. M. Pollaine, J. R. Albritton, R. Kauffman, C. J. Keane, R. L. Berger, R. Bosch, N. D. Delameter, and B. H. Failor. Stagnation and interpenetration of laser-created colliding plasmas. *APS Meeting Abstracts*, pages 12–16, 1990.
- [20] C. Chenais-Popovics, P. Renaudin, O. Rancu, F. Gilleron, J.-C. Gauthier, O. Larroche, O. Peyrusse, M. Dirksmüller, P. Sondhaus, T. Missalla,

I. Uschmann, E. Förster, O. Renner, and E. Krousky. Kinetic to thermal energy transfer and interpenetration in the collision of laser-produced plasmas. *Physics of Plasmas*, 4:190–208, 1997.

- [21] R. Fabbro, B. Faral, J. C. Gauthier, C. Chenais-Popovics, J. P. Geindre, and H. Pepin. Study of the emissivity of the rear face of a shocked foil with temporal and x-uv spectral resolution in single and colliding foil experiments. *Laser and particle beams*, 8(1-2):73–79, 1990.

## Chapter 4

# Emission Imaging and Spectroscopic Studies

### 4.1 Overview of Visible Emission Experiments

Emission imaging and spectroscopy were used to track the expansion dynamics of a single plasma plume and to determine the corresponding time and space resolved plasma parameters, specifically electron temperature and density. The second part of this chapter contains specific results from colliding plasma systems. In this case, imaging and spectroscopy were used to examine the interaction of the two colliding plasma plumes and the properties of the stagnation layer formed in the vicinity of the collision plane. The final section of the chapter is concerned with results obtained from emission images of counter-propagating colliding plasma systems where the 'seed' plasmas were generated on wedge-shaped targets thereby facilitating the formation of horizontally (or vertically) opposed plasma plumes.

The move of the photon diagnostic systems from the X-ray to the visible spectral region was motivated by a lack of information on the colliding plasmas gathered using the former time-integrated detectors. Firstly, the collection, manipulation and dispersion of radiation in the near UV to near IR spectral range is easily accomplished using readily available optics and spectrometers. Secondly, this spectral range is covered by standard laboratory intensified CCD cameras so that images and spectra can be recorded with nanosecond time resolution and spatial resolution of microns. Thirdly, the UV-Vis/NIR spectra of almost all charge states of low to medium atomic number atoms such as carbon, aluminium, calcium, etc. are well known and line assignments can be obtained from Internet databases such as the

one hosted by the NIST [1]. Finally, the Stark parameters for many of the emission lines are known and so electron densities can be readily extracted from these spectra.

In the case of colliding plasma systems, the shift from the soft X-ray to the visible spectral region will result in a small but very significant change in the value of the collisionality parameter which characterizes the collision between the two plasma plumes. The colliding plasma system in the soft X-ray region (described in Chapter 3) involved the collision of two relatively hot seed plasmas ( $T_e \geq 100$  eV), where the ion-ion mean free path or mfp ( $\lambda_{ii}$ ) of the plasmas was calculated to be  $\sim 165$   $\mu\text{m}$ . This was comparable to (and sometimes greater than) the separation between the two seed plasmas (i.e.,  $\lambda_{ii} \geq D$ ). In this case the system was characterized by a fairly low value collisionality parameter ( $\xi < 1$ ) and so the degree of plume interpenetration was expected to be high. The experimental data showed that the X-ray imaging and spectroscopy revealed no significant emission which could be attributed to stagnating seed plasmas which supported our theoretical calculations, though the result did not completely rule out the possibility of a stagnation layer that was emitting radiation at longer wavelengths. Moving the study of colliding plasma systems to the visible spectral region where the two seed plasmas are separated by a few millimeters means that the collisionality parameter defining the system will be increased somewhat. This is because the ion-ion mfp of species emitting in this spectral region (the lowly-ionized species) becomes smaller than the separation between the two seed plasmas (i.e.,  $\lambda_{ii} < D$ ). In this case, the collision between the two seed plasmas can be expected to result in the formation of a bright and well-defined stagnation layer. In the work presented here, two different target geometries and two different focusing arrangements have been used to vary the value of the collisionality parameter (to a small degree) which enabled the study of its impact on the formation and evolution of the collision process. Comparisons will be drawn between the collision of plasmas generated from picosecond lasers here with previous work done using lasers of different pulse durations, see Luna *et al.* [2], Harilal *et al.* [3], Pollaine *et al.* [4], Chenais-Popovićs *et al.* [5], to name but a few.

## 4.2 Single Plasma Studies

This chapter begins with the characterization of single laser-produced plasmas generated on flat metal targets. The move to the visible spectral region permits

the use of time-resolved detectors, where information on the expansion dynamics of the plume as well as on plasma parameters such as electron density and temperature diagnostics can be obtained, unlike the time-integrated measurements done in the soft X-ray case (Chapter 3).

The first section deals specifically with the study of the expansion dynamics of the plasma with the aid of emission imaging. The dynamics of the plume are influenced by several factors, many of which are determined by the parameters of the laser used to create the plasma: focal spot size and shape [6], pulse duration [7] and wavelength [8]. To ensure a direct comparison with the experiments performed in the soft X-ray spectral region the same short focal length lens has been retained, ensuring that the high on-target irradiance is maintained.

#### 4.2.1 Emission Imaging of Single Plasmas

Spectrally-filtered and time-resolved images were obtained using the imaging system described in section 2.5.3. Images of the expanding plasma were acquired every 10 ns for the duration of emission from the plasma (0 ns – 500 ns). The ICCD was operated with a gate-width of 5 ns and was synchronized to the Pockels cell trigger of the laser. The arrival time of the laser pulse at the target surface was found by scanning the delay between the camera and the laser and noting the time at which the first emission from the plasma was visible. In this way, it was possible to determine the time delay measurement accuracy of  $\pm 5$  ns. Moving either side of this delay would (i) yield no emission if the camera captured an image before the laser arrival time, or (ii) bright emission if the camera shutter was opened after the arrival of the laser pulse on the target. A filter wheel which contained a selection of transmission filters was used to spectrally filter the light reaching the CCD.

Figure 4.1 shows an array of images tracking the expansion of an aluminium plasma in vacuum from 25 ns – 150 ns. Beyond 150 ns the plasma has cooled significantly and the emission in this spectral region becomes quite faint. Each image represents a snap-shot in the life of the expanding plasma where the exposure time of each shot was  $\sim 5$  ns (the gate width of the ICCD). The laser beam enters the region from left to right and impinges on the target which is represented by the solid white line. Presented in the first column are images obtained using a broadband transmission filter. This is an edge-pass filter which transmits light below 950 nm, thereby passing white-light from the plasma while rejecting 1064 nm scattered laser light. The luminosity of each image represents the spatial distribution of the bulk plasma material and was used to determine the overall shape and

size of the plume. In the second column are images taken using a narrow band transmission filter centered at 390 nm which will selectively track emission from the  $\text{Al}^0$  spectral lines at 394.4 nm and 396.15 nm originating from transitions between the  $3s^23p(^2P_{3/2,1/2}) - 3s^24s(^2S_{1/2})$  levels in neutral aluminium. The third column contains images which have been spectrally filtered over a narrow window (10 nm FWHM) centered at 470 nm. These images reveal the spatial distribution of multiply ionized species with the largest contribution to the overall emission originating from the  $\text{Al}^+$  spectral line at 466.3 nm corresponding to the  $3p^2(^1D) - 3s4p(^1P^o)$  transition in singly ionized aluminium. The intensity of each image has been corrected for the peak transmission efficiency of the respective filter, but the intensity scales vary between individual plots in order to permit the faint emission at later time delays to be perceptible. Each image in figure 4.1 contains  $256 \times 256$  pixels and represents an area of interest (AOI) of approximately  $5.5 \text{ mm} \times 5.5 \text{ mm}$ .

The images in figure 4.1 (second and third columns) were normalized to the same luminosity scale and reveal that the intensity of emission from the neutral species in the plasma is inherently weak when compared to the images of the singly-ionized species (470 nm filter) in the plume. This observation may be the result of one or more of the following factors: Plasma opacity, meaning that the plasma is likely to be optically thick for transitions involving the ground state. This filter tracks the emission from the 394.4 nm and 396.15 nm emission lines ( $3p(^2P_{3/2,1/2}) - 4s(^2S_{1/2})$ ) and so the emission may be somewhat suppressed. Strong self-absorption was observed in the emission spectra from these plasmas and the determination of plasma parameters in its presence is a topic which will be dealt with in detail in section 4.2.2. The trend observed in figure 4.1 could also be due to the fact that the plasmas are initially relatively hot and so the neutral species population could be very low relative to the ion populations. Alternatively, the ionization balance within the plasma may be weighted predominantly in favour of more highly charged states (refer to the ionization balance of an aluminium plasma shown in figure 1.5 on page 20) and it is reasonable to expect a very low density of neutral species in the plasma (at least at early times in both cases before significant cooling has set in).

### **Plasma Expansion Velocities**

The expansion velocity of the plasma plume was determined by taking the time-resolved images of the bulk plasma (first column in figure 4.1) and extracting the intensity profile along a line which cuts through the center of the plume. The dashed

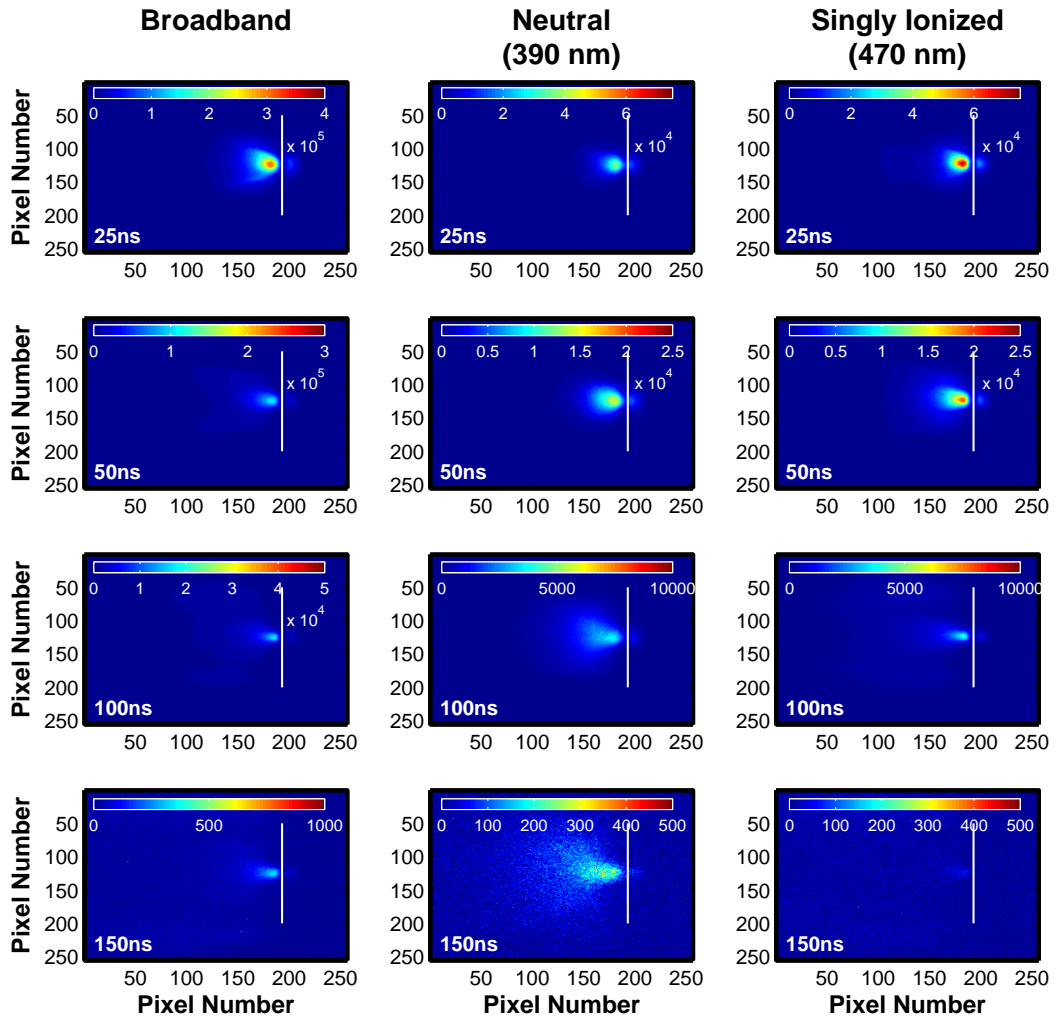


Figure 4.1: Spectrally filtered time-resolved image array of an expanding aluminum plasma produced on a flat metal target. First column: Images obtained using a broadband transmission filter showing white-light from the bulk plasma. Second column: Images obtained using a transmission filter centered at 390 nm which corresponds to emission from neutral aluminium species. This filter had a transmission of 18.5% and 7.5% at 394.4 nm and 396.15 nm respectively. Third column: Images taken using a filter with a center wavelength of 470 nm which transmits light from singly ionized species within the plasma plume. The  $\text{Al}^+$  spectral line at 466.3 nm corresponding to the  $3p^2(^1D) - 3s4p(^1P^\circ)$  transition dominates the emission in this spectral window. This filter had a transmission of 40% at this wavelength. The approximate position of the target is represented by the white line. The images have been corrected for the peak transmission of the relative filter and the luminosity scale of the second and third columns have been set equal. The limits of the luminosity scale decreases between rows in order to make the faint emission at the later time delays observable. Each  $256 \times 256$  pixel image represents an area of interest of  $5.5 \text{ mm} \times 5.5 \text{ mm}$ .

white line in figure 4.2 (a) highlights the position of the intensity line-out. The intensity profile of this lineout along the length of the plasma plume can be seen at the bottom of this figure. The plume-front position was chosen as the point where the intensity drops to 10% of the maximum intensity value. By tracking the position of this leading edge one can estimate the forward expansion velocity of the plasma. In certain cases, where expansion of the plasma is observed in both the forward and backward directions, the plume front position criterion was substituted by the full-width half-maximum value of this intensity profile to determine the total bi-directional expansion velocity.

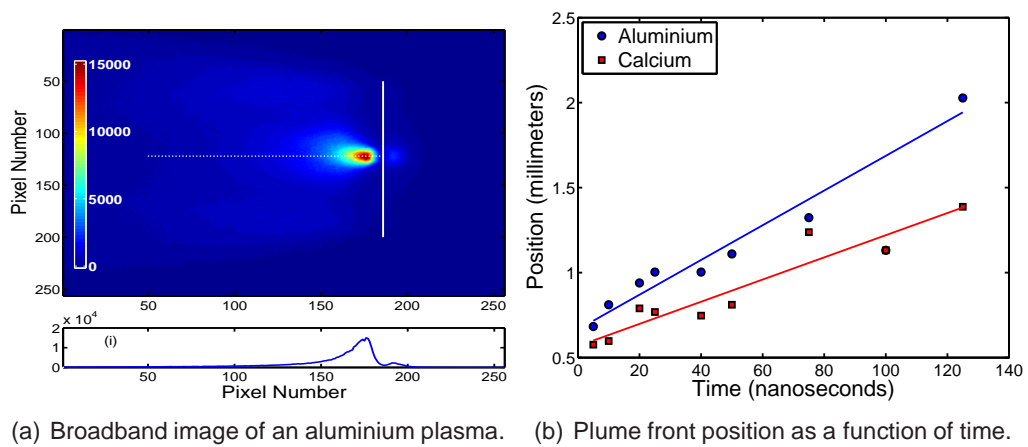


Figure 4.2: (a) Broadband image of an aluminium plasma produced on a flat target in vacuum ( $p \approx 10^{-5}$  mbar). The image was recorded 50 ns after the plasma was first created. The target edge is represented by the white line. The intensity line-out, used to determine the expansion velocity, is shown by the dashed white line (see text for details). Bottom left panel: Intensity profile through the plasma in the direction of the dashed line which is used to determine the position of the plume front used in the calculation of the expansion velocity. (b) Plume front position as a function of time delay for broadband emission from aluminium and calcium plasmas generated using the picosecond laser system. A simple linear fit is made to the data and the slope of the resulting line yields an approximate value for the expansion velocity.

Presented in figure 4.2 (b) are plots showing the time evolution of the plume front position for both aluminium and calcium plasmas. A simple linear fit to the data reveals an approximate value for the plasma expansion velocity of  $\sim 1 \times 10^6$  cm/s for aluminium and  $\sim 6.5 \times 10^5$  cm/s for calcium. As time progresses one may see that the velocity becomes constant for both types of plasma. The results show, as expected, that the less massive aluminium plasma plume expands at a greater velocity than calcium. At later time delays ( $\geq 120$  ns) the plume front position reaches a plateau, indicating that from this time onwards the plume has slowed

significantly. This occurs earlier in the case of the calcium plasma and which agrees with the general trend predicted by the Singh and Naraynan adiabatic expansion model [9].

The peak in the intensity of these images appears to be localized to within 1 mm of the target surface. While the plasma appears stationary in these images it is in fact continuously evolving and expanding into vacuum. There is a rapid initial expansion of the plasma plume away from the surface of the target which takes place within the first 25 ns, after which the bulk of the plasma remains localized into a small region. Beyond 25 ns it appears that material ejected from the deflagration zone accumulates at this region as it meets slower moving material in the corona which results in a dynamic zone of heating and bright optical emission<sup>1</sup>. From the bulk images (figure 4.1 on page 95) the plasma plume dimensions for calcium at 25 ns and 100 ns were estimated at 290  $\mu\text{m}$  and 490  $\mu\text{m}$ . So the plasma is growing, and while the plume front position may reach a plateau at 120 ns and beyond the plasma continues to grow and expand, but back towards the target surface where the reduced pressure gradient now facilitates this. At 300 ns the FWHM of the plasma plume is approximately 570  $\mu\text{m}$ .

Emission imaging can reveal only the expansion dynamics of the plasma. To estimate the electron density and temperature of the plume, spectroscopy is required. Discussed in the following section is the spectroscopy of the aluminium plasma. The Chromex™ 0.5 m spectrometer was used to obtain the space- and time-resolved electron density and temperature of the plasma.

#### 4.2.2 Spectroscopy of Single Plasmas

The data presented in the previous section revealed that plasmas produced by focusing the intense beam of the picosecond laser on flat targets have a rapid initial expansion away from the surface of the target and then reach a stationary state at 100 ns and beyond where it appears that material ejected from the deflagration zone is aggregated and localized as it meets slower moving material in the bulk corona resulting in a dynamic zone of collisional heating and bright optical emission. The key to understanding laser-produced plasmas is the determination of the fundamental parameters such as electron density and temperature which may for example be subsequently used as inputs to computer models.

---

<sup>1</sup>Caution must be used in the interpretation of plume dynamics using emission images, which fail to show dense regions of colder non-emitting plasma material.

The first step was the analysis of the width of spectral lines in order to determine the electron density within plasma. During this analysis it was found that the plasma showed signs of significant self-absorption in the regions of the plasma close to the target surface. Self-absorption (described in detail later) distorts and attenuates the spectral lines emitted by dense plasmas thereby rendering conventional Stark analysis which relies on spectral line shapes prone to significant errors. Therefore, two different methods have been used to determine the electron density within plasma. The first employs a conventional method of analysis based on the broadening of spectral lines due to the Stark effect, applicable in cases where the lines are unaffected by opacity; while the second incorporates an analytical model that accounts for opacity along the direction of viewing, to compare synthetic spectra to experimentally measured spectra. The temperature profile across the plasma was determined using the ratio of spectral line intensities between different charge states, the results of which are presented at the end of this section.

#### 4.2.2.1 Electron Density

Spatially-resolved spectra of individual aluminium plasmas were obtained using a Chromex™ 0.5 m visible spectrometer. The spectrometer was positioned so that the entrance slit (set to 60  $\mu m$ ) was aligned perpendicular to the plasma expansion axis. Optical radiation from the plasma was focused onto the entrance slit of the spectrometer using a relay lens system located inside the vacuum chamber. A dove prism was placed between these two lenses rotating the image of the plasma by 90° and the magnified image of the expanding plasma was formed with its expansion axis vertically aligned with the slit of the spectrometer. This optical arrangement gave a degree of spatial resolution in the plane normal to the target surface which in this case was the plasma expansion axis.

Time-resolved spectral images like the one shown in figure 4.3 were recorded at 10 ns intervals using the Andor™ intensified-CCD camera. The gate-width of the MCP intensifier (5 ns) was controlled using a Stanford™ delay gate generator which was temporally synchronized to the Pockels cell of the laser system. The image shows the spatial distribution of the emission from the plasma in the region of 400 nm. The two spectral lines in the image correspond to emission from the Al<sup>0</sup> doublet  $3s^23p(^2P_{3/2,1/2}) - 3s^24s(^2S_{1/2})$  at 394.4 nm and 396.15 nm respectively. The system had a magnification factor of 2 which was determined by the ratio of the focal lengths of the optics used in the relay lens system that coupled light from the plasma to the entrance slit of the spectrometer. Therefore, the viewable area of the

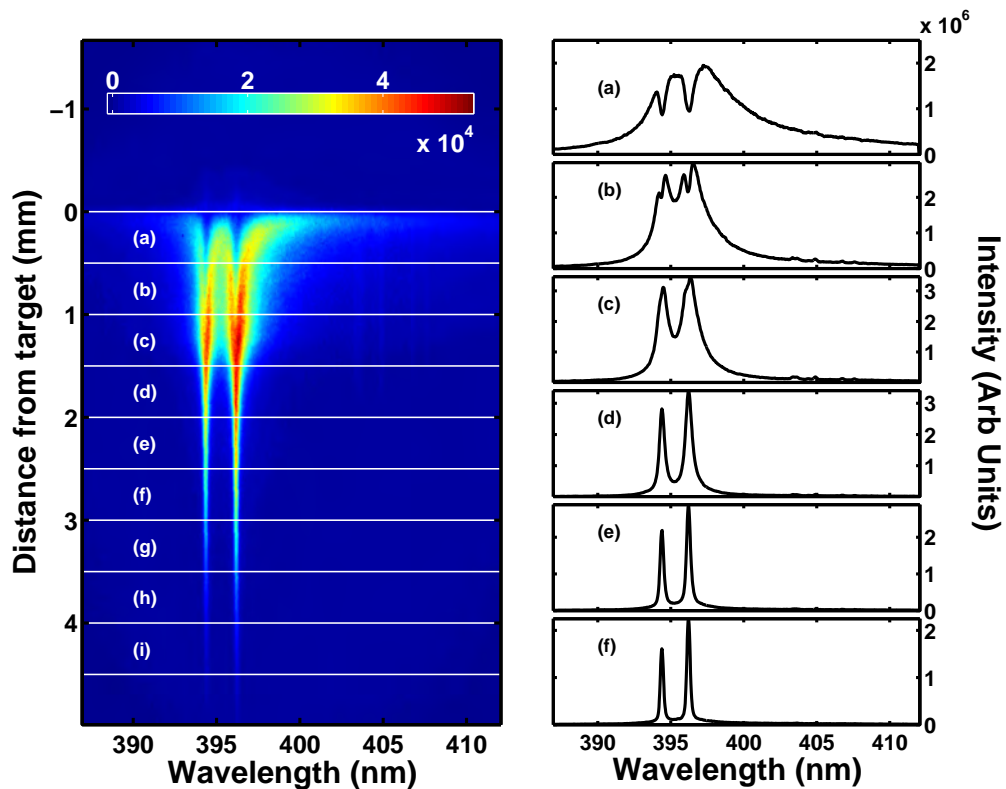


Figure 4.3: Spectral image of a single aluminium plasma generated on the surface of a flat metal target. The image has been divided into nine sections, each 75 pixels in height. Each section represents a distance of  $\sim 0.5$  mm from the target surface, and each sectioned sub-image has been full vertically binned, with the resultant one-dimensional spectra from the first six sections displayed on the right-hand side panel. The two spectral lines correspond to the  $\text{Al}^0$  doublet  $3s^23p(^2P_{3/2,1/2}) - 3s^24s(^2S_{1/2})$  at 394.4 nm and 396.15 nm respectively. The plasma is optically thick at these wavelengths and one may see clear signs of self-reversed line profiles in the region closest to the target surface ( $x \leq 2$  mm).

13 mm  $\times$  13 mm CCD chip (1024  $\times$  1024 pixels) corresponded to a footprint of approximately 6.5 mm  $\times$  6.5 mm at the plasma plume (object) plane.

When a spectral image like the one shown in figure 4.3 (left) is acquired the emission from the plasma is divided into nine equal regions each 75 pixels in height which corresponds to a spatial dimension of  $\sim 0.5$  mm. These regions are highlighted by the white lines in figure 4.3 (left) which begin at the surface of the target (position 0 mm on the image). The CCD counts were summed vertically (full vertical binning) within these regions and the resultant spectra are shown on the right of the figure. Figure 4.3 (a) shows emission from the region of the plasma closest to the target. The spectrum shows clear signs of strong self-absorption, with a

pronounced attenuation of both spectral lines at the transition wavelength. Moving away from the target surface, the deleterious effects of self-absorption are gradually reduced and the intensity ratio approaches the theoretical value of 2.

Figure 4.3 (a) shows that the effects of self-absorption greatly alters the magnitude and shape of spectral lines. This renders the measurement of electron density by spectral line width analysis prone to significant errors. In this region the widths of the spectral lines are not solely affected by the usual broadening mechanisms (natural, Stark, Doppler) alone. Therefore the conventional analysis which employs fitting convoluted Lorentzian (natural/Stark) and Gaussian (thermal Doppler) or Voigt functions profiles to the spectral lines is not directly applicable. The regions of the plasma where self-absorption is strong are found here to lie within 2 mm of the target surface.

So, to summarize, from figure 4.3 one can see that the emission from neutral aluminium species in the plasmas presented here exhibit two distinct regions, the first, close to the surface of the target where strong self-absorption is observed; and the second, far from the target surface where there appears to be little or no self-absorption. It is of interest to probe all regions of a plasma plume and therefore in the following section the two different methods which were used to determine the electron density across the full extent of the plasma, in both regions of high and low self-absorption will be presented. In the regions of the plasma where there was little or no self-absorption (regions (d-f) in figure 4.3) the electron density has been measured by extracting the Stark-broadened widths of the spectral lines. When the ratio of the intensity between the two spectral lines approaches the ratio of their statistical weights it can be assumed that there is little or no self-absorption occurring, therefore the conventional method of analysis becomes applicable and reliable.

On the other hand, in the regions of the plasma where significant self-absorption was observed, the self-reversed line profiles shown in figure 4.3 (a,b) being a characteristic sign, a simple self-absorption model (Sakka *et al.* (2002) [10]) was implemented for comparison with the experimental spectra. The model is based on a solution of the equation for radiative transfer which can account for the emission in the core and the absorption in the periphery as well as the usual Stark broadening and shifts on the spectral lines, which are taken to be small in the context of this model. The profile of a self-absorbed line produced by this model depends critically on a small number of parameters: the spatial distribution of the atomic or ionic populations of the upper and lower states, the electron density distribution across the plasma along the line of sight, and to a lesser degree on the plasma electron

temperature. These parameters are adjusted and through an iterative minimization procedure the synthetic spectrum from the model is fitted to the experimentally acquired spectrum. In doing so it was possible to extract a good approximation of the electron density of the plasma in the regions lying within 2 mm of the target surface.

In what follows, the electron density profile is obtained using both direct extraction from the line profile and, in the case of lines distorted by opacity, by comparison of the solution of the 1-dimensional radiative transfer equation with observed spectra. Using both methods provides a means to obtain electron density results throughout the space-time history of a plasma plume or stagnation layer.

### **Method I - Direct Stark Broadened Line Profile Analysis**

The discussion begins with the presentation of the plasma electron density obtained using the direct extraction from the widths of spectral lines. The region of applicability for this method was found to be  $\geq 2$  mm from the target surface for times  $\geq 100$  ns after the termination of the laser pulse. In this time and space domain, the spectral line shapes appeared to be largely undistorted by opacity effects. To confirm this observation, the intensity ratio of the spin-orbit doublet to be analyzed was measured to ensure that the ratio approached the theoretical value determined by the degeneracies of the individual upper levels ( $2j+1$ ). The spectral lines under examination were the  $\text{Al}^0$  doublet  $3s^23p(^2P_{3/2,1/2}) - 3s^24s(^2S_{1/2})$  at 394.4 nm and 396.15 nm respectively. The theoretical intensity ratio should be  $2(3/2)+1$  to  $2(1/2)+1$  or 4:2 (i.e., 2:1). This meant that there was little or no self-absorption and therefore it was safe to proceed with this analysis method.

The various mechanisms by which an emission line emanating from a transition in an atom or ion located in a dense plasma may become broadened were discussed in Chapter 5. In dense plasmas, such as those produced when an intense laser is focused on to the surface of a metal, the dominant mechanism which leads to significant broadening of a spectral line is due to collisions between the emitter and electrons (and ions) [11]. In this way the spectral line will be shifted and broadened due to the Stark effect, the magnitude of which is dependent on the local electron density. Broadening via electron/ion collisions (known as pressure broadening) will introduce a Lorentzian component to the shape of the spectral line. Therefore the full-width half-maximum (FWHM) in nm of a Stark-broadened spectral line can then

be related to the electron density using the following equation [12, 13]:

$$\Delta\lambda_{FWHM} = 2w \left( \frac{n_e}{10^{16}} \right) + 3.5A_i \left( \frac{N_e}{10^{16}} \right)^{\frac{1}{4}} \left[ 1 - 1.2N_D^{-\frac{1}{3}} \right] w \left( \frac{n_e}{10^{16}} \right) \quad (4.1)$$

The first term on the right-hand side of equation 4.2 describes the contribution due to electron-emitter collisions, where  $w$  is the electron-impact parameter in nm [14]. The second term in equation 4.1 is the contribution to the line broadening from ion-emitter collisions, where  $A_i$  is the ion broadening parameter and  $N_D$  is the number of particles in the Debye sphere. In the case of relatively low temperature but dense ( $n_e > 10^{14} \text{ cm}^{-3}$ ) plasmas the contribution to the line broadening from ion-emitter collisions becomes negligible compared to electron-emitter collision contribution, and so has been ignored in the present work. Therefore, the electron density (in  $\text{cm}^{-3}$ ) of the plasma can be approximated to:

$$n_e = \left( \frac{\Delta\lambda_{FWHM}}{2w} \right) 10^{16} \quad (4.2)$$

Another broadening mechanism inherent in plasmas is related to the motion of the emitters, known as (thermal) Doppler broadening. The contribution from Doppler broadening introduces a Gaussian component to the spectral line profile, the width of which can be estimated using the following equation [15]:

$$\delta\nu_D = \nu_0 \times 7.16e^{-7} \sqrt{T/M} \quad (4.3)$$

where  $T$  is the electron temperature,  $M$  is the atomic mass, and  $\nu_0$  is the transition frequency. In this work, equation 4.3 was used to estimate of the contribution to the width from Doppler broadening. The width of this Gaussian component for the  $\text{Al}^0$  emission line at 394.4 nm ( $7.6 \times 10^{14}$  Hz) in a hot plasma ( $T \approx 30000$  K) was found to be  $\sim 0.01$  nm. As the resolution of the spectrometer was  $\sim 0.16$  nm [16] any contribution to line broadening by the (thermal) Doppler effect is not measurable and so has been ignored in the present work. This broadening mechanism is due to the random thermal motion of atoms/ions within the plasma and one would expect it to be symmetric in all directions as the motion should not have a 'preferred' direction. However, the general motion of emitters (atoms/ions) in an expanding plasma will not be random and hence may give rise to broadening of the spectral lines. Depending on the point of view of the optical diagnostic system this so-called 'motional-Doppler' broadening of spectral lines in dense plasmas may be non-negligible. In the current experimental arrangement the optical axis of the

spectrometer is perpendicular to the major expansion axis of the plasma (normal to the target surface). This would result in a symmetric contribution to the line profile assuming that the plasma expansion is symmetric about the major expansion axis. The expansion velocity along this direction was determined from emission images to be a few times  $10^5$  cm/s for an aluminium plasma and the frequency shift  $\nu'$  due to the motional-Doppler effect can be determined from the general Doppler equation [17],

$$\nu' = \nu_0 \left( 1 \pm \frac{v}{c} \right) \quad (4.4)$$

where  $\nu_0$  is the transition frequency,  $v$  is the velocity of the emitter in the direction of the observer, and  $c$  being the speed of light. It is clear that at a velocity of  $10^6$  cm/s the magnitude of motional-Doppler broadening ( $\pm 0.013$  nm) is below the limits of detection of our system.

The various broadening mechanisms contribute differently to the overall shape of the observed spectral line. Doppler broadening will result in a Gaussian profile contribution to the overall spectral line shape while the natural and collisional broadening will introduce a Lorentzian component to the shape of the spectral line. Motional Doppler (when present) can lead to asymmetric Gaussian contributions. In laser-produced plasmas, one is rarely in a regime where only one broadening mechanism exists. Instrumental broadening mechanisms must also be taken into account. In earlier work which used this specific spectrometer [16], it was found that the instrument function was well approximated by a Gaussian profile of width 0.16 nm. A spectral line will therefore contain a mixture of the broadening mechanisms discussed above and a mixture of both Gaussian and Lorentzian profiles. The convolution of these two types of functions will result in a so-called Voigt profile [18].

During the course of this work Voigt profiles were fitted to the spectra using a Matlab program. In doing so the important parameters, such as peak intensity, area and the widths of the independent Lorentzian and Gaussian components could be extracted for use in the determination of plasma density and temperature. The plasma electron density was determined using equation 4.2 along with the Lorentzian component of the Voigt profile fitted to each profile of the Al<sup>0</sup> doublet. The electron impact parameters ( $w$ ) for the transitions of interest which were obtained from Konjević *et al.* (1990) [19] and are listed in table 4.1.

Figure 4.4 shows the electron density along the length of an aluminium plasma for time delays of 100, 200 and 300 ns after plasma ignition. As mentioned previously, these results are restricted to a time and space domain where there is no self-

$\lambda$ (nm)	T (K)	$n_e$ ( $\text{cm}^{-3}$ )	Broadening ( $\text{nm}/\text{m}^{-3}$ )	Shift ( $\text{nm}/\text{m}^{-3}$ )
396.152	11700	$2.5 \times 10^{17}$	$4.22 \times 10^{-25}$	$2.42 \times 10^{-25}$
394.401	11700	$2.5 \times 10^{17}$	$4.22 \times 10^{-25}$	$2.42 \times 10^{-25}$

Table 4.1: Stark parameters for the  $\text{Al}^0$  doublet  $3s^23p(^2P_{3/2,1/2}) - 3s^24s(^2S_{1/2})$  at 394.4 nm and 396.15 nm respectively [19].

absorption in the spectral lines. The results show that the electron density reaches a maximum value of  $6 \times 10^{17} \text{ cm}^{-3}$  1 mm from the target surface at 100 ns and falls away very slowly with distance. As time progresses the electron density drops, with the higher density region remaining 1 mm from the target.

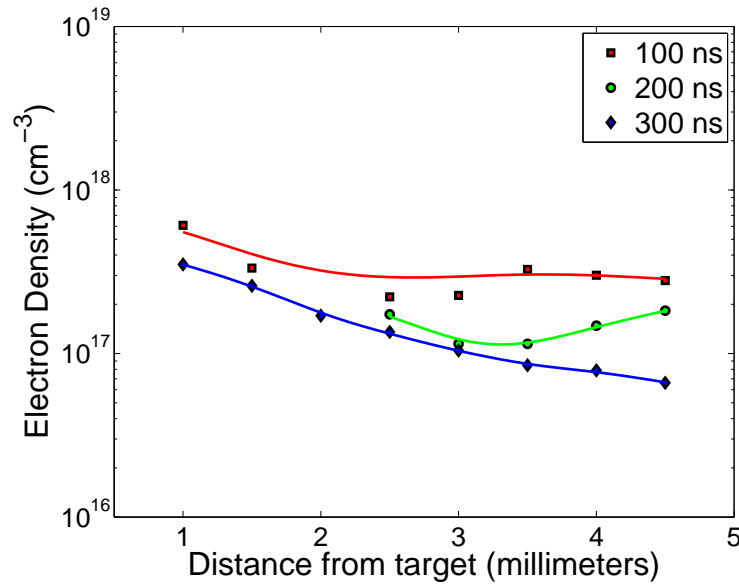


Figure 4.4: Temporally-resolved electron density distributions along the expansion axis of a laser produced aluminium plasma plume obtained using Stark broadened line profile analysis. The transition used in the analysis was the the  $\text{Al}^0$  doublet  $3s^23p(^2P_{3/2,1/2}) - 3s^24s(^2S_{1/2})$  at 394.4 nm and 396.15 nm respectively. Due to significant self-absorption close to the target surface the analysis was limited to regions of the plasma  $\geq 1$  mm from the target surface, however this exclusion zone extended to 2.5 mm for the data at 200 ns (see text for details).

At 100 ns, the effects of self-absorption restricted the measurement to regions of the plume greater than 1 mm from the target surface. Similarly, the plasma plume is assumed to be quite small at this time delay, resulting in a high signal-to-noise ratio for the data beyond 2 mm. At 200 ns the hot dense core of the plasma had

expanded somewhat, and the emission from the region up to 2.5 mm was affected by significant self-absorption, which limited the deployment of the Stark method. At 300 ns, the plasma was quite large but had expanded and cooled sufficiently to become less dense which resulted in a reduction in self-absorption below detectable limits over the full range of sampling positions (1 mm – 4.5 mm). Once again, it is possible to probe fairly close to the target surface without significant line profile distortion by self-absorption.

While this result using the conventional method of analysis gives a good estimate of the electron density in the regions of the plasma which are far away from the target surface [20], they are not sufficient to tackle the regions of the plasma close the target, which are prone to significant self-absorption. An alternative method to determine electron density which is based on a solution of the one-dimensional equation of radiative transfer will be presented in the next section. Synthetic spectra generated with the aid of the model will be compared to the experimental spectra. By controlling and/or fitting three parameters, namely, the electron density, the spatial distribution of the upper state and the spatial extent of the upper state one can extract estimates of the electron density distribution in the core of the plasma.

### **Method II - Simple 1D Self-Absorption Model**

The second part of the analysis concerns the regions of the plasma lying within 2 mm of the target surface, where strong gradients in plasma particle densities (at least at early times in the plasma lifetime) and strong self-absorption as the radiation makes its way from the hot core through the corona to the spectrometer are expected. Shown in figure 4.3 (a – c) on page 99 are the spectral lines from the aluminium doublet transition which exhibited some peculiar distortions. A number of striking features of the doublet, which included significant line broadening, characteristic of a high electron density in the emitting region, were observed; along with suppression of the overall intensity of the spectral lines accompanied by a dip at the transition frequency. One can clearly see that in this region conventional Stark analysis for the determination of electron density will simply not suffice, since the line profile contains a mixture of distortions which are due to Stark-broadening and self-absorption. Discussed in this section is the phenomenon of self-absorption and a method is described which uses it to determine electron density in this region of the plume.

Using soft X-ray imaging and spectroscopy it was shown that the plasma comprised of a hot core containing highly charge ions which extended over a distance of less

than ten microns from the target surface. Looking at longer wavelengths, and concomitantly more lowly charged ions, the emitting core can extend over some hundreds of microns. The studies into time-resolved imaging in the visible spectral region reveal that the core is surrounded by a large region of cooler and fainter emitting plasma. This structure of the plume is similar to the two-zone model described by Hermann *et al.* in 1998 [21]. The core of the plasma localized near to the surface of the target contains atomic and ion species in excited states, the emitters. The second zone is the surrounding plasma which is cooler and contains the less-excited or ground state atoms and ions, the absorbers.

As the light generated by the relaxation of an excited atom or ion in the core travels through the cooler peripheral regions of the plume it will be re-absorbed by the ground state species. Therefore, the spectral line observed from the transition in the core of the plasma will appear to be attenuated. This effect is most clearly seen in figure 4.3(b–c) on page 99. The ratio of the intensity of the two lines should match the ratio of their statistical weights but in the figure the intensity of the two lines is nearly equal. Although both lines are affected by opacity, the spectral line corresponding to the 396.15 nm transition has a greater weighted oscillator strength than the line at 394.401 nm and so it experiences the greater attenuation.

Line emission generated in the region of the core will also tend to suffer from significant spectral broadening due to the Stark effect, the magnitude of which is proportional to the electron density. The pronounced dip seen in figure 4.3 (a and b) on page 99 is caused by an extreme case of self-absorption. This dip is known as self-reversal and is caused when the broadened radiation from the high density core passes through the lower density peripheral region. Because the absorbers in the periphery experience a lower electron density the Stark broadening of the atomic levels is quite small and consequently the absorption profile in this region is narrow. Therefore the center of the observed spectral line will be attenuated to a greater extent than the wings, which results in the characteristic dip in intensity known as self-reversal.

Another property of self-absorption and one which was noticed during the course of this work was the profile of a self-reversed spectral line can sometimes appear asymmetric which can be accounted for by the shift of the transition wavelength due again to the Stark effect. Suffice it to say that the modification of the spectral lines due to self-absorption makes accurate determination of the electron density rather difficult but nonetheless worthwhile in the interests of getting at least good estimates to make the space-time maps of this parameter as complete as possible.

The model used during the course of this thesis was based on the work of by Sakka *et al.* (2002) [10]. The first version of the model was implemented in Matlab™ by Kevin Kavanagh and a detailed description including outputs at the various stages is contained in Kavanagh (Ph.D. thesis (2006) [22]). The procedure to simulate and eventually fit synthetic spectra to the experimental spectra can be broken into five key steps:

1. Choose Initial Variables
2. Include Stark Effect
3. Compute Emission/Absorption Coefficients
4. Perform Convolution
5. Perform Minimization

These steps will be discussed in the following pages, with the results from the model presented at the end of this section.

### **Initial Variables**

The spatial distributions of atoms in the upper  $3s^23p(^2P_{3/2,1/2})$  and lower  $3s^24s(^2S_{1/2})$  energy levels (in the case of aluminium) are an important determining factor of the magnitude of self-absorption these lines are likely to experience. In this model it is assumed that there is a difference between the two where the upper distribution is likely to be concentrated in the central core of the plasma, while the lower level distribution extends out to the plasma periphery. These distributions form one of the salient tenets of the model as they determine to what degree photons produced in the core of the plasma are absorbed by atomic/ionic species residing in lower energy levels in the periphery. In practice the widths of both distributions greatly affect the degree of self-absorption observed. In order to make an estimate of the excited state spatial distribution spectrally filtered images were recorded in the same manner to that described in the previous section. An image of the plasma at a certain time delay during its expansion was divided up into regions of 0.25 mm width which lie parallel to the surface of the target. The pixel counts contained in these regions were full-vertically binned resulting in 1D intensity profiles which represented the extent of the plasma in the plane parallel to the target, i.e., along the axis of observation of the spectrometer. The  $1/e$  width of this profile, which corresponds to the position at which the intensity drops to  $\sim 37\%$  of

the maximum intensity, was extracted for each region. This  $1/e$  width was taken as the width of the spatial distribution of the excited state selected by the spectral filter used with the ICCD. This procedure was repeated for a number of different time delays over the course of the lifetime of the expanding plasma. These values were then assigned to the parameters  $\sigma_2$  and  $\sigma_e$  in the model, which define the width of the upper and electron population distributions. It is implicitly assumed here that excitation is predominantly due to electrons and so these two distributions should have a similar spatial distribution. The original version of the computer model by Kavanagh [22] did not explicitly take into account the fact that the magnitude of each parameter changes over the lifetime of an expanding plasma. In the case of rapidly evolving plasmas as is the case with the plasmas presented here this would result in unrealistic values for the population distributions of the upper and lower states, hence yielding an inaccurate value of the electron density. The computer model was adapted to ensure that the analysis of each file included the automatic addressing of a matrix which contained the characteristic set of parameters defining the plasma in that spatial and temporal frame.

The time-resolved images of the plasma taken in the visible spectral region showed that the luminosity across the width of the plasma could be approximated to a Gaussian shape. Therefore it is reasonable to assume a Gaussian spatial distribution in the population of the upper and lower levels. It is also assumed that the distribution of the free electrons in the plasma can also be approximated by a Gaussian distribution. These distributions are described by,

$$n_e(x) = N_{e0} \exp\left(-\frac{x^2}{\sigma_e^2}\right) \quad (4.5)$$

$$n_1(x) = N_1 \exp\left(-\frac{x^2}{\sigma_1^2}\right) \quad (4.6)$$

$$n_2(x) = N_2 \exp\left(-\frac{x^2}{\sigma_2^2}\right) \quad (4.7)$$

where  $\sigma_e$ ,  $\sigma_1$  and  $\sigma_2$  are the width parameters for the electrons and atoms in the upper and lower levels respectively while  $N_{e0}$ ,  $N_1$  and  $N_2$  are their maximum values. Here  $\sigma_2 = \sigma_e = 1/e$  width of the plasma and it is assumed that  $\sigma_1 = \sigma_{1a} = \sigma_{1b}$  where  $\sigma_{1a}$  and  $\sigma_{1b}$  are the width parameters for each  $^2P^\circ$  spin orbit component.

During the calculation of the synthetic spectra the spatial distributions of both the electrons and the upper state atoms were kept constant for a particular time delay,

and only the lower state distribution was varied in the minimization process. As time progressed the width of these distributions was increased in order to account for the change in shape and size of the plume as the plasma expanded into vacuum.

The parameters ( $N_1$  and  $N_2$ ) are the maximum populations of the upper and lower levels and were estimated by assuming a Boltzmann population distribution at a temperature  $T_0$ , given by the following equation:

$$\frac{N_2}{N_1} = \frac{g_2}{g_1} \exp\left(-\frac{h\nu_0}{k_B T_0}\right) \quad (4.8)$$

where  $k_B$  is the Boltzmann constant and  $T_0$  is the temperature of atoms at the centre of the plasma. In the present work, an initial temperature in the range of  $1 \times 10^5$  K –  $4 \times 10^5$  K corresponding to 0.86 eV – 3.44 eV is used as an initial estimate which is used in the computer model. It was found that temperature had only a small effect on the level of self-absorption in the synthetic spectra, so an average temperature of  $2 \times 10^5$  K was used throughout this work. The lower level has a fine-structure doublet  $^2P_{3/2}$  and  $^2P_{1/2}$  and so the lower population distribution breaks down into two components,

$$n_{1a}(x) = N_{1a} \exp\left(-\frac{x^2}{\sigma_{1a}^2}\right) \quad (4.9)$$

$$n_{1b}(x) = N_{1b} \exp\left(-\frac{x^2}{\sigma_{1b}^2}\right) \quad (4.10)$$

where  $N_{1a}$  and  $N_{1b}$  are the population density at the center of the plasma for the levels  $^2P_{1/2}$  and  $^2P_{3/2}$  respectively. The populations are distributed over the two states according to the following equation:

$$N_{1a} = N_{1b} \frac{g_a}{g_b} \quad (4.11)$$

where  $g_a$  and  $g_b$  are the degeneracies of the  $^2P_{3/2}$  and  $^2P_{1/2}$  spin-orbit components of the Al I doublet of interest. For simplicity in the calculation,  $\sigma_{1a}$  and  $N_{1b}$  have been set as the adjustable parameters.

### Stark Effect

The next step in the procedure is to introduce the Stark effect, which will act to broaden and shift the spectral lines. The Stark effect is dependent on the electron density, and so the spatial distribution of the electron density ( $n_e(x)$ ) calculated in

the previous step is used to determine the position dependent magnitude of both the Stark shift and Stark broadening for each spectral line. The Stark broadening and shift of the spectral lines was determined using the following simplified equations:

$$\begin{aligned}\Delta\lambda_{width}(x) &= wn_e(x) \\ \Delta\lambda_{shift}(x) &= dn_e(x)\end{aligned}\tag{4.12}$$

where  $w$  and  $d$  are the Stark width and the Stark shift parameters respectively. The values of these two parameters were obtained from the literature [23]. Equation 4.12 gives the position dependent magnitude of the Stark width and shift of each spectral line.

Having calculated the magnitude of the Stark width and shift the model then calculates the spectral distribution function. The function is represented by a Lorentzian profile, with a width dependent on the magnitude of the Stark broadening, and a center frequency which depends on the magnitude of the Stark shift. The exact form of the function is given by the following equation:

$$f(x, \nu) = \frac{1}{\pi} \frac{\Delta\nu_{width}/2}{[\Delta\nu_{width}(x)/2]^2 + [\nu - \nu_0 + \Delta\nu_{shift}(x)]^2}\tag{4.13}$$

where  $\nu_0$  is the unperturbed resonant frequency,  $\Delta\nu_{width}(x) = (c/\lambda_0^2)\Delta\lambda_{width}(x)$  and  $\Delta\nu_{shift}(x) = (c/\lambda_0^2)\Delta\lambda_{shift}(x)$  are the variation in the resonant frequency due to the Stark effect. Equation 4.13 gives the spectral distribution as a function of transition frequency  $\nu$  and also of position  $x$ . The spectral distributions for both transitions are calculated independently and subsequently combined to yield the spectral distribution for the Al I doublet of interest here. The final procedure in this step is to normalize the total spectral distribution function over the frequency range of interest such that

$$\int_{-\infty}^{\infty} f(x, \nu) d\nu = 1\tag{4.14}$$

This normalization ensures that the magnitude of the two spectral lines remain in the correct ratio, the total area of the spectrum is equal to 1 and that the subsequent convolution with the normalized instrument function yields a distribution which is itself automatically normalized to unity.

## Computing the Emission/Absorption Coefficients

As light passes through the plasma, the intensity will change depending on the level of emission and absorption along the optical path. The one-dimensional equation for radiative transfer describes the change in intensity of light as it propagates through an optical medium and can be written as [10]

$$\frac{dI(\nu)}{dx} = \epsilon(x, \nu) - \kappa(x, \nu)I(\nu) \quad (4.15)$$

where  $\epsilon(x, \nu)$  and  $\kappa(x, \nu)$  are the spectral emission and absorption coefficients respectively.

Integrating the one dimensional, equation 4.15, along  $x$  the radiant flux density is obtained as [10]

$$I(\nu) = \frac{1}{\phi(\infty, \nu)} \int_{-\infty}^{\infty} \phi(x, \nu) \epsilon(x, \nu) dx \quad (4.16)$$

where

$$\phi(x, \nu) = \exp \left[ \int_{-\infty}^x \kappa(x, \nu) dx \right] \quad (4.17)$$

Equation 4.16 is for the case of far-field where the distance over which the emission and absorption takes place is significantly shorter than the integrating interval (the entire optical path to the detector). The far-field criterion ensures that all optical paths of the collected light are characterized by the same emission and absorption coefficient.

Before the radiant flux density in far field  $I(\nu)$  can be calculated one must determine the values of  $\epsilon(x, \nu)$  and  $\kappa(x, \nu)$ , the spectral emission and absorption coefficients. These are given by [10]

$$\epsilon(x, \nu) = \frac{A_{21} n_2(x) h \nu f(x, \nu)}{4\pi} \quad (4.18)$$

$$\kappa(x, \nu) = \frac{[B_{12} n_1(x) - B_{21} n_2(x)] h \nu f(x, \nu)}{c} \quad (4.19)$$

where  $n_1(x)$  and  $n_2(x)$  are the population density distributions of the lower and upper levels respectively and  $A_{21}$ ,  $B_{21}$  and  $B_{12}$  are the Einstein coefficients which represent spontaneous emission, stimulated emission and (stimulated) absorption respectively.

The Einstein absorption coefficient is related to the spontaneous emission coeffi-

cient  $A_{21}$  and transition frequency  $\omega_{21}$  and can be calculated using [24]

$$B_{12} = \frac{\pi^2 c^3}{\hbar \omega_{21}^3} \frac{g_2}{g_1} A_{21} \quad (4.20)$$

where  $\hbar$  is Planck's constant divided by  $2\pi$ . The absorption coefficient  $B_{12}$  can then be related to the stimulated emission coefficient  $B_{21}$ , by the following expression,

$$g_1 B_{12} = g_2 B_{21} \quad (4.21)$$

where  $g_1$  and  $g_2$  are the lower and upper state degeneracies respectively. Finally the spontaneous emission coefficient  $A_{21}$  can be calculated from the stimulated emission coefficient  $B_{21}$  using [25]

$$A_{21} = \left( \frac{\hbar \omega_{21}^3}{\pi^2 c^3} \right) B_{21} \quad (4.22)$$

Once these parameters are calculated, the radiant flux  $I(\nu)$  can be determined along the length of the plasma, for a defined optical frequency interval.

### Convolution with Instrument Function

The experimentally obtained spectra will be broadened by the Chromex™ 0.5m spectrometer which has yet to be accounted for in the above model of radiative transfer. The radiant flux density  $I(\nu)$  calculated using equation 4.16 was convolved with the instrument function  $g(\nu)$  of the spectrometer. In 2007, Luna *et al.* [16] reported that the instrument function of the Chromex™ 0.5m is spectrometer exhibited a Gaussian profile. They measured the width of the caesium red line at 622 nm for different widths of the entrance slit widths and found that the optimum setting of 60  $\mu\text{m}$  resulted in a spectral profile that was approximated well by a Gaussian instrument function of width 0.16 nm for the 1200 grooves/mm grating. This Gaussian component acts as an additional broadening mechanism, and so in order to make comparisons between the synthetic spectra and the experimental data one must convolve the instrument function with the far-field radiant flux density.

### Minimization

In the final step the model spectrum is fitted to the experimental data with the aid of an iterative minimization procedure implemented in Matlab™. The important parameters used in the computer model and their method of evaluation are listed

Symbol	Definition	Value (unit)	Method of Evaluation
$\sigma_e$	distribution parameter of the electrons	$5 \times 10^4$ (m)	estimated <sup>a</sup>
$\sigma_1$	distribution parameter of $^2P^o$ state	$7.5 \times 10^5$ (m)	adjusted
$\sigma_2$	distribution parameter of $^2S$ state	$5 \times 10^5$ (m)	assumed <sup>b</sup>
$N_{e0}$	electron density parameter <sup>†</sup>	$1 \times 10^{22}$ (m <sup>-3</sup> )	adjusted
$N_{1a}$	population parameter of $^2P_{3/2}^o$ state <sup>†</sup>	$5 \times 10^{21}$ (m <sup>-3</sup> )	calculated <sup>c</sup>
$N_{1b}$	population parameter of $^2P_{1/2}^o$ state <sup>†</sup>	$2.5 \times 10^{21}$ (m <sup>-3</sup> )	adjusted
$N_2$	population parameter of $^2S$ state <sup>†</sup>	$2.5 \times 10^{17}$ (m <sup>-3</sup> )	calculated <sup>d</sup>
$g_a$	degeneracy of $^2P_{3/2}^o$ level	4	Ref. [26]
$g_b$	degeneracy of $^2P_{1/2}^o$ level	2	Ref. [26]
$g_2$	degeneracy of $^2S_{1/2}$ level	2	Ref. [26]
$A_{2a}$	radiative rate for $^2P_{3/2}^o - ^2S_{1/2}$ transition	$9.8 \times 10^7$ (s <sup>-1</sup> )	Ref. [26]
$A_{2b}$	radiative rate for $^2P_{1/2}^o - ^2S_{1/2}$ transition	$4.93 \times 10^7$ (s <sup>-1</sup> )	Ref. [26]

Table 4.2: Parameters and the typical values used in the self-absorption computer model for the simulation of the self-reversed Al<sup>0</sup> doublet  $3s^23p(^2P_{3/2,1/2}) - 3s^24s(^2S_{1/2})$  at 394.4 nm and 396.15 nm respectively. <sup>a</sup>Estimated from visible emission images. <sup>b</sup>Assumed to be equal to  $\sigma_e$ . <sup>c</sup>Calculated in order to keep  $N_{1a}/N_{1b} = g_a/g_b = 2$ . <sup>d</sup>Calculated from  $T_0$  and  $N_{1b}$  using equation 4.8. <sup>†</sup>Corresponding to the population at the center of the plasma.

in table 4.2. Initial estimates of the three adjustable parameters, namely  $\sigma_{1a}$ ,  $N_{1b}$  and  $N_{e0}$  which represent the distribution parameter of the lower ( $^2P_{3/2}^o$ ) state, the population parameter of the  $^2P_{1/2}^o$  lower state and the electron density parameter respectively, were entered into the Matlab code and a first synthetic spectrum was calculated. This initial estimate was usually only a very weak approximation to the actual experimental spectrum and so the parameters were then adjusted by the minimization routine and through an iterative process the difference between the experimental and synthetic spectrum was reduced. In this way, an estimate of the electron density, the various population distributions and their width parameters ( $\sigma_{e,1a,1b,2}$ ) of the emitters and absorbers could be determined.

## Results

The spectral images of the aluminium plasma emission in the 400 nm spectral range were divided up into areas or regions of interest as before and a spectrum was extracted from each one. The resulting space resolved experimental spectra were entered into the computer model for comparison with those computed with the 1D radiative transfer equation. The analysis of aluminum plasmas concentrated on the regions within 2 mm of the target surface, where the effects of self-absorption

on the spectral line profiles were clearly evident (refer to figure 4.3 (a–c) on page 99).

Before running the computer simulation the initial estimates of the input parameters, namely  $\sigma_1$ ,  $\sigma_2$ ,  $N_{1b}$ ,  $N_{e0}$  were made. The emission images recorded in section 4.2.1 were used to aid in the estimation of  $\sigma_1$ ,  $\sigma_2$  and  $\sigma_e$ ; the width parameters for the spatial distributions of the lower and upper states, and the electron density distribution respectively. The  $1/e$  width corresponding to the position at which the luminosity dropped to  $\sim 37\%$  of its maximum value. As stated earlier, this distance was designated to both  $\sigma_2$  and  $\sigma_e$  values, as the excited state and electron distributions are taken to be equal based on the assumption that excitation is predominantly due to electron collisions.

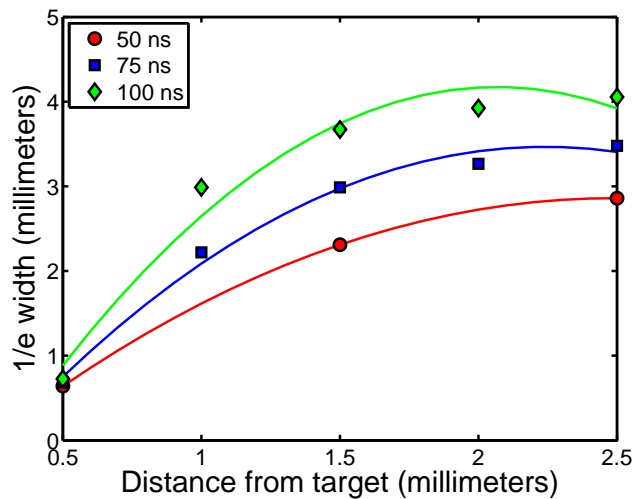


Figure 4.5:  $1/e$  width of laser-produced aluminium plasmas for different distance from the target surface for three time delays. These curves represent the lateral expansion of the plasma and are determined using emission images which are spectrally filtered using a narrow-band ( $\pm 10$  nm) transmission filter centered on a wavelength of 390 nm. The  $1/e$  width of the plasma corresponds to the point at which the intensity drops to 37% of the maximum intensity. This width was assigned to the  $\sigma_2$  parameter in the model. While the  $\sigma_2$  value is held fixed while analyzing the distorted spectrum corresponding to a given point in space and time, it was slightly altered for different space-time resolved spectra using the  $\sigma_2$  values in this figure.

Figure 4.5 contains the  $1/e$  widths of an aluminium plasma for three time delays after plasma initiation, namely 50 ns, 75 ns and 100 ns. It is clear from this figure that the lateral expansion (and hence the  $1/e$  width) of the plasma grows strongly with time and space. In fact, the  $1/e$  width is seen to increase quite quickly over the lifetime of the plasma and this will have a major effect on the optical path length

through the plasma. This change in  $1/e$  width with time was accounted for in the model by varying values of  $\sigma_2$  and  $\sigma_e$  in accordance with the values displayed in this figure. The initial value of  $\sigma_1$ , the lower state distribution width was typically set to 125% of the  $1/e$  width. The initial value of this parameter was not so critical, so long as one ensured that  $\sigma_1 \geq \sigma_2$ , as the minimization procedure tended to yield a sensible fitted value.

It is a reasonable assumption that the region of the plasma in the current study has a higher density than that studied using the conventional method described previously in section 4.2.2.1. Therefore the values of the other initial variables,  $N_{1b}$  and  $N_{e0}$  were expected to be higher than the maximum density recorded previously. Hence the two parameters were typically set to values in the region of  $1 \times 10^{21} \text{ m}^{-3}$  and  $1 \times 10^{25} \text{ m}^{-3}$  respectively.

Once the initial parameters were set, the model solves the equation of radiative transfer. Between each iteration, these initial parameters are adjusted, until the difference between the synthetic and experimental spectra is reduced to some acceptable minimum. Displayed in figure 4.6 are some sample space-resolved spectra taken at time delays of 130 ns (a – c) and 250 ns (d – f), along with the corresponding fits obtained from the opacity model. One can immediately see that the spectrum lines at 394.4 nm and 396.15 nm are highly distorted due to the combined effects of self-absorption, extreme Stark broadening, and the additional continuum emission. The self-absorption in this high density region appears to manifest itself in significant self-reversal of the emission lines. Figure 4.6 (a) clearly shows self-reversal of the spectrum lines emitted from the core of the plasma at approximately 0.25 mm from the target. The general trend in this figure of increasing intensity going from the short wavelength (left-hand-side) to the long wavelength (right-hand-side) may be due to continuum emission caused from recombination. The middle plot in the figure 4.6 (b & e) were obtained at later time delays (130 ns and 250 ns), and a little further out in the plasma (0.75 mm and 0.5 mm). Here one can see that the spectrum lines are becoming quite distinct but the self-reversed profile still remains. In the final plot, one can see that the effects of self-absorption are reduced but the intensity of the spectral lines is still strongly attenuated. The blue line in each of the plots represents a fit of the computer model to the experimental data. The model fits the data very well, albeit sometimes overestimating the level of the self-reversed dip, possibly due to either an overestimate of the value of  $N_{1b}$  (the lower-state population parameter), or of  $\sigma_1$  (the lower-state population distribution).

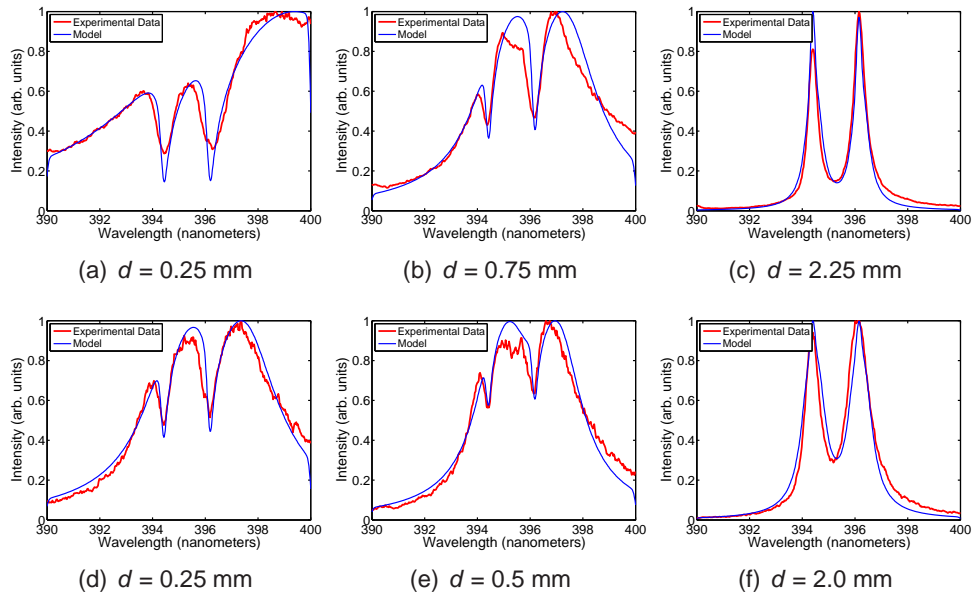


Figure 4.6: Emission spectra from a laser-produced aluminium plasma for different distances ( $d$ ) from the target surface for time delays of 130 ns (a – c) and 250 ns (d – f). The main feature corresponds to the the  $\text{Al}^0$  doublet  $3s^23p(^2P_{3/2,1/2}) - 3s^24s(^2S_{1/2})$  at 394.4 nm and 396.15 nm respectively. Spectra (a) and (d) show strong distortions of the spectral lines due to self-absorption which manifests itself as self-reversed line profiles. Spectra (b) and (e): Further out in the plasma plume (at a distance of 0.75 mm and 0.5 mm respectively) the spectral lines show a small reduction in the effects of self-absorption and remain considerably broadened due to the Stark effect. Spectra (c) and (f): Obtained at a distance of 2.25 and 2.00 mm from the target surface where opacity is still manifested as a strong departure in the intensity ratio from the statistical value of 2:1 for 3/2:1/2 spin orbit components.

The spatial variation in the electron density which gives rise to the model spectra in figure 4.6 (blue traces) is presented in figure 4.7. For this analysis method, the plasma image was divided up into smaller regions of 0.25 mm width, reducing the binning interval, which in turn helps to reveal the finer details.

One may observe that for a time delay of 100 ns the plasma density at 0.25 mm from the target is approximately  $3 \times 10^{19} \text{ cm}^{-3}$  and decreases to  $5 \times 10^{17} \text{ cm}^{-3}$  at 2.25 mm from the target. It is also clear that throughout all time intervals there remains a steep gradient in the electron density in the plasma close to the target surface in the 0 - 2.5 mm range. This is in sharp contrast to the data that was reported in the previous section using direct Stark line profile analysis where for  $x \geq 2$  mm the electron density became quite flat as time progressed. Importantly, the average density at 2.5 mm found using the computer model was in the region of

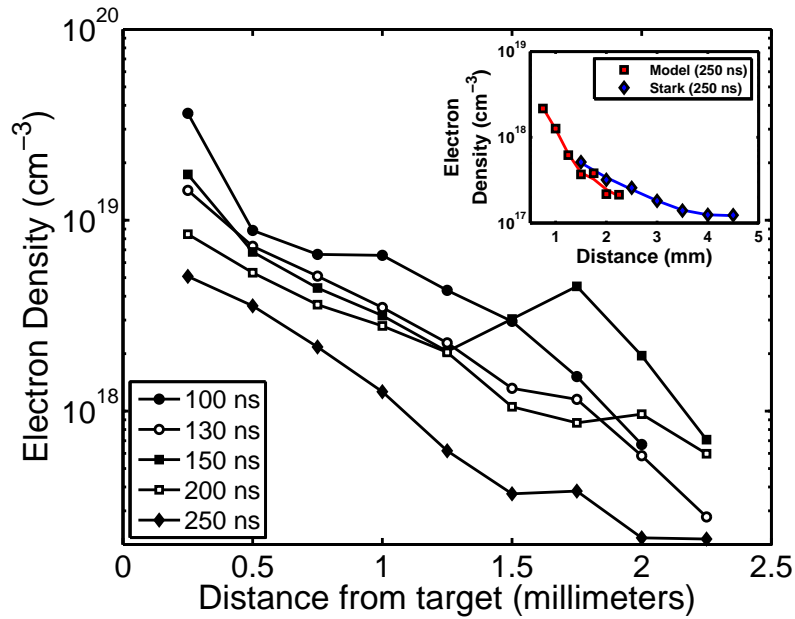


Figure 4.7: Temporally-resolved electron density distributions along the expansion axis of a laser-produced aluminium plasma obtained from the fitting of simulated spectra from the computer model to the experimentally obtained spectra. The model allowed the probing of the dense regions of the plasma which lie close to the target surface. Inset: Comparison between the results obtained from the computer model versus direct Stark analysis (see section 4.2.2.1 for a time delay of 250 ns).

$3 \times 10^{17} \text{ cm}^{-3}$  which actually compares well with the values obtained using direct Stark broadened line profiles in section 4.2.2.1 where the averages values were in the region of  $2 \times 10^{17} \text{ cm}^{-3}$ . This comparison is illustrated in the inset in figure 4.7. The results obtained from the computer model are represented by the red squares (with the red trace representing a simple smoothing fit to the data) while the results from the Stark analysis of the spectral line profiles are represented by the blue diamonds. There appears to be good agreement between the two methods. The general decrease of the plasma electron density with distance from the target are similar for both analysis methods. Furthermore, there is good overlap between the results from the two methods at a distance of approximately 2 mm from the target surface. In this region the density of the plasma has reduced sufficiently permitting the use of Stark analysis of the spectral lines while the opacity model is still applicable. This gave an opportunity to test the validity of both analysis methods in the regions of the plasma where their applicability overlapped. An emission spectrum from this region was presented earlier (figure 4.6 (f) on page 116) and revealed that the spectral lines still exhibited the characteristic signs of opacity, i.e.,

the intensity ratio between the two spectral lines departed from that predicted by theory but not so greatly as to significantly compromise the inherent Stark width excessively.

In summary, the obtained results show that the plasma plume can be divided into two major sections, a high density region close to the target surface where the effects of self-absorption distort the spectral lines, and a region beyond 2 mm from the target where the density was determined directly from the widths of the spectral lines. The results show that the highest density regions exist close to the target surface, and that there is a steep gradient up to 2 mm. Beyond 2 mm, it was found that the density varies slowly, and in fact almost flattens out in the 2 mm – 5 mm interval. Beyond 5 mm, the density drops below the minimum value measurable ( $7.6 \times 10^{15} \text{ cm}^{-3}$ ). The two methods of analysis are quite distinct, but both have resulted in similar values for the electron density in overlapping regions, leading a smooth cross-over at 2 mm.

#### 4.2.2.2 Electron Temperature

For the purposes of determining the electron temperature in the plasma, it was necessary to assume that the plasma was in a state of local thermodynamic equilibrium (LTE). In LTE all particles can be described by a population distribution within a specific ion stage determined by the Boltzmann equation while the total population of plasma species are distributed amongst all possible ion stages in the plasma according to the Saha equation. Experimental measurements of the plasma temperature were performed 25 ns after the laser pulse had terminated, when the plasma had expanded into vacuum, and when continuum emission had reduced. As mentioned in section 1.5.1, in LTE the populations of atomic and ionic states are dominated by electron collisions rather than any competing radiative processes [27], meaning that the electron density must be sufficiently high. The minimum electron density which is necessary to support the assumption of LTE can be determined from the McWhirter [28] criterion, given by

$$N_e \geq 1.6 \times 10^{12} T^{\frac{1}{2}} \Delta E^3 \quad (4.23)$$

where  $T$  is the plasma temperature in Kelvin and  $\Delta E$  (eV) is the energy difference between the states of interest in electron volts. At a temperature of  $2 \times 10^4$  K ( $\sim 1.7$  eV) the lower limit to the electron density is  $5 \times 10^{15} \text{ cm}^{-3}$  for the 394.4 nm transition ( $3p_{1/2} - 4s_{1/2}$ ) in neutral aluminium, meaning that it is reasonable to assume that the plasma is in a state of LTE. In fact for a typical lower density bound

of  $10^{17} \text{ cm}^{-3}$ , the plasma can still be considered to be in LTE for temperatures up to 45 eV ( $5 \times 10^5 \text{ K}$ ).

This assumption allows us to estimate the electron temperature in the plasma from the intensity ratio between two spectral lines. Using the Boltzman equation, the intensity ratio between two spectral lines from the same charge state is given by [13]

$$\frac{I_1}{I_2} \approx \left( \frac{\omega_1 A_1 g_{b1}}{\omega_2 A_2 g_{b2}} \right) \exp \left( \frac{E_{b1} - E_{b2}}{k_b T_0} \right) \quad (4.24)$$

where  $A$  is the oscillator strength of the transition and  $\omega$  is the frequency,  $g_b$  is the degeneracy of the upper level and  $E_b$  is the energy of the upper level. The subscripts 1 and 2 refer to the individual spectral lines.

A more accurate determination of the excitation temperature can be found if one uses the ratio of the intensities between spectral lines from two successive ion stages of the same element. The population distribution across the ion stages can be described by the Saha equation. Therefore the ratio of the intensity from two consecutive ion stages is given by [13]

$$\frac{I_1}{I_2} = \frac{f_1 g_1 \lambda_2^3}{f_2 g_2 \lambda_1^3} (4\pi^{3/2} a_0^3 n_e)^{-1} \left( \frac{k_b T_e}{E_H} \right)^{3/2} \exp \left( \frac{-E_1 + E_2 - E_\infty + \Delta E_\infty}{k_b T_e} \right) \quad (4.25)$$

where  $I$ ,  $\lambda$ ,  $g$  and  $f$  are: total intensity (integrated over the profile), wavelength, statistical weight and absorption oscillator strength, respectively.  $E_1$  and  $E_2$  are the excitation energies of the upper and lower states respectively.  $E_\infty$  and  $\Delta E_\infty$  are the ionization energy of the lower ionic state and the high density correction factor which accounts for the shift in the ionization energy due to strong electric fields. The higher or subsequent ionization stage is denoted by a subscript 1. The additional energy between the stages ( $E_\infty$ ) yields a more accurate determination of the electron temperature than from lines from the same charge state.

The spectral lines under consideration were the  $\text{Al}^+$  line at 466.3 nm ( $3p^2 - 3s4d$ ) and the  $\text{Al}^{2+}$  line at 452.89 nm ( $2p^6 4p(^2P_{3/2}) - 2p^6 4d(^2D_{3/2})$ ). Importantly the lower level involved in both transitions lies well above the ground state energy, meaning that ions in the lower energy state are unlikely to exist in the periphery and so are very unlikely to be affected by plasma opacity. Spectroscopic constants for these lines were obtained from [1]. Spectra were acquired in the same manner as in the previous experiment, whereby each spectral image was divided up into intervals,

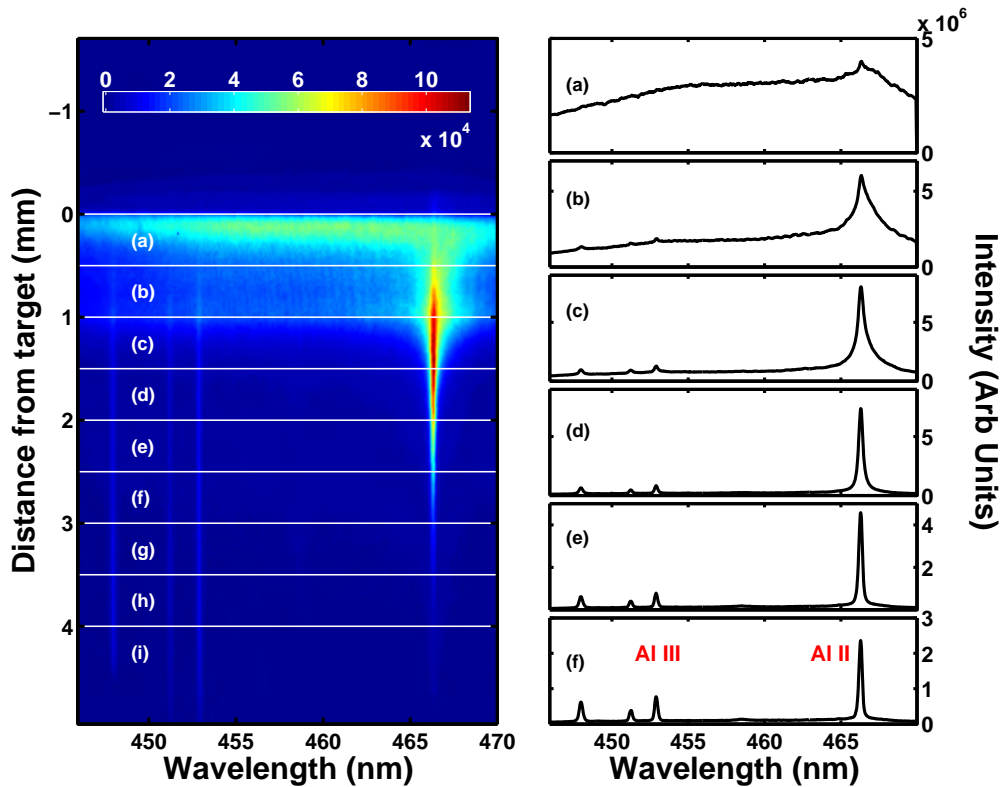


Figure 4.8: Spectral image of an aluminium plasma centered at 460 nm used in the determination of the plasma electron temperature. The spectral image (taken at a time delay of 100 ns) has been divided into nine sections, each 75 pixels in width. These sections, corresponding to approximately 0.5 mm in width, are full vertically binned. The resultant spectra from the first six bins are shown on the right-hand side of the figure. In these spectra, the spectral line on the extreme right corresponds to the  $\text{Al}^+$  emission line at 466.3 nm, while at left-of-center the  $\text{Al}^{2+}$  emission line at 452.89 nm is visible. The intensity ratio of these spectral lines was used in the determination of the plasma electron temperature.

each one 75 pixels in width and full vertically binned (see figure 4.8). Voigt profiles were fitted to the spectral lines and the area under each line (corresponding to the total line intensity or strength) was extracted. Equation 4.25 was minimized with respect to  $T_e$  using a Matlab subroutine. An average electron density of  $4 \times 10^{17} \text{ cm}^{-3}$  was used in the calculation which corresponds to the density of the plasma  $\sim 1 \text{ mm}$  from the target surface at 100 ns (the mid-life of the plasma) obtained in the previous section.

Figure 4.9 shows the electron temperature distributions along the plasma expansion axis as a function of time. At early times (100 – 200 ns) the results show that there is a small decrease in the temperature along the length of the plasma,

between 1 mm and 5 mm from the target. A maximum temperature of  $\sim 2.5$  eV is reached at  $\tau_d = 100$  ns and at  $x = 0.5$  mm. At later times delays (250 ns), one may see that the temperature along the plasma becomes fairly uniform, a possible indication that we are probing the free-expansion phase of the plasma plume.

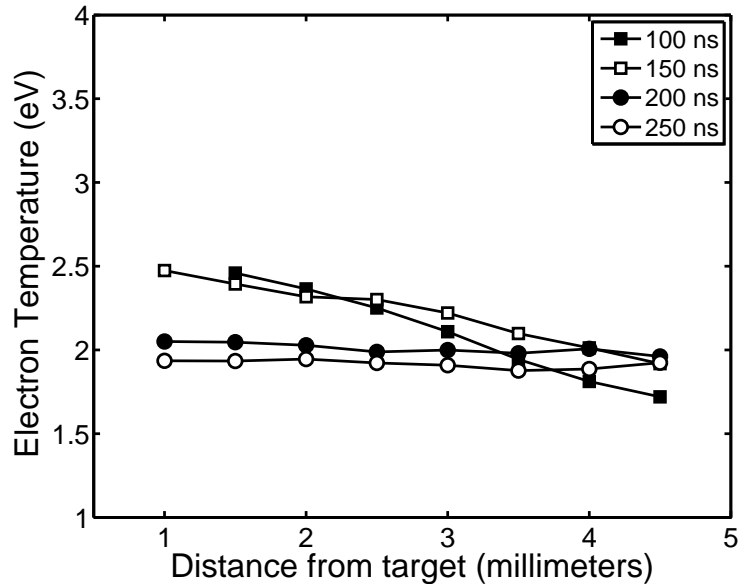


Figure 4.9: Spatially and temporally resolved electron temperature distribution along the expansion axis of a single aluminium plasma produced on a flat metal target.

The spectrum closest to the target surface (labeled (a) in figure 4.8) appears to be dominated by continuum emission. This hampers the accurate determination of the plasma temperature in this region and restricts the application of the procedure to distances greater than 1 mm from the target surface.

### 4.2.3 Summary

In summary, visible emission imaging was used to determine the shape and size of the the bulk material, as well as the neutral and singly ionized species within the plume, as a function of time. By tracking the plume front position it was possible to obtain an approximate value for the plasma expansion velocity. Results showed that an aluminium plasma expanded faster than a calcium one. Images also showed that after the initial phase of the plasma expansion (i.e., at time delays  $> 25$  ns), the bulk emission from the plasma plume appeared to be localized within a region up to 1 mm from the target surface. While the interpretation of luminosity images can be somewhat subjective, (*emission images fail to reveal the*

*non-emitting regions of the plasma, which play a significant role in the evolution of the plasma*), this effect may be explained by the following hypothesis: Material ejected from the deflagration zone accumulates within this region as it catches up on the slower moving material in the corona resulting in a dynamic zone of heating and bright optical emission.

Spectroscopy was used to determine the electron density and temperature along an axis through the plasma plume (usually the expansion axis). Due to significant self-absorption close to the target surface two methods of analysis were used in order to determine the electron density. The first method, based on the analysis of spectral line shapes was used to probe the regions of the plasma  $> 2$  mm where the effect of self-absorption was less of a problem. In this region the spectral lines were not measurably distorted from Voigt-like shapes and therefore the widths could be used (after deconvolution of Gaussian thermal and instrumental components) to obtain the electron densities.

The second method used to determine the electron density in the regions closest to the target surface ( $< 2$  mm) was an analytical model based on the calculation of the one-dimensional equation of radiative transfer. The model produces synthetic spectra by combining a position dependent Stark width and shift with that of a flux which includes both emission and absorption along the optical path. Through an iterative process, where three parameters  $\sigma_1$ ,  $N_{1b}$ ,  $N_{e0}$  representing the population distribution and the population parameter (at the center of the plasma) of the  $3s^23p(^2P_{1/2}^o)$  state, and the maximum electron density are adjusted to obtain a synthetic spectrum that is minimized to best fit the experimental spectrum. The temperature in the plasma was calculated by assuming LTE and relating the ratio of the intensities of lines from successive ion stages via the Saha equation.

The combined results indicate that these plasmas are initially considerably smaller than those generated from table-top nanosecond laser systems. However, after a delay of approximately 100 ns, during the free-expansion stage, these plasmas begin to display similar characteristics (*e.g.*: *electron density and temperature*) to that of 'nanosecond' plasmas.

To conclude, although the picosecond laser system is delivering more than an order of magnitude greater on-target irradiance to produce a hot X-ray emitting plasma, the duration of emission in the soft X-ray region is very short-lived. Rapid initial expansion, taking place over a few nanoseconds results in this very hot plasma cooling and expanding to eventually display characteristics of a plasma not unlike

that generated with nanosecond laser systems. Armed with a solid knowledge of the characteristics of single plasma plumes produced by the EKSPLA™ 312p laser, the next section extends this study to the colliding plasma region.

### 4.3 Colliding Plasma Systems

The concept of colliding plasma systems was introduced in section 1.6 where it was explained that when two counter-propagating laser-produced plasmas collide one of two phenomena may occur. At one extreme the two plasma plumes may simply pass through each other in what is known as *interpenetration*. The heating process in this scenario will be driven by charge exchange collisions between the species. On the other hand, the two colliding plumes may collide and not interpenetrate. The two plumes will decelerate rapidly and material will *stagnate* along the collision front. The kinetic energy of the plumes will be converted into thermal energy, and compression at the interface, caused by the arrival of more and more material, will result in an increase in the local density. Within a short time, typically a few tens of nanoseconds, the material will become highly excited which leads to bright emission.

Colliding plasmas have been extensively studied in the past with photon diagnostics in both the extreme-ultraviolet [3] and visible spectral regions [2]. These studies were based on the use of table-top nanosecond lasers to produce the seed plasmas while the ion-ion mean-free paths of the counter-streaming seed plasmas was typically smaller than the separation between them. When this happens, equation 4.26 [5] yields a high value of the collisionality parameter, which in turn leads to the formation of what is known as a *stagnation layer*.

The collisionality parameter, introduced in Chapter 5, was used to determine which collision scenario to expect, and is repeated here for the reader's convenience [5, 29],

$$\xi = D/\lambda_{ii} \quad (4.26)$$

where  $D$  is the plasma-plasma separation and  $\lambda_{ii}$  is the ion-ion mean free path which is given by [5],

$$\lambda_{ii}(1 \rightarrow 2) = \frac{m_i^2 v_{12}^4}{4\pi e^4 Z^4 n_i \ln \Lambda_{12}} \quad (4.27)$$

where  $n_i$  is the average plasma ion density at the collision plane,  $v_{12}$  is the relative velocity,  $z$  is the average ionization state of the plasma,  $m_i$  is the ion mass,  $e$  is the charge of the electron and  $\ln \Lambda_{12}$  is the so-called Coulomb logarithm for collisions

between the two plumes, in cgs units. The contribution from ion-electron collisions has been ignored because the ion-electron mfp is usually much larger than ion-ion mean free path for medium  $z$  plasmas, especially for laser-produced plasmas in the density range of  $10^{16} - 10^{19} \text{ cm}^{-3}$ , as is the case here. The ion-ion mfp for ionic species within each seed plasma was calculated using equation 1.26 (refer to section 1.6) to be on the order of a fraction of a micron, implying that these plasmas are in the highly collisional regime. From equation 4.27 one may see that the interaction between the two plasmas is highly dependent on  $v$  the relative velocity of the colliding plume pair and to a lesser extent on  $n_e$ , the electron density of the plasma plumes.

For the experiments presented in the forthcoming section, the separation between the two seed plasmas ( $D$ ) remained fixed at 2 mm. By experimenting with different focusing arrangements or using different target configurations it was possible to vary the collisionality parameter which defined the system. Flat targets, where the two seed plasmas collided along their slower lateral expansion plane<sup>2</sup>, resulted in a system where the collisionality parameter was very high, yielding strong stagnation between the plumes. Wedge-shaped targets on the other hand meant that the two seed plasmas were more opposing and subsequently they collided at a higher relative velocity, which yielded a small value for the collisionality parameter and a higher degree of plume interpenetration. The emission images of a single plasma produced by this laser system revealed that the expansion velocity of the bulk plasma material was in the region of  $10^6 \text{ cm/s}$  for aluminium and a few times  $10^5 \text{ cm/s}$  for calcium. The broadband images used to obtain these values, like the one in figure 4.2 on page 96, showed clear signs of a faint but significant halo of emission surrounding the plasma and extending up to about 4 mm from the target surface. Images tracking the neutral ionized species in an aluminium plasma also showed this signature, which may be due to emission from a higher charge states, specifically the  $\text{Al}^+$  transition  $3s3p(^1P^\circ) - 3p^2(^1D)$  at 390 nm is quite bright and it lies within the bandwidth of the filter used to select emission from neutral species.

### Calculation of the Collisionality Parameter

Section 4.2.1 revealed that the expansion velocity of an aluminium was in the low  $10^6 \text{ cm/s}$  range and the value of the electron density in the plasma plume (see section 4.2.2) was a few times  $10^{19} \text{ cm}^{-3}$  near the target surface ( $x = 0.25 \text{ mm}$ ) decreasing to a few times  $10^{17} \text{ cm}^{-3}$  in the periphery of the plasma plume ( $x =$

---

<sup>2</sup>Plane parallel to target surface.

2.25 mm). Substituting these values into equation 4.27 yields an ion-ion mfp of approximately  $30 \mu\text{m}$  (using the density in the periphery and assuming a Coulomb potential value of 10 [30] and an average charge of  $z = 1$ ). The collisionality parameter of the colliding plasma system was calculated using equation 4.26 and yielded a high value of the collisionality parameter,  $\xi = 665$ , which places the experiment firmly into the stagnating regime. This value implies that the interaction of the two plumes would be collision dominated, leading to the formation of a well-defined stagnation layer. Contrast this with the same calculation performed in the soft X-ray studies earlier (refer to section 3.3 of this thesis) where the ion-ion mfp was on the order of the separation between the two seed plasmas ( $\lambda_{ii} \approx D$ ). In that case, the value of the ion-ion mfp was  $165 \mu\text{m}$  and the separation between the seed plasmas was  $150 \mu\text{m}$ . This yielded a low value of the collisionality parameter ( $\xi \approx 1$ ) and no significant stagnation was observed between the two seed plasmas, although it may be occurring later on when the colliding plumes have cooled significantly and so the collisionality has increased - a motivation for moving to the optical range of the electromagnetic spectrum.

While these calculations serve to highlight the two extremes of the colliding plasma systems, namely the expectation of interpenetration between the two high temperature plasmas ( $T_e \geq 100 \text{ eV}$ ) in the soft X-ray studies, and stagnation between the two low temperature plasmas ( $T_e \leq 5 \text{ eV}$ ) studied in the visible spectral region, the calculations are only a guide. In reality, the expansion velocity of the single plasma plume used in the calculation is not comparable to the expansion velocity of the seed plasma. One will see in the forthcoming section that the two seed plasmas are produced in close proximity and as such the dynamics of their expansion are inextricably linked. The expansion of each plasma will be perturbed by its neighbour through a combination of forces, from electrostatic, to pressure. The mutual interaction results in a distortion/perturbation of the evolution of the seed plasmas. In effect, the expansion velocity will be different from that in the single plasma case, and so these calculations have to be adjusted accordingly.

Of interest here is the determination of the electron density and temperature in this interaction zone using visible emission spectroscopy, techniques which have already been discussed in the previous section on single plasmas. Using the picosecond laser system, our study of colliding plasmas lies in a region of irradiance which is somewhat neglected in the literature. Extensive studies have been done using either ultra-intense lasers operated at power densities in excess of  $10^{14} \text{ W/cm}^2$  [4, 5] or relatively low intensity nanosecond lasers [2, 3]. In all of these stud-

ies a well-defined stagnation layer was formed in the region of the plasma-plasma interface. A small degree of interpenetration was reported in the experiments using ultra-intense lasers, where the plume expansion velocities were typically very high (which results in a large value of the ion-ion mean free path). In contrast to the preliminary studies of colliding plasmas in the soft X-ray spectral region, where there was no clear sign of stagnating plasmas, in the visible spectral region one would expect to see significant emission from the collision front between the two plumes. The approximate calculations shown above reveal that whether experimenting with flat targets or wedge-shaped targets in the visible spectral region, the ion-ion mfp will always remain smaller than the value of the inter-plasma separation ( $D$ ). Therefore, strong stagnation is expected to occur, with varying degrees of interpenetration between the plumes, depending on the target configuration.

In this section, the results from time-resolved imaging and spectroscopy on colliding plasmas generated on flat metal targets are presented. The emission images were used to determine the expansion velocity, or more correctly, the rate of growth of the stagnation layer. Spectroscopy of the interaction region, defined as the mid-plane region between the two plasmas, revealed the electron density and temperature of the stagnation layer. Tracking these parameters over time yielded information about the formation of the stagnation layer which was compared to the other studies in the literature. The growth rates of the seed plasmas and the stagnation layer were extracted from the emission images. The images were also used as a qualitative measure of the dynamics of the collision process between the two counter-propagating streams. The overall shape of the stagnation layer was examined, and it was concluded that its length depended on the relative collision velocity (normal to the target), while its width depended on the degree of interpenetration between the two seed plasmas.

Presented in the second part of this main section, are the results from studies on colliding plasma systems using wedge-shaped targets, where the two seed plasmas were produced on targets positioned at  $90^\circ$  with respect to each other. In this almost vertically (or horizontally) opposing configuration, the two plumes expand and interact at a greater relative velocity. Therefore, according to equation 4.26, one would expect to see a higher degree of plume interpenetration before the onset of any significant stagnation, a scenario sometimes known as soft-stagnation [29].

### 4.3.1 Colliding Plasmas on Flat Targets

This section begins with the presentation of results from time-resolved imaging and spectroscopy of two colliding plasmas which were generated on flat targets. The two focal spots and consequently the two plasmas were separated by approximately 2 mm. As the two plasmas expanded they collided along their lateral expansion plane. The expansion velocity of the plume along this direction can be an order of magnitude slower than that along the axis normal to the target. Therefore, in this sense, one would expect the level of plume interpenetration to be fairly small.

#### 4.3.1.1 Imaging of Colliding Point Plasmas

##### Aluminium

Spectrally-filtered and time-resolved images of the colliding plasma system are presented in figure 4.10. The two aluminium plasmas were produced on a flat target with an approximate separation of  $\sim 2$  mm. *The referral to point plasmas is done so as to differentiate between the two optical setups used in this work (point-focus and line-focus of the laser beam). The transient nature of laser-plasmas means that point-like plasmas rarely exist beyond 100 ns.* Presented in the first column are images of the bulk plasma emission obtained using a broadband filter covering the 300 nm to 950 nm spectral range. The luminosity of each image represents the spatial distribution of the bulk of plasma material and was used to determine the overall shape and size of the plume. In the second column, images taken using a narrow band transmission filter centred at 390 nm which will selectively track emission from the Al<sup>0</sup> spectral lines at 394.4 nm and 396.15 nm originating from transitions between the  $3s^23p(^2P_{3/2,1/2}) - 3s^24s(^2S_{1/2})$  levels in neutral aluminium are presented. The filter has a transmission efficiency of 18.5% and 7.5% at 394.4 nm and 396.15 nm respectively. The third column contains images which have been spectrally filtered over a narrow window (10 nm FWHM) centered at 470 nm. These images reveal the spatial distribution of multiply ionized species with the largest contribution to the emission within the spectral window of the filter coming from the Al<sup>+</sup> spectral line at 466.3 nm originating from the  $3p^2(^1D) - 3s4p(^1P^\circ)$  transition in singly ionized aluminium. This filter has a transmission efficiency of 40% at this wavelength. The intensity scale on the plots has been normalized according to the transmission efficiencies of the respective filters, but the color scales vary between the rows (different time delays) in order to reveal the faint emission at longer

time delays.

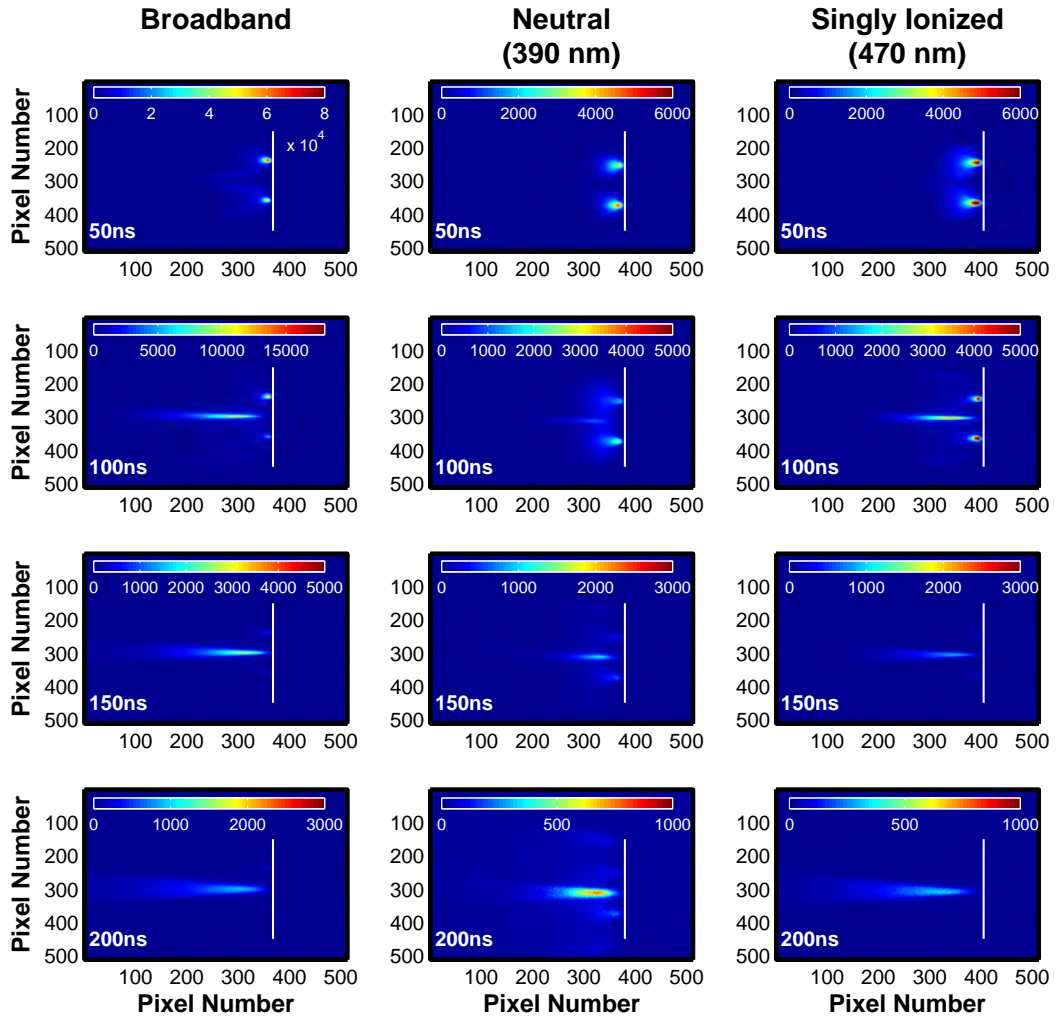


Figure 4.10: Spectrally filtered time-resolved image array of two colliding aluminum plasmas produced on a flat metal target by a point focus of the laser beam. First column: Images taken using the broadband transmission filter showing white-light or the bulk plasma emission. Second column: Images obtained using a transmission filter centered at 390 nm which corresponds to emission from neutral aluminium species. This filter has a transmission of 18.5% and 7.5% at 394.4 nm and 396.15 nm respectively. Third column: Images taken using a filter with a center wavelength of 470 nm which transmits light from singly ionized within the plasma plume. The  $\text{Al}^+$  spectral line at 466.3 nm corresponding to the  $3p^2(^1D) - 3s4p(^1P^\circ)$  transition dominates the emission in this spectral window. This filter has a transmission of 40% at this wavelength.

In these images the laser enters from left to right, producing a pair of point-like plasmas with an emitting size on the order of 0.5 mm FWHM after 100 ns or so.

It is clear from figure 4.10 that the  $\text{Al}^+$  images are generally brighter than the  $\text{Al}^0$  images, even after the transmission efficiencies of the respective filters has been accounted for. This is not surprising when one considers that the plasmas are hot resulting in the populations of the higher charge states being greater than that of the neutral species. The overall size of the seed plasmas is quite small, never exceeding a millimeter or so in length along the largest dimension normal to the target in optical imaging.

In the broadband images, the bright core of the seed plasmas is  $\sim 100 \mu\text{m}$  in diameter and the bulk of the emission from the seed plasmas is localized within 1 mm of the target surface. One may notice the existence of two lobes emanating from the plasma core in figure 4.10. From 50 ns onwards one can see that these lobes begin to merge at the collision plane. The collision of these lobes initiates the formation of a very narrow but long stagnation layer. Material from the lobes appears to have substantial forward momentum (more so than the seed plasmas) and appears to collide at angles from about  $60^\circ$  to  $20^\circ$ , resulting in a jet-like stagnation layer having a high aspect ratio<sup>3</sup>. As time progresses the bulk of the expanding material from the seed plasmas reaches this interaction zone which fuels an increase in emission from this region.

At 150 ns one can see that emission from the seed plasmas is nearly extinct and that there is now a long, narrow and brightly emitting stagnation layer. The length of the stagnation layer at this time is approximately  $\sim 2.5 \text{ mm}$  which was determined by calculating the FWHM of an intensity lineout through the center of the stagnation layer in the direction normal to the target surface (i.e., the plasma expansion axis). The length of the stagnation layer gives a qualitative measure of the dynamics involved in the collision between the two counter-propagating streams. When the colliding material has a large velocity in the forward direction, normal to the target, a long stagnation layer is formed; while a small velocity results in a shorter stagnation layer. This effect becomes clear when the images of colliding plasmas produced on flat targets are compared with those from orthogonally colliding plasmas presented later (section 4.3.2) generated on wedge-shaped targets, where the slower forward velocity component yields a fairly short stagnation layer.

The stagnation layer evolves through the collision of material from the seed plasmas. As more and more material rushes into the interaction region, which is defined as the area around the mid-point axis between the two seed plasmas, the stagnation

---

<sup>3</sup>Aspect ratio here is taken to be the ratio between the length and width of the stagnation layer.

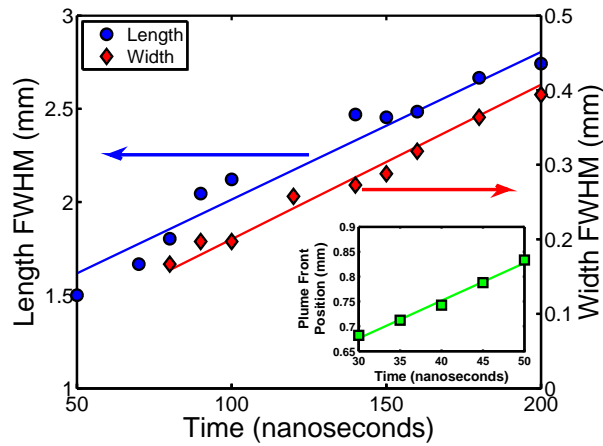


Figure 4.11: Full-width half-maximum along the length (blue circles) and width (red diamonds) of a stagnation layer generated by the collision of two aluminium seed plasmas as a function of time delay. A simple linear fit to the experimental data (solid traces), yielded an approximate value for the growth rates of the stagnation layer in the two orthogonal directions ( $8 \times 10^5$  cm/s and  $2 \times 10^5$  cm/s, respectively). The stagnation layer has a high aspect ratio, whereby the length is long, reaching a maximum value of 3 mm, in comparison to the width which remains quite narrow and never exceeds 0.5 mm. The time interval of the x-axis was limited to the period when the stagnation layer was initiated (50 ns), to when it ceased to emit strongly (250 ns). Inset: FWHM of an aluminium seed plasma before the onset of a collision. The linear fit to the data (green trace) yields an expansion velocity of  $7.5 \times 10^5$  cm/s which was used in the calculations of the collisionality parameter (see text for details).

tion layer grows in size through the accumulation of material around the midplane between the two seed plasmas (the area defining the interaction region). The formation of the stagnation layer can be charted by extracting the FWHM of an intensity profile along the length of the layer normal to the target surface. Presented in figure 4.11 are the FWHM dimensions of the stagnation layer normal to the target surface and parallel to the target surface at a distance of 1.5 mm from the target surface. Also shown in the figure is the lateral expansion velocity of the plasma plume which is used in the calculation of the ion-ion mfp. The rate of growth (as the stagnation layer expands in both directions, both towards and away from the target) of the stagnation layer is  $2 \times 10^5$  cm/s in the lateral direction and  $8 \times 10^5$  along its length, while the layer reaches a maximum length of 3 mm and width of 0.5 mm at around 200 ns. Figure 4.11 shows that the stagnation layer is quite narrow, never exceeding 0.5 mm thick which implies that the degree of interpenetration between the two plumes is quite small. Calculations using equation 4.27 reveal that the ion-ion mfp was small in comparison to the distance between the two aluminium seed

plasmas,  $\lambda_{ii} \leq D$ , which yielded a high value for the collisionality parameter. The inset in figure 4.11 shows the FWHM (*in the plane parallel to the target surface, i.e., the lateral expansion plane*) of the top seed plasma, obtained before the onset of the collision. A simple linear fit to the data revealed an expansion velocity of  $7.5 \times 10^5$  cm/s, which is slower than that of the single plasma reported in section 4.2.1. The ion-ion mfp was calculated to be approximately  $10 \mu\text{m}$  (for  $n_e = 10^{17} \text{ cm}^{-3}$ ,  $v = 7.5 \times 10^5$  cm/s, and  $T_e = 2.5$  eV) which yields a very high value for the collisionality parameter ( $\xi = 2100$ ), indicating a low degree of plume interpenetration is to be expected. Contrast this with the results obtained in the soft X-ray spectral region, where a ion-ion mfp ( $\lambda_{ii} = 165 \mu\text{m}$ , for copper ions) yielded a small value of the collisionality parameter. In that experiment the separation between the two seed plasmas was on the order of the ion-ion mfp length ( $\lambda_{ii} \approx D$ ), and so a higher degree of plume interpenetration was observed. The tightly defined stagnation layer observed in the emission images in figure 4.10 indicate that there was little or no plume interpenetration occurring along the mid-plane between the two plasma plumes 100 ns after the laser pulse.

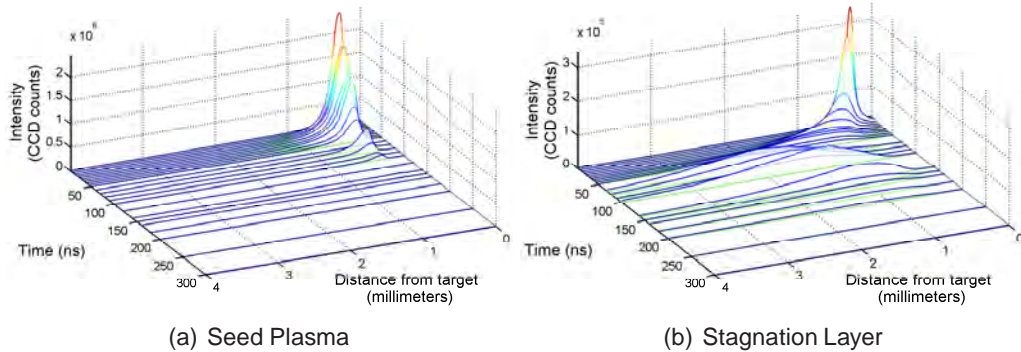


Figure 4.12: Spatial and temporal luminosity distribution along the length of an aluminium seed plasma (a) and a stagnation layer (b). The emission images reveal that the seed plasma remains localized to a region within 1 mm of the target surface, while the stagnation layer extends up to 4 mm from the surface.

Figure 4.12 shows the spatial and temporal distribution of the emission along an axis normal to the target surface for both the stagnation region and one of the seed plasmas. These plots are useful at illustrating the overall difference in size between the seed plasma and the stagnation layer. In this case, there is a bright region close to the target surface at early times, due to the seed plasmas expanding laterally along the surface of the target. Therefore the two plasmas collide first at

the midway point between them, at approximately 1 mm from the surface. As time progresses, the collisions near the surface recede and emission from the colliding material further out in the interaction region begins to grow. A long stagnation layer is formed about 1 mm from the target surface which extends up to 4 mm from the target surface as material from the seed plasmas meets at the midplane after the longer flight times associated with these longer distances of 1 mm to 4 mm. The seed plasmas on the other hand are quite small and the peak of the emission distribution appears to be localized to within 1 mm of the target surface in this figure. The observation lends credence to the proposal that the main expansion phase of the plume occurs within the first few tens of nanoseconds. In a subsequent phase, it appears that material from the hot core collides with cooler, more slowly moving material in front of it causing it to heat up and emit radiation. Hence the mid region of the image appears stationary but is in fact quite a dynamic collisional part of the plasmas plume. Cooler material at the plasma front is ejected into the midplane where it collides and aggregates to form the stagnation layer. In figure 4.12 the peak of the emission appears near stationary in time from 5 ns to 200 ns. The peak decays in the same position as the plume slowly expands into vacuum.

To summarize, point-like seed plasmas were produced 2 mm apart on a flat metal target. The seed plasmas appeared quite stationary in the emission images, which seems to indicate that either (i) the majority of the hot material ablated from the target was confined to an area close to the target surface by a region of cooler material further away from the target, or (ii) the emission is fed by the recombination of highly-charged ions which were remained in the laser interaction region close to the target surface. The collision between the two seed plasmas produced a long and narrow stagnation layer and the overall shape of the the layer was used as a quantitative measure of the dynamics occurring between the plasma plumes during the collision process. It was proposed that the length of the stagnation layer is a good indicator of the magnitude of the forward expansion velocity of the colliding material. A long stagnation layer (in the case of aluminium presented in this section) indicated that the velocity of the material normal to the target surface was fairly high (at least when compared to that of colliding calcium plasmas). Moreover, the width of the stagnation layer provided a measure of the degree of interpenetration occurring between the two counter-streaming seed plasmas, and thus was a qualitative measure of the collisionality of the system. In the case of the colliding aluminium plasmas which were presented in this section, the ion-ion mean free path was typically a few tens of microns, and orders of magnitude smaller than the separation distance between the two seed plasmas. As a result, the collision-

ality parameter which is the ratio of the seed plasma separation and the ion-ion mfp remained quite high, meaning that little or no interpenetration between the two plasma plumes would occur. This was supported by the time-resolved emission images, where a very narrow (width  $< 0.5$  mm) stagnation layer was observed, indicating that the level of interpenetration was quite low and that the counter-streaming material came to an abrupt stop at the collision interface. In the next subsection, the case of aluminium will be contrasted with calcium, and these conclusions will re-examined to see if they remain supported by experimental observation.

## Calcium

The discussion moves on to the collision of two calcium plasmas using the same optical and target experimental configuration and where the seed plasmas are again separated by  $\sim 2$  mm. Calcium was chosen as its optical spectrum is well known and Stark parameters are available for a number of its emission lines. In addition, its atomic weight of 40 means that one can compare its expansion and collision plane dynamics to the lighter aluminium. In the experiments on single plasmas, it was revealed that calcium plasma plumes expanded (normal to the target) more slowly than their lighter aluminium counterparts. Therefore, it is interesting to examine whether this small difference in velocity translates to a large difference in the collision processes involved in colliding plasma systems using calcium.

Figure 4.13 shows spectrally-filtered time-resolved images of the colliding plasma system for bulk, neutral and singly-ionized plasma species. Again the plasmas are relatively small, but the calcium plasmas appear to be wider than that of aluminium plasmas, which may be due to a greater contribution of radiation transport to the heating of the plasma within the laser interaction region. After approximately 200 ns the emission from the seed plasmas becomes quite faint and a bright stagnation layer  $\sim 2$  mm in length and  $\sim 300\mu\text{m}$  in width has been formed. Above 200 ns the intensity of the emission from the stagnation layer begins to fade, as the heating processes in this region recede. As the layer grows with time, cooling in the absence of additional material being supplied to the interaction region from the now extinct seed plasmas means that the layer begins to cool and the emission intensity in this midplane region declines.

The size and shape of the stagnation layer obtained from emission images can be used as a quantitative measure of the type of collision (*either interpenetration or stagnation*) taking place. The width of the stagnation is related to the degree of interpenetration between the two seed plasmas at the collision front. If there

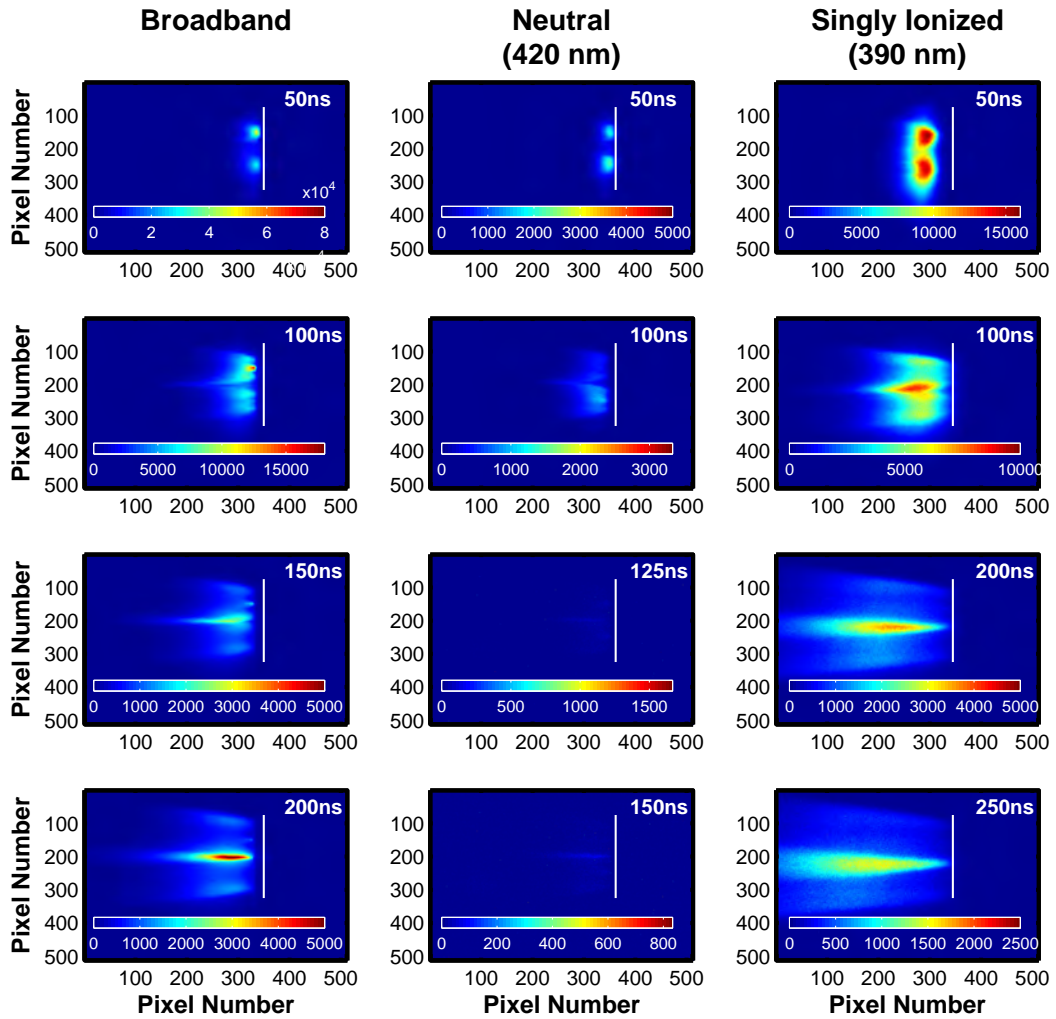


Figure 4.13: Time-resolved filtered emission images of colliding plasmas produced on flat calcium targets in the visible spectral region. The plasmas were separated by approximately 2 mm, and the laser beam entered the image from the left. Left-hand column: Images obtained using the broadband transmission filter corresponding to white-light or the bulk plasma emission. Middle column: Images taken with a transmission filter centered on 420 nm where the emission is dominated the  $\text{Al}^0$  transition ( $4s^2(^1S) - 4s4p(^1P^\circ)$ ) at 422.67 nm. Right-hand column: Images taken using a filter with a center wavelength of 390 nm which transmits light from singly ionized species, specifically the  $\text{Ca}^+$  doublet at 393.366 nm and 396.847 nm originating from the  $3p^64s_{1/2} - 3p^64p_{3/2,1/2}$  transitions. The luminosity images have been corrected for the respective efficiencies of the respective transmission filters. The luminosity scale in the middle column is not at the same scale as the right-hand column.

is a low degree of interpenetration occurring (i.e., hard stagnation, as seen in the case of aluminium), then the stagnation layer is likely to appear to be narrow, as

material accumulates along a plane which is narrow. On the other hand, if the stagnation layer is relatively wide, then the evidence suggests that material from the two plumes interpenetrated to a measurable degree. Hence one can conclude that the width of the stagnation layer provides an insight into the degree of stagnation or interpenetration for colliding plasma plumes.

The calcium results show that at a time delay of approximately 150 ns the stagnation layer is certainly wider (FWHM) than that observed in the case of two colliding aluminium plasmas,  $\sim 750 \mu\text{m}$  for calcium versus  $300 \mu\text{m}$  for aluminium. This appears to indicate that there is a greater degree of plume interpenetration occurring for colliding Ca plasmas. Furthermore, the length of the stagnation layer shown in figure 4.13 is a few millimeters shorter than that of aluminium, 1.5 mm versus 4 mm for aluminium. A long stagnation layer is consistent with the collision of two plumes which have a fast expansion velocity, i.e., fast moving ions travel longer distances more quickly and collide at higher relative velocity resulting in long bright stagnation layers. The short overall length of the calcium stagnation layer is a consequence of the two plasmas colliding at a lower relative velocity than in the case of aluminium. Noted earlier was the fact that the expansion velocity of a single calcium plasma was significantly smaller than that of the lighter-species aluminium plasma. Finally, the stagnation layer is formed close to the target surface, as there is a high degree of lateral expansion from the seed plasmas along the target surface, so the plasmas collide near the surface before doing so further away in the space ahead of the target surface.

In figure 4.13 it is clear that the middle column that contains images of the emission from the neutral species in the plasma is substantially fainter than that of the third column, containing emission from singly ionized species. This trend was also observed in the case of aluminium plasmas for both single or colliding plasma systems. The trend can be attributed to the fact that each seed plasma is hot and therefore the ionization balance is weighted predominantly in favour of higher charge states. Therefore it is reasonable to expect a very low density of neutral species in both the seed plasmas and the energetic stagnation layer (at least at early times in both cases before significant cooling has set in).

The growth of the stagnation layer was tracked by plotting the FWHM of an intensity lineout through the center of the layer normal to the target surface, represented in figure 4.14 (a) by the red diamonds. From the slope of a simple linear fit to the experimental data one can determine the growth rate of the layer, calculated to be  $\sim 7.5 \times 10^5 \text{ cm/s}$ . The value is in fact comparable to that for aluminium ( $7 \times 10^5$

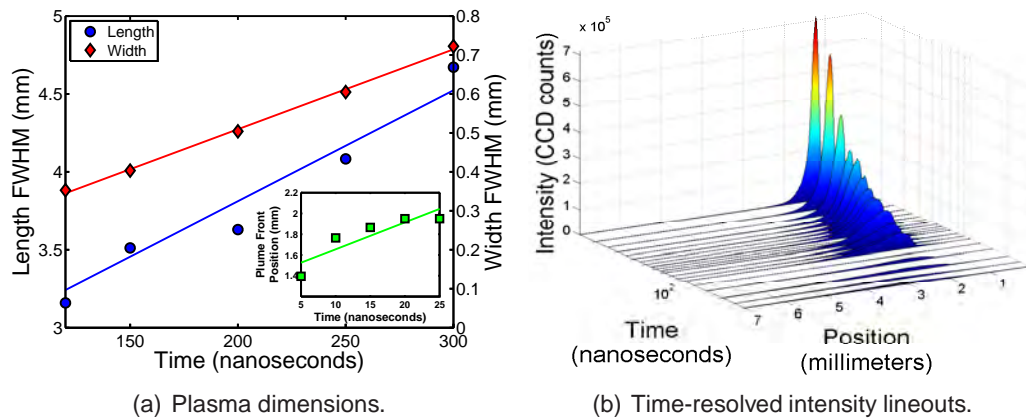


Figure 4.14: Full-width half-maximum along the length (blue circles) and width (red diamonds) of a stagnation layer generated by the collision of two calcium seed plasmas (a) and intensity profile along the length of the stagnation layer normal to the target surface (b) as a function of time delay. A simple linear model was fitted to the experimental data (solid traces), the slopes of which yielded an approximate value for the growth rates of the stagnation layer in the two orthogonal directions ( $7 \times 10^5$  cm/s and  $2 \times 10^5$  cm/s, respectively). The stagnation layer has a high aspect ratio, whereby it is long, reaching a maximum value of 3 mm, in comparison to the width which remains quite narrow and never exceeds 0.5 mm. The time interval on the x-axis was limited to the period from when the stagnation layer formed (50 ns) to when it ceased to emit strongly (250 ns). Inset: FWHM of an aluminium seed plasma before the onset of a collision. The linear fit to the data (green trace) yields an expansion velocity of  $7.5 \times 10^5$  cm/s which was used in the calculations of the collisionality parameter (see text for details). The waterfall plot in (b) shows bright emission at the target surface which is attributed to the seed plasmas.

cm/s) and the lengths of the two stagnation layers are comparable also.

As mentioned previously, the width of the stagnation layer can be used as a measure of the degree of interpenetration occurring between the two plasma plumes. Previous results have already shown that the collision of two aluminium plasmas results in a well-defined narrow stagnation layer. The emission images of two colliding calcium plasmas presented in figure 4.13 show that the stagnation layer is quite large. The width of the layer as a function of time delay was obtained by taking a lineout across the image parallel to the target surface at a distance of approximately 1.5 mm from the target (corresponding to the center position of the stagnation layer). The data shows that the FWHM of the calcium stagnation layer is  $\sim 400 \mu\text{m}$  at a time delay of 150 ns and reaches a width of over  $700 \mu\text{m}$  at 300 ns. Contrast this result with the result from an aluminium stagnation layer which had a width of  $300 \mu\text{m}$  at a time delay of 150 ns. The results imply that there is a greater degree of plume interpenetration in the case of calcium caused by the increase in

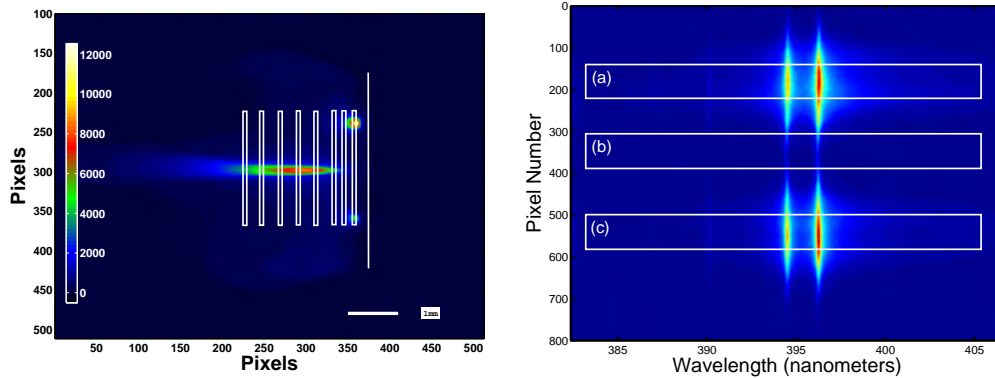
the value of the ion-ion mfp. Using equations 4.26 and 4.27, the ion-ion mfp for this calcium plasma is approximately  $20 \mu\text{m}$ . While this value is only slightly larger than that calculated for aluminium ( $10 \mu\text{m}$ ) it seems to be sufficient enough to provide an small increase in the width of the stagnation layer seen in the experimental results.

Figure 4.14 (b) shows the emission profile along the length of the stagnation layer (in the direction normal to the target surface). The waterfall plot shows that there is bright emission at the target surface between the two seed plasmas which can be attributed to the lateral expansion of the seed plasmas. As time progresses the bulk of the material collides at approximately 1 mm from the target surface emitting brightly. Over time it is clear from the figure that the stagnation layer moves away from the target surface, as the general motion of the material is in the forward direction.

#### 4.3.1.2 Spectroscopy of Colliding Point Plasmas

Visible emission spectroscopy using the Chromex™ spectrometer was applied to measure the electron density and temperature of the stagnation layer. The setup for this experiment was the same as for the single plasma case with the exception that the dove-prism was removed. As mentioned in section 2.5.4, the dove prism acts to rotate the image of the plasma by  $90^\circ$ , thereby forming an image of the expanding plasma vertically along the entrance slit of the spectrometer. By removing it, the image of the colliding plasma system was orientated at right angles to the slit direction. This enabled the simultaneous capture of emission from the two seed plasmas and the midplane-interaction region between them. The spectrometer was then translated along the image of the entire colliding plasma system and a full spatial-temporal-spectral map of the system could be compiled.

The arrangement of the entrance slit of the spectrometer and the plasma can be explained with the aid of figure 4.15. Displayed in figure 4.15 (a) is an image of the entire colliding plasma system where emission from the two seed plasmas and the midplane region where the stagnation layer is expected to form can be viewed. The position of the target is indicated by the solid white line, while the various positions where the entrance slit of the spectrometer sampled the colliding plasma system are highlighted by the white boxes. When a spectral image, like the one shown in figure 4.15 (b), was acquired by the ICCD camera, the image would contain emission from the two seed plasmas and from the interaction region in the centre. Processing of the spectral-images was done by firstly dividing the image into three sections, each 50 pixels wide, containing the emission from the two seed plasmas



(a) Relative position of entrance slit of the Chromex™ spectrometer.

(b) Regions of interest.

Figure 4.15: Broadband image of the colliding plasma system with the approximate positions of the spectrometer entrance slit (a) and spectral image of a colliding plasma system taken at the position of one of the boxes highlighted in (a) centered on a wavelength of 395 nm (b). During the experiment the whole spectrometer is moved thereby sampling different regions of the colliding plasma system, indicated by the boxes. Right: The spectral image shows emission from the  $\text{Al}^0$  doublet at 394.4 nm and 396.15 nm. The three regions of interest, namely the emission from the two seed plasmas and the emission from the interaction region between them are highlighted by the boxes labeled (a), (c) and (b) respectively. Spectra were extracted by fully vertically binning the CCD counts in these three regions of interest.

(box a and c) and the interaction region between them (box c). Next, the luminosity counts in each of these regions of interest were vertically integrated, resulting in three spectra. Finally, these spectra were then analyzed using the procedures described in section 4.2.2 in order to extract the local electron density and temperature in the region of interest. By repeating these steps for a different time-delays, and for different positions of the spectrometer (highlighted by the white boxes in figure 4.15 (a)) a temporal and spatial distribution of the electron density and temperature across the entire colliding plasma system could be created.

## Aluminium

The spatially-resolved electron density and temperature distributions along the length of a stagnation layer created by the collision of two aluminium plasmas is presented in this section. At the time delays reported here, no self-absorption affected the spectral lines in question and so the Stark analysis method described on page 101 was used. As was the case in the analysis of the single plasmas, Voigt profiles were fitted to the two spectral lines under consideration, which correspond to the

$\text{Al}^0$  doublet  $3s^23p(^2P_{3/2,1/2}) - 3s^24s(^2S_{1/2})$  at 394.4 nm and 396.15 nm. The width of the Lorentzian components of the Voigt functions were used in equation 4.2 on page 102 to determine the local electron density. This method was then repeated as the spectrometer was scanned across the entire region of the colliding plasma system.

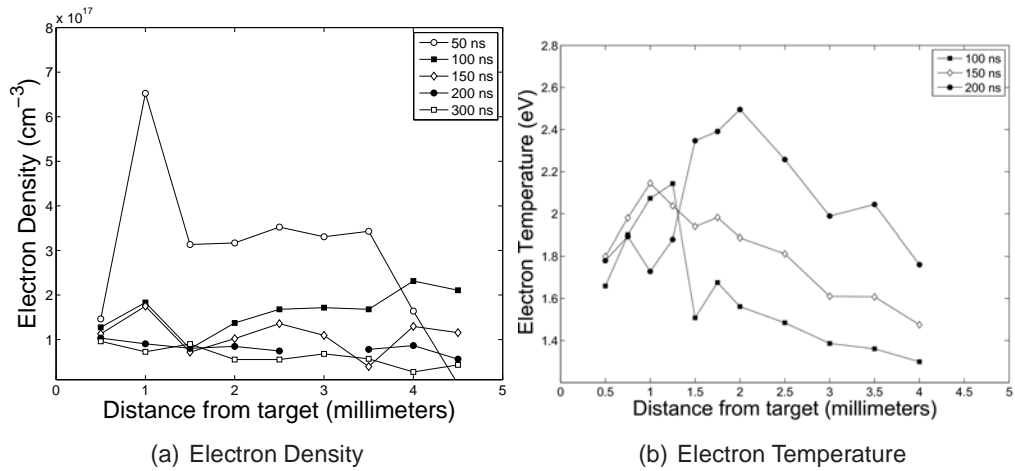


Figure 4.16: Spatial distribution of the electron density (a) and temperature (b) along the length of a stagnation layer created by the collision of two aluminium plasmas generated on flat metal targets using a point focus optical scheme. Left-hand panel: The electron density was determined using direct Stark-width analysis of the aluminium doublet at 394.4 nm and 396.15 nm. No significant self-absorption was observed in the stagnation layer for the delay times quoted here. Right-hand panel: The electron temperature was determined using the ratio of intensity from the Al II line ( $3p^2 - 3s4p$ ) at 466.30 nm to the intensity of the Al III line ( $2p^64p - 2p^64d$ ) at 452.89 nm.

Figure 4.16 (a) shows the electron density along the length of the stagnation layer for different times after the laser pulse has terminated. The results reveal that the density is highest at early times, peaking here at 50 ns, and decreases as time progresses and the stagnation layer expands into vacuum. The data at 50 ns indicates that the stagnation layer has a high-density region of  $6.5 \times 10^{17} \text{ cm}^{-3}$  approximately 1 mm from the target surface. The density of the layer decreases as the distance from the target increases. Over time, it appears from the data that the highest density region moves away from the target. The density becomes quite homogenous throughout the length of the stagnation layer, reaching an average value of  $1 \times 10^{17} \text{ cm}^{-3}$  at approximately 300 ns.

The temperature along the length of the interaction region was determined by extracting the ratio of the intensities of spectral lines from successive ion stages. The

process is similar to that used in the case of single plasmas. Again, Voigt profiles were fitted to the two spectral lines under consideration, namely the Al II line ( $3p^2(^1D) - 3s4p(^1P^o)$ ) at 466.30 nm and the Al III line ( $2p^64p(^2P^o) - 2p^64d(^2D)$ ) at 452.89 nm. Figure 4.16 (b) shows the spatial distribution of the electron temperature in the stagnation layer for three different time delays. At 100 ns, the temperature reaches a peak value of 2.2 eV at approximately 1 mm from the target surface. Moving away from the target the temperature drops to  $\sim 1.4$  eV at 4 mm. At 200 ns one will see that the temperature of the stagnation layer is hotter than at any other time, and reaches as peak value of 2.4 eV. This time-delay may correspond to the time at which the bulk of the material from each of the seed plasmas reaches the interaction region. The stagnation layer is continuously forming, and the collision of this bulk material leads to significant heating within the interaction region, causing the increase in temperature seen in the experimental data. However, beyond 200 ns, the temperature of the plasma begins to drop, as the seed plasmas which supply the material to the collision region become extinct. At this point onwards, the stagnation layer behaves as an isolated entity, expanding into the surrounding vacuum over the course of a few hundred nanoseconds and cooling fairly slowly as it does so.

## Calcium

The electron density along a calcium stagnation layer was estimated using the the  $Ca^+$  doublet  $3p^64s(^2S_{1/2}) - 3p^64p(^2P_{3/2,1/2})$  at 393.36 nm and 396.48 nm. These lines involve transitions to the ground state of the  $Ca^+$  ion and therefore suffered from significant self-absorption. Self-reversed line profiles were observed in the emission spectra from the stagnation layer during its initial formation, an extreme example of which is shown in figure 4.17 (a).

Displayed in figure 4.17 are three emission spectra sampled at a time delay of approximately 100 ns after seed plasma formation and at three different transverse positions along the length of the stagnation layer, namely 1.5 mm, 2.5 mm and 3.5 mm. It is clear from these spectra that close to the target surface the spectral lines show signs of significant self-reversal. As the distance from the target is increased the effects of self-absorption decrease. At approximately 3.5 mm from the surface the attenuation of the spectral lines becomes small and the ratio of the intensity between the two lines approaches the ratio of their statistical weights.

However, in practice, it was found that there was significant self-absorption in the spectral lines emitted throughout the majority of the space-time evolution of the

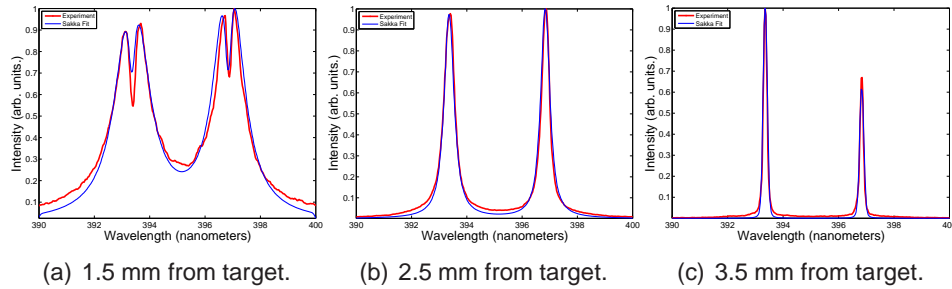


Figure 4.17: Emission spectra from a calcium stagnation layer taken at different distances from the target surface. The ICCD camera was operated with a gate width of 5 ns (FWHM) and the images were acquired at a time delay of approximately 100 ns after seed plasma formation. (a) Approximately 1.5 mm from the target surface, where the stagnation layer appears to be at its most dense. One finds here that the level of self-absorption is high with clear evidence of self-reversal in the spectral lines. (b) Acquired at approximately 2.5 mm from the target surface. Here one can see the effect of self absorption is reduced, but the spectral lines are still strongly attenuated. (c) Far from the target surface ( $\sim 3.5$  mm) where there appears to be little or no self-absorption and the intensity ratio of the two spectral lines approaches the ratio of their statistical weights. The red line in each case represents a fit to the spectrum using the radiative-transfer model and was used to extract the electron density.

stagnation layer, therefore the radiative transfer model was used to extract the electron density. The simulated spectra generated using the computer model (figure 4.17) appear to fit nicely to the experimental data, the results of which are presented in figure 4.18 for a range of space-time values from 0.5 mm to 4.5 mm and from 100 ns to 300 ns.

At 100 ns one can see from figure 4.18 that the density at 0.5 mm is quite high, reaching a value of  $1 \times 10^{19} \text{ cm}^{-3}$ . One may recall from the emission imaging section that the calcium seed plasmas tended to collide much closer to the target surface than in the case of aluminium which resulted in quite a short stagnation layer with the highest density region lying within 1 mm of the target surface. As time progresses and the stagnation layer grows in size, the density along its spine up to a distance of approximately 2.5 mm becomes more uniform. The peak density occurs at a time delay of approximately 300 ns following seed plasma initiation which coincides with the time when the seed plasmas are at their largest extent and the stagnation layer is brightest, as seen in the emission images on page 134. Beyond 200 ns the seed plasmas are all but extinct and so there is very little additional material being supplied to the interaction region. The overall density is

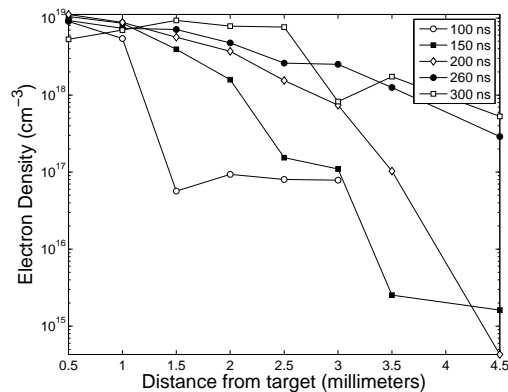


Figure 4.18: Temporally-resolved spatial distribution of the electron density along the spine of the stagnation layer created by the collision of two calcium plasmas. The two seed plasmas were produced on a flat metal target by a point focus optical arrangement with an initial separation of approximately 2 mm. The density was extracted from the emission spectra using the radiation transport model.

reduced and becomes more homogenous over the 5 mm region.

The accurate determination of the electron temperature along the length of the stagnation layer using the methods described in section 4.2.2 was severely hampered by the effects of self-absorption on the emission spectra. While the emission lines originating from transitions involving neutral calcium did not appear to suffer from self-reversal (an extreme form of opacity, shown in figure 4.17 (a)), they did suffer from varying degrees of attenuation. This meant that extracting the electron temperature using the ratio of intensities between lines from the same or successive charge states would be prone to significant errors. As an alternative, the self-absorption computer model was used to estimate an average electron temperature in the stagnation layer. The best fits between the simulated spectra generated using the model and the experimental data were achieved when an average plasma temperature of 20000 K or 1.7 eV was used in the computer code.

To summarize the results in this section, it was shown that when two plasmas collide a brightly emitting stagnation layer will form at the collision plane between the two plasmas. The collision of the two calcium plumes produced a stagnation layer which was shorter and wider than in the case of colliding aluminium plasmas. It was proposed in this section that the overall shape of the stagnation layer could reveal certain properties of the collision process. While an aluminium plasma was found to grow/expand at close to an order of magnitude faster than that of a calcium plasma, the increase in the atomic number (in the calcium case) means that there is

only a slight difference in the value of the ion-ion mfp between the two. This small difference between the two elements gave rise to a small change in the overall width of the stagnation layers. Stagnation layers produced from colliding calcium plasmas were typically twice the width of their aluminium counterparts, suggesting that the degree of interpenetration between the two plumes was slightly larger in the calcium case.

Spectra revealed that calcium suffered from strong self-absorption, and accordingly the radiative-transfer computer model was used to extract the electron density. The peak density for aluminium was  $\sim 3 \times 10^{17} \text{ cm}^{-3}$  while for calcium it was in the region of  $5 \times 10^{18} \text{ cm}^{-3}$ . The higher degree of lateral expansion along the surface of the target in the case of calcium had resulted in confinement of the stagnation layer which may have led to the increase in the local electron density observed in this region.

In the next section the discussion is moved to the case of the collision between two line plasmas, produced by focusing the laser beam onto a flat target using a cylindrical lens. The on-target irradiance is smaller, as the energy of the laser is now spread out over a larger area. This reduces the overall temperature of the seed plasmas which may result in small but significant changes in the collision process.

#### **4.3.1.3 Imaging of Colliding Line Plasmas**

We now move on to study the collision between two line plasmas generated on flat targets. The experimental and optical setup is the same as that which was used in the previous study on point plasmas with the exception of the focusing lens. The spherical lens which provided a point focus was replaced by a cylindrical lens which focused the laser beam to a line on the target surface. The cylindrical lens only focuses along one axis thereby producing a focal spot which is  $\sim 50 \mu\text{m}$  wide and 12 mm in length (the width of the laser beam).

The interest in using such an optical setup is two-fold. Firstly, and most importantly, the line focus results in a reduction in the on-target irradiance as the energy of the laser beam is now spread over a larger surface area. The reduction in irradiance means that the seed plasmas will be slightly cooler and less dense than those previously studied, which will lead to a change in the collisionality parameter defining the system. As the ion-ion mean free path depends on  $z^{-4}$  and the average charge state for line plasmas is lower than for point-like seed plasmas, one would expect to observe a softer stagnation and greater interpenetration than in the colliding line

plasmas case.

A second motivation to using line focusing is that shape of the stagnation layer is quite different from the previous study. Here, the collision between the two line plasmas will be along a plane, therefore it is expected that this will create a stagnation layer which resembles a wide sheath or surface. For colliding point plasmas, one can view the interaction as akin to colliding cones. Hence the intersection at the collision front will result in flat but slight irregular stagnation layers. The stagnation layers in the colliding line plasma case will also have a large surface area and a narrow cross-section in the orthogonal direction. The properties of the layer spectroscopically should also be quite different. As the layer is now extended over a larger area the effect of self-absorption could become even more significant. The light reaching the detector will have to travel through a larger path-length through the layer (on average) thus increasing the likelihood of absorption by atomic species in ground and/or low-lying states. In this case, it is expected that the effects of self-absorption be quite significant in the emission spectra of the stagnation layer.

## **Aluminium**

Figure 4.19 shows time-resolved images of two colliding aluminium plasmas which were created using a line focus of the picosecond laser beam. The camera is positioned at right angles to the target surface and the laser beam enters from the left-hand side of the image. The line plasma has a width on the order of a few hundred microns, while the length will be on the order of the diameter of the laser beam (i.e., 12 mm). Because the camera is positioned in an orthogonal plane to the expansion axis it will capture a side-view of the colliding plasma system. Therefore, one can only observe the minor axis of the stagnation layer, and the full width of the layer is not directly observable.

Collision of the seed plasmas occurs within a few tens of nanoseconds and by 50 ns a well defined stagnation layer is seen to have formed. The stagnation layer produced by the collision of two line plasmas was found to be broad, having a full width half maximum of approximately 1.2 mm; and long, having a length of  $\sim 3.75$  mm at the peak of its brightness ( $\sim 150$  ns after the laser pulse has terminated). The stagnation layer in this case is substantially wider than in the case of the collision of two plasmas generated by a point focus of the laser beam.

The intensity distribution of the two seed plasmas at 25 ns appear somewhat different, with the bottom plasma appearing fainter than the top plasma. The image

is inverted when projected onto the CCD chip and so the bottom plasma is generated by the portion of the laser which has been deviated by the wedge prism. This diverging beam does not strike the focusing lens at normal incidence and so the focal spot will be broadened somewhat due to astigmatism.

An intensity line-out was taken across the length of the stagnation layer and the plume-front position was extracted. The position of the plume front is plotted in figure 4.20 with respect to time. A linear fit to the initial growth phase of the layer (from 50 ns – 100 ns) is represented by the red line in the figure. It can be seen from figure 4.20 that initially the stagnation layer appears to be quite stationary (up to a time delay of 60 ns) until there is enough material in the interaction region to drive expansion and growth of the layer.

### **Spectroscopy**

Significant self-absorption in the emission spectra of aluminium was observed (due to the increase in the absorption path length) and so the self-absorption computer model was used exclusively for the determination of the electron density within the interaction region between the two colliding line plasmas.

The spatial distribution of the electron density is shown in figure 4.21 (a) where the typical trends seen throughout the previous work are again evident. There is a high density region close to the target surface with a decrease in the density as distance from the target increases. Again one can see the maximum density at around 200 ns indicating that the growth of the stagnation layer peaks at this epoch. The maximum density achieved was  $1.4 \times 10^{17} \text{ cm}^{-3}$  which is slightly less than that recorded for the colliding point-like seed plasmas.

The temperature was determined from the ratio of emission line intensities from two consecutive charge states. The same spectral lines were used as in the previous analysis, namely the  $\text{Al}^+$  line at 466.3 nm and the  $\text{Al}^{2+}$  line at 452.9 nm. The temperature along the interaction region between the two plasmas is shown in figure 4.21 (b). At 100 ns the temperature peaks at 2.4 eV near the target surface. As time progresses one can see that the peak in the temperature shifts further away from the target. At 250 ns the temperature has decreased to  $\sim 2$  eV along the length of the interaction region, with the hottest section remaining in the mid-section at around 2 mm from the target.

## Calcium

Displayed in figure 4.22 are time-resolved images of two colliding calcium plasmas generated by a line-focus of the laser beam onto a flat metal target. Once again, the images reveal that the bulk of the emission is located close to the target surface with emission from the top plasma being brighter than that from the bottom seed plasma due to a difference in the focal spot shape caused by astigmatism. Emission due to collisions begins to become evident at a time delay of  $\sim 100$  ns, and occurs close to the target surface. A bright stagnation layer  $\sim 2.5$  mm in length and 1.4 mm in width appears to form at approximately 150 ns after the termination of the laser pulse. This layer is wider than in the case of colliding point plasmas, where the stagnation layer had a width and length of  $300 \mu\text{m}$  and 1.5 mm respectively. This supports the proposal that there is more plume interpenetration occurring in the case of the colliding line plasmas. The seed plasmas become extinct by  $\sim 150$  ns and the stagnation layer continues to emit brightly for a further few hundred nanoseconds.

As before, the broadband images were used to determine the growth rate of the stagnation layer. Because the layer expands backwards (towards the target) as well as forwards, the FWHM of an intensity line-out along the length of the midplane region was used to determine the growth rate of the stagnation layer. This data is presented in figure 4.23 and from a simple linear fit one can extract the growth rate of the layer. For the case of two colliding line plasmas, the stagnation layer was found to grow by an average of  $0.75 \times 10^6$  cm/s.

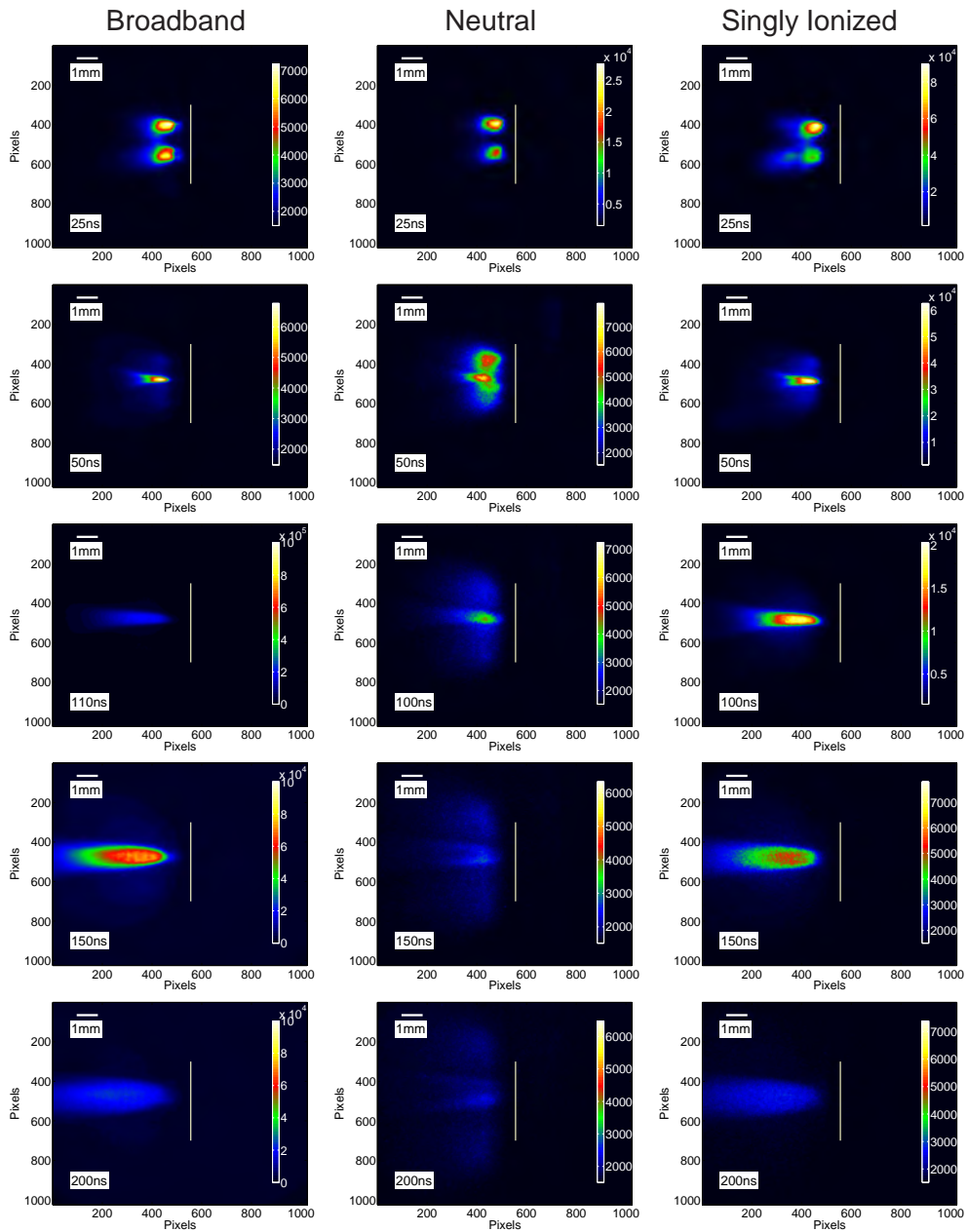


Figure 4.19: Spectrally filtered and time-resolved image montage of two colliding aluminum plasmas produced on a flat metal target by a line focus of the laser beam. Left-hand column: Images taken using the broadband transmission filter showing white-light or the bulk plasma emission. Middle column: Images recorded with a transmission filter centered on 390 nm which corresponds to emission from neutral aluminium species. Right-hand column: Images acquired using a filter with a center wavelength of 470 nm which transmits light from singly ionized and a small proportion of doubly ionized species. The laser beam enters from the left hand-side of each of the image and the approximate position of the target surface is represented by the white line.

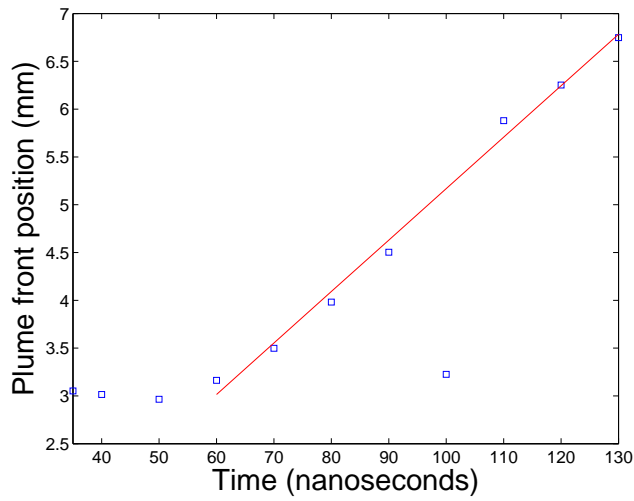


Figure 4.20: Plume-front position of the stagnation layer as a function of time delay for an aluminum plasma produced on a flat target using a line focus of the laser beam. The position of the plume-front corresponds to the point where the intensity drops to 10% of the maximum intensity, determined using broadband images in figure 4.19. The solid line represents a linear fit to the data, the slope of which yields a growth velocity of  $5.4 \times 10^6$  cm/s.

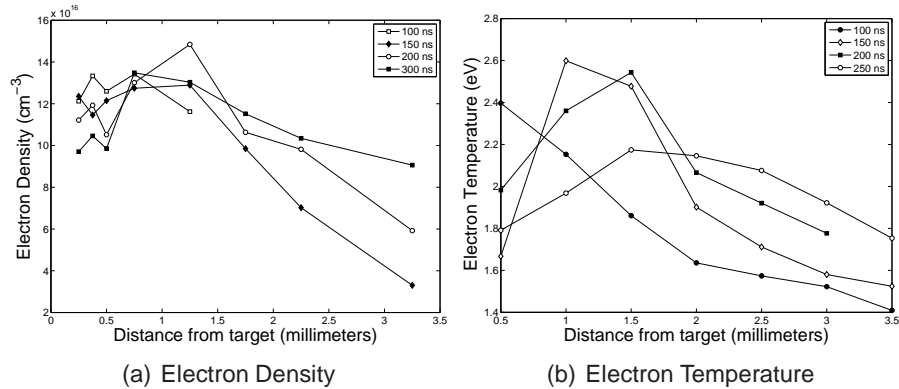


Figure 4.21: (a) Electron density and temperature plots for the interaction region at the interface of the collision of two Aluminium line plasmas. The electron density was determined by comparing synthetic spectra generated by the radiative transfer model with the experimental spectra. (b) The temperature plot was determined using the ratio of the intensities of the  $\text{Al}^+$  466.3 nm and  $\text{Al}^{2+}$  452.89 nm spectral lines.

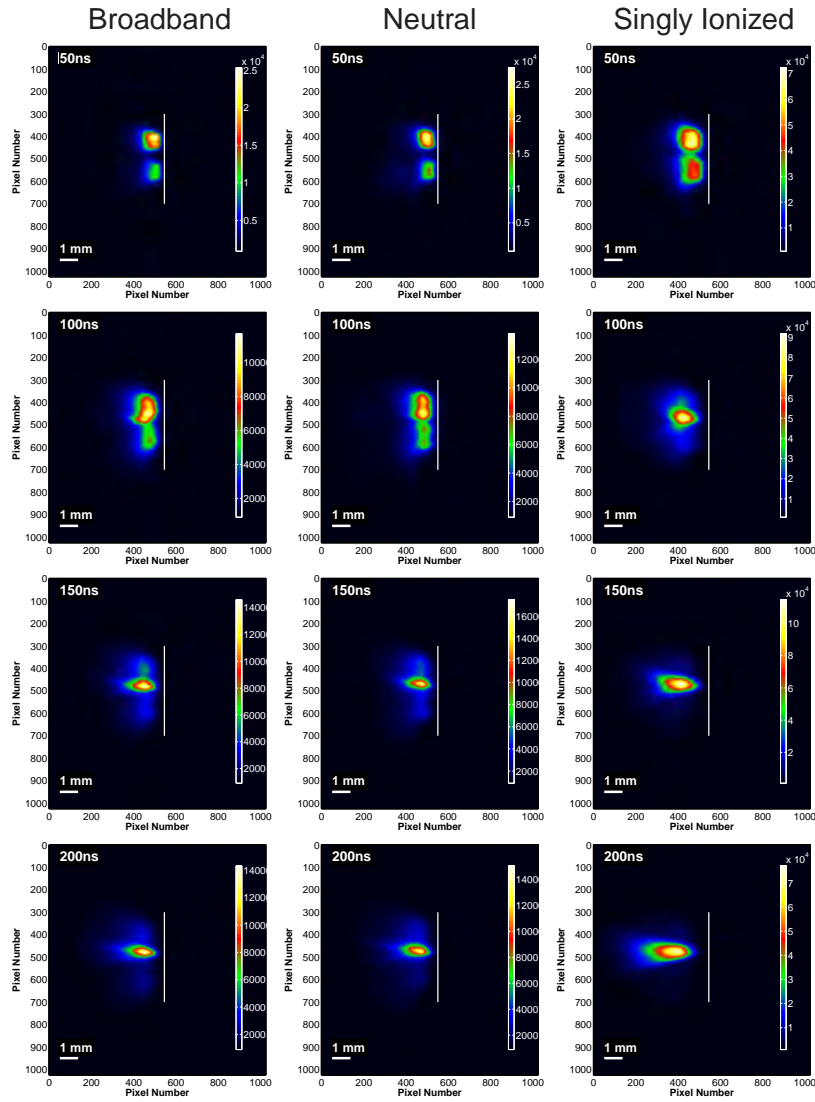


Figure 4.22: Spectrally filtered and time-resolved image array of two colliding calcium plasmas produced on a flat metal target by a line focus of the laser beam. Left-hand column: Images taken using the broadband transmission filter showing white-light or the bulk plasma emission. Middle column: Images taken with a transmission filter centered on 420 nm which corresponds to emission from neutral aluminium species. Right-hand column: Images taken using a filter with a center wavelength of 390 nm which transmits radiation from singly ionized species. The laser beam enters from the left-hand side of each image and the approximate position of the target surface is represented by the white line.

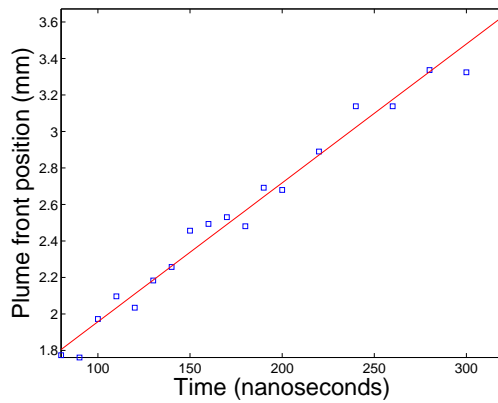


Figure 4.23: Plume front position as a function of time delay for broadband plume emission of the stagnation layer created by the collision of two calcium line plasmas.

When spectroscopy was performed on the collision region between the two calcium line plasmas two distinct regions were observed, characterized (at the extremes) by strong, or hardly any, evidence of self absorption. The electron density of the entire region was determined using a combination of the two methods. At early time delays where self-absorption was strong, the radiation transport model was used to determine the electron density of the region. At delays greater than 300 ns, conventional Stark analysis of the spectral line was used.

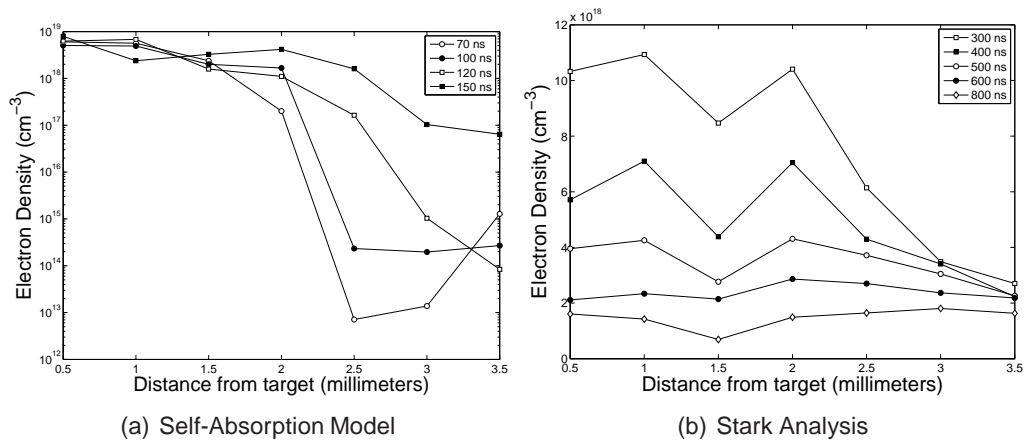


Figure 4.24: Electron density calculated using both the radiation transport computer model (a) for the early time delays close to the target and conventional Stark broadening analysis (b) for later time delays.

The spatial distribution of the electron density extracted from the computer model is shown in figure 4.24 (a). The data shows a high density region close to the target

surface followed by an extended region characterized by decreasing density as the distance from the target increases. One can see here that the density yielded by the radiative transfer model drops rapidly at  $\sim 2$  mm. This is simply due to the fact that, at the short time delays, there is no significant emission from the plasma in this area. It is not until approximately 150 ns that the stagnation layer has expanded into this region. As time progresses more material enters the collision region and this fuels the density up to a level of  $\sim 1 \times 10^{17} \text{ cm}^{-3}$  at a distance of 3 mm from the target. Compare this to the data obtained from the Stark analysis of the spectral lines, shown in figure 4.24 (b) measured at longer time delays when the stagnation layer has established itself. In this case, the density across the region is relatively flat, with the exception of a few modulations at around 300 ns. The density of the stagnation layer at the target reported by this method is  $1 \times 10^{18} \text{ cm}^{-3}$  which is an order of magnitude smaller than that predicted by the computer model 150 ns earlier. The density obtained from the model shows that over time the high density region close to the target surface travels outwards. The Stark analysis indicates that by 300 ns the density is fairly flat, and certainly by 600 ns the density becomes quite homogenous across the entire length of the interaction region. The overlap between the two models does not appear to be perfect, which may be due in part to the underestimation of the input parameter ( $\sigma_{e,1,2}$ ) in the model. The reader is reminded that these parameters represent the spatial width of the distribution of the electrons, lower and upper states respectively, and their values play a critical role in the level of self-absorption calculated. Extracting accurate values for these parameters from the emission images proved quite difficult. As mentioned previously the stagnation layer formed by the collision of two line plasmas is a wide sheath. The length of this sheath could be on the order of a centimeter, comparable to the length of the line focus. But it is more likely to be less than this, as it is assumed that the line plasma will only be sufficiently hot towards the center. Also, hot-spots contained in the seed plasmas due to irregularities in the laser focus across the line may also translate into the formation of a stagnation layer with density hot-spots across its length. This would result in a density modulation along the optical path length which would greatly affect the absorption length, and thus the level of self-absorption suffered by the spectral lines.

## Summary

This section contained the results from the collision of two plasmas which have been generated using intense EKSPLA™ 312p picosecond laser system. Plasmas were formed on flat aluminium and calcium targets using both spherical and cylin-

drical lenses which produced a point and line focus on the target surface respectively. Upon collision at a time delay of approximately 50 ns, significant stagnation was observed between the two counter propagating seed plasmas. Depending on the target metal used, this layer was born at a time delay typically 50 ns after the laser pulse has terminated.

The difference between the two metals was small but significant. In both optical arrangements the two aluminium plasmas collided before the calcium seed plasmas, indicating that aluminium expanded faster from the target surface than calcium. This has been seen in our previous study on single laser-produced plasmas. The stagnation layer itself was found to be quite narrow in the case of aluminium and wider for calcium. Irrespective of target metal, the stagnation layer formed on the collision existed for hundreds of nanoseconds after the seed plasmas had cooled and become extinct.

In the next section, the effects of producing the plasmas on wedge-shaped targets where the two seed plasmas are more opposing will be examined. In this case one would expect the two plasmas to collide with a greater component of their fast forward expansion velocity. Therefore, this target configuration is expected to impact on the collisionality of the system resulting in an increase in the interpenetration between the two seed plasmas when compared to the laterally colliding case.

#### **4.3.2 Colliding Plasmas on Wedge-Shaped Targets**

Presented in the final section of this chapter are the results from the collision of two plasmas which were generated on targets oriented at  $90^\circ$  with respect to each other. Time-resolved emission images were used to track the expansion and collision of the two seed plasmas, along with the growth of the stagnation layer.

The two seed plasmas were produced on wedge-shaped targets and so were orientated in a more opposing configuration. As a consequence they expanded and collided with a larger component of their forward expansion velocity. It was seen in Chapter 5 that the ion-ion mfp of counter-propagating plasma plumes has a strong dependence on  $v$ , the relative collision velocity. Therefore, this target configuration should lead to a substantial decrease in the value of the collisionality parameter. One would expect to see significant plume interpenetration occurring because of this decrease. Again, a simple calculation was done using equation 4.27 which reveals that for a expansion velocities above  $1 \times 10^6$  cm/s (deduced from emission images presented later) the ion-ion mean free path is approximately  $30 \mu\text{m}$ . While

this value is not much larger than that calculated in the case of flat targets, which was approximately  $10 \mu\text{m}$ , it may be sufficient to cause the onset of 'soft-stagnation' [29] giving rise to wide stagnation layers.

#### **4.3.2.1 Emission Imaging of Colliding Point Plasmas**

The study begins with the presentation of spectrally-filtered and time-resolved images of colliding point plasmas. The next two pages contain images of the collision of two aluminium (figure 4.25) and calcium (figure 4.26) colliding plasma systems respectively.

In the case of aluminium, one can see that the two seed plasmas begin to collide at approximately 50 ns, and by 100 ns a brightly emitting stagnation layer has formed. The width and length of the stagnation layer at this point are  $480 \mu\text{m}$  and  $\sim 1.5 \text{ mm}$  (FWHM) respectively. This shows that the width of the stagnation layer has increased by approximately  $80 \mu\text{m}$ , which is a small amount, but consistent with an increase (from  $10 \mu\text{m} \rightarrow 30 \mu\text{m}$ ) of the ion-ion mean free path. At  $1.5 \text{ mm}$  FWHM, the length of the stagnation layer formed at 100 ns is much shorter than that produced with a flat target ( $2.75 \text{ mm}$ ). This is to be expected given that the geometrical arrangement of the two plasmas is now in a more horizontally opposed configuration, i.e., the component of the expansion velocity normal to the surface of the target is reduced.

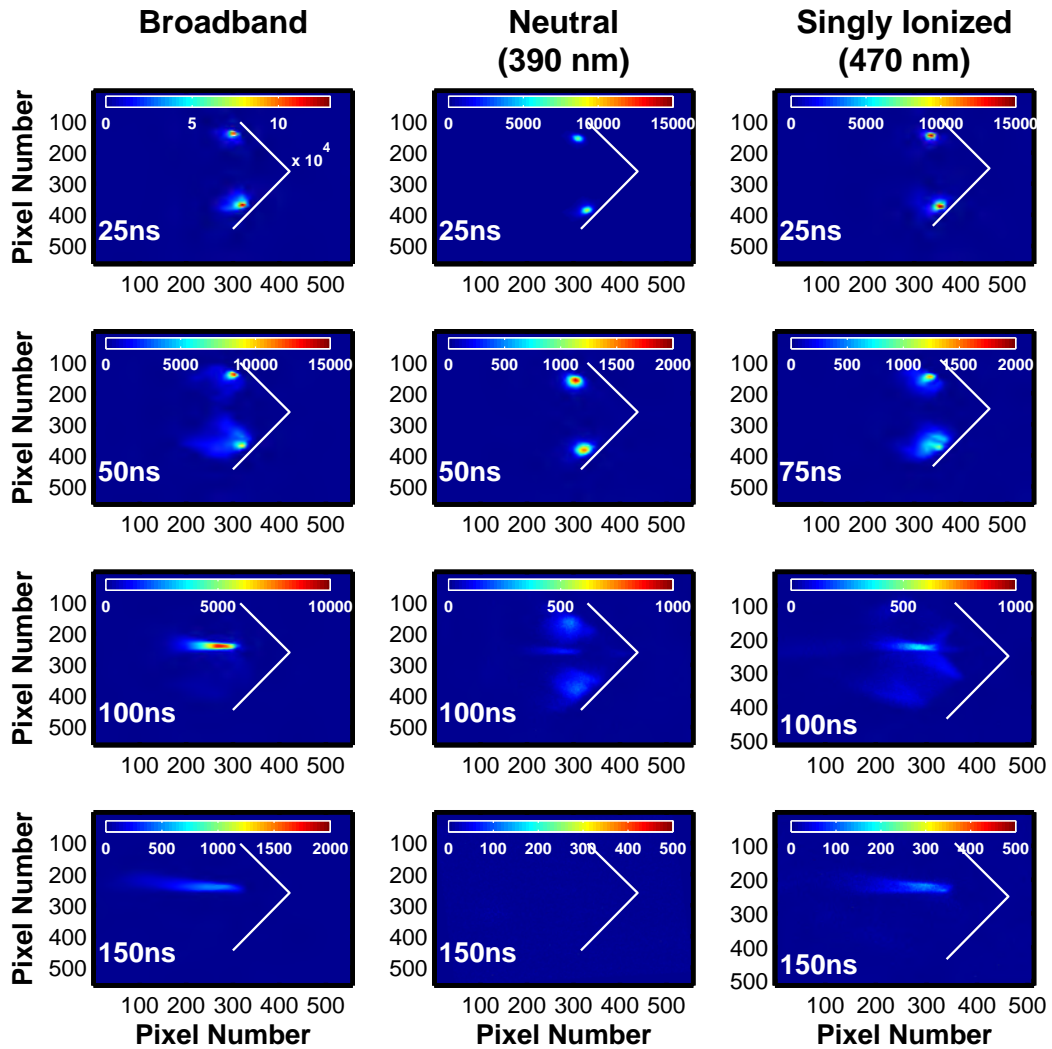


Figure 4.25: Spectrally filtered and time-resolved emission images of colliding plasmas produced on wedge-shaped aluminium targets in the visible spectral region. Left-hand column: Images obtained using the broadband transmission filter showing white-light or the bulk plasma. Middle column: Images recorded with a transmission filter centered on 390 nm which corresponds to emission from neutral aluminium species. Right-hand column: Images acquired using a filter with a center wavelength of 470 nm which transmits light from singly ionized species. The two plasmas are separated by  $\sim 2$  mm and the approximate position of the target is represented by the white line. Each image contains  $512 \times 512$  pixels which corresponds to a field of view of  $7.5 \text{ mm} \times 7.5 \text{ mm}$  and is the summation of 15 laser shots on the same spot. The gate width of the ICCD camera in all emission images (past and present) was 5 ns.

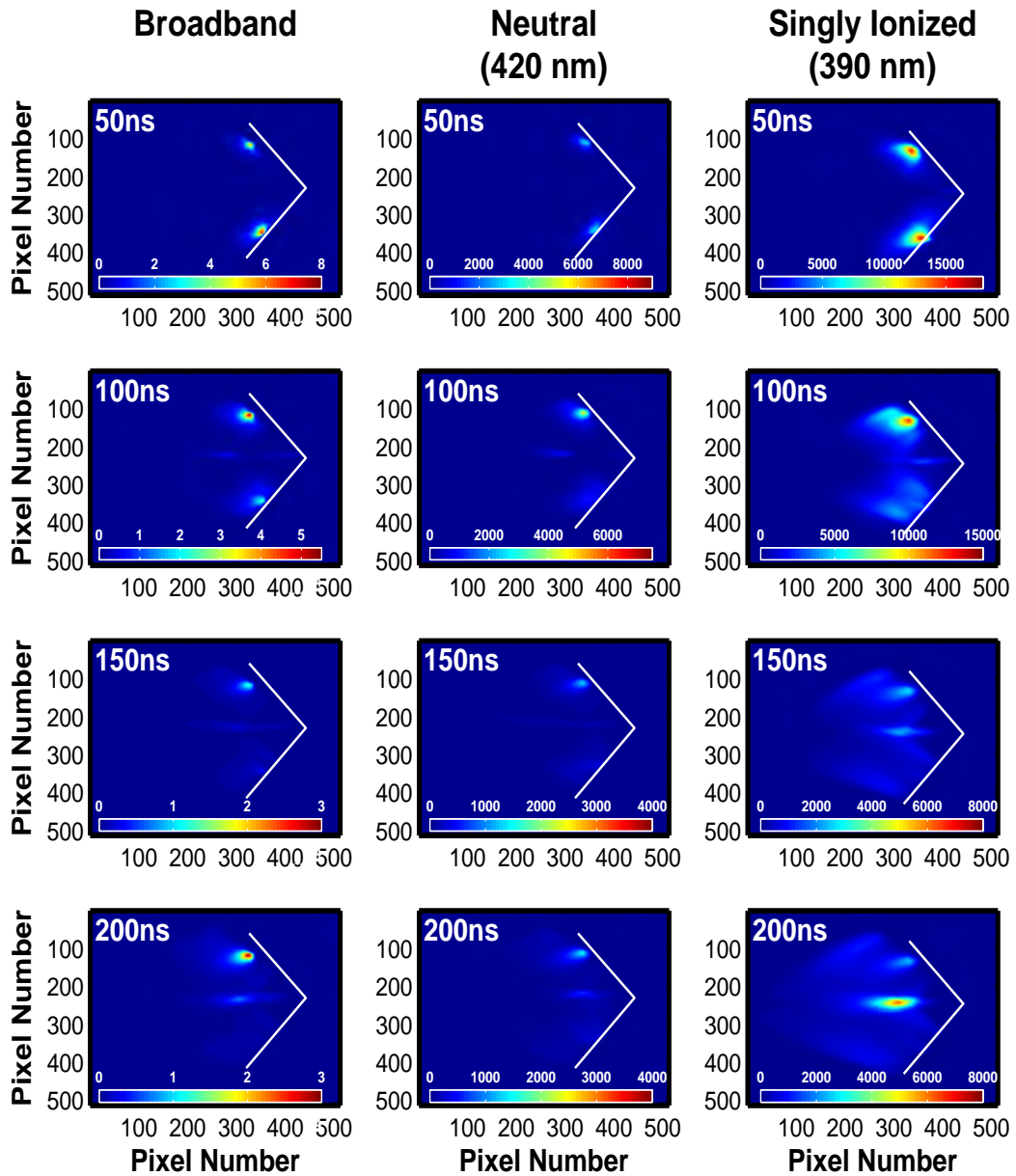


Figure 4.26: Spectrally filtered and time-resolved emission images of colliding plasmas produced on wedge-shaped calcium targets in the visible spectral region. Left-hand column: Images obtained using the broadband transmission filter showing white-light or the bulk plasma. Middle column: Images recorded with a transmission filter centered on 420 nm which corresponds to emission from neutral calcium species. Right-hand column: Images acquired using a filter with a center wavelength of 390 nm which transmits light from singly ionized species. The two plasmas are separated by  $\sim 2$  mm and the approximate position of the target is represented by the white line. Each image contains  $512 \times 512$  pixels which corresponds to a field of view of  $7.5 \text{ mm} \times 7.5 \text{ mm}$  and is the summation of 15 laser shots on the same spot. The gate width of the ICCD camera in all emission images (past and present) was 5 ns. The maximum luminosity in the second column is half that of the third column.

The emission images of colliding calcium plasmas show quite different results from that seen in the case of aluminium. At approximately 200 ns after the laser pulse one can see from the images that a well-defined stagnation layer has formed. It is not until approximately 200 ns when a very short but well-defined stagnation layer begins to form. The dimensions of the calcium stagnation layer at this time follow the general trend seen also in the aluminium data when compared to that of flat-targets. There is a decrease in the length of the layer from approximately 4 mm in the case of flat targets to 1.2 mm (FWHM) as seen here. Similarly, there has been a slight increase in the width of the stagnation layer, from  $700\ \mu\text{m}$  to  $800\ \mu\text{m}$  here. Again one may notice that throughout this time the emission from singly ionized species is substantially brighter than that of the neutral species.

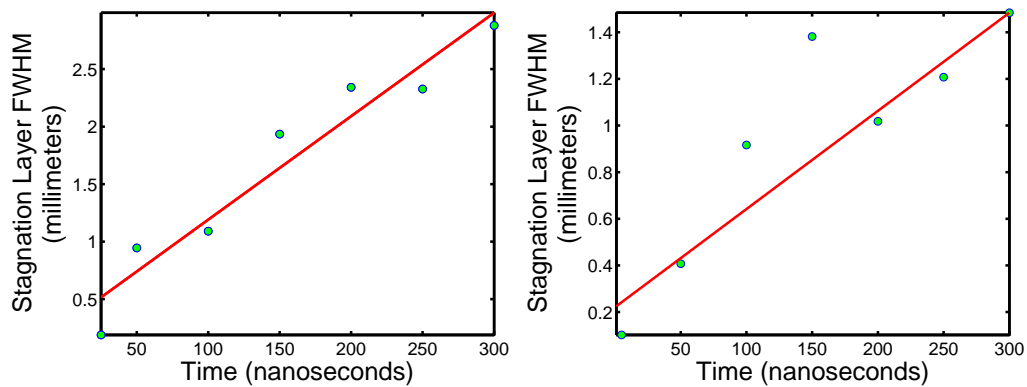


Figure 4.27: Full width half maximum of the length of the stagnation layer produced by the collision of two aluminium (a) and calcium (b) seed plasmas. The FWHM was extracted from the broadband emission images presented earlier. A linear fit (red line) to the data yields a longitudinal growth rate of  $9 \times 10^5\ \text{cm/s}$  and  $4 \times 10^5\ \text{cm/s}$  for aluminium and calcium stagnation layers, respectively.

The FWHM of the stagnation layers from both aluminium and calcium colliding plasmas were extracted from the broadband emission images and their evolution over time plotted in figure 4.27. A linear fit to both plots yielded for the aluminium stagnation layer a growth rate of approximately  $9 \times 10^5\ \text{cm/s}$  while for calcium it was  $4 \times 10^5\ \text{cm/s}$ . The overall trend shows that the equilibrium lengths of both stagnation layers at midlife delays of a few hundred nanoseconds were less than those reported in the case of plasmas generated on flat targets. This can be attributed to the fact that the seed plasmas are in an opposing configuration and so the direction of expansion which is always normal to the target surface is now orientated downwards (and upwards in the case of the lower seed plasma), perpendicular to

the plane used in determining the length of the stagnation layer. Interestingly, the width of the stagnation layer (determined from the broadband emission images) at 150 ns is 480  $\mu\text{m}$  for aluminium and 450  $\mu\text{m}$  for calcium, which are larger than that reported in the case of flat-targets. The width of the stagnation layer in laterally-colliding plasma plumes at the same time delay was typically 300  $\mu\text{m}$  for aluminium and 400  $\mu\text{m}$  for calcium. The increase in the width of the layer in both cases comes down to the fact that the seed plasmas are colliding at a faster relative velocity, which acts to drive up the value of the ion-ion mfp. This results in the two plasma plumes interpenetrating to a much greater degree in the this target configuration than in the flat-target configuration studies in section 4.3.1.

#### **4.3.2.2 Emission Imaging of Colliding Line Plasmas**

The study of colliding plasma systems using wedge-shaped targets now moves to that of line plasmas. The previous experiments into colliding line plasmas produced on flat targets revealed that there is a significant increase in the width of the stagnation layer when compared to plasmas generated from a point focus of the laser. In the case of calcium, the results indicated that there was an increase of approximately a factor of 4 in the width, from 300  $\mu\text{m}$  width for colliding point plasmas increasing to 1.5 mm for colliding line plasmas. The previous discussion also noted that the use of line plasmas created a broad stagnation layer which resembled a sheath plasma layer.

Presented in this subsection are images from colliding line plasmas which were generated on wedge-shaped targets. In the case of aluminium (figure 4.28) it is noticeable that the evolution of the colliding plasma system begins nicely, with the formation of two equally sized and equally bright seed plasmas. It is important to note that the gain on the intensifier of the CCD was set to its maximum value during the recording of the neutral and singly ionized images. This is a non-linear amplification of the intensity and acts to enhance the emission from the low background signal. One can see that the lower seed plasma expands quickly into the center region, while the top plasma remains fairly stationary. In doing so, a bright and very long stagnation layer is seen to form at 70 ns. At this time one can observe that the neutral images contain an abundance of hot-spots localized near the target surface.

There is a faint background emission covering the entire area which would suggest that the entire area contains heated material. As time progresses a very wide stagnation layer is observed. The difference between the neutral images and the

singly ionized images is quite striking. According to the images, the majority of the emission from the stagnation layer is from multiply ionized species. The neutral species in the layer remains quite dark. The images in the second column showing the emission from the neutral species appear to contain an abundance of localized hot-spots near the target surface. The lower seed plasma appears to initially expand very rapidly into the center region, but after 70 ns the emission is extinguished. The stagnation layer is localized towards the top of the image where the top seed plasma is still emitting.

Figure 4.29 shows the results from the imaging of colliding calcium plasmas generated by a line focus on wedge-shaped targets. Two bright plasmas were produced separated by approximately 2 mm. The first row in the figure shows images taken at approximately 20 ns after the laser pulse has terminated. The emission from the singly ionized species appears to be stronger than that of the neutral species. The neutral species are located in a small core in close proximity to the target surface. Within a few tens of nanoseconds the two plasmas have expanded sufficiently to permit their outer edges to collide. The second row of images were recorded at a time delay 100 ns where brightly emitting and stagnated neutral atomic species are evident.

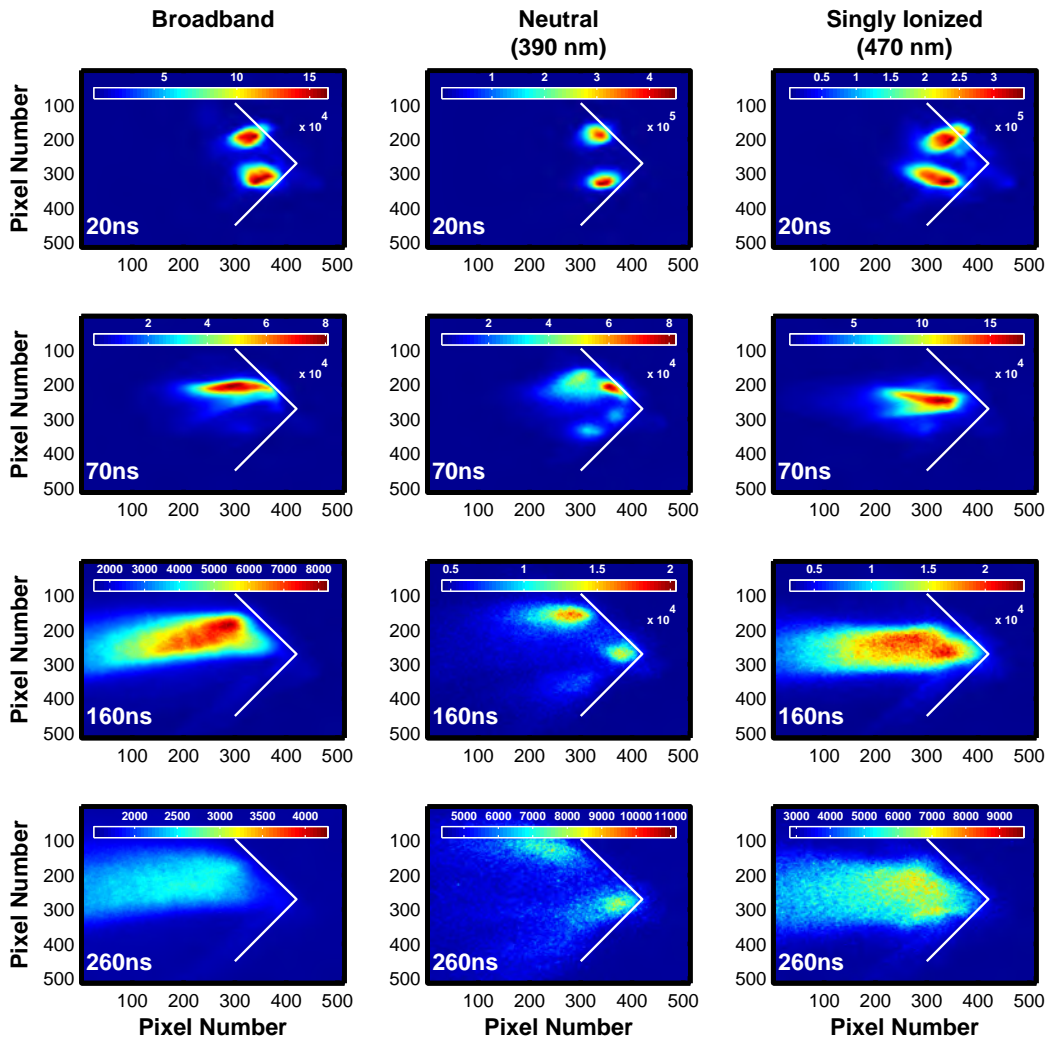


Figure 4.28: Spectrally filtered and time-resolved image array of two colliding aluminium plasmas produced on a wedge-shaped metal target by a line focus of each laser beam. Left-hand column: Images acquired using the broadband transmission filter showing white-light or the bulk plasma emission. Middle column: Images obtained with a transmission filter centered on 390 nm which corresponds to emission from neutral aluminium species. Right-hand column: Images recorded using a filter with a center wavelength of 470 nm which transmits light from singly ionized species. The laser beam enters from the left-hand side of each image and an approximate position of the target surface is represented by the white line. The dimensions of the focal spot was 12 mm long and estimated to be  $80 \mu\text{m}$  in width. The two seed plasmas were separated by 2 mm and each image represents a region  $6 \text{ mm} \times 6 \text{ mm}$  in size. The second and third columns were acquired at the maximum intensifier gain setting of 255.

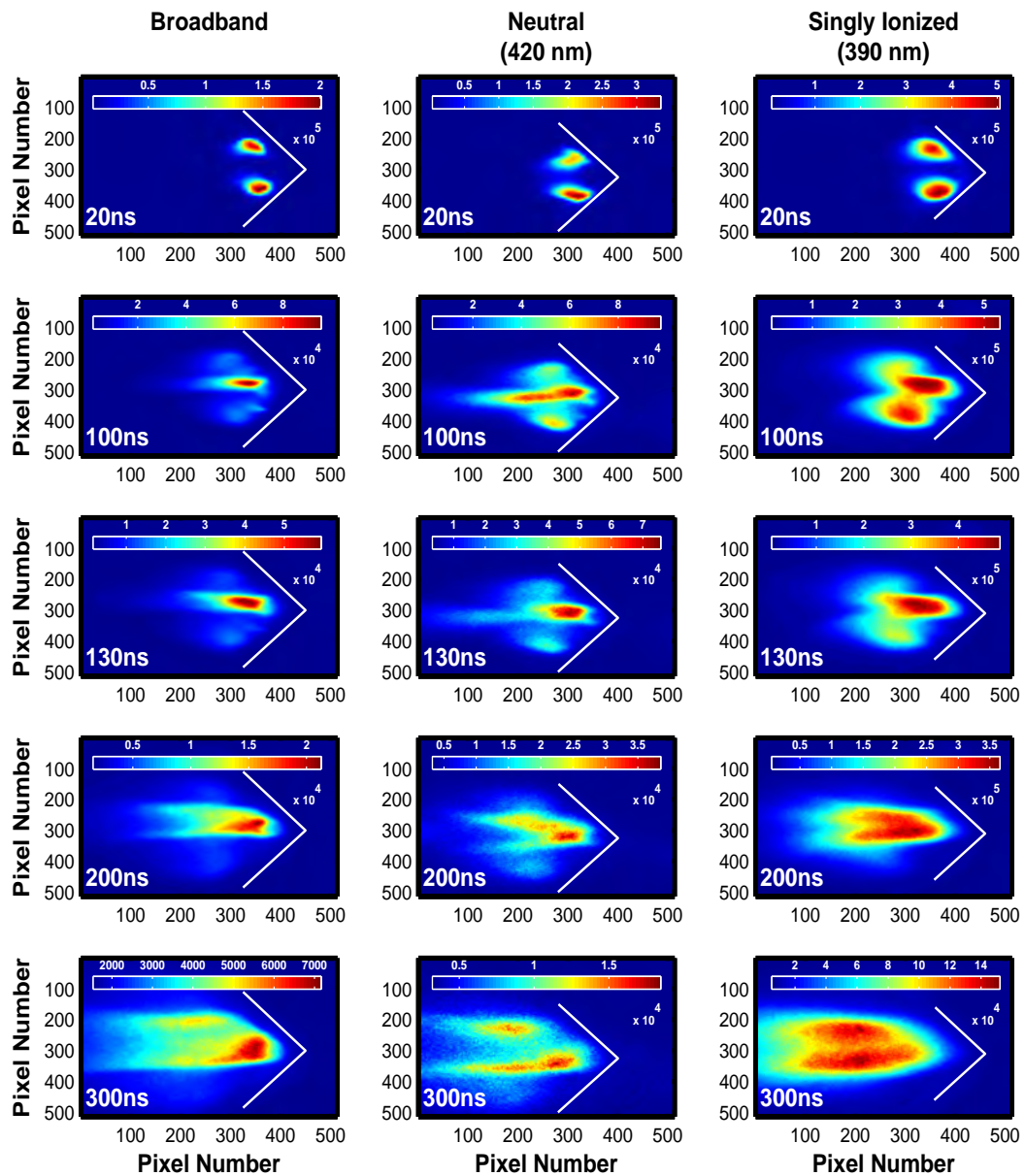


Figure 4.29: Spectrally filtered and time-resolved image montage of two colliding calcium plasmas produced on a wedge-shaped metal target by a line focus of each laser beam. Left-hand column: Images acquired using the broadband transmission filter showing white-light or the bulk plasma emission. Middle column: Images obtained with a transmission filter centered on 390 nm which corresponds to emission from neutral aluminium species. Right-hand column: Images recorded using a filter with a center wavelength of 470 nm which transmits light from singly ionized species. The laser beam enters from the left-hand side of each image and an approximate position of the target surface is represented by the white line. The dimensions of the focal spot was 12 mm long and estimated to be  $80 \mu\text{m}$  in width. The two seed plasmas were separated by 2 mm and each image represents a region  $6 \text{ mm} \times 6 \text{ mm}$  in size. The second and third columns were acquired at the maximum intensifier gain setting of 255.

Beyond 100 ns the emission from the seed plasmas is all but extinct and a bright stagnation layer has formed. Over time, the stagnation layer evolves into two separate regions with a distinct 'dark' region at the center of the stagnation layer. The exact reason for this observation is not yet clear but the effect has been seen at in much higher energy density colliding plumes [31]. In that case the explanation is as follows. Since radiative losses scale quadratically with average ionization state, the hotter collision front radiatively cools more rapidly than the periphery which leads to a collapse of the layer and concomitant densification of the cold core. Further material from the seed plasmas then collide with the periphery of this hard core, emitting radiation as it does so. This effect gives the appearance of a faint emission or glow around a cold core region.

The width of the stagnation layer in these images is many times larger than that observed before. At 160 ns, the stagnation layer has a width that approaches 1 mm. This may be a true physical phenomenon, in that the combination of the orientation of the two seed plasmas along with the reduction in the laser irradiance will substantially increase the value of the ion-ion mean free path. But the width of the stagnation layer may be exaggerated due to a slight misalignment of the CCD camera. If the camera is misaligned with respect to the optical axis then the CCD will capture emission from both extreme ends of the 1 cm long stagnation layer.

Notwithstanding these issues, the broadband images have been used to determine the FWHM along the length of the aluminium and calcium stagnation layers, shown in figure 4.30. Again, the FWHM values were used to determine the growth rate of the stagnation layer, as the layer expands in both directions, towards and away from the surface of the target. The growth rates of the the two stagnation layers were determined by fitting a simple linear model to the data, revealing a value of  $2.6 \times 10^5$  cm/s for aluminium and  $1 \times 10^5$  cm/s in the case of calcium.

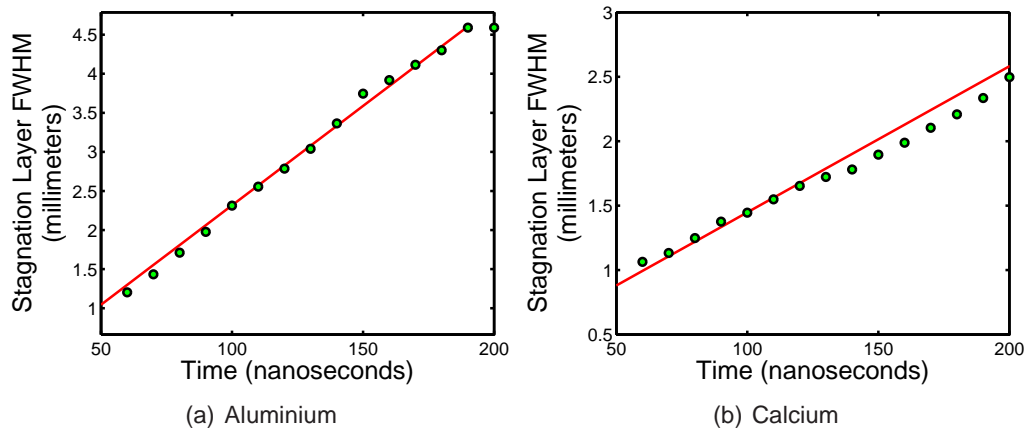


Figure 4.30: Full-width half-maximum along the length of a stagnation layer generated by the collision of two line-like aluminium (a) and calcium (b) seed plasmas on a wedge-shaped target as a function of time delay. A simple linear fit to the experimental data (solid traces) yielded approximate values for the growth rates of  $2.5 \times 10^5$  cm/s and  $1 \times 10^5$  cm/s, respectively.

## 4.4 Conclusions

The visible emission imaging and spectroscopy of plasmas generated by EKSPLA™ 312p picosecond laser system were presented in this chapter. The expansion velocity of aluminium and calcium plasmas was determined using the time-resolved broadband emission images, which revealed that the aluminium plasmas expanded more quickly than their heavier counterparts. Spectra of the plasmas revealed two distinct regions of interest along the expansion axis of the plasma, namely, close to the target where the high density plume resulted in strong self-absorption of the spectral lines, and far from the target where there was little or no self-absorption. Accordingly, the analysis of the emission spectra from the plasmas was carried out using two different methods. The first method used direct Stark analysis which involved measuring the width and shape of a spectral line that is broadened by the Stark effect. The region of applicability for this method was  $\geq 2$  mm from the target surface. In the second method, a computer model based on the solution of the one-dimensional equation of radiative transfer was used to probe the regions of the plasma which were strongly affected by self-absorption. The electron density was determined in both cases and a good degree of overlap in the results from the two methods was observed.

Colliding plasmas were also studied in this chapter. Images and spectra of two colliding point (and line) plasmas produced on flat metal targets were investigated. Unlike the results from colliding plasma systems in the soft X-ray spectral region (presented in Chapter 3), here the formation of a bright and well-defined stagnation layer was observed. An increase in the width of the stagnation layer was observed when the orientation of the two seed plasmas was rotated by  $90^\circ$ , making them more opposing. In this case, the plasmas collided at a faster relative velocity. This increased the value of the ion-ion mfp and resulted in a greater degree of plume interpenetration.

The shape of the stagnation layer was related to the dynamics of the collision. Firstly, the length of the layer was observed to depend somewhat on the relative collision velocity of the two seed plasmas, especially in the case of laterally colliding plasmas (formed on flat targets). Aluminium had a larger expansion velocity than calcium and consequently the stagnation layer was typically longer. Secondly, the width of the layer was used to qualitatively determine the degree of interpenetration between the two seed plasmas. In the case of laterally colliding plasmas, the collision of two aluminium plasmas produced a stagnation layer that had a very narrow width. This indicated that the colliding material came to a sudden stop along the collision front (the midplane between the two plasmas) due to the high value of the collisionality parameter. Calcium, on the other hand produced quite a wide stagnation layer, typically a few hundred microns wider than that of aluminium. This implied that there was an increase in the interpenetration between the two seed plasmas, an idea which was supported by theoretical calculations. This trend was enhanced in the case of orthogonally colliding plasmas where the increased angle led to a small but very significant increase in the relative collision velocity ( $v$ ). Because the ion-ion mean free path (equation 1.26) scales with  $v^4$ , this small increase (half an order of magnitude) resulted in a substantial decrease in the value of the collisionality parameter, permitting interpenetration to play a more dominant role in the collision process.

# Bibliography

- [1] National Institute of Standards and Technology. Atomic Spectra Database. <http://physics.nist.gov/PhysRefData/ASD/index.html>.
- [2] H. Luna, K. D. Kavanagh, and J. T. Costello. Study of a colliding laser-produced plasma by analysis of time and space-resolved image spectra. *Journal of Applied Physics*, 101(1):1–6, 2007.
- [3] S. S. Harilal, C. V. Bindhu, and H.-J. Kunze. Time evolution of colliding laser produced magnesium plasmas investigated using a pinhole camera. *Journal of Applied Physics*, 89(9):4737–4740, 2001.
- [4] S. M. Pollaine, J. R. Albritton, R. Kauffman, C. J. Keane, R. L. Berger, R. Bosch, N. D. Delameter, and B. H. Failor. Stagnation and interpenetration of laser-created colliding plasmas. *APS Meeting Abstracts*, pages 12–16, 1990.
- [5] C. Chenais-Popovics, P. Renaudin, O. Rancu, F. Gilleron, J.-C. Gauthier, O. Larroche, O. Peyrusse, M. Dirksmüller, P. Sondhaus, T. Missalla, I. Uschmann, E. Förster, O. Renner, and E. Krousky. Kinetic to thermal energy transfer and interpenetration in the collision of laser-produced plasmas. *Physics of Plasmas*, 4:190–208, 1997.
- [6] S. S. Harilal. Influence of spot size on propagation dynamics of laser-produced tin plasma. *Journal of Applied Physics*, 102(12):123306, 2007.
- [7] S. Amoruso, G. Ausanio, R. Bruzzese, L. Gragnaniello, L. Lanotte, M. Vitiello, and X. Wang. Characterization of laser ablation of solid targets with near-infrared laser pulses of 100 fs and 1 ps duration. *Applied Surface Science*, 252(13):4863–4870, 2006.
- [8] S. Amoruso. High fluence visible and ultraviolet laser ablation of metallic targets. *Applied Surface Science*, 127:1017–1022, 1998.

- [9] R. K. Singh and J. Narayan. Pulsed-laser evaporation technique for deposition of thin films: Physics and theoretical model. *Physical Review B*, 41(13):8843–8859, 1990.
- [10] T. Sakka, T. Nakajima, and Y.H. Ogata. Spatial population distribution of laser ablation species determined by self-reversed emission line profile. *Journal of Applied Physics*, 92(5):2296–2303, 2002.
- [11] B. Y. Man, Q. L. Dong, A. H. Liu, X. Q. Wei, Q. G. Zhang, J. L. He, and X. T. Wang. Line-broadening analysis of plasma emission produced by laser ablation of metal cu. *Journal of Optics A: Pure and Applied Optics*, 6(1):17–21, 2004.
- [12] H. R. Griem. *Spectral Line Broadening by Plasmas*. Academic, New York, 1974.
- [13] H. R. Griem. *Principles of Laser Plasmas*. Cambridge University Press, Cambridge, U.K., 1997.
- [14] N. Konjevic, A. Lesage, J. R. Fuhr, and W. L. Wiese. Experimental stark widths and shifts for spectral lines of neutral and ionized atoms (a critical review of selected data for the period 1989 through 2000). *Journal of Physical and Chemical Reference Data*, 31(3):819–927, 2002.
- [15] A. Thorne, U. Litzén, and S. Johansson. *Spectrophysics*. Springer-Verlag, 1999.
- [16] H. Luna, J. Dardis, D. Doria, and J.T. Costello. Analysis of time-resolved laser plasma ablation using an imaging spectra technique. *Brazilian Journal of Physics*, 37:1301–1305, 2007.
- [17] F. E. Irons. Radiative transfer across expanding laser-produced plasmas I: Line profiles. *Journal of Physics B: Atomic, Molecular and Optical Physics*, 8(18):3044–3068, 1975.
- [18] P. A. Jansson. *Deconvolution: with applications in spectroscopy*. Academic Press, New York, 1984.
- [19] N. Konjević and W. L. Wiese. Experimental stark widths and shifts for spectral-lines of neutral and ionized atoms (A critical-review of selected data for the period 1983 through 1988). *Journal of Physical and Chemical Reference Data*, 19(6):1307–1385, 1990.

- [20] N. M. Shaikh, S. Hafeez, B. Rashid, and M. A. Baig. Spectroscopic studies of laser induced aluminum plasma using fundamental, second and third harmonics of a Nd:YAG laser. *The European Physical Journal D - Atomic, Molecular, Optical and Plasma Physics*, 44(2):371 – 379, 2007.
- [21] J. Hermann, C. Boulmer-Leborgne, and D. Hong. Diagnostics of the early phase of an ultraviolet laser induced plasma by spectral line analysis considering self-absorption. *Journal of Applied Physics*, 83(2):691–696, 1998.
- [22] K. Kavanagh. *Imaging and Spectroscopy of Laser-Produced Colliding Plasmas*. Ph.D. Thesis, Dublin City University, 2006.
- [23] N. Konjevic, M. S. Dimitrijevic, and W. L. Wiese. Experimental stark widths and shifts for spectral lines of positive ions (a critical review and tabulation of selected data for the period 1976 to 1982). *Journal of Physical and Chemical Reference Data*, 13(3):649–686, 1984.
- [24] A. Corney. *Atomic and laser spectroscopy*. Clarendon Press, New York, 1977.
- [25] B. H. Bransden and C. J. Joachain. *Physics of Atoms and Molecules*. Longman, New York, 1983.
- [26] K. Borje, S. Eriksson, and B. S. Isberg. The spectrum of atomic aluminium Al-I. *Arkiv for Fysik*, 23(6):527, 1963.
- [27] D. Colombant and G. F. Tonon. X-ray emission in laser-produced plasmas. *Journal of Applied Physics*, 44(8):3524–3537, 1973.
- [28] R. W. P. McWhirter. *Plasma diagnostic techniques*. Academic Press Inc., 1965.
- [29] P. W. Rambo and J. Denavit. Interpenetration and ion separation in colliding plasmas. *Physics of Plasmas*, 1(12):4050–4060, 1994.
- [30] J. D. Huba. Naval Research Laboratory: Plasma Formulary. <http://www.ppd.nrl.navy.mil/nrlformulary/>, Naval Research Laboratory, Washington, DC 20375, 2004. Revised Edition.
- [31] D. R. Farley, K. G. Estabrook, S. G. Glendinning, S. H. Glenzer, B. A. Remington, K. Shigemori, J. M. Stone, R. J. Wallace, G. B. Zimmerman, and J. A. Harte. Radiative jet experiments of astrophysical interest using intense lasers. *Physical Review Letters*, 1999.

## **Part II**

# **Intense EUV Laser Interactions with Atoms**

## Chapter 5

# Photoionization of Atoms

The interaction of high intensity ( $> 10^{12}$  W/cm<sup>2</sup>) laser radiation with dilute matter (atoms and molecules) and solids has revealed some interesting non-linear phenomena, for example, multiphoton ionization [1], leading to the discovery of above-threshold ionization (ATI); high-harmonic generation [2]; Coulombic explosion [3] and bright X-ray emission from laser-produced plasmas [4], to name but a few.

Free-electron lasers based on the principle of self-amplified spontaneous emission currently hold the record for producing the brightest, laser-like radiation at the lowest wavelengths [5]. The fundamental FEL photon energy lies far above the ionization potential of most stable matter which therefore permits the study of inner-shell transitions and a whole new plethora of non-linear atomic phenomena. By combining the beam from a femtosecond optical laser (Ti:Sapphire) with an EUV beam from an FEL, the so-called pump-probe scheme [6], one can make many precise studies into diverse areas of atomic, molecular and optical physics, e.g., two-color photoionization [7], dichroic behavior of photoionization processes [8, 9, 10], insight into the photo-dissociation dynamics of molecules, and much more.

In the presence of an intense laser field, an atom may become ionized through a variety of competing channels. An electron may absorb a single high-energy photon and become liberated from the parent atom, or the electron may absorb multiple low-energy photons, each of which bring the electron energy close to (and eventually above) the ionization energy of the atom, so-called *multiphoton ionization*. If the laser is sufficiently intense, then the atomic potential may become distorted to the extent that the electron can tunnel through the potential barrier in a process known as *tunneling ionization*. At very high intensities, the field of the laser can become strong enough to distort the potential barrier of the nucleus so that the electron may

slip over the barrier, in what is commonly referred to as *field-ionization*.

Part 2 of this thesis discusses the interaction of the intense EUV beam from FLASH with rare gas targets. Specifically, two-color above-threshold ionization using a combination of extreme ultra-violet (EUV) and near-infrared (NIR) photons was investigated. This work was performed at the free-electron laser in Hamburg (FLASH) over the past four years or so. Our work at FLASH began with the first exploratory experiments using the ‘first light’ radiation from the then newly commissioned FEL in mid 2004 and has included some prescient experiments on coherent photoionization processes on superposed XUV and optical laser fields, two-photon (FEL only) ionization in xenon and the dissociation of molecular hydrogen. Along with designing and partaking in many fruitful experiments on the photoionization of rare gas atoms, the author has also aided in the development of the facility as a whole by designing and commissioning of a system which is used to temporally synchronize the two independent photon sources (EUV and NIR) on a picosecond timescale using photodiodes. This compact device has become an essential tool in the majority of pump-probe experiments being performed at FLASH today and is described in detail in Chapter 2.

This section provides a brief introduction to the interaction of intense lasers with atoms. The target, a gaseous atomic beam, is so dilute that one may consider the atom to be an isolated entity, i.e., atom-atom and atom-ion collisions can be ignored. A distinction will be made between processes where the Coulomb field of the parent atom plays the significant role and those where the oscillating field of the laser begins to dominate. We examine the various mechanisms through which an atom or ion can be ionized which forms the foundation for the understanding of the primary result presented in Chapter 7, two-color above threshold ionization of rare gas atoms.

## 5.1 Single-Ionization Mechanisms

Normally, excitation of an atom occurs when the frequency of the radiation is resonant with the frequency difference of two or more electronic states (and all the necessary selection rules are conformed to). Similarly, ionization of an atom can occur if a photon is absorbed whose energy lies above the binding energy of the electron in the atom. The kinetic energy of the ejected electron in the continuum is then given by

$$E_{kin} = \hbar\omega - E_b \quad (5.1)$$

where  $E_b$  is the binding energy of the electron. This is the normal photoelectric effect as originally proposed by Einstein in 1905 [11]. In this case, it is assumed that the ionization rate is proportional to the intensity of the laser. This can be checked experimentally by measuring the number of ions produced per laser pulse as a function of the pulse intensity. In a log-log plot the experimental points lie on a straight line whose slope is equal to  $N$ , the number of photons absorbed.

### 5.1.1 Multiphoton Ionization

But ionization of atoms by photons whose energy is considerably less than the binding energy of the valence electrons has been observed over the past three decades (see for example [12, 13, 14, 15, 16, 17]). In 1966, Voronov and Delone [12] noted the first observation of this effect when they used a ruby laser ( $h\nu = 1.78$  eV) to ionize xenon atoms which have a first ionization potential<sup>1</sup> of 12.23 eV. In order to ionize xenon the absorption of multiple laser photons was required. The process by which an atom is ionized by the simultaneous absorption of several photons is called multiphoton ionization or MPI. The resulting kinetic energy of the ejected electron can be described by

$$E_{kin} = N\hbar\omega - E_b \quad (5.2)$$

where  $N$  is the number of photons absorbed and  $E_b$  the binding energy of the electron. On absorption of one photon the electron in the atom is promoted to a virtual state for a very brief period of time that is governed by the uncertainty principle. The probability of the electron absorbing another photon within the (natural) lifetime of this virtual state becomes high only when the intensity of the laser field is typically  $> 10^{11}$  W/cm<sup>2</sup>. In this case, ionization may occur even if the energy of the laser photon is much smaller than that required for direct photoionization ( $\hbar\omega \ll E_b$ ).

Illustrated on the left-hand side of figure 5.1 is the process of multiphoton ionization. If however, during the course of MPI, the absorption of an integer number of photons brings the energy of the electron coincident with a bound state within the atom/ion, then the probability of ionization is greatly enhanced. This process is known as resonantly-enhanced multiphoton absorption, or REMPI [19] and is displayed in the middle of figure 5.1.

---

<sup>1</sup>The lowest energy required to remove an electron from the a valence shell, thus ionizing the atom.

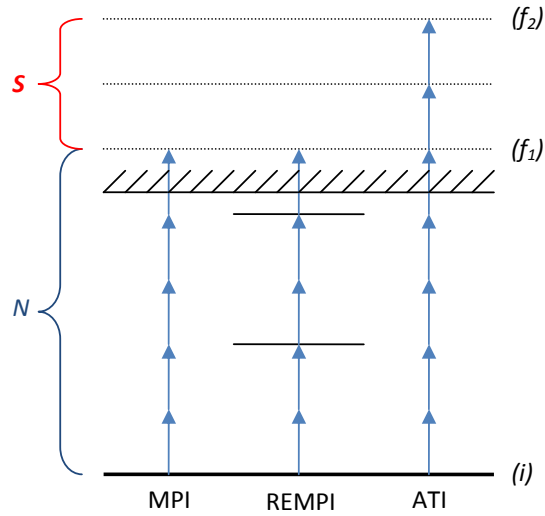


Figure 5.1: Simplified energy level diagram showing the processes of multiphoton ionization, resonantly-enhanced multiphoton ionization and above-threshold ionization. The absorption of  $N$  photons is sufficient to ionize the atom (MPI), but a higher final state can be reached by the absorption of  $S$  excess photons (ATI) [18]. Should the absorption of  $N$  photons coincide with a bound state in the atom then the probability of ionization is greatly enhanced in a process known as resonantly-enhanced multiphoton ionization or REMPI [19].

### 5.1.2 Above-Threshold Ionization

In most cases the number of photons absorbed by the electron (while in the presence of the atom/ion) will be greater than the minimum required for ionization. The ejected electron will therefore have an excess energy corresponding to the number of additional laser photons absorbed above the ionization threshold. Peaks will appear in the photoelectron spectrum which will be separated by the photon energy of the laser. The kinetic energy of the ejected electron in this case can be described by the following equation,

$$E_{kin} = (N + S)\hbar\omega - E_b \quad (5.3)$$

where  $S$  is the number of excess photons absorbed while the electron is in the continuum (see figure 5.1). The process by which the outgoing electron absorbs additional photons when in the continuum and still under the influence of the parent atomic potential, is known as *above-threshold ionization* or ATI. The first observations of signatures from this process were made by Agostini *et al.* in 1979 [1].

When the intensity of the laser exceeds  $\sim 10^{15}$  W/cm<sup>2</sup> the electromagnetic field

strength approaches that of the Coulomb potential which binds the electrons to the atom/ion. At this point, the atomic states can no longer be considered as an unperturbed system since they will be affected by the strong coupling forces with the laser field which act to shift the energy levels in a dynamic fashion (AC-Stark shift) [20]. Electrons in the lower energy levels (the states located closest to the core) are tightly bound, and as such will be least affected by the intense oscillating field of the laser. These core electrons only experience a relatively small energy shift due to the laser, known as the AC Stark shift. On the other hand, the electrons occupying the high Rydberg states (and those free electrons in the continuum - placed there through ATI) where the binding energies are very low will experience the full effects of the intense laser field. The energy of the electron in these Rydberg and continuum states will gain an additional time-dependent quiver energy associated with the motion of an electron in the oscillating field of a laser. When compared to the field-free scenario (i.e., when the laser is off) the energy of these higher states will have shifted by an amount which will depend on the field strength of the laser, known as the ponderomotive energy and which is given by [21],

$$U_p = 9.337 \times 10^{-20} I_0 \lambda^2 \quad (5.4)$$

where  $I_0$  is the peak intensity of the laser in  $\text{W}/\text{cm}^2$  field of the laser and  $\lambda$  is the wavelength of the laser in nanometers. Typical values for the ponderomotive shift on a free-electron induced by a laser field of intensity  $10^{13} \text{ W}/\text{cm}^2$  (800 nm Ti:Sapphire) is 0.598 eV. This simple calculation shows that the Rydberg and continuum states shift away from the core bound states by an energy equal to  $U_p$  thereby increasing the ionization threshold (from the point of view of the core electrons). If the intensity of the laser becomes sufficiently large the ionization threshold increases beyond the range of the  $n\hbar\omega$  absorption channel, where  $n$  can be any integer number of absorbed photons. As the intensity of the laser continues to rise the ionization threshold will also rise beyond the energy of the  $n\hbar\omega$  channel. This effectively closes the ionization pathway for this order in a process known as channel-closure [22]. To quote P. Lambropoulos [23]:

*“... the so-called channel closing in above-threshold ionization (ATI), where ionization of a particular order is suppressed, as the ionization potential moves upward with increasing intensity due to the ponderomotive energy.”*

Early evidence of this effect was observed by Kruit *et al.* in 1983 [24], see figure

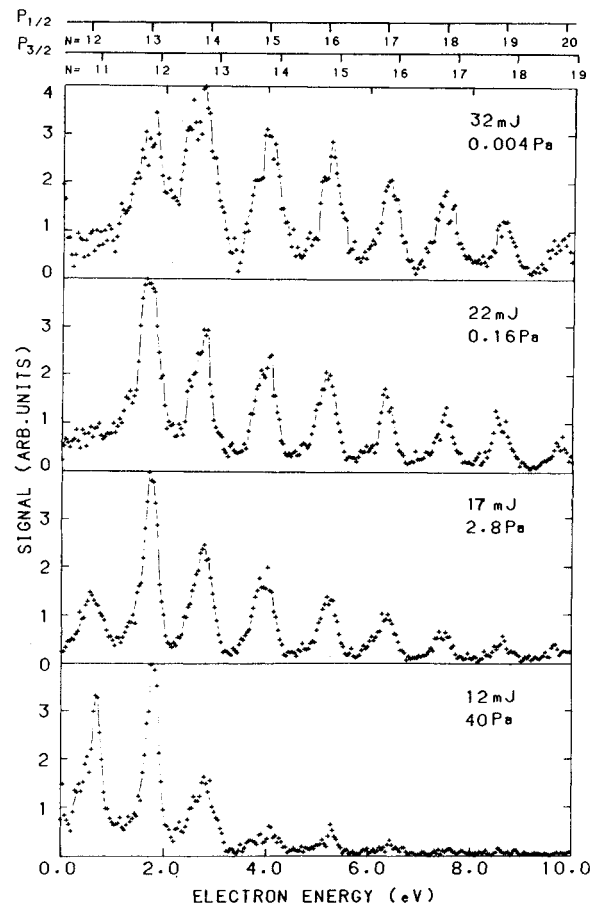


Figure 5.2: Electron spectra from the multiphoton ionization of xenon using a Nd:YAG laser system operating at the fundamental wavelength of 1064 nm. The intensity of the laser field can be evaluated using the pulse energy ( $F$ ) quoted in the figures and using  $F(\text{mJ}) \times 2.10^{12} \text{ W/cm}^2$ . The laser had a pulse duration of 10 ns – 15 ns and a maximum pulse energy of 1 J. An increase in the intensity of the optical laser (moving from bottom panel to top panel) leads to the suppression of the low-order ATI peaks located at low kinetic energy (see text for details). After [24].

5.2. Using a relatively intense Nd:YAG laser system operating at the fundamental wavelength of 1064 nm they observed multiphoton ionization in xenon (see figure 5.2 bottom panel). As the intensity of the laser increased from  $2.4 \times 10^{13} \text{ W/cm}^2$  to  $6.4 \times 10^{13} \text{ W/cm}^2$  they observed a suppression of the low-order (low-energy) ATI photoelectron peaks. From figure 5.2 one can see that the first ATI feature, at a kinetic energy of approximately 0.5 eV disappears as the intensity of the laser increases. The peak does not disappear altogether, as the intensity of the field experienced by the electron will vary over the duration of these relatively long

nanosecond pulses.

### 5.1.3 Tunneling ionization

Following on from the effect of channel closure on the ATI process, when the laser field becomes strong enough and the frequency low enough so that the electron experiences a static-like potential, the laser field is able to distort the atomic potential to such an extent that a potential barrier is formed through which the electron can tunnel. The lower the frequency of the laser the more likely the electron will have tunneled through the barrier before the barrier is restored to its correct potential. This approximation will lead on to the Keldysh parameter [25] discussed in detail later. This mechanism is called tunnel ionization or TI and is illustrated in figure 5.3 (b).

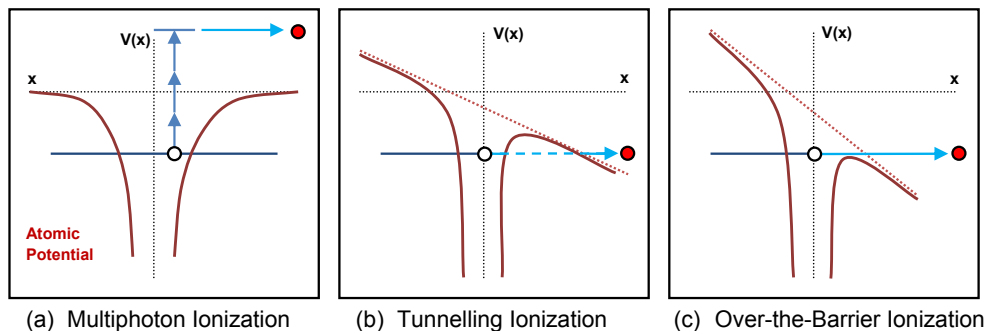


Figure 5.3: Schematic diagram showing the three possible mechanisms for ionization by an intense laser field. (a) At moderate laser intensities typically in the range  $10^{10}$  and  $10^{12}$  W/cm<sup>2</sup> multiphoton ionization dominates. (b) At higher intensities ( $10^{13}$  and  $10^{14}$  W/cm<sup>2</sup>) the atomic potential is distorted and the electron may tunnel through the potential barrier in tunneling ionization. (c) Above a laser intensity of  $10^{15}$  W/cm<sup>2</sup> the barrier is suppressed to such an extent that the electron is free to escape from the atomic potential over barrier.

Beyond this intensity the electric field binding the electron is even further distorted and the barrier becomes smaller until eventually the ground state is no longer bound. This is known as over-the-barrier (OB) or barrier-suppression ionization (BSI) [26] and is illustrated in figure 5.3 (c).

An approximate feel for the laser intensity required to cause the transition from tunneling ionization to over-the-barrier (field) ionization can be determined by equating the maximum distortion induced by the laser field in the atomic potential to the

binding energy of the electron. The threshold laser intensity ( $I_{OB}$ , in  $\text{W}/\text{cm}^2$ ) for over-the-barrier ionization is given by [27],

$$I_{OB} = \frac{c}{128\pi} \left( \frac{4\pi\epsilon_0}{e^2} \right)^3 \frac{I_p^4}{Z^2} \quad (5.5)$$

where  $I_p$  is the ionization potential in electron volts and  $Z$  is the effective charge state of the atom/ion. From this equation one may see that for over-the-barrier ionization in neutral helium ( $I_p = 24.587$  eV) a minimum intensity of  $\sim 1.5 \times 10^{15}$   $\text{W}/\text{cm}^2$  would be required. This is an approximate intensity, where the Coulomb barrier is suppressed and the transition from tunneling ionization to over-the-barrier ionization occurs.

#### 5.1.4 The Keldysh Parameter

While there is no clear-cut divide between the multiphoton and tunneling ionization mechanisms, the Keldysh parameter [25] can be used to determine the intensities where the transition between the above mechanisms occur. A model of quasistatic tunneling was proposed by Keldysh in 1964 which could be used to determine the ionization behavior of atoms in strong laser fields [25]. The Keldysh parameter  $\gamma$  which relates the ionization potential to the ponderomotive energy (field strength) was introduced to define the transition between the multiphoton and tunneling regimes. Expressed in atomic units this parameter is defined as,

$$\gamma = \frac{\omega_L}{\omega_T} = \sqrt{\frac{I_p}{2U_p}} \quad (5.6)$$

where  $\omega_L$  and  $\omega_T$  are the laser and tunneling angular frequencies respectively,  $I_p$  is the ionization potential of the atom/ion and  $U_p$  is the ponderomotive potential, given by equation 5.4. In the case of multiphoton ionization,  $U_p$  is less than the ionization potential of the atom, hence the value of the Keldysh parameter is greater than unity in that case. At the opposite extreme, when the ponderomotive is a good deal larger than the ionization potential (i.e., when the intensity of the laser is high), the potential barrier experienced by the electron is suppressed (see figure 5.3 (c)) and the atom will be liberated via field ionization. In this case the Keldysh parameter is smaller than 1. In the intermediate regime, where the intensity of the laser is not sufficient to completely suppress the atomic potential, tunneling ionization is expected to dominate (see figure 5.3 (b)).

Our discussion of intense laser interactions with atoms has been limited to the case of table-top laser systems which have photon energies of one to perhaps a few electron volts (Ti:Sapphire: 800 nm = 1.55 eV; Nd:YAG: 1064 nm = 1.17 eV or 355 nm = 3.5 eV). However, when a high energy photon from a high intensity EUV free-electron laser impinges upon an atom or ion the value of the ponderomotive potential, given by equation 5.4, is significantly smaller than in the case of the optical laser. As the energy of the photon increases (i.e., as the photon wavelength moves towards the EUV spectral range) the value of the ponderomotive potential drops quadratically while the Keldysh parameter increases linearly. A large value of the Keldysh parameter indicates the dominance of the multiphoton ionization (MPI). One may think of this as follows: As the energy, and concomitantly the frequency, of the photon increases beyond the tunneling ionization rate ( $\omega_L$ ) the electron will have less time in which to complete the tunneling process before the field of the laser has switched direction, effectively raising the barrier. Intuitively, it should also be understandable that high energy (XUV or X-ray) photons are more likely to cause photoionization (PI) than field ionization and so PI (and to a lesser extent MPI) should persist up to quite high intensities (perhaps to  $10^{15}$  W/cm<sup>2</sup>) in EUV/X-ray FEL interactions with atoms and molecules.

In the next section the process of double-ionization of atoms where the mechanisms of MPI, ATI and TI become the primary step in a two-step ionization process will be presented. The discussion will be broken into two sections, the first detailing work done using table-top laser systems, while the second will discuss multi-electron ionization using high photon-energy sources like the EUV FEL at FLASH.

## 5.2 Double-Ionization Mechanisms

Multiple electron ejection from an atom, known as double- (or multiple-) ionization can occur via many different and competing processes. In the simplest case, multiple-ionization occurs in a sequential manner, where each electron is released into the continuum by the interaction of the ionic core with the laser field. However, a discrepancy between theoretical models and experiment was observed in [28, 17, 29] during the early 90s. This gave an early indication of the presence of a non-sequential ionization process, which in some cases can dominate the sequential one [17].

The following section will be divided into two subsections. The first will be based on photoionization using table-top laser systems (e.g., Nd:YAG or Ti:Sapphire) where

the value of the Keldysh parameter defining the laser-atom-ionization process is less than 1. This means that the ponderomotive potential ( $U_p$ ) is on the order of the ionization potential of the atom and so tunneling ionization is expected to dominate. The second subsection will contain a discussion of the ionization processes involved with the use of high photon energy sources such as the EUV FEL at FLASH. In this case, the Keldysh parameter is greater than unity and therefore multiphoton processes are expected to be the dominant ionization processes.

### 5.2.1 Case I: Low-Energy Photons ( $h\nu \approx 1 \text{ eV}$ )

When double ionization using a solid-state laser systems was first observed by Suran *et al.* in 1977 [30] it was immediately realized that there was a large discrepancy between the theory and the experimental results. This was later seen by L'Hullier *et al.* [14] in 1983 in their studies on xenon and krypton. They used 532 nm radiation and sequential double ionization occurred when the neutral atom absorbed six optical photons, while the subsequent ionization of the ground state ion occurred by the absorption of a further ten photons. This sequence would produce  $\text{Xe}^{2+}$  and a log-log plot of the ion yield versus laser intensity should result in a linear relationship the slope of which would equal  $N$ , the number of photons absorbed. But it became immediately clear that this was not to be the case. What was observed by L'Huillier *et al.* was the early production of  $\text{Xe}^{2+}$ .

Figure 5.4 from Walker *et al.* [17] shows a similar result to that of [30] and [14] in their studies published in 1994. The figure shows the yield plot of helium ions measured over a wide range of optical (768 nm) laser intensities. The results show that the  $\text{He}^+$  yield grows rapidly with laser intensity. The yield in the intensity range  $0.1 - 5 \times 10^{14} \text{ W/cm}^2$  can be attributed to multiphoton-ionization. Above a few  $10^{14} \text{ W/cm}^2$  the slope of the  $\text{He}^+$  yield begins to decrease as tunneling ionization and finally field ionization become the dominant ionization mechanisms. Eventually it begins to saturate when all atoms in the focus of the laser are ionized. The yield continues to increase very slowly beyond  $10^{15} \text{ W/cm}^2$  as the intensity across the laser focus becomes more uniform and atoms in the periphery of the focus region begin to be ionized.

Examining the  $\text{He}^{2+}$  yield in figure 5.4 one can see the presence of an inflection (or 'knee'). Also obvious from the figure is the discrepancy between the yield predicted by the so-called single-active electron (SAE) approximation (solid line) and the actual experimental data. Below  $10^{15} \text{ W/cm}^2$  the experimental data is an order of magnitude different from that predicted by the model. Agreement between

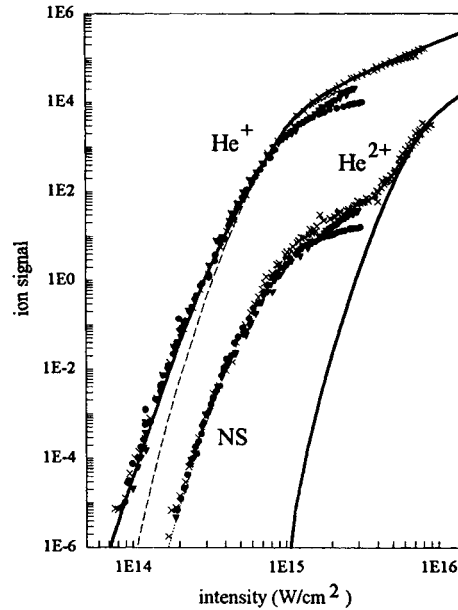


Figure 5.4: Measured ion yields from the ionization of atomic helium using an intense laser operating at a wavelength of 780 nm. Calculations of the single-active electron approximation are shown as solid lines. There is a clear departure from the predictions of the model in the case of the  $\text{He}^{2+}$  yield.  $\text{He}^{2+}$  ions are detected at a laser intensity of  $10^{14} \text{ W/cm}^2$ , nearly a full order of magnitude difference with the model. This shows one of the first observations of a non-sequential double-ionization process. After [17].

the two only occurs when the intensity of the laser has increased to beyond  $10^{15} \text{ W/cm}^2$ . The theoretical model breaks down because it relies on the fact that just one electron is interacting with the laser field at any one time. Under this approximation, double-ionization is strictly limited to the sequential case. Sequential double-ionization (SDI) is a two-step process whereby an atom absorbs a photon which leads to ionization and the ejection of a photoelectron. This ion can then absorb another photon becoming doubly ionized, with the ejection of a second photoelectron in the process. This scheme is applicable to the SAE model because only one electron is active at any one time. The double-ionization yield in figure 5.4 appears to saturate at the same intensity as the single-ionization yield which indicates that the ionization is not occurring sequentially (i.e., the two yields are inextricably linked). This discrepancy between the theoretical model and the experimental data suggests the existence of another process. Non-sequential double ionization by a single low-energy (long wavelength) photon can occur via two similar processes, the first of which will be described in the following paragraph.

### 5.2.1.1 The Recollision Model

The first of two possible mechanisms which may account for the discrepancy between theory and experiment illustrated in figure 5.4 will now be discussed. After an ionization event such as multiphoton ionization or tunneling ionization, the electron is now in the continuum of the parent ion. Corkum *et al.* in 1993 [31] suggested a classical description to explain the non-sequential double-ionization process. This description is explained with the aid of figure 5.5. When an electron in an atom is subjected to a strong laser field it may undergo tunnel ionization and be promoted to the continuum. While in the intense field of the laser the free electron can be accelerated. On the next half of the laser cycle the electric field changes direction and the electron can be driven back towards the nucleus. When this occurs, three distinct events can happen. The energetic electron may recombine with the parent atom to produce a high energy photon in a process known as high-order harmonic generation (HOHG), illustrated in figure 5.5. Or the electron may scatter inelastically with the core. If the kinetic energy of the electron acquired from the laser field exceeds the binding energy of the second electron then this  $e - 2e$  scattering event would in turn liberate a second electron and therefore creating a doubly-ionized core. Or lastly, no double ionization event may occur, the single ionized core remains so and the energetic electron passes through the atomic diameter without any interaction and is detected as an above-threshold ionization or ATI peak on the photoelectron spectrum. Quite recently it was suggested that the three processes describe above can be used in the ultrafast imaging diagnostic of atoms and molecules (see review article by Lein *et al.* (2007) [32]). Each re-scattering process can be used to reveal valuable information about the final state of the atom or molecule after the re-scattering event (i.e., either recombination (HOHG), inelastic scattering (double-ionization) or elastic scattering (ATI)) on a femtosecond time-scale.

The interaction of the intense electromagnetic field with the electron will mean that the electron will have an initial velocity and trajectory dependent on the phase and polarization direction of the laser cycle. Different initial phases of the field will result in different velocities of the ejected electron. Corkum *et al.* [31] discovered that the highest kinetic energy attainable by the ejected electron occurred if it emerged into the continuum when the phase of the optical cycle was at  $\omega t = 17^\circ, 197^\circ$ , or integer multiples thereof. The maximum energy which could be transferred to the electron was then found to be  $3.17 U_p + I_p$  in the HHG case [34] and typically  $\sim 10 U_p$  in the case of ATI [35, 36, 37]. Similarly, the rescattering model supported the

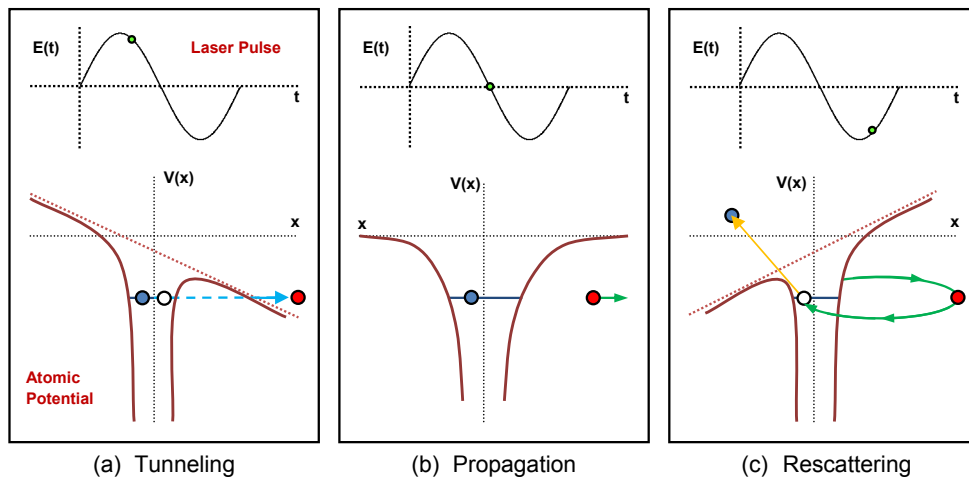


Figure 5.5: Schematic diagram showing the Corkum [31] rescattering proposal when an intense laser interacts with an atom or ion. (a) The intense laser field distorts the atomic potential enabling a bound electron to escape the atom via tunneling ionization. (b) The electron is then accelerated away from the core by the intense electric field of the laser. (c) After a  $\frac{1}{2}$  cycle the E-field of the laser reverses direction and the electron is driven back towards the origin where it can collide with the core. On recollision, the electron may do one of three things. (i) It may recombine with the parent atom to produce a high energy photon (high order harmonic generation [33]). (ii) The electron may scatter inelastically with the core, liberating another bound electron (*illustrated here*). (iii) Or the electron may pass through the core without any interaction and be detected as an ATI peak in the photoelectron spectrum. The green dot represents the approximate position on the  $E(t)$  plot of the laser pulse where each step in the rescattering process takes place.

strong polarization dependence of the non-sequential ionization process observed in the work of Walker *et al.* [17] when using circularly as opposed to linearly polarized light. They found that the circular polarization of the laser field introduced a small transverse drift velocity which prevented the electron from returning to the origin. The effect of circular polarization therefore acts to “*quench the non-sequential process*” [29]. In a simple classical picture one can view the rescattering collisional probability to be reduced in the case of circular polarization since the returning electron wave will be maximum away from the nuclear core it ‘orbits’ while in the linear polarization case it will have strong overlap with it.

### 5.2.1.2 The Electron Shake-Off Model

Another possible mechanism which may occur is the electron shake-off model from Fittinghoff *et al.* [28]. The absorption of one (or many) optical photons can ini-

tially liberate a single inner-shell electron (equation 5.7). The sudden loss of this inner-shell electron creates an imbalance in the potential experienced by the other valence electrons and leaves the ion in an excited state lying above the lowest ionization potential of the ion. The state relaxes by the emission of one or more (usually) valence electron so called autoionization or Auger decay. This is the typical case for single-photon double- (or multiple-) ionization and is often called the electron shake-off model.



This is the general case in those atoms where electron correlation is weak and so the photon is unable to act simultaneously and separately on each of the electrons, i.e., before one electron leaves the other one relaxes and the photoelectron emission is followed almost immediately by Auger electron emission. However, the Corkum model [31] is now generally accepted as the most applicable in the case of the interaction of optical and infrared lasers with atoms, molecules and other small quantum systems.

## 5.2.2 Case II: High-Energy Photons ( $h\nu \geq 20 \text{ eV}$ )

When an intense beam of high-energy photons like that of the FEL at the FLASH facility impinges on an atom there are enormous number of photons streaming through the atomic diameter. In the context of the EUV FEL at FLASH, the moderate focusing of the FEL beam (spot diameter  $\approx 100 \mu\text{m}$ ) can easily yield an irradiance of up to  $10^{13} \text{ W/cm}^2$ . In this intensity region and at these EUV wavelengths, the Keldysh parameter ( $\gamma$ , see equation 5.6 on page 175) is quite large ( $\gamma \gg 1$ ) which places the experiment firmly into the multiphoton (and ATI) regime. Within this space, multi-electron ionization of atoms occurs in a slightly different manner to that discussed in the low-photon energy regime. The  $\text{He}^{2+}$  yield reported by Walker *et al.* [17] (figure 5.4) was attributed to a non-sequential process whereby the primary photoelectron was accelerated in the laser field, and subsequently driven back to the vicinity of the parent ion when the laser field switched direction. This rescattering model proposed by Corkum [31] is now widely accepted as just one of the processes by which an intense (low-photon energy) laser can induce double-ionization. But this ionization scheme requires that the electron tunnels through the

potential barrier induced by the intense laser field, a process which is not possible when the ponderomotive potential is weak in comparison to the ionization potential of the atom (i.e., the Keldysh parameter is very large).

Figure 5.6 illustrates the single-ionization and two additional double-ionization channels which are the dominant processes involved in the ionization of rare gas atoms when using 50 eV ( $\sim 25$  nm) photons, a typical operational wavelength of the EUV FEL at FLASH.

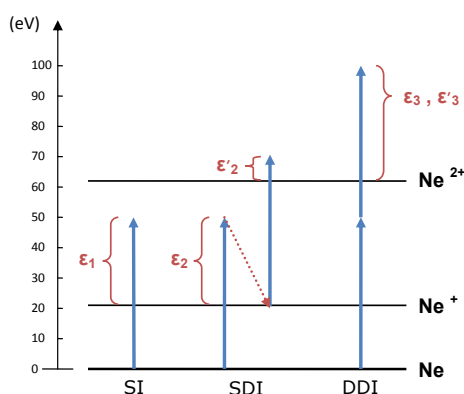


Figure 5.6: Simplified energy level diagram showing the dominant channels involved in the ionization of neon atoms by 50 eV ( $\sim 25$  nm) photons. On the left-hand side shows the single ionization of neon via the direct one-photon absorption channel. The kinetic energy of the ejected electrons ( $\epsilon_1$ ) is approximately 28.5 eV. The middle process illustrates the sequential double ionization (SDI) scheme in neon. The absorption of a single EUV photon ionizes the neon atom and ejects a photoelectron with a kinetic energy ( $\epsilon_2$ ) of 28.5 eV. In a second step, the Ne<sup>+</sup> ion absorbs another EUV photon resulting in Ne<sup>2+</sup> and another photoelectron ( $\epsilon'_2 = 9$  eV). The direct double ionization (DDI) channel is illustrated on the right-hand side of the figure. The simultaneous absorption of two EUV photons leads to Ne<sup>2+</sup> and the simultaneous ejection of two electrons. The excess energy ( $E_k = 37.5$  eV) is shared between the two photoelectrons ( $\epsilon_3$  and  $\epsilon'_3$ ).

In figure 5.6 neon was chosen as the example target along with an EUV photon (25 nm or 50 eV) because they correspond nicely with the results on the photoionization of rare gases that are presented in Chapter 7. On the left-hand side of figure 5.6 the single ionization of neon via the direct one-photon absorption channel is illustrated. This produces a photoelectron with a kinetic energy of approximately 28.5 eV. The sequential double ionization (SDI) scheme is shown in the center of the figure. As mentioned previously, this is a two step process whereby the absorption of one EUV photon will directly ionize the atom and yield a photoelectron with a kinetic energy of 28.5 eV. In the second step, the Ne<sup>+</sup> ion absorbs another EUV photon

which results in  $\text{Ne}^{2+}$  and the ejection of another photoelectron ( $E_k = 9 \text{ eV}$ ). The final ionization scheme illustrated in figure 5.6 is direct double ionization (DDI). The simultaneous absorption of two EUV photons leads to  $\text{Ne}^{2+}$  and the simultaneous ejection of two electrons. The excess energy ( $2 \times 50 \text{ eV} - 62.5 \text{ eV} = 37.5 \text{ eV}$ ) is shared between the two photoelectrons.

These observations lead one to conclude that there is no one specific mechanism for double-ionization. Double-ionization may occur through a multi-photon interaction either via the shake-off model [28] or the recollision model [31]. These two processes (where the Corkum model is generally accepted as being the most applicable) are specific to intense laser systems which have low photon energies, (e.g., Ti:Sapphire:  $800 \text{ nm} = 1.55 \text{ eV}$ ; Nd:YAG:  $1064 \text{ nm} = 1.17 \text{ eV}$  or  $355 \text{ nm} = 3.5 \text{ eV}$ ). Furthermore, in the regime of intense EUV lasers, double-ionization can occur through two main processes: (i) Direct-double ionization (DDI), when the ejection of a pair of electrons occurs through the absorption of a single EUV photon. Electron correlations are important in this case [38]. Or (ii), via sequential double ionization (SDI), where the absorption of a single EUV photon ejects a core electron. This leaves behind a inner-shell hole that can then be filled by an outer shell electron, the excess energy (virtual photon) subsequently ionizing a valence electron. This is characteristically an Auger process. A more detailed discussion on this topic can be found in the review articles from Di Mauro & Agostini [29] and Becker *et al.* [37]. All-in-all, strong-field two-electron ejection still remains a largely open question and the reader is directed towards an enlightening discussion by Charalambidis *et al.* [39]. In the next section a second possible step, that of further ionization caused by the interaction of the electron in the continuum with the oscillating laser field will be introduced.

### 5.3 Two-Color Above-Threshold Ionization

The previous section dealt with the interaction of a single laser with an atom. This discussion was divided into to subsections concerning ionization using either an intense table-top system (Nd:YAG or Ti:Sapphire) or the EUV FEL at FLASH. In this section the interaction of two independent photon sources with an atom will be described. The combination of two photon sources opens up the possibility to examine a new realm of experiments. In what is called the pump-probe scheme, two independent lasers are used to first prepare an atom or molecule to desired state, after which the second photon can be used to interrogate, induce or even

assist in a secondary photo-process. The pump-probe scheme allows the study of transitions between states which are forbidden by a single photon process because of dipole selection rules. The versatility of this setup also permits the study of atomic and molecular dynamics within timescales limited only by the temporal jitter between the two sources. The work presented in this thesis is based on the two-color photoionization of rare gas atoms using a combination of extreme ultra-violet (EUV) and intense infrared (IR) photons.

The laser-induced coupling of continuum states is of major interest in the field of intense laser interactions with atoms. Transitions between continuum states are known as free-free transitions [40]. Free-free transitions play a central role in the heating of plasmas by electromagnetic radiation (*inverse-Bremsstrahlung*, refer to section 1.4) and so the study of such systems is important in both the laser-atom and laser-solid interactions presented in this thesis. But the probing of these continuum states was quite challenging before the invention of fast (and sufficiently intense) laser systems and bright synchrotron sources.

Of special interest to the work in this thesis is the laser coupling of continuum states in rare gas atoms using the pump-probe method. In our case, an EUV photon from the free-electron laser (the pump) causes a photoionization event and ejects an electron from an atom (or ion) into the continuum. A second photon from an intense time-synchronized NIR laser (the probe) subsequently interrogates this free electron and induces a transition to another continuum state. In 1996, Glover *et al.* [41] investigated laser-induced transitions between two continuum states using a combination of EUV photons produced by high-harmonic generation and NIR photons from an intense femtosecond laser (Ti:Sapphire). They firstly ejected an electron into the continuum via multiphoton ionization. This ejected photoelectron was born into the intense field of the time-synchronized optical laser which ‘dressed’ the system and exchanged photons with the dressing field via stimulated emission (or absorption) which resulted in a comb of sidebands disposed on both sides of the main photoelectron line separated by  $\hbar\omega_L$ , the photon energy of the optical laser.

The energy of the ejected electrons is given (in atomic units) by [42]

$$E = \hbar\omega_X \pm n\hbar\omega_L - I_p - U_p \quad (5.9)$$

where  $\hbar\omega_X$  and  $\hbar\omega_L$  is the energy of the EUV and optical laser photons respectively,  $n$  is the number of photons absorbed/emitted,  $I_p$  is the ionization potential of the atom and  $U_p$  is the ponderomotive shift induced by the intense laser field. The

number and magnitude of the sidebands depends on the intensity of the dressing field. The presence of the dressing field also acts to shift the mean energies of the peaks due to the ponderomotive potential which acts to shift the ionization limit (from the point of view of the bound electrons) of the parent atom (see equation 5.4 on page 172).

However the use of EUV photons produced by high-harmonic generation as the pump beam in this way had one inherent limitation. Analysis of the photoelectron spectra produced using high harmonic EUV sources becomes complicated by contributions from the many harmonics in the pump beam. Since the harmonics and dressing field were derived from the same laser, the primary photoelectrons and secondary dressed-electrons are phase related. The photoelectron sidebands will appear between the odd harmonics, with the upper sideband of one overlapping with the lower sideband of the next. Since one cannot separate the individual contributions, and since they are phase coherent, in fact these two photoelectron states interfere in a manner analogous to the classic Young's double slit experiment. At high dressing field intensities, many harmonically related sidebands appear and so the intensity of one sideband is now composed of many interfering pathways, in effect it becomes the analogue of the 'N' slit experiment where N is the number of interfering sidebands.

In the work presented in this thesis the unique properties of the Free Electron Laser in Hamburg (FLASH) have been used to perform the first study of the polarization dependence of photoelectron sidebands in the interference-free regime.

It was observed that the intensity and number of the sidebands depends critically on the temporal and spatial overlap of the pump and probe beams and also on the intensity and relative angle between the linear polarization vectors of the optical laser and EUV field. In the simple case (see figure 5.7 left-hand side), where the NIR laser is set to low intensity ( $\sim 10^{11}$  W/cm<sup>2</sup>) only two photons, one EUV photon from the free-electron laser and one NIR photon from the laser are necessary to generate a single sideband on either side of the He 1s photoline. This sideband can then be described by a two-photon process, ionization by an EUV photon followed by the subsequent ATI event caused by the NIR photon. In the case of helium, the magnitude of this single sideband is determined by a superposition of both  $\epsilon s$  and  $\epsilon d$  electron waves.

If the intensity of the optical laser is increased to  $10^{12}$  W/cm<sup>2</sup> or above (see figure 5.7 right-hand side) multiple sidebands will appear in the photoelectron spectrum.

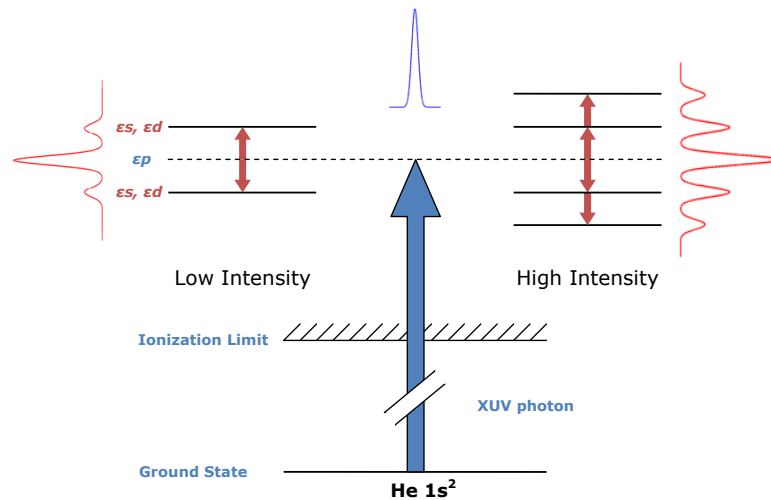


Figure 5.7: Simplified energy level diagram illustrating the two-color above-threshold ionization (ATI) of the helium 1s electron using a combination of 13.7 nm and 800 nm photons from the FEL and optical laser respectively. The scheme for low-intensity ( $\sim 10^{10}$  W/cm<sup>2</sup>) and high-intensity ( $\sim 10^{12}$  W/cm<sup>2</sup>) of the optical dressing field are on the left and the right-hand side of the figure respectively [7].

The increased intensity means that the probability of an electron absorbing (or emitting) more than one photon while in this dressing field is quite high and so multiple photoelectron sidebands are produced. In contrast to the simple two-photon case, the sidebands are now composed of a more complex mixture of electrons which have either even (*s, d, g, ...*) or odd (*p, f, h, ...*) symmetries. It is also worth emphasizing that as the sideband intensity increases, the intensity of the main photoline decreases, i.e., electrons in the main photoline are redistributed to the sidebands by the optical dressing field. The total ionization yield remains constant as the optical laser does not contribute to the initial photoionization step.

Part of the work on photoionization of atoms using the intense beam from the EUV FEL was focused on the determination of the relative contributions that each outgoing electron wave makes to the overall amplitude of the sidebands. The specific case of helium where photoionization originates from the *s*-shell and where the electron is promoted to an  $\epsilon p$  state in the helium photoionization continuum was examined. Free-free transitions are induced by the optical dressing field between this  $\epsilon p$  state to either  $\epsilon s$  or  $\epsilon d$  states ( $\Delta l = \pm 1$ ). In order to map the angular distribution of the photoelectrons and to determine the relative contribution each channel makes to the overall magnitude of the sideband, the polarization vector of the optical laser was rotated with respect to the fixed plane of polarization EUV

FEL fiend. With the aid of theoretical calculations by Grum-Grzhimailo [7] it was possible to connect these measurements to the angular distributions of the photoelectrons and determine the relative contribution which the two ionization channels make to the formation of the sidebands.

The experimental work at FLASH has also been compared to a theoretical model due to Maquet *et al.* [43] which can be used to compare the magnitude of the sidebands to experiment, described in detail in section 7.2.2. Briefly, the model is based on the ‘soft-photon’ approximation developed by Kroll and Watson [44] for their study of laser-assisted potential scattering (*inverse-Bremsstrahlung*). The main result of the model can be summarized using a single equation. The model reveals that the differential cross-section for the exchange of  $n$  laser photons of frequency  $\omega_L$  together with the absorption of the EUV photon  $\omega_x$  is given by

$$\frac{d\sigma^{(n)}}{d\theta} = J_n^2(\alpha_0 \cdot \mathbf{K}) \left( \frac{d\sigma^{(0)}}{d\theta} \right) \quad (5.10)$$

where  $\alpha_0 = \mathbf{F}_{0L}/(\omega^2)$  is the classical excursion vector of a free electron embedded within the laser field with amplitude  $\mathbf{F}_{0L}$  and  $\mathbf{K} = \mathbf{k} - \mathbf{k}_0$  is the momentum transfer, with  $\mathbf{k}_0$  the wave vector of the incoming electron.  $\mathbf{k}$  is the wave-vector of the dressed electron in the final state. The quantity on the extreme right is the one-photon (EUV) cross-section in the absence of the optical dressing field. In general terms, this approximation holds if the inequality  $|\alpha_0 \cdot \mathbf{K}/n| < 1$  is true, i.e. if the intensity of the NIR laser is relatively low.

The effect of the dressing field on the ejected electron is entirely contained within the Bessel function and the exchange of the laser photons appears through the factor  $(\alpha_0 \cdot \mathbf{K})$ . This results in the modulation of the one-photon cross-section through the absorption or stimulated emission of optical photons. The intensity dependence of the sidebands on the angle between the linear polarization vectors of the FEL and optical laser fields was also nicely simulated by the soft-photon approximation.

A detailed description of the experimental apparatus including a brief overview of the free-electron laser will be presented in the next chapter. Results from the work at the FLASH facility and a more detailed description of the soft-photon approximation will be presented in Chapter 7.

# Bibliography

- [1] P. Agostini, F. Fabre, G. Mainfray, G. Petite, and N. K. Rahman. Free-free transitions following six-photon ionization of xenon atoms. *Physical Review Letters*, 42(17):1127–1130, 1979.
- [2] A. McPherson, G. Gibson, H. Jara, U. Johann, T. S. Luk, I. A. McIntyre, K. Boyer, and C. K. Rhodes. Studies of multiphoton production of vacuum-ultraviolet radiation in the rare gases. *Journal of the Optical Society of America B*, 4, 1987.
- [3] J. H. Posthumus, K. Codling, L. J. Frasinski, and M. R. Thompson. The field-ionization, coulomb explosion of diatomic molecules in intense laser fields. *Journal of Physics B: Atomic, Molecular and Optical Physics*, 29:5811–5829, 1996.
- [4] M. Murnane, H. Kapteyn, M. Rosen, and R. Falcone. Ultrafast X-ray pulses from laser-produced plasmas. *Science*, 251(4993):531 – 536, 1991.
- [5] W. Ackermann. Operation of a free-electron laser from the extreme ultraviolet to the water window. *Nature Photonics*, 1(6):336, 2007.
- [6] F. J. Wuilleumier and M. Meyer. Pump probe experiments in atoms involving laser and synchrotron radiation: An overview. *Journal of Physics B: Atomic, Molecular and Optical Physics*, 39:425, 2006.
- [7] M. Meyer, D. Cubaynes, D. Glijer, J. Dardis, P. Hayden, P. Hough, V. Richardson, E. T. Kennedy, J. T. Costello, P. Radcliffe, S. Dusterer, A. Azima, W. B. Li, H. Redlin, J. Feldhaus, R. Taieb, A. Maquet, A. N. Grum-Grzhimailo, E. V. Gryzlova, and S. I. Strakhova. Polarization control in two-color above-threshold ionization of atomic helium. *Physical Review Letters*, 101(19):193002, 2008.
- [8] Th. Dohrmann, A. von dem Borne, A. Verwey, B. Sonntag, M. Wedowski, K. Godehusen, and P. Zimmermann. Linear dichroism in the core-resonant

- photoelectron spectra of laser-aligned Cr atoms. *Journal of Physics B: Atomic, Molecular and Optical Physics*, 29(23):5699–5710, 1996.
- [9] A. von dem Borne, T. Dohrmann, A. Verweyen, B. Sonntag, K. Godehusen, and P. Zimmermann. Dichroism in the  $3p$  photoionization of polarized Cr atoms. *Physical Review Letters*, 78(21):4019–4022, 1997.
- [10] K. Godehusen, P. Zimmermann, A. Verweyen, A. von dem Borne, Ph. Wernet, and B. Sonntag. A complete photoionization experiment with polarized atoms using magnetic dichroism and phase tilt measurements. *Physical Review A*, 58(5):R3371–R3374, 1998.
- [11] A. Einstein. Über einen die erzeugung und verwandlung des lichtetes betreffenden heuristischen gesichtspunkt. *Annals of Physics*, 17, 1905.
- [12] G. S. Voronov and N. B. Delone. Multiphoton ionization of xenon atoms by radiation from a ruby laser. *Zhurnal Eksperimental'noi i Teoreticheskoi Fiziki*, 50(1):78–84, 1966.
- [13] F. W. Byron and Charles J. Joachain. Multiple ionization processes in helium. *Physical Review*, 164(1):1–9, 1967.
- [14] A. L'Huillier, L. A. Lompre, G. Mainfray, and C. Manus. Multiply charged ions induced by multiphoton absorption processes in rare-gas atoms at  $1.064\mu\text{m}$ . *Journal of Physics B: Atomic, Molecular and Optical Physics*, 16:1363–1381, 1983.
- [15] P. Agostini, J. Kupersztych, L. A. Lompré, G. Petite, and F. Yergeau. Direct evidence of ponderomotive effects via laser pulse duration in above-threshold ionization. *Physical Review A*, 36(8):4111–4114, 1987.
- [16] P. B. Corkum, N. H. Burnett, and F. Brunel. Above-threshold ionization in the long-wavelength limit. *Physical Review Letters*, 62(11):1259–1262, 1989.
- [17] B. Walker, B. Sheehy, L. F. DiMauro, P. Agostini, K. J. Schafer, and K. C. Kulander. Precision measurement of strong field double ionization of helium. *Physical Review Letters*, 73(9):1227–1230, 1994.
- [18] P. Agostini and G. Petite. Photoelectric effect under strong irradiation. *Contemporary Physics*, 29(1):57–77, 1988.

- [19] R. N. Compton, J. C. Miller, A. E. Carter, and P. Kruit. Resonantly enhanced multi-photon ionization of xenon - photoelectron energy analysis. *Chemical Physics Letters*, 71(1):87–90, 1980.
- [20] P. Lambropoulos and P. Zoller. Autoionizing states in strong laser fields. *Physical Review A*, 24(1):379–397, 1981.
- [21] H. G. Muller, P. H. Bucksbaum, D. W. Schumacher, and A. Zavriyev. Above-threshold ionization with a two-colour laser field. *Journal of Physics B: Atomic, Molecular and Optical Physics*, 23(16):2761–2769, 1990.
- [22] K. Burnett, V. C. Reed, and P. L. Knight. Atoms in ultra-intense laser fields. *Journal of Physics B: Atomic, Molecular and Optical Physics*, 26(4):561–598, 1993.
- [23] P. Lambropoulos, L. A. A. Nikolopoulos, M. G. Makris, and Andrej Mihelić. Direct versus sequential double ionization in atomic systems. *Physical Review A*, 78(5):055402, 2008.
- [24] P. Kruit, J. Kimman, H. G. Muller, and M. J. van der Wiel. Electron spectra from multiphoton ionization of xenon at 1064, 532, and 355 nm. *Physical Review A*, 28(1):248–255, 1983.
- [25] L. V. Keldysh. *Soviet Physics*, 10(1307), 1965.
- [26] N. B. Delone and V. P. Krainov. Tunneling and barrier-suppression ionization of atoms and ions in a laser radiation field. *Uspekhi Fizicheskikh Nauk*, 168(5):531–549, 1998.
- [27] J. Weiner, P. T. Ho, and W. T. Hill. *Light-matter interaction*. Berlin, 2006. pg. 55.
- [28] D. N. Fittinghoff, P. R. Bolton, B. Chang, and K. C. Kulander. Observation of nonsequential double ionization of helium with optical tunneling. *Physical Review Letters*, 69(18):2642–2645, 1992.
- [29] L. F. DiMauro and P. Agostini. Ionization dynamics in strong laser fields. *Advances in Atomic, Molecular, and Optical Physics*, 35, 1995.
- [30] I. S. Aleksakhia, I. P. Zapesochuyi, and V. V. Surau. The process of double multi-photon ionization of the strontium atom. *Pis'ma v Zhurnal Eksperimental'noi i Teoreticheskoi Fiziki*, 26(1):14–16, 1977.

- [31] P. B. Corkum. Plasma perspective on strong field multiphoton ionization. *Physical Review Letters*, 71(13):1994–1997, 1993.
- [32] M. Lein. Molecular imaging using recolliding electrons. *Journal of Physics B: Atomic, Molecular and Optical Physics*, 40(16):R135–R173, 2007.
- [33] A. L’Huillier, P. Balcou, S. Candel, K. J. Schafer, and K. C. Kulander. Calculations of high-order harmonic-generation processes in xenon at 1064 nm. *Physical Review A*, 46(5):2778–2790, 1992.
- [34] J. L. Krause, K. J. Schafer, and K. C. Kulander. High-order harmonic generation from atoms and ions in the high intensity regime. *Physical Review Letters*, 68(24):3535–3538, 1992.
- [35] K. J. Schafer, B. Yang, L. F. DiMauro, and K. C. Kulander. Above threshold ionization beyond the high harmonic cutoff. *Physical Review Letters*, 70(11):1599–1602, 1993.
- [36] G. G. Paulus, W. Becker, W. Nicklich, and H. Walter. Rescattering effects in above-threshold ionization - A classical-model. *Journal of Physics B: Atomic, Molecular and Optical Physics*, 27(21):L703–L708, 1994.
- [37] W. Becker, F. Grasbon, R. Kopold, D. B. Milosevic, G. G. Paulus, and H. Walther. Above-threshold ionization: From classical features to quantum effects. In *Advances in atomic, molecular and optical physics*, volume 48 of *Advances in atomic, molecular and optical physics*, pages 35–98. 2002.
- [38] V. Schmidt, N. Sandner, H. Kuntzemüller, P. Dhez, F. Wuilleumier, and E. Källne. Double ionization of rare gases II: Ion formation by photon impact. *Physical Review A*, 13(5):1748–1755, 1976.
- [39] D. Charalambidis, P. Lambropoulos, H. Schröder, O. Faucher, H. Xu, M. Wagner, and C. Fotakis. Settling a long-standing question on strong-field double ionization. *Physical Review A*, 50(4):R2822–R2825, 1994.
- [40] A. Weingartshofer, E. M. Clarke, J. K. Holmes, and C. Jung. Experiments on multiphoton free-free transitions. *Physical Review A*, 19(6):2371–2376, 1979.
- [41] T. E. Glover, R. W. Schoenlein, A. H. Chin, and C. V. Shank. Observation of laser assisted photoelectric effect and femtosecond high order harmonic radiation. *Physical Review Letters*, 76(14):2468–2471, 1996.

- [42] A. Bouhal, R. Evans, G. Grillon, A. Mysyrowicz, P. Breger, P. Agostini, R. C. Constantinescu, H. G. Muller, and D. von der Linde. Cross-correlation measurement of femtosecond noncollinear high-order harmonics. *Journal of the Optical Society of America B: Optical Physics*, 14:950–956, 1997.
- [43] Maquet A. and Taieb R. Two-colour IR+XUV spectroscopies: the ‘soft-photon approximation’. *Journal of Modern Optics*, 54(13-15):1847–1857, 2007.
- [44] N. M. Kroll and K. M. Watson. Charged-particle scattering in the presence of a strong electromagnetic wave. *Physical Review A*, 8(2):804–809, 1973.

## Chapter 6

# Experimental Systems and Procedures II

The Free Electron LASser in Hamburg (FLASH) is just one of a new type of fourth generation light sources which unite the benefits of both linear accelerator and synchrotron based technologies. The goal of FLASH is to combine peak brilliance with high average flux. A key milestone in the extreme ultraviolet (EUV) and X-ray FEL road-map at DESY, and a world record, was achieved in June 2006 when FLASH produced saturated laser-like radiation at 13.7 nm, with the 5th harmonic of the fundamental ( $\lambda = 2.75$  nm) lying within the all-important water-window. This was a first for free electron laser based technology with the latter wavelength shorter than any produced to date by other light sources [1, 2]. The blue colored points in figure 6.1 represent the first experimental confirmation of what had been up to then only peak brilliance predictions (*red lines*) and demonstrated the leap taken by FLASH compared to other conventional sources.

By accelerating free electrons to relativistic speeds in linear accelerators and injecting them into long undulators, tunable laser-like radiation which is extremely bright, coherent, polarized and of ultra-short pulse duration is produced. FELs can produce radiation with wavelengths from millimeters to  $< 1$  nm (the soft X-ray spectral region) with pulse durations of below 100 fs. Brilliance<sup>1</sup>, coherence and timing down to the femtosecond regime are the three properties which provide the potential for new science. These parameters make FLASH an ideal source for the study of nonlinear experiments in the EUV region. While there is a long list of various

---

<sup>1</sup>The absolute spectral brilliance of a source B is defined as the number of photons N per time interval  $t$ , solid angle  $\Delta\Omega$ , source area A, and  $10^{-3}$  relative bandwidth (BW)  $\Delta\nu/\nu$  in units of  $(\text{s} \times \text{sr} \times \text{mm}^2 \times 0.1\% \text{ BW})^{-1}$  [3].

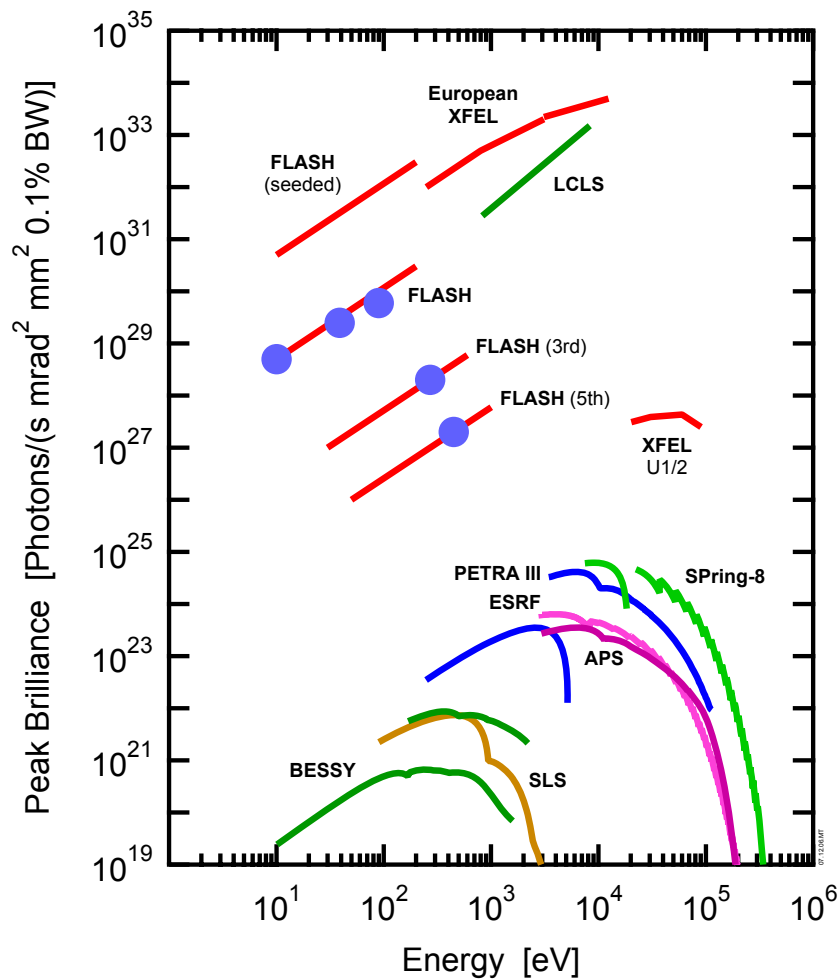


Figure 6.1: Peak brilliance of EUV and X-ray FELs versus 3rd generation synchrotron light sources. Blue points indicate the first ever measured values of the peak brilliance of FLASH for fundamental and harmonic emission [1].

subjects under study at FLASH [4, 5], of interest to our collaboration is the study of one- and multi-photon ionization of rare gases, two-color (FLASH and IR laser) above-threshold ionization and time-resolved pump-probe experiments.

The author of this thesis was part of the pump-probe collaboration (Meyer, Feldhaus, Costello; CNRS, DESY, DCU) that played a key role in the recording of the 3rd and 5th harmonics of the FEL beam in 2006 [2]. The author was also centrally involved with the initial synchronization of the 800 nm Titanium:Sa laser (800 nm, 120 fs pulse length) with the EUV pulse (6 – 40 nm,  $\leq 20$  fs pulse length)

from FLASH. In particular, the author developed a fast photodiode based detector system [6] for monitoring the time delay between the EUV and optical pulses on a picosecond (coarse tuning) timescale at the point of interaction in the experimental chamber. The author also played a key role in setting up and carrying out experiments and analyzing resulting data to determine the time delay/jitter between these pulses on a femtosecond timescale [6, 7] and to elucidate the polarization dependence of the sidebands [8].

This section begins with a brief introduction to the operation of the free electron laser in Hamburg. The main components of the experimental setup used for the photoionization experiments will be presented, with particular attention being paid to the systems which were used to characterize the temporal and spatial overlap between the optical laser and the EUV FEL beam.

## 6.1 The Free Electron Laser in Hamburg

At the free electron laser in Hamburg (FLASH), laser amplification and saturation occurs within a single pass of an electron bunch, moving at relativistic velocity, through an undulator. The lasing process is initiated by spontaneous undulator radiation in an amplified spontaneous emission (ASE) process. The term self-amplified spontaneous emission (SASE) is often used when discussing short-wavelength FELs, which serves to highlight the fact that amplification occurs in the same device which produced the spontaneous emission. This single-pass design dispenses with the need for an oscillator type system with mirrors and allows unprecedented peak powers to be generated at soft X-ray wavelengths.

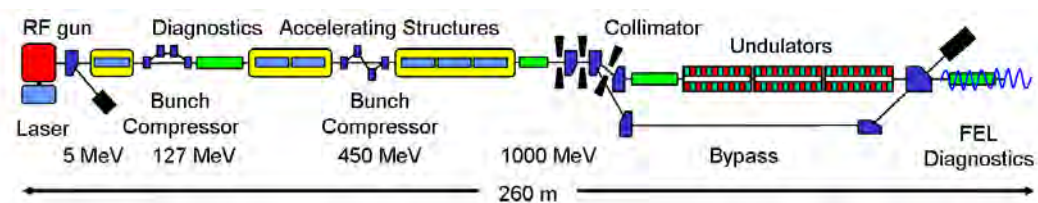


Figure 6.2: Schematic diagram of the layout of the EUV-FEL beamline at the FLASH facility (after [9]).

A schematic diagram of the layout of the EUV-FEL beamline at FLASH is shown [9] in figure 6.2. The RF gun which produces the initial electron bunches, the bunch compressor system which compresses the electron bunches longitudinally during their flight and the accelerating modules which accelerate the bunch up

to an energy of 1 GeV comprise the linear accelerator or LINAC section of the system. Radiation is generated in the undulator module where a periodic magnetic field produced by alternating north-south permanent magnet pole pieces sets the electron bunches into an oscillatory (or slalom type) motion as they travel through its length.

### **6.1.1 The Photoinjector**

The initial electron bunches are created when a photocathode in the photoinjector is irradiated with a train of laser pulses (pulse duration: 10 ps) from a neodymium: yttrium-lithium-fluoride (Nd:YLF) laser. The pulsed UV laser is synchronized to the radio-frequency signal that drives the linear accelerators with a precision greater than 100 femtoseconds [9]. The photocathode is positioned inside a radio-frequency (RF) cavity which creates an initial accelerating field of a few MV/m with a peak beam current at this point of typically 50 A.

### **6.1.2 Electron Acceleration & Bunch Compression**

The electron bunches are accelerated in the linear accelerator (LINAC) to relativistic velocities as quickly as possible, preventing the electrons in the bunch from drifting apart due to the mutual repulsion between the negative charges. At relativistic velocities the repulsive forces between the negatively charged electrons are canceled by the attractive magnetic forces between the parallel currents generated by the moving charge. The electron bunches are accelerated to GeV energies in a sequence of five 12 meter long super-conducting accelerator modules. The electron bunches traveling at near the speed of light are compressed longitudinally by two magnetic chicanes located at regular intervals between the five accelerator modules (see figure 6.2). The bunch compression system [9, 10] works in two ways: Firstly, the phase of the RF pulse driving the accelerating modules is adjusted so that the electron bunch is accelerated on the rising edge of the pulse. This gives the electrons positioned in the tail of the bunch a slight increase in energy compared to those at the front of the bunch. Secondly, as the electrons travel through the chicane this energy difference means that the force acting on the electrons by the magnetic field will be different. The higher energy electrons in the rear of the bunch experience a larger force which results in them traveling through each of the corners of the chicane at a smaller radius, thereby traveling a shorter distance overall than those at the front of the bunch. At the exit of the chicane, the electrons

positioned at the tail of the bunch will have caught up with those at the front. What results is an electron bunch containing a narrow leading spike with a width of less than 100 femtoseconds containing approximately 10% – 20% of the total bunch charge which is followed by the remaining part of the bunch spread out over a few picoseconds in duration. This leading spike provides the high peak currents (peak current = 2 kA) necessary to initiate the SASE process in the undulator, while the long tail does not possess sufficient beam current to expect any significant FEL gain.

### 6.1.3 The Undulator

The 1 nC bunch exiting the LINAC enters the 30 m long undulator, having been accelerated to  $\sim 1$  GeV, and compressed longitudinally during its flight. As the relativistic bunch traverses the periodic magnetic field of the undulator (12 mm pole-to-pole separation, period length of  $\lambda_u = 27.3$  mm and a peak magnetic field of  $B_u = 0.47$  T) they are forced to travel in an oscillatory path. The electrons begin to emit radiation in a narrow bandwidth around a resonance wavelength  $\lambda_{FEL}$  given by [1]

$$\lambda_{FEL} = \frac{\lambda_u}{2\gamma^2} \left( 1 + \frac{K^2}{2} \right) \quad (6.1)$$

where  $\lambda_u$  is the undulator period in millimeters,  $K = eB_u\lambda_u/2\pi m_e c$  is the undulator parameter,  $B_u$  is the rms value of the undulator field in Tesla, and  $\gamma = \frac{E}{m_e c^2}$  is the relativistic factor.

### 6.1.4 FEL Radiation

The key to the SASE-FEL process is the interaction of the electrons with the radiation field generated in the undulator. As the electrons travel through the undulator on their oscillatory trajectory, the transverse component of their motion will couple to the transverse electric field of the radiation. This causes an energy transfer between the electron and the light wave. In order for this to work effectively the charge density of the electron bunch has to be very high. This interaction between the electron and the radiation field leads to an instability in the electron bunch known as the 'FEL instability'. Depending on the phase of the electron with respect to the radiation field it may either be accelerated or decelerated by the field. This leads to a periodic modulation in the velocity of the bunch along the longitudinal direction

which in turn leads to a density modulation with a period equal to the wavelength of the undulator fundamental radiation ( $\lambda_{FEL}$ ).

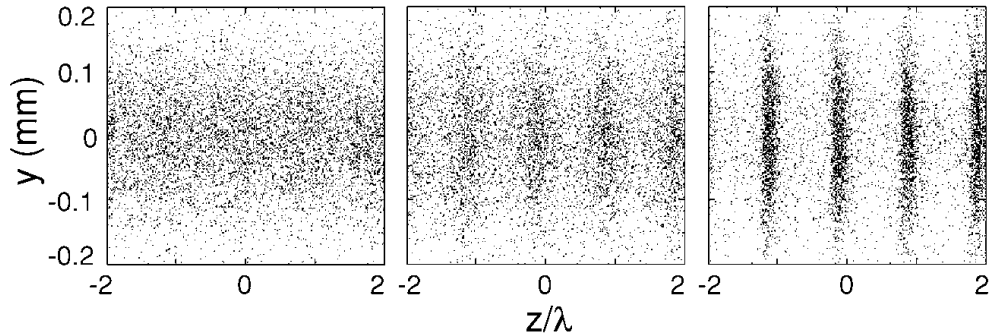


Figure 6.3: Density modulation induced in the electron bunch by the FEL instability. The electron density is represented by the density of dots. Left: density at the undulator entrance, middle: spatial profile of the electron density at the center of the exponential growth regime, right: density profile at the undulator exit [11].

The velocity and subsequently the longitudinal density of the electrons become quantized along the length of the undulator. The effect of this density modulation was simulated by Feldhaus *et al.* [11], the results of which are shown in figure 6.3. The left-hand panel in figure 6.3 shows that the density of electrons is initially distributed randomly over the length of the bunch. This corresponds to an electron bunch at the entrance to the undulator. The middle panel in figure 6.3 shows the density profile of the electron bunch when it has reached the center of the undulator. Here the density is showing the early signs of the periodic spatial modulation due to the interaction of the electron bunch with the radiation field. The right-hand panel in figure 6.3 corresponds to the bunch profile at the exit of the undulator. Here it can be seen that the electron density along the length of the bunch is deeply modulated. The effect of this micro-bunching is to cause the electrons within the injected bunch to radiate coherently. Amplification of the radiation grows exponentially along the undulator length until saturation occurs [12]. The key feature of the SASE process is that laser saturation occurs within a single pass of an electron bunch through an undulator. This eliminates the need for multiple passes and/or mirrors to form an optical cavity meaning that FELs based on the SASE principle are ideal candidates for the next generation high-gain coherent X-ray amplifiers.

The electrons exit the undulator and are deflected into a water cooled beam-dump while the EUV radiation passes through a diagnostics section at the end of the accelerator tunnel before entering the ultra-high vacuum beamlines in the exper-

Parameter	Value
Wavelength range (fundamental)	6.9 – 47 nm
Higher harmonics 3 <sup>rd</sup>	~ 2.3 nm
Higher harmonics 5 <sup>th</sup>	~ 1.4 nm
Pulse energy (average)	10 – 50 $\mu$ J
Peak power	several GW
Pulse duration (FWHM)	10 – 50 fs
Spectral width (FWHM)	0.5 – 1%
Angular divergence	$90 \pm 10$ $\mu$ rad
Peak brilliance <sup>†</sup>	$10^{29} - 10^{30}$

Table 6.1: Operational parameters of the EUV-FEL at FLASH operating in saturation at a fundamental wavelength of 30nm [9, 13]). <sup>†</sup>The peak spectral brilliance is defined as the number of photons  $N$ , per time interval  $t$ , solid angle  $\Delta\Omega$ , source area  $A$ , and  $10^{-3}$  relative bandwidth (BW)  $\Delta\nu/\nu$  and is expressed in units of  $(\text{s} \times \text{sr} \times \text{mm}^2 \times 0.1\% \text{ BW})^{-1}$ .

imental area. The radiation emitted by a SASE undulator has a narrow spectral spread (typically 0.5 - 1%) , and a very small beam divergence (typically < 1 mrad). The main parameters of FLASH are displayed in table 6.1.

The timing structure of an EUV pulse from FLASH is illustrated in figure 6.4. The FEL can be operated in single- or multi-bunch, up to a maximum of 30 micropulses per macropulse mode at a macropulse repetition rate of 5Hz or 10 Hz. For most of the experiments reported here FLASH worked in single bunch mode at a macropulse repetition frequency of 5 Hz.

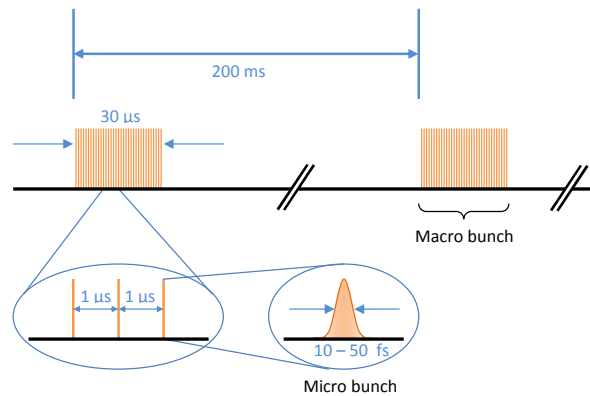


Figure 6.4: Pulse structure of the FEL radiation operating at a macropulse repetition rate of 5 Hz (after [9]). Each macrobunch of 30  $\mu$ s duration contains 30 microbunches, each separated by 1  $\mu$ s. A microbunch corresponds to a single electron bunch which in turn will produce a single pulse of EUV light of femtosecond duration.

### 6.1.5 The Experimental Hall

The FLASH experimental hall contains five beamlines with different focusing arrangements (see figure 6.5). Three beamlines (labeled BL1-3 in figure 6.5) couple the FEL radiation to the experimental end-stations, two of which provide a focused beam of  $20\ \mu\text{m}$  and  $100\ \mu\text{m}$  spot diameters respectively. The third such beamline contains no focusing optics, supplying a millimeter scale (typically  $7\ \text{mm}$ ) diameter beam. Because FLASH has an inherent bandwidth of about 1%, two additional beam-lines incorporating a high-resolution plane-grating monochromator are also available. These two beam-lines (labeled PG1 and PG2 in figure 6.5) supply the user with FEL pulses of narrower bandwidth (essentially spectrally sliced pulses with concomitantly lengthened pulse durations since FLASH can generate Fourier transform limited pulses).

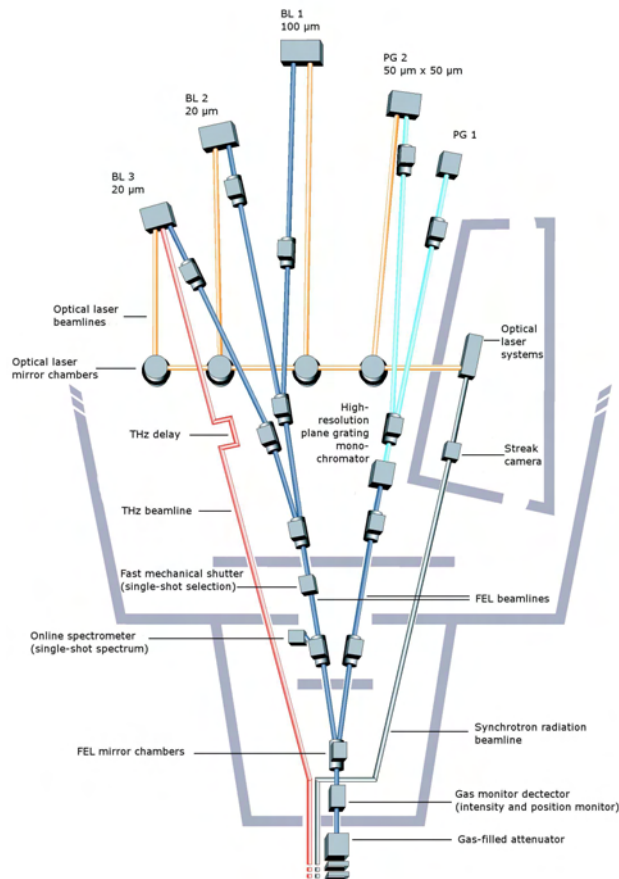


Figure 6.5: Layout of the experimental hall showing the five EUV FEL beamlines, the optical laser beamlines and the newly commissioned THz radiation beamline [14]. After [9].

A complementary optical laser system provides either intense infrared pulses from a Ti:sapphire system (1 to 20 mJ, 800 nm, 120 fs to 4 ps) or frequency doubled pulses of up to 500  $\mu$ J, 523 nm, 12 ps from a Nd:YLF laser, both of which are electronically synchronized with the FEL pulses. This laser system is located in an isolated room inside the experimental hall. Radiation from this laser is channeled down a separate set of evacuated beamlines to the experimental end-stations.

## 6.2 The Experimental Chamber

Experiments on two-color photoionization of rare gases were performed on BL2 using a combination of the EUV FEL beam and the intense optical laser (800 nm), operated at a variety of wavelengths and pulse durations. Figure 6.6 is a schematic of the experimental system located at the end-station of BL2 in the experimental hall [6]. The diagram can be broken into three main sections, the focusing optics for the pump and probe beams, the electron spectrometer and the beam characterization systems. The focusing optics for the optical laser consisted of a telescope comprising of one concave (L1) and one convex (L2) lens (*Galilean configuration*) used in conjunction with a focusing parabolic mirror. The main elements of the electron spectrometer included a magnet, retardation grids and a long flight tube terminated by either a channel electron multiplier (CEM) or a micro-channel plate (MCP) detector. An EUV spectrometer was located behind the main experimental chamber at the end of the beamline and was connected via a bellows to the main vacuum chamber. This spectrometer contained a Harada grating [15, 16] and a back-illuminated CCD camera to record the spectral distribution of the FEL beam. Also shown in the diagram is the phosphor screen, used to determine the spatial overlap of the pump and probe beams, and the photodiode used (with the gold mesh) to determine the temporal overlap of the two beams. The vacuum in the chamber was maintained by a turbo-molecular pump capable of reaching a base pressure of  $5 \times 10^{-10}$  mbar after baking [6].

The converging EUV beam from FLASH, operating at 13.7 nm (90.5 eV) was directed through a hole in the parabola and was brought to a focus in front of the entrance slit of the electron spectrometer at the centre of the vacuum chamber. The optical laser entered the experimental chamber collinearly with the FEL beam and was brought to a focus at the same position using the parabolic mirror. The polarization state of the optical laser was controlled using a half-wave plate. Both the EUV FEL and the optical laser beams were ca. 100% linearly polarized. The

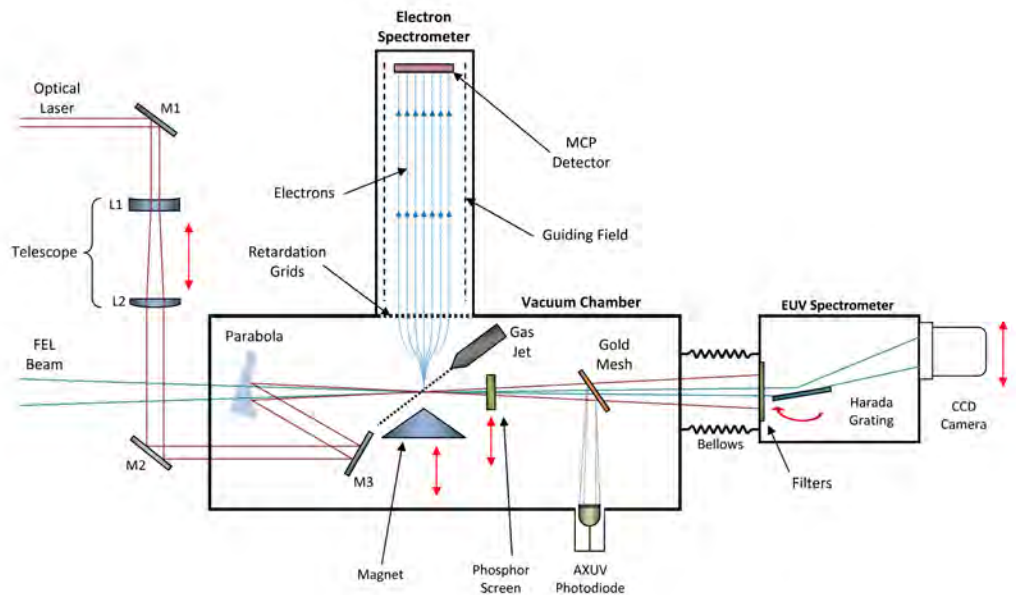


Figure 6.6: Schematic diagram of the pump-probe experimental chamber showing the main components of the experimental system. The experimental chamber was located at the end-station of BL2 in the experimental hall. The red arrows indicate the translation direction of the telescope, magnet, phosphor screen, Harada grating and CCD camera respectively [6].

diameters of the optical and FEL beams measured at this point were found to be in the region of  $50 \mu\text{m}$  and  $30 \mu\text{m}$  respectively.

A magnetic bottle electron spectrometer (MBES) [17, 18] was used to measure the kinetic energy of electrons produced in the photoionization of rare gas atoms by the EUV FEL beam. The main parts of the electron spectrometer are the extraction region, the field-free drift tube and the MCP or CEM electron detectors. Electrons produced by photoionization in the interaction region where the two laser beams overlap with the gas jet were directed towards the entrance slit of the 0.65 m long flight tube by a strong permanent magnet (0.5 T). The divergent field of the permanent magnet forms a magnetic mirror so that electrons are collected and their paths parallelized from almost the whole  $4\pi$  solid angle. A solenoid producing a weak guiding field (0.5 mT) which causes the electrons to undergo a spiral path to the micro-channel plate (MCP) detector. A time-of-flight (TOF) detection scheme allows the kinetic energies of all the photoelectrons to be measured from a single oscilloscope trace. The resolution of the spectrometer can be improved by placing electrostatic retardation fields at the entrance aperture of the flight tube. This has

the effect of reducing the energy spread of the electrons entering the flight tube. Single shot or averaged TOF spectra were recorded with the aid of a fast digital oscilloscope (LeCroy Wavemaster 8600A). The energy resolution in the electron spectra was mainly determined by the bandwidth of the FEL (0.5% – 1%) and the MBES (at best 1% – 2% of the electron kinetic energies) [6].

A gold wire mesh mounted on a moveable manipulator was positioned to interrupt the two laser beams after the interaction region. By moving the wire mesh into the center of the chamber a small fraction of the two laser beams was deflected onto a picosecond photodiode which was attached to a vacuum feed-through inside the chamber. A detailed discussion of the method to overlap the EUV FEL and optical laser beams in both time and space is presented in section 6.2.1.

A flat-field spectrometer was coupled to the end of the experimental chamber via a bellows and was used to measure the spectral content of the FEL beam. The dispersive element of the spectrometer consisted of a concave variable-line-spaced grating incorporating 1200 grooves/mm which were mechanically ruled. Spectra of the EUV FEL beam were recorded using a EUV sensitive CCD camera (ANDOR Technology, Belfast, Northern Ireland) consisting of a  $2048 \times 512$  pixel array with a  $13 \mu\text{m}$  pitch. The concave grating results in a flat focal plane which is ideal when using a flat CCD detector and this configuration was first demonstrated by Harada *et al.* in 1983 [16]. The spectrometer was operated without an entrance slit which gave a degree of spatial resolution in the direction perpendicular to the wavelength dispersion axis of the grating. As the harmonics were well separated in wavelength the reduction in spectral resolution in this mode was not a problem. The pressure in the spectrometer chamber was kept at a constant  $10^{-4}$  mbar using a 250 litre/s turbo-molecular pump. High vacuum was maintained in the primary experimental chamber through the use of a series of small diameter holes (5 mm) cut in the copper gasket plates located at each end of the bellows connecting the two chambers. This proved adequate to isolate the low ( $10^{-8}$  mbar) and high pressure ( $10^{-4}$  mbar) chambers. When a spectrum of the FEL beam was to be recorded, the beam was allowed to pass through the experimental chamber undeflected, where it was incident on the grating and the dispersed radiation was recorded on the CCD detector. The beam diameter was on the order of a few millimeters at the entrance to the spectrometer. The grating was fixed to motorized translation stages giving angular movement which was externally controlled.

One characteristic of the Harada type grating is the high efficiency in the higher orders. Thin film metal EUV filters were placed between the entrance slit and the grat-

ing to further attenuate the FEL beam before striking the grating and CCD camera and to block radiation at the fundamental wavelength thereby reducing the effect of higher order blending. A  $1.5\ \mu\text{m}$  thick aluminium filter was used to block emission from the fundamental at  $13.7\ \text{nm}$  and pass emission from the higher harmonics, while a  $3\ \mu\text{m}$  thick polypropylene (CH) filter was used for the opposite, to pass FEL radiation at the fundamental wavelength and attenuate emission from the higher harmonics. The EUV transmission profiles of both filters are presented in figure 6.7.

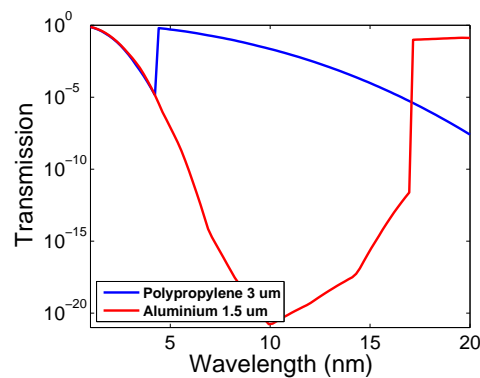


Figure 6.7: Transmission of the  $3\ \mu\text{m}$  thick polypropylene ( $\text{C}_3\text{H}_6$ ) and the  $1.5\ \mu\text{m}$  thick aluminium filters used during the experiments to determine the spectral content of the FLASH beam [19].

## Data acquisition

The various detector systems, namely the fast digital oscilloscope which recorded the photoelectron spectra (PES) and the EUV-sensitive CCD camera which recorded spectra of the FEL beam were both controlled via a LabView<sup>TM</sup> interface. This software was linked to an in-house distributed object-oriented control system (DOOCS) [20] which labeled each electron bunch with a specific timestamp (*a unique number given to each electron bunch*) and appended it to the filename. DOOCS not only assigns the individual timestamps but also stores the operational parameters for hundreds of machine critical devices and saves them to an online database. During data analysis, abnormal trends in the recorded spectra (*e.g. an unexpected decrease in a peak intensity, or shift in a peak position*) could be cross-referenced with this parameter database. During a single 12-hour shift, thousands of spectra were recorded using the electron and EUV spectrometers, and so the DOOCS system proved invaluable at helping to correlate photoelectron and EUV spectral

data with appropriate diagnostic information such as FLASH pulse energy obtained from the gas monitor detector or GMD [21].

### 6.2.1 Pump-Probe Synchronization

Critical for the two-color pump-probe experiments was the spatial and temporal overlap of the two independent beams. In two-color above-threshold experiments, the intensity of optical laser experienced by photoelectrons generated by the EUV FEL beam is greatly influenced by the extent of spatial and temporal overlap between the ionizing (EUV) and dressing (800 nm) pulses.

### Focusing

Both laser beams are brought to a focus in the center of the experimental chamber. The FEL beam is focused using an ellipsoidal mirror which has an effective focal length ( $efl$ ) of 2 m. Because the position of the focal spot of the FEL was not easily changed the focal configuration for the FEL beam was fixed for the duration of our experiments at FLASH and the focal point of the optical laser was adjusted (in three dimensions) in order to overlap it with the FEL spot. The optical laser was brought to a focus using an off-axis parabolic mirror ( $30^\circ$  off-axis,  $efl = 272$  mm, 76 mm diameter) located inside the experimental chamber. A Galilean telescope was constructed using a negative diverging lens, followed by a plano-convex lens ( $f_1 = -200$ mm and  $f_2 = 300$  mm respectively) and was placed into the path of the optical laser beam outside the chamber. This allowed control of the longitudinal position of the focal spot over the length of the interaction region inside the chamber. By changing the separation between the two lenses the divergence of the optical laser beam was altered and the point of focus was translated by up to  $\pm 1$  mm along the length of the interaction region; defined by the width of the entrance slit of the electron spectrometer (typically 30 mm). As mentioned previously, the parabolic mirror had a hole in its centre (6 mm diameter) which allowed the FEL beam to pass through in collinear geometry with the optical beam.

### Spatial Overlap

The focal spot diameters of the FEL and optical laser beams were estimated to be  $\sim 30$  and  $50 \mu\text{m}$  respectively [8]. This was determined using a moveable screen coated with Ce-YAG phosphor ( $\text{Y}_3\text{Al}_5\text{O}_{12}:\text{Ce}$ ). When EUV light was incident on the phosphor screen, the fluorescence was captured by a CCD camera coupled

to a long working distance microscope. Movement of the FEL focal position was limited, so that the optical laser was overlapped with the FEL spot by adjusting the orientation of the parabola (see figure 6.6). The parabola was adjusted until the focal spot of the optical laser was concentric with the FEL focal spot.

## Temporal Overlap

The intensity of the optical laser experienced by an electron produced in the primary ionization step is highly dependent on the temporal delay between the pump and probe beams. If the delay between the two laser pulses is large (*e.g. exceeding the pulse width of either laser beam*), then an electron will be born into the interaction region in the absence of the optical laser field. Therefore, to ensure the above-threshold ionization step takes place, one must control the delay between the FEL and optical laser pulses with femtosecond temporal resolution.

The synchronization of two independent pulses of femtosecond duration, generated by two very distinct processes on the femtosecond timescale is far from a trivial challenge. The problem was tackled in two distinct stages, the first (*a description of which is to follow*) used a fast silicon photodiode to achieve a measure of the 'overlap' to within  $\pm 25$  ps. The second step (described in section 7.1.1 on page 215) utilized a two-color cross correlation method [7] which achieved a temporal overlap with a jitter of a few hundred femtoseconds.

Long term drifts of up to  $\pm 3$  ps between the optical laser and the FEL (due in part to the variation in the arrival time of the electrons at the entrance to the undulator) were monitored by a fast streak camera (Hamamatsu C5680) with better than 1 ps (rms) resolution. The streak camera detects the bending magnet radiation which is produced when the electrons are dumped at the end of the accelerator. This broadband optical radiation pulse is inherently synchronized to the EUV FEL pulse [6]. The time delay between the two laser pulses was controlled by passing the optical laser through a variable delay stage. Coarse synchronization down to the tens of picoseconds range was achieved using a selection of high-speed EUV-sensitive p-n junction diodes supplied by International Radiation Detectors Inc. (*Torrance, California*).

These diodes were chosen because they have the advantage of being sensitive to both radiation from the FEL and the optical laser. Also, and of importance to their use with intense EUV and X-ray radiation, these diodes are radiation hardened. Three diodes were tested (see table 6.2), but only the AXUV-HS3 was selected for

Series	Sensitive area (mm <sup>2</sup> )	Package type	Risetime (ps) <sup>†</sup>
AXUV-HS4	0.026	SMA	200
AXUV-HS3	0.005	SSMA	80
AXUV-HS6	0.00063	SSMA	50

Table 6.2: High-speed EUV-sensitive photodiodes used for the coarse temporal overlap of the pump and probe beams at FLASH. Specifications are quoted for a bias voltage of 50 V [22].

use throughout the experiment. The fast rise-time and relatively large active area resulted in short-pulse detection and easy optical alignment.

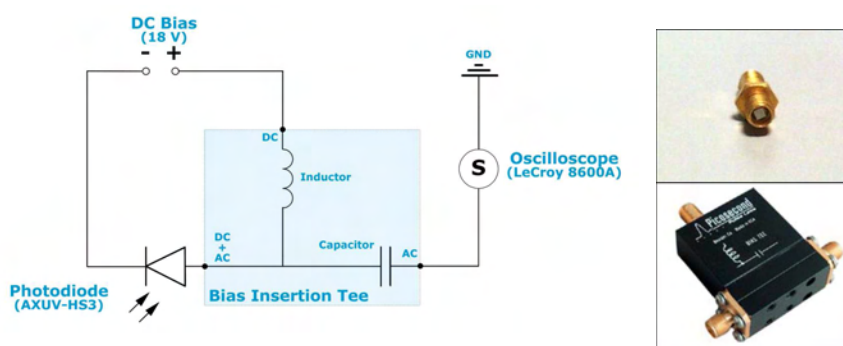


Figure 6.8: Components of the photodiode based temporal overlap system. Left: Diagram of the electronic circuit used to bias the photodiodes; Right: an AXUV-HS3 diode (top panel) and a bias insertion tee (bottom panel).

Shown in figure 6.8 is the electronic circuit (left), the AXUV diode (top-right) and the bias insertion tee (bottom-right) used in the temporal overlap experiment. The entire electronics (save for the bias insertion tee and photodiode) were integrated into a small insulated box. The electronic circuit was fabricated on Veroboard™. An 18 V bias was applied to the photodiode using two 9 V batteries (6LR61) contained inside the enclosure. The key requirement for this device was to pass high-speed signals from the photodiode to the oscilloscope which was located a few meters away from the experimental chamber. In order to ensure minimum distortion of the waveform the system incorporated gold-plated SMA<sup>2</sup> connectors and high-quality semi-rigid coaxial cables. The SMA connectors have excellent electrical performance and are ideal for passing high-speed signals with a bandwidth stretching from DC up to 18 GHz. BNC connectors with their lower bandwidth (operating frequency range: DC – 4 GHz [23]) were tested during the prototyping stages but

<sup>2</sup>Acronym for Sub-Miniature version A, specifications can be found at [23].

results indicated that the reduced performance combined with signal reflections at BNC-BNC interfaces lead to significant broadening of the picosecond duration signal. The DC bias on the photodiode was isolated from the oscilloscope (LeCroy 8600A) using a bias insertion tee (model 5541A) which was supplied by Picosecond Pulse Labs (Boulder, Colorado). The capacitor in the bias-tee passes only transient signals (low impedance) like the pulse from the photodiode, but blocks the 18 V bias thereby protecting the oscilloscope channel from overload ( $\pm 5$  V input limit). This model was ideal for high-speed applications, having a risetime of 8 ps, thereby transmitting the picosecond pulse with a minimum of waveform distortion. A manipulator arm with a mesh of gold wires intersected either the FEL or the optical laser beam.

Figure 6.9 shows a trace of the FEL and optical laser as seen by the diode. By monitoring and overlapping the rise time between each trace a temporal window of  $\pm 25$  ps could be achieved. The optimum overlap was achieved by varying the optical delay line in the optical laser hutch so that the negative-going dip in the signal from the optical laser coincided with the rise in the signal from the FEL. The x-axis figure 6.9 displays the actual time delay between each photodiode signal and this trigger pulse. The inset in figure 6.9 shows a magnified plot of the two traces. The slope of each trace is fairly similar, indicating that the detected signal is, as one would expect, limited by the risetime of the photodiode and bias circuit.

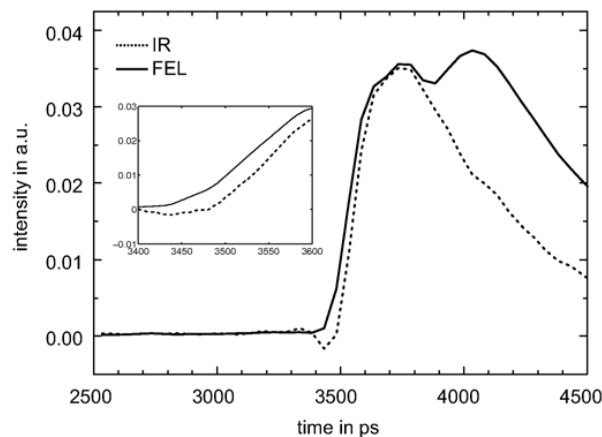


Figure 6.9: Output from the fast photodiode recorded using a fast digital oscilloscope (LeCroy 8600A) showing the signal from FLASH (solid line) and the IR pulses (dashed line). Inset: A magnified view of the rising edge of the two traces.

From the insert in figure 6.9, the time delay between the IR and EUV pulses was

estimated from the delay in ‘turn-on’ of each trace, here  $\sim 50$  ps. Importantly, the diode output indicated to the user which pulse came first so that the optical delay could be adjusted in the correct direction to ensure overlap. This coarse tuning was essential when using the EUV – IR cross correlation technique described later which only produced a signal when the two femtosecond scale pulses were overlapped. The method described here has proven to be a highly effective way of determining the temporal overlap of the optical laser and the FEL to within 20 ps to 30 ps. Consisting of just three major components, namely the enclosure containing the electronic circuit and batteries, the bias insertion tee and finally the photodiodes; the entire setup is relatively small and portable. As demonstrated it can achieve a temporal overlap window in the region of  $\pm 25$  ps and so the uncertainty in the overlap corresponds to a maximum total distance of 20 mm inside the vacuum chamber. Given that the EUV and NIR beams emanate from undulator and laser apertures some 70 m and 20 m respectively from the overlap point, this uncertainty is acceptable.

Synchronizing this complex machine with an optical laser based represents a significant achievement. The author is happy to report that EUV-optical pulse delay system has to date been used by numerous other groups working at the FLASH facility, a testament to the versatility/robustness of the system.

### **6.3 Summary**

In this section an overview and brief introduction to the operation of the free electron laser in Hamburg was presented. Also discussed were the key components of the experimental chamber including the magnetic bottle electron spectrometer which was used to record the photoelectron signal produced from the photoionization of rare gases by the FEL beam. The first task undertaken solely by the author was to create a timing system based on fast silicon photodiodes to overlap the EUV photons produced from the FEL with that from an optical laser located in the experimental hall. The system presented in this thesis was used to overlap the two beams to within  $\pm 25$  ps. This coarse synchronization method formed the basis for a much more precise method to overlap the two laser beams using a two-color photoionization process to be discussed in the forthcoming chapter.

# Bibliography

- [1] W. Ackermann. Operation of a free-electron laser from the extreme ultraviolet to the water window. *Nature Photonics*, 1(6):336, 2007.
- [2] Deutsches Elektronen-Synchrotron (DESY). Free-electron laser at DESY delivers highest power at shortest wavelengths and reaches water window. Press Release 07092006, 2006.
- [3] T. Wilhein, D. Altenbernd, U. Teubner, E. Förster, R. Hässner, W. Theobald, and R. Sauerbrey. X-ray brilliance measurements of a subpicosecond laser plasma using an elliptical off-axis reflection zone plate. *Journal of the Optical Society of America B*, 15(3):1235–1241, 1998.
- [4] Deutsches Elektronen-Synchrotron (DESY). Highlights, (<http://zms.desy.de/>). Technical report, 2008.
- [5] R. Treusch. Research highlights from FLASH. In *Proceedings of FEL, Novosibirsk, Russia*, number THBAU01, pages 499–500, 2007.
- [6] P. Radcliffe, S. Düsterer, A. Azima, W.B. Li, E. Plönjes, H. Redlin, J. Feldhaus, P. Nicolosi, L. Poletto, J. Dardis, J.P. Gutierrez, P. Hough, K.D. Kavanagh, E.T. Kennedy, H. Luna, P. Yeates, J.T. Costello, A. Delyseries, C.L.S. Lewis, D. Glijer, D. Cubaynes, and M. Meyer. An experiment for two-color photoionization using high intensity extreme-uv free electron and near-ir laser pulses. *Nuclear Instruments and Methods in Physics Research Section A: Accelerators, Spectrometers, Detectors and Associated Equipment*, 583(2-3):516 – 525, 2007.
- [7] P. Radcliffe, S. Dusterer, A. Azima, H. Redlin, J. Feldhaus, J. Dardis, K. Kavanagh, H. Luna, J. Pedregosa Gutierrez, P. Yeates, E. T. Kennedy, J. T. Costello, A. Delserieys, C. L. S. Lewis, R. Taieb, A. Maquet, D. Cubaynes, and M. Meyer. Single-shot characterization of independent femtosecond extreme ultraviolet free electron and infrared laser pulses. *Applied Physics Letters*, 90(13):131108, 2007.

- [8] M. Meyer, D. Cubaynes, D. Glijer, J. Dardis, P. Hayden, P. Hough, V. Richardson, E. T. Kennedy, J. T. Costello, P. Radcliffe, S. Dusterer, A. Azima, W. B. Li, H. Redlin, J. Feldhaus, R. Taieb, A. Maquet, A. N. Grum-Grzhimailo, E. V. Gryzlova, and S. I. Strakhova. Polarization control in two-color above-threshold ionization of atomic helium. *Physical Review Letters*, 101(19):193002, 2008.
- [9] K. Tiedtke, A. Azima, N. von Bargen, L. Bittner, S. Bonfigt, S. Dusterer, B. Faatz, U. Fruhling, M. Gensch, Ch. Gerth, N. Guerassimova, U. Hahn, T. Hans, M. Hesse, K. Honkavaar, U. Jastrow, P. Juranic, S. Kapitzki, B. Keitel, T. Kracht, M. Kuhlmann, W. B. Li, M. Martins, T. Nunez, E. Plonjes, H. Redlin, E. L. Saldin, E. A. Schneidmiller, J. R. Schneider, S. Schreiber, N. Stojanovic, F. Tavella, S. Toleikis, R. Treusch, H. Weigelt, M. Wellhofer, H. Wabnitz, M. V. Yurkov, and J. Feldhaus. The soft x-ray free-electron laser FLASH at DESY: beamlines, diagnostics and end-stations. *New Journal of Physics*, 11(2):023029, 2009.
- [10] H. Delsim-Hashemi, O. Grimm, A.F.G. van der Meer, H. Schlarb J. Rossbach, B. Schmidt, and P. Schmüser. Bunch compression monitor. In *Proceedings of EPAC 2006 - Synchrotron Light Sources and FELs*, pages 86–88, 2006.
- [11] J. Feldhaus, J. Arthur, and J. B. Hastings. X-ray free-electron lasers. *Journal of Physics B: Atomic, Molecular and Optical Physics*, 38(9):S799–S819, 2005.
- [12] E. L. Saldin, E. A. Schneidmiller, and M. V. Yurkov. Properties of the third harmonic of the radiation from self-amplified spontaneous emission free electron laser. *Physical Review Special Topics: Accelerators and Beams*, 9(3):030702, 2006.
- [13] E. L. Saldin, E. A. Schneidmiller, and M. V. Yurkov. Expected properties of the radiation from VUV-FEL at DESY (femtosecond mode of operation). Technical report, DESY, 2004.
- [14] M. Gensch, L. Bittner, A. Chesnov, H. Delsim-Hashemi, M. Drescher, B. Faatz, J. Feldhaus, U. Fruhling, G. A. Geloni, Ch. Gerth, O. Grimm, U. Hahn, M. Hesse, S. Kapitzki, V. Kocharyan, O. Kozlov, E. Matyushevsky, N. Morozov, D. Petrov, E. Ploenjes, M. Roehling, J. Rossbach, E. L. Saldin, B. Schmidt, P. Schmueser, E. A. Schneidmiller, E. Syresin, A. Willner, and M. V. Yurkov. New infrared undulator beamline at FLASH. *Infrared Physics & Technology*, 51(5):423 – 425, 2008.

- [15] T. Harada and T. Kita. Mechanically ruled aberration-corrected concave gratings. *Applied Optics*, 19(23):3987–3993, 1980.
- [16] T. Kita, T. Harada, N. Nakano, and H. Kuroda. Mechanically ruled aberration-corrected concave gratings for a flat-field grazing-incidence spectrograph. *Applied Optics*, 22(4):512–513, 1983.
- [17] A. M. Rijs, E. H. G. Backus, C. A. de Lange, N. P. C. Westwood, and M. H. M. Janssen. Magnetic bottle spectrometer as a versatile tool for laser photoelectron spectroscopy. *Journal of Electron Spectroscopy and Related Phenomena*, 112:151 – 162, 2000.
- [18] J. H. D. Eland, O. Vieuxmaire, T. Kinugawa, P. Lablanquie, R. I. Hall, and F. Penent. Complete two-electron spectra in double photoionization: The rare gases Ar, Kr, and Xe. *Physical Review Letters*, 90(5):053003, 2003.
- [19] Lawrence Berkeley National Laboratory Centre for X-ray Optics. X-ray transmission of solids tool. [http://henke.lbl.gov/optical\\_constants/filter2.html](http://henke.lbl.gov/optical_constants/filter2.html).
- [20] S. Goloborodko, G. Grygiel, O. Hensler, V. Kocharyan, K. Rehlich, and P. Shevtsov. DOOCS: an object oriented control system as the integrating part for the TTF linac. In Zhao, J. J. and Daneels, A., editor, *Accelerator and Large Experimental Physics Control Systems*, pages 397–399, 1997.
- [21] A. A. Sorokin, S. V. Bobashev, J. Feldhaus, Ch. Gerth, A. Gottwald, U. Hahn, U. Kroth, M. Richter, L. A. Shmaenok, B. Steeg, K. Tiedtke, and R. Treusch. Gas-monitor detector for intense and pulsed VUV/EUV free-electron laser radiation. volume 705, pages 557–560, 2004.
- [22] International Radiation Detectors. Torrance, California. <http://www.ird-inc.com/index.html>.
- [23] Amphenol-Connex. Manufacturer’s Website. <http://www.amphenolconnex.com/>.

## Chapter 7

# Two-Color Photoionization Experiments at FLASH

The Free Electron Laser in Hamburg (FLASH) began operation in mid. 2005 and currently offers a unique opportunity to study the interaction of intense EUV radiation with atoms and molecules. At present there is no rival facility which can match the combination of femtosecond pulse duration, coherent output, unprecedented peak and average EUV powers nor achieve laser-like emission from the VUV to deep in the EUV spectral band. That said, the Linac Coherent Light Source (LCLS) at Stanford will be the second such facility to come online in late 2009 and will provide similar ultrashort pulses of  $< 100$  fs duration with energies of up to  $100 \mu\text{J}/\text{pulse}$ , albeit at much higher photon energies, in the 0.8 to 12 keV range. In contrast to the relatively intense infrared laser-solid interactions discussed in the previous two chapters of this thesis, where valence electrons are the primary participants, the fundamental FEL photon energy lies far above the ionization potential of most stable matter which therefore permits the study of inner-shell transitions and a whole new plethora of non-linear atomic phenomena.

From its inception in the early 90s the DCU-Orsay-DESY collaboration has been a key contributor to the development of the FLASH facility. Since joining the group the author has played a central role in the further characterization of the FEL, most notably in the design and commissioning of a picosecond photodiode system [1] used to determine the temporal overlap of the FEL and optical laser beams at the interaction point in endstations which has now become a core component of nearly all of the pump-probe experiments performed at FLASH to date. I was a key member of the team who recorded the 5<sup>th</sup> harmonic of the fundamental radiation [2] inside the all-important water window in the summer of 2006 (see Appendix

A.1). My main physics interest became the dependence of coherently coupled two-colour photoionization processes on the relative orientation of the EUV and near infrared (NIR) polarization directions and results on this work constitute the core of this chapter.

In this chapter, fine-tuning of the temporal overlap between the pump and probe laser pulses using an EUV-NIR photoionization cross correlation technique are described [1]. Along with the general characterization of the pump-probe setup using photoelectron spectroscopy, the spectral content of the FLASH beam was measured with FLASH operating in the saturated regime [2]. Finally, the primary result of the study based at FLASH was on one- and two-color photoionization of rare gas atoms performed over a period of four years which will be presented towards the end of this chapter.

## 7.1 Characterization of Pump-Probe Setup

This chapter deals specifically with the study of one- and two-photon ionization of rare gas atoms by the intense EUV beam from the FLASH FEL. The case of two-color above-threshold ionization is examined, where a near-infrared (NIR) laser that is spatially and temporally overlapped with the EUV beam from the FEL is able to couple to (or dress) the photoelectrons produced by the one-photon ionization event (FEL). In effect, the free electrons can exchange photons with the NIR laser field, similar to above-threshold ionization, and increase or decrease their energy by  $\pm n\hbar\nu$  depending on the number of photons ( $n$ ) absorbed (+) or emitted (–). The gain and loss processes are thus stimulated by the intense NIR field.

But before any of these experiments can be realized, the pump-probe setup had to be characterized. Critical to all two-color photoionization experiments is the overlap of the two laser pulses in both time and space. Overlapping two independent photon sources which have pulse durations on the order of a few tens of femtoseconds represents a significant challenge. In this section a novel technique is described which is based on above-threshold ionization and is used to overlap the two laser pulses on a sub-picosecond timescale. This method builds upon the diode-based system that has already been discussed in section 6.

Furthermore, the radiation generated by the SASE process in the planar undulator is often labeled 'laser-like', in reference to its near-monochromaticity and almost full spatial coherence even if it lacks any measurable temporal coherence. The

operation of the undulator however results in the amplification of high-order harmonics of the fundamental FEL radiation [3, 4, 5]. In particular, when operating at saturation FLASH will produce relatively bright odd order harmonic radiation with weak even order harmonics present in the SASE FEL output. FEL theory predicts [6] that when FLASH operates at saturation the odd-harmonics will be preferentially amplified over the even-harmonics and their intensity may reach 2% of the fundamental. The presence of harmonics in the beam can be both a blessing and a curse. On one hand the harmonics can shift the operating wavelength band of the facility to shorter wavelength, possibly even into the soft X-ray region ( $< 1$  nm). But on the other hand, these harmonics provide an unwanted background for the two-color experiments and in particular the multiphoton absorption experiments. The presence of strong second harmonic radiation is a particular problem as it makes it difficult to distinguish between  $2 \times \omega$  and  $1 \times 2\omega$  events. Therefore in the second section the spectral content of the FEL determined from an EUV spectrometer will be presented.

### 7.1.1 Temporal Overlap using the Cross-Correlation Method

In practice, the fine tuning of the temporal overlap between the pump and probe beams begins having already achieved a relative time delay accuracy of  $\pm 25$  ps using the photodiode system described earlier. When an electron is promoted into the free electron continuum of an atom or molecule in the presence of an intense laser field, it can gain or lose an integer number of laser photons in a process similar to above-threshold ionization (see section 5.3). When this occurs the photoelectron spectrum is modified and a comb of photoelectron peaks will appear distributed on either side of the main photoline separated by the photon energy of the dressing field. These photoelectron peaks are commonly referred to as sidebands. The number and intensity of sidebands is highly dependent on the intensity of the dressing field at the time of the single-photon EUV ionization event. The intensity of the dressing field experienced by the ejected electron will depend on the degree of spatial and temporal overlap of the two EUV and NIR laser fields. Therefore, these sidebands can be used as a self-diagnostic tool to determine the degree of temporal and spatial overlap between the pump and probe pulses.

This technique is clearly a cross-correlation method [7, 8, 9, 10] where the sideband intensity becomes the measured correlated variable or 'correlative'. By plotting the intensity of the first photoelectron sideband as a function of relative delay, one can build up a cross-correlation trace or function. If the temporal profile of both

radiation sources is known then the temporal jitter between the two sources can be deconvolved from this curve.

This technique has been used in experiments at FLASH to determine the temporal delay between the FEL pulse and the 532 nm picosecond (2006 [11]), and 800 nm femtosecond (2007 [12]) duration optical laser pulses inside the experimental chamber at FLASH beamline BL2 . As will be shown in detail later, xenon produces the largest number of photoelectron sidebands for a given optical intensity compared to the other rare gases and so it was the ideal choice for use in these experiments. Therefore, xenon provided a sensitive monitor of the temporal overlap of the FEL and optical pulses and gave the ability to operate in single-shot mode.

The procedure begins by spatially overlapping the foci of the two lasers at the interaction point (gas jet region) in the experimental chamber using the Ce-YAG phosphor screen method (described in section 6.2.1 on page 205). The time delay measurements with the photodiode system had an accuracy of ca. 25 ps and so narrowed the temporal window in which to scan the optical laser down to  $\pm 25$  ps. A series of single-shot photoelectron spectra, recorded as the optical laser was scanned 'through' the FEL beam in time are shown in figure 7.1 (a). The time delay between the two laser pulses was controlled by passing the optical laser through a variable delay stage in the laser hutch [1]. When the two pulses were at optimum temporal overlap sidebands up to the fourth order were observed. The delay time at this point was designated zero. If on the other hand there was no sideband signal then this would indicate a time difference larger than the width of the optical pulse (the optical pulse at 120 fs was larger than the FEL pulse which had a duration in the 10 fs – 30 fs range). Anywhere in between would produce a varying number of sidebands. This is illustrated in figure 7.1 (a).

To determine the relative jitter between the two independent photon sources the intensity of the first sideband was plotted against the delay and a Gaussian profile was fitted to the data, figure 7.1 (right). The full width half-maximum (FWHM) of the fit was  $600 \pm 50$  fs. The pulse duration of the optical laser was measured to be 120 fs [1] while the pulse duration of the FEL was estimated to be less than 50 fs determined from FEL theory [6]. An EUV autocorrelator has been built [13] to determine the pulse duration of the EUV FEL pulse but has had little success to date. Therefore the majority of the width of this cross-correlation curve could be attributed to the jitter between the FEL and the optical laser. Through de-convolution of the two Gaussian curves belonging to the temporal width of the FEL and optical laser, the overall jitter between the two femtosecond pulses was found to be 590 fs

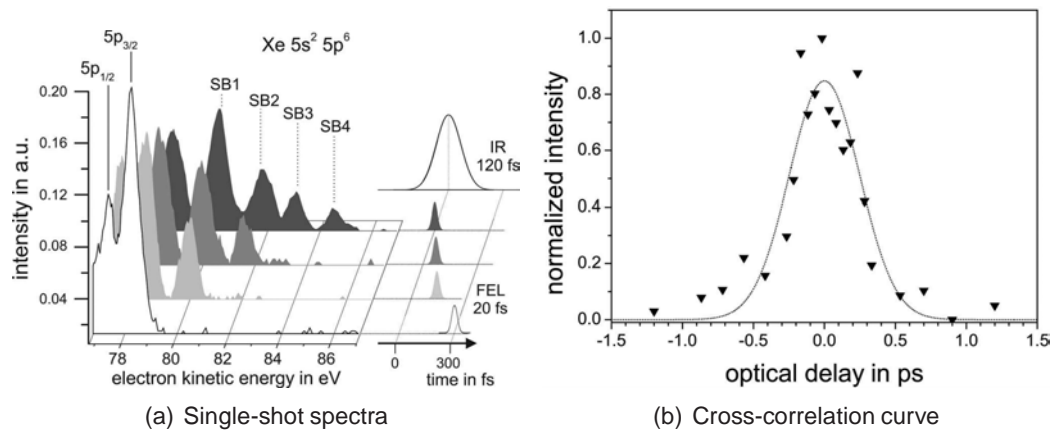


Figure 7.1: Single-shot photoelectron spectra in the region of the Xe  $5p^{-1}$  main photoline and the high-energy sidebands taken at the nominal temporal overlap ( $\Delta t = 0$ ). The FEL operated at a wavelength of 13.8 nm. The spectra are normalized to total FEL + NIR intensity. (b) Intensity of the first photoelectron sideband in xenon as a function of the time delay between the NIR and EUV pulses. The solid curve represents a Gaussian fit to the experimental data [12].

FWHM, which corresponded to an rms value of 250 fs.

This value of jitter was consistent with the findings of other experiments based similar techniques [14, 15] and also using alternative techniques, the most notable of which being the electro-optic sampling technique [16, 17]. The timing by electro-optic sampling (TEOS) technique is able to determine whether the jitter is positive or negative, i.e, whether the FEL pulse comes before or after the peak of the NIR pulse; something which is not possible via the cross-correlation method described above. However, our method of cross-correlation is still an effective method to determine the temporal jitter between the two pulses on a femtosecond time scale at the very center of the experimental chamber. With the two beams characterized temporally, the discussion moves on to characterizing the pump beam in terms of its spectral content.

### 7.1.2 Recording the Spectral Content of FLASH

SASE FELs operating at saturation emit relatively strong contributions from both odd high-frequency harmonics of the fundamental radiation [3], in some instances the intensity of the odd harmonics can even reach the percent level [4]. In a planar undulator the ratio of the third harmonic to the fundamental intensity grows strongly within the linear regime of operation and may reach a theoretical maximum of 2%

when the FEL output reaches saturation [18]. If the beam does not undergo slalom-like undulator motion in a single plane not only will the degree of ellipticity of the radiation increase, but it is observed that the intensity of even harmonic radiation also increases. This section describes an experiment performed to independently measure the spectral content of the FEL beam at 13.7 nm. The collaboration was extended to include Queen's University Belfast. The apparatus consisted of a flat-field spectrometer (provided by QUB) and a back-illuminated EUV sensitive CCD camera (provided by DCU and described in more detail in section 6).

The EUV spectrum of the FEL fundamental wavelength and its higher order harmonics were measured using three different grazing incidence spectrometer systems. A detailed description of the first and second systems can be found in Poletto *et al.* (2004) [19] and in Martins *et al.* (2006) [20], respectively. The third spectrometer, mentioned above, was a flat field system equipped with a Harada grating and an EUV sensitive back-illuminated CCD camera (Andor Technology).

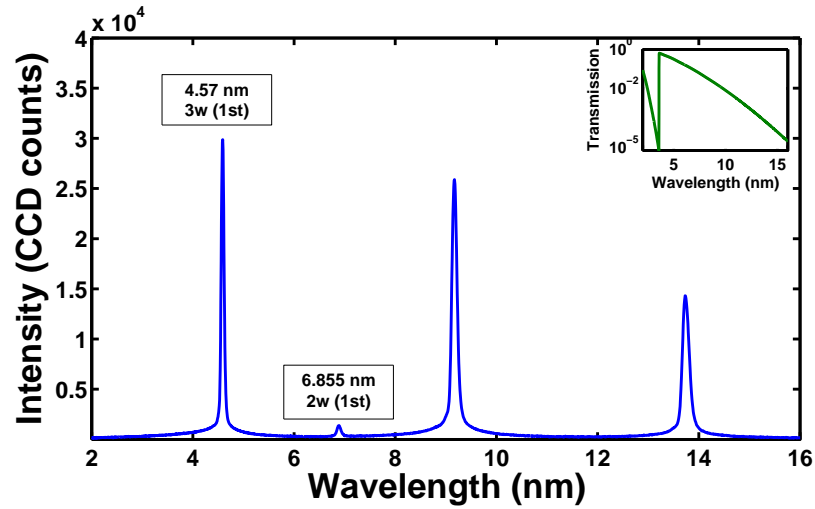
The spectrometer was located at the end of beamline-2 (BL2) where it was coupled to the experimental chamber via a bellows. The vacuum in the spectrometer chamber was kept at a constant  $10^{-4}$  mbar using a 250 litre/s turbo-molecular pump. A pressure of  $\sim 10^{-8}$  mbar was maintained in the primary experimental chamber with the aid of a differential pumping system. The high- and low-vacuum chambers were separated by a bellows that had a copper gasket containing a  $\sim 0.5$  cm hole in the center used as the CF vacuum seal at each end, thereby producing a differential pumping stage. The FEL beam passed through the experimental chamber un-deflected where it was incident on the grating. The intensity of the SASE FEL beam was low at this point as it had diverged to a diameter of a few millimeters. The grating was fixed to translation stages which gave both linear and angular movement. Filters were placed between the entrance slit and the grating for two reasons, to attenuate the beam before striking the CCD camera, and to select radiation from either the fundamental radiation or the high-harmonics. The CCD was operated in full-vertical binning mode and spectra were recorded with the FEL operating at a 'macropulse' repetition frequency of 5 Hz with 30 micropulses of femtosecond duration per macropulse. Figure 7.2 shows EUV spectra of the FEL output containing emission from the fundamental at 13.7 nm and the higher-order harmonics for two different filters [1, 2]. A 3  $\mu\text{m}$  thick polypropylene ( $\text{C}_3\text{H}_6$ ) filter was used to attenuate the fundamental radiation (13.7 nm) and pass radiation from the low 2<sup>nd</sup> and 3<sup>rd</sup> harmonics although some of the intense fundamental radiation leaked through. A 1.5  $\mu\text{m}$  thick aluminium filter was used to block emission from the fundamental and

pass emission from the higher harmonics (see inset in figure 7.2 (bottom)). The spectra shown in figure 7.2 are a summation of 100 shots and are uncorrected for the efficiency of the grating or for the transmission of the respective filters.

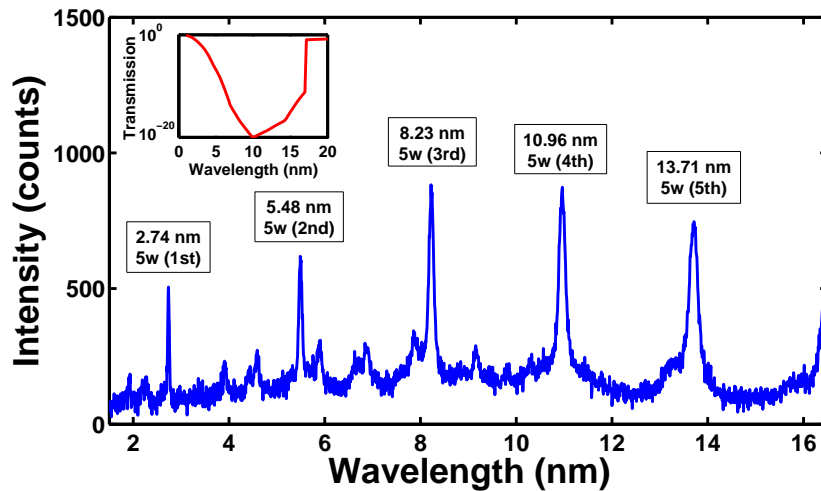
The 5<sup>th</sup> harmonic is visible in figure 7.2 (b) at a wavelength of 2.74 nm. There is some evidence (although not conclusive) of the presence of the 7<sup>th</sup> harmonic at 1.95 nm also. The first observation of the 5<sup>th</sup> harmonic at soft X-ray wavelengths and more importantly at these intensities was greeted with much enthusiasm and was the subject of a press release co-written by DCU and DESY [21]. At 2.74 nm, the 5<sup>th</sup> harmonic resides in the so-called water window. The water window is the wavelength region between 2.3 nm and 4.4 nm where the carbon atoms in organic matter absorb radiation, whereas the water or aqueous environment remains transparent. This was a very important milestone in the development roadmap to ultrashort wavelength FELs such as the XFEL [22].

Measurements of the even harmonics made during this period (Summer 2006) showed that they are significantly suppressed with respect to the odd harmonics [1]. One can see clearly from figure 7.2 for instance, that the intensity of the 2nd harmonic is nearly an order of magnitude less than that of the 3rd harmonic. When the transmission of the polypropylene filter was taken into account the 3<sup>rd</sup> harmonic energy was  $0.25 \pm 0.1 \mu\text{J}$  and a value of  $10 \pm 4 \text{ nJ}$  was obtained for the 5th (2.75 nm) harmonic. These values correspond to a relative contribution to the total EUV output energy of  $0.6 \pm 0.2\%$  and  $0.03 \pm 0.01\%$  for the 3<sup>rd</sup> and 5<sup>th</sup> harmonics which are in agreement with FEL theory [4]. This result [2] was achieved with FLASH operating at saturation. At the the time the maximum energy available from the saturation energy of the accelerating modules was 700 MeV (as opposed to the current 1 GeV) and the experiment served to show that radiation from relatively low energy FELs can easily reach well into the soft X-ray spectral region.

With the pump-probe system spectrally characterized, spatially overlapped and temporally synchronized the study of the photoionization of rare gases could begin. In this next section results from the two-color (EUV and IR) photoionization will be presented.



(a) EUV FEL spectrum obtained using a 3  $\mu\text{m}$  thick polypropylene ( $\text{C}_3\text{H}_6$ ) filter.



(b) EUV FEL spectrum obtained using a 1.5  $\mu\text{m}$  thick aluminium filter.

Figure 7.2: Averaged photon spectra of the output from the FEL in the vicinity of 13.5 nm using a 3  $\mu\text{m}$  thick polypropylene ( $\text{C}_3\text{H}_6$ ) filter (a) and a 1.5  $\mu\text{m}$  thick aluminium filter (b) which select either the emission from the fundamental and low order harmonics ( $2\omega$  and  $3\omega$ ) or solely from the higher-order (mainly  $5\omega$ ) harmonics, respectively. The spectra are complicated by the presence of higher orders of the grating.

## 7.2 Two-Color Above-Threshold Photoionization Studies

The work presented in this section is based on the photoionization of rare gas atoms by the intense EUV beam from FLASH. The work will go beyond the conventional one-photon ionization processes observed with synchrotron and other weak field EUV sources and will introduce in further detail the concept of two-color ionization. In this ionization scheme a time-synchronized IR laser will be used to couple to the free-electrons produced in the one-photon (EUV) process to induce further free-free transitions within the continuum. The ordinary one-photon photoelectron spectrum which contained a single electron peak will now contain multiple peaks which are disposed on either side of the main photoline and separated from it and each other by the photon energy of the optical laser (800 nm = 1.55 eV). This ionization scheme is referred to as two-color above-threshold ionization (ATI).

The theory which governs the formation of these free-free transitions is not unlike that which describes the process of inverse-Bremsstrahlung (IB) in plasmas. IB has been of fundamental interest to most plasma physicists over the last 60 years because the free-free transitions in this process constitute the primary mechanism by which laser radiation heats a plasma. Therefore the study of this scheme, both experimentally and with aid of theoretical models, will help to extend the body of knowledge in this area.

Work of this kind has been done before [23, 24, 25, 26] but with the use of EUV photons originating from a high-harmonic generation source. This leads to interferences between the different harmonics and to significant complexities in the analysis of the data. In stark contrast the emission from the FEL is relatively monochromatic which permits the interference-free study of the two-color multiphoton process for the first time.

This section introduces the theory which describes the two-color ATI process. With the aid of computer simulations the model will be compared to experimental data for a variety of different scenarios. This will lead to the relatively new and interesting study of dichroic effects on the two-color process.

### 7.2.1 Orientation

When an electron is promoted into the continuum via EUV photon absorption in the presence of an intense optical dressing field, then this electron may exchange photons with the optical field resulting in a gain or loss of kinetic energy. The electron

is said to have undergone transitions between two free states in the continuum ( $\epsilon'/l \rightarrow \epsilon''/l \pm 1$ ) where  $\epsilon$  and  $l$  are the kinetic energy and orbital angular momentum of the free electron.

In the typical two-color experiment of interest here, where an optical laser, having an average intensity ( $\sim 10^{12}$  W/cm<sup>2</sup>), is overlapped with a beam of EUV photons from FLASH, the photoelectron spectrum consists of a main peak, associated with the one-photon (EUV) ionization event accompanied by sidebands, disposed symmetrically on either side of this main peak (often referred to as the main photoline). The effect of the optical laser can be summarized by the following: The sidebands indicate that the photoelectron is exchanging photons with the optical dressing field. Secondly, there may be a shift of the mean energies of each peak due to the ponderomotive effect. And finally, in the case of ultrashort optical or NIR dressing pulses (with respect to the EUV pulse duration) the features in the photoelectron spectrum may become broadened due to the fact that the intensity of the dressing field is not constant during the presence of the EUV field [10].

A study of the kind undertaken here will reveal more precise information about the two-color process. As will be shown in the following sections, in the specific case of helium, the intensity of the photoelectron sidebands will depend on the ratio of the amplitudes of the outgoing *s* and *d* electrons. Through the use of a theoretical model [27] a comparison is made to the experimental data on the dependence of the sideband intensity on the angular deviation between the polarization planes of the EUV and optical fields which will help to reveal the relative contribution that these electrons make to the overall intensity of the first sideband. This model, known as the soft-photon approximation, will be discussed before introducing the experimental results.

### 7.2.2 The Soft Photon Approximation

Free-free deexcitation/ionization channels in laser-produced plasmas, namely Bremsstrahlung and its inverse process were discussed in section 1.4. Briefly, the process of inverse-Bremsstrahlung occurs when a free electron in the vicinity of an atom or ion absorbs a photon from a radiation field and is accelerated, thereby increasing the kinetic energy of the electron. The process of inverse-Bremsstrahlung is of central importance to plasma physics because it constitutes a key process by which a plasma is heated by electromagnetic waves.

Laser-assisted electron scattering, as it was formally known was first observed by

Weingartshofer *et al.* in 1977 [28] with the advent of very intense table-top laser systems. Even before the earliest experimental observations theoretical models were being formulated in order to describe the process. Many of the first models on electron-atom scattering were based on the perturbative methods [29, 30, 31, 32]. These models were more suited to bound-bound (excitation) and bound-free (ionization) radiative processes. With the emergence of more intense lasers these models quickly became unsuitable. Problems arose when the transition amplitudes associated with the exchange of photons with frequency  $\omega$  became divergent in the limit  $\omega \rightarrow 0$ . This is the so-called ‘Low-theorem’, named after F. E. Low in 1958 [33] which emerged from his work on Bremsstrahlung arising from collisions of very low-energy electrons with atoms. The Low theorem was generalized by Kroll and Watson in 1973 [34] for the specific case of laser-assisted potential scattering with high-intensity lasers, using non-perturbative methods. The first experiments to explore this phenomenon by Weingartshofer *et al.* in 1977 [28] and in [35] agreed with the predictions of this new formalism.

The Kroll-Watson generalization [34] is valid when the energy of the laser photon ( $\hbar\omega_L$ ) is significantly smaller than the kinetic energy of the photoelectron ( $E_k$ ) [27], often referred to as the ‘soft-photon’ limit. While the process of electron-atom scattering described in this thesis may be different from the e-beam experiments performed in the 70s, the underlying physics dictating the free-free transition amplitudes remains the same. Therefore the analysis of the experimental data will be complemented with a theoretical model developed by A. Maquet and R. Taïeb [27] which is based on the Kroll-Watson generalization.

Kroll and Watson [34] have shown that when the photon energy of the laser which dresses a continuum state is significantly smaller than the kinetic energy of the photoelectron ( $\hbar\omega_L \ll E_k$ ) then the differential cross-section for a collision process, accompanied with the exchange (via absorption or stimulated emission) of  $n$  photons from the optical laser factorizes as follows:

$$\frac{d\sigma^{(n)}}{d\Omega} = J_n^2(\alpha_0 \cdot \mathbf{k}_n) \frac{d\sigma}{d\Omega} \quad (7.1)$$

where  $\mathbf{k}_n = [2(E + \omega_x + n\omega_L - U_p)]^{1/2}$  is the shifted wave number of the ejected electron, where  $E$  is the binding energy of the electron,  $\omega_x$  and  $\omega_L$  are the angular frequencies of the FEL and the NIR photons respectively, and  $U_p$  is the magnitude of the ponderomotive shift; and  $\vec{\alpha}_0 = \vec{F}_{0L}/\omega_L^2$  is the classical excursion vector of a free electron embedded in a laser field of amplitude  $\vec{F}_{0L}$ . The quantity on the

extreme right is the one-photon (EUV) cross-section, in the absence of the optical dressing field. In general terms, this approximation holds if the inequality  $|\alpha_0 \cdot \mathbf{K}/\eta| < 1$  is true, i.e. if the intensity of the NIR or optical laser is relatively low.

The dressing of the ejected electron by the optical laser is entirely described within the Bessel function and the exchange of the laser photons appears through the factor  $(\alpha_0 \cdot \mathbf{k}_n)$ . This results in the modulation of the one-photon cross-section through the absorption or stimulated emission of an integer number of optical photons. At high laser intensities the peak in the Bessel function will shift to higher and higher orders which results in the formation of more and more sidebands.

To arrive at the generalized solution of equation 7.1 an S-matrix expansion of the electron-atom scattering is performed. Special Volkov waves [36] are used which define a free electron in an intense laser field. In the case of helium, the corresponding S-matrix transition amplitude from the photoionization of a 1s electron by the absorption of one EUV photon in the presence of the NIR or optical laser field is given by [37],

$$S = -i \int_{-\infty}^{\infty} dt \langle \psi_k(t) | \frac{1}{c} \mathbf{A}_x(t) \cdot \mathbf{p} | \psi_{1s^2}(t) \rangle \quad (7.2)$$

where  $\mathbf{A}_x(t)$  is the vector potential of the EUV field. The ket  $|\psi_i(t)\rangle$  is a time-dependent wavefunction representing the atomic ground state in the presence of the optical laser field and is given by,

$$\langle \mathbf{r} | \psi_{1s^2}(t) \rangle = \exp(-iE_{1s^2}(t)) \psi_{1s^2}(\mathbf{r}) \quad (7.3)$$

Similarly  $|\psi_k(t)\rangle$  represents a positive energy electron with momentum  $k$  which is subjected to the combined field from the Coulomb potential of the nucleus and the optical laser. This is given by,

$$\langle \mathbf{r} | \psi_k(t) \rangle = \exp(-i\frac{1}{2}k^2(t)) \psi_k(\mathbf{r}) \quad (7.4)$$

The interaction Hamiltonian between the fields and the electron is given by,

$$\frac{1}{c} \mathbf{A}_x(t) \cdot \mathbf{p} = \frac{1}{2} A_{0x} \exp[(-i\omega_x t + \phi_x)] \hat{\epsilon}_x \cdot \mathbf{p} \quad (7.5)$$

where  $A_x(t)$  is the classical vector potential of the EUV field.

The dressing of the continuum state by the optical laser is now considered. A Volkov wave [36] is used to describe the wave-function of the positive energy elec-

tron. The Volkov wave used in this model is defined as follows [27],

$$\langle \mathbf{r} | \chi_k^V(t) \rangle = \exp \left[ -i(\alpha(t) \cdot \mathbf{k} + \frac{1}{2}k^2 t) \right] \chi_k(\mathbf{r}) \quad (7.6)$$

where

$$\chi_k(r) = \frac{1}{(2\pi)^{3/2}} \exp(i\mathbf{k} \cdot \mathbf{r}) \quad (7.7)$$

represents a plane wave and the effect of the field strength of the laser is introduced through

$$\alpha(t) = \alpha_0 \sin(\omega_L t + \phi_L) \quad (7.8)$$

where

$$\alpha_0 = \frac{F_{0L}}{\omega_L^2} \quad (7.9)$$

This Volkov wave-function was substituted into the continuum state wave-function (equation 7.4) replacing  $|\psi_k(t)\rangle$  with  $|\chi_k^V(t)\rangle$ . The influence of the Coulomb field of the nucleus on the final state of the electron which would have the effect of slightly modifying the wave-function of the electron in the continuum is ignored in the current approximation. A more rigorous method which accounts for the Coulomb potential is described in [37] where a Coulomb wave-function is multiplied by a Volkov-like term, leading to the so-called Coulomb-Volkov wave [38]. But past experiments [8] have shown good agreement between data and theory using Volkov waves only indicating that these effects are not significant.

Using the Fourier-Bessel expansion with sinusoidal argument, where

$$\exp(-i\eta_k \sin \omega t) = \sum_n J_n(\eta_k) \exp(-in\omega t) \quad (7.10)$$

one obtains

$$\chi_k^V(r, t) = \frac{1}{(2\pi)^{3/2}} \sum_{+\infty}^{-\infty} J_n(\alpha_0 \cdot k) \exp[-in(\omega_L t + \phi_L)] \exp \left[ i(k \cdot r - \frac{1}{2}k^2 t) \right] \quad (7.11)$$

where the index  $n$  is associated with the net number of laser photons exchanged in the course of the process. When  $n < 0$  then the electron has gained energy (absorption) and vice-versa when  $n > 0$ .

Equation 7.11 is substituted back into equation 7.2 (the S-matrix transition ampli-

tude) and by performing the time integration one obtains,

$$S = \sum S^{(n)} \delta \left( \frac{k^2}{2} - (E_{1s^2} + \omega_x + n\omega_L) \right) \quad (7.12)$$

where the components  $S^{(n)}$ , which are associated with the net exchange of  $n$  laser photons in addition to the absorption of the EUV photon, are of the general form

$$S^{(n)} = -2\pi i J_{-n}(\alpha_0 \cdot \mathbf{k}_n) \exp[-i(\phi_x + n\phi_L)] \langle \chi_{k_n} | \epsilon_x \cdot \mathbf{p} | \chi_{1s^2} \rangle \quad (7.13)$$

where

$$k_n \approx [2(E_{1s^2} + \omega_x + n\omega_L)]^{1/2} \quad (7.14)$$

is the shifted wave number of the ejected electron. There value of  $k_n$  is approximate because there is a small (but significant) shift of the ionization potential (ponderomotive shift) of the atom in an intense laser field which has not been accounted for in equation 7.14.

The bound-free atomic matrix element in equation 7.13 is known in closed form [37] and the corresponding cross section can be calculated without further approximation. The corresponding differential cross section is

$$\frac{d\sigma^{(n)}}{d\Omega} = J_n^2(\alpha_0 \cdot \mathbf{k}_n) \frac{d\sigma}{d\Omega} \quad (7.15)$$

where  $(d\sigma/d\Omega)$  is the one-photon cross section pertaining to the absorption of one EUV photon.

The angle integrated cross section deduced from the expression in equation 7.15 is proportional to integrals of the general form:

$$\sigma^{(n)} \propto \int_0^\pi \sin\theta d\theta J_n^2(\alpha_0 k_n \cos\theta) \left( \frac{d\sigma^{(0)}}{d\theta} \right) \quad (7.16)$$

where  $\theta$  is the angle between the linear polarization vector of the FEL and the wave vector of the ejected electron. In the case of photoionization from the He  $1s^2$  ground state the one-photon differential cross section  $(\frac{d\sigma^{(0)}}{d\theta})$  in the dipole approximation is given as [39],

$$\frac{d\sigma^{(0)}}{d\theta} \approx [1 + \beta P_2(\cos\theta)] \quad (7.17)$$

where  $\beta$  is the angular distribution asymmetry parameter and  $P_2$  is the second

Legendre polynomial given as,

$$P_2 = \frac{1}{2}(3x^2 - 1) \quad (7.18)$$

where  $x = \cos \theta$ . Substituting equation 7.18 into equation 7.16 leads to the magnitude of the photoelectron sidebands given by

$$B(\alpha_0 k_n) = \int_0^\pi \sin \theta d\theta J_n^2(\alpha_0 k_n \cos \theta) \left[ 1 - \frac{\beta}{2} + \left( \frac{2}{3} \beta \cos^2 \theta \right) \right] \quad (7.19)$$

Through the Bessel sum rule which is given as

$$\sum_{n=-\infty}^{\infty} J_n^2(z) = 1 \quad (7.20)$$

one finds that the maximum electron yield from the two-color process is  $2/3$ .

The relative magnitudes of the sidebands  $S^{(n)}$  are directly related to the numerical values of the integrals  $B(\alpha_0 k_n)$ . A computer model [40] was used to solve equation 7.19 for up to ten sidebands ( $n = \pm 11$ ) on either side of the main photoline. The model calculates the total sideband signal corresponding to the area of each photoelectron sideband, therefore in order to produce a spectrum, this theoretical prediction distributed over a Gaussian profile where the width corresponded to the width of the experimental sideband peaks. This results in a simulated spectrum where the total intensity of the individual sidebands was in good agreement with that of the experimental data.

Shown in figure 7.3 are two simulated two-color, angle integrated photoionization spectra of helium. In this case the two optical fields are both linearly polarized with field vectors parallel. The effects of the temporal and spatial overlap of the two beams have not been taken into account in these plots. The red lines in figure 7.3 represent the one-photon ionization of the He 1s electron in the absence of the optical laser. When the optical dressing field is turned on the spectrum becomes significantly modified (blue lines). The central peak ( $S^{(0)}$ ) is strongly depleted, while sidebands have appeared and are symmetrically distributed around the main photoline. The lower energy sidebands can be attributed to the stimulated emission of optical photons from the ejected electron, while the peaks on the high-energy side correspond to the ejected electron absorbing optical photons from the dressing field. One can see that the magnitude of sidebands scales with the intensity of the optical laser. At a higher intensity, there are more sidebands, indicating that the

ejected electron has exchanged multiple photons with the dressing field. The level of redistribution is determined purely by the Bessel function, specifically with the  $\alpha_0$  parameter in the argument of the Bessel function. As the intensity of the sidebands increases there is a corresponding decrease in the height of the main photoline. The optical laser intensity quoted here is not sufficient to cause multi-photon ionization and so the optical laser plays no part in the initial ionization process (this has been checked experimentally). The overall number of electrons in the main photoline and the sidebands remains constant throughout.

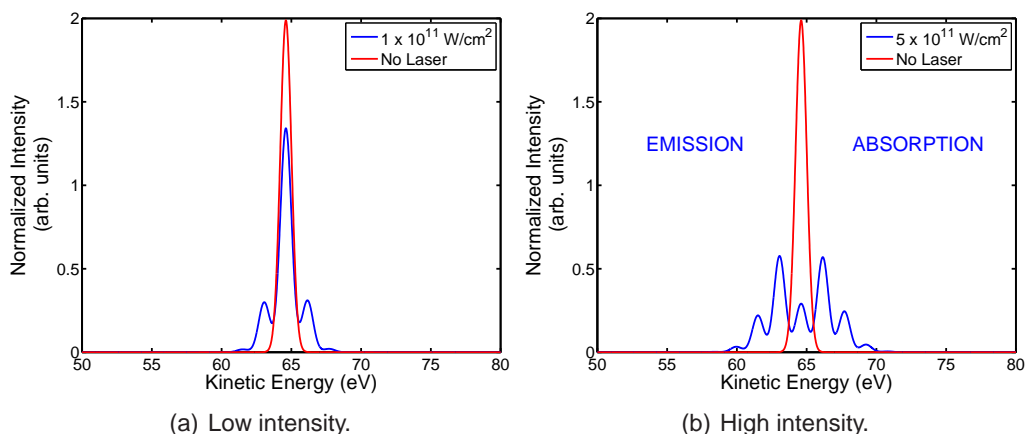


Figure 7.3: Helium photoelectron spectra simulated using the soft-photon approximation model for low- (a) and high- (b) intensity of optical dressing field. The solid red line is the one-photon (EUV) signal in the absence of the optical laser.

The spectra shown in figure 7.3 were simulated for ionization from the He  $1s^2$  ground state, but in principle it is possible to produce spectra for ionization of the valence electrons in all the rare gases. When comparing the model to the experimental spectra, slight modifications were made to the code in order to account for the varying experimental conditions. The model assumes an infinitely narrow interaction region which is defined as the overlap between the foci of the two lasers. But in the experiment the two lasers enter the chamber in a collinear geometry, meaning that the length of the interaction region could be quite large, depending on the focal conditions and on the extent of the entrance slit or aperture of the photoelectron spectrometer which was typically 4 mm long. Therefore the intensity of the optical laser varied along the length of this region so that electrons born into the field at the optimum focus of the optical laser experienced a high field and hence absorbed and/or emitted more optical photons than those located in the low intensity region at the periphery of the interaction region.

From the simulated spectra in figure 7.3 one can see that the main photoline scales with the intensity of the sidebands. But from early experimental data this trend was not observed. What was observed was a very strong signal from the main photoline and fairly weak sidebands. The ratio of the intensity of the main photoline to that of the first sideband would never match that of the computer model. This was mainly due to the fact that the spectrometer captured electrons along the length of the interaction region, and at the extreme edges there was insufficient intensity to induce a free-free transition. The result was that the intensity of the main photoline was amplified due to the influx of those weakly and even un-dressed electrons.

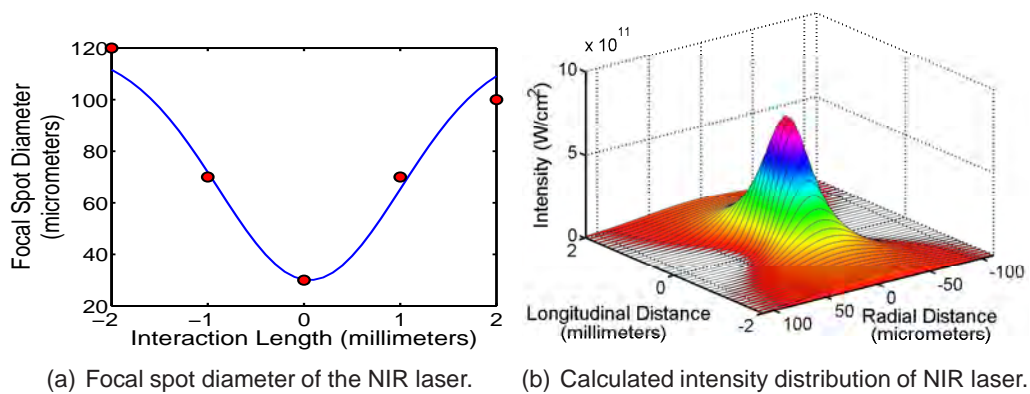


Figure 7.4: Diameter of the optical laser along the length of the interaction region. The variation in the intensity is from  $1 \times 10^{10}$  W/cm<sup>2</sup> at the periphery to  $7.5 \times 10^{11}$  W/cm<sup>2</sup> at the beam waist. Right: Calculated two-dimensional intensity distribution of the optical laser along the length of the interaction region. The distribution was determined by assuming a Gaussian beam with a pulse duration of 4.5 ps and a pulse energy of 350 μJ.

In order to overcome this issue, the spatial variation of the intensity of the optical laser along the length of the interaction region was determined. The focal spot diameter of the optical laser was measured (by S. Düsterer and W. Li at FLASH) over the length of this interaction volume using the Ce-YAG phosphor screen described in section 6. The results are displayed in figure 7.4 (a). Red circles represent the measured diameters while the solid blue line represents a Gaussian fit to the data. The minimum focal diameter is approximately 30 μm and is located at the center of the interaction region coinciding with the centre point of the entrance slit of the magnetic bottle electron spectrometer. This diameter corresponds to an intensity of  $\sim 7.5 \times 10^{11}$  W/cm<sup>2</sup> (assuming a Gaussian beam with a pulse duration of 4.5 ps and a pulse energy of 350 μJ). The diameter of the beam increases to  $\sim 120$  μm at the extreme edges of the interaction region ( $\pm 2$  mm). Here the intensity

is calculated to be  $1 \times 10^{10}$  W/cm<sup>2</sup>. A Gaussian spatial profile across the beam was assumed and a two-dimensional intensity distribution was calculated, figure 7.4 (b). The FEL on the other hand is focused using a 2 m focal length lens, and so the beam divergence is assumed to be fairly small over the length of the interaction region. A range of different intensities were selected from this intensity distribution (figure 7.4 (b)) and used in the generation of simulated spectra. By repeating the calculations for the different intensities and averaging the results, it was possible to simulate the random fluctuations of the laser intensity in the experiment. For convenience this procedure was fully automatic, and the batch of simulated spectra would be averaged. The process would cease when the the simulated spectra approximated to the experimental spectra (determined by comparing the sideband intensity ratios from both spectra).

### 7.2.3 Dependence of Photoelectron Sideband Intensity

The soft-photon approximation reveals that the two-color process is dependent on a multitude of independent variables. Equation 7.15 shows that the intensity of the photoelectron sidebands produced in the two-color process depends upon the parameter  $\alpha_0$ , the classical excursion vector of an electron embedded in the electric field of a laser. Therefore, the intensity and quantity of the photoelectron sidebands will depend critically on the intensity and wavelength of the optical laser. To a lesser extent, the intensity of the sidebands depends also on the wavelength of the FEL (through  $k_n$  in equation 7.15) and on the atom being examined, through the one-photon cross section.

The differential cross-section for the two-photon process has been broken into three sections, namely, the dependence of the sideband intensity on the wavelength of the FEL, on the wavelength of the optical laser and on the atomic number of the element under examination. These will be examined in sequence in the following pages where firstly the computer model will be used to provide an initial prediction. Then the experimental data will be examined and compared with this simulation. A difficulty arises when there are many variables in the experimental data, so where possible special normalization routines are used to restrict the degrees of freedom.

#### 7.2.3.1 Electron Kinetic Energy

This section begins by examining the effect of changing the wavelength of the FEL on the magnitude of the two-color ATI signal. As stated earlier, the process of laser-assisted electron scattering was first observed experimentally by Weingartshofer *et*

*al.* in 1977 [28]. They collided a beam of mono-energetic electrons with an argon gas jet in the presence of a CO<sub>2</sub> laser and recorded the photoelectron signal. They found that additional features were generated which were separated by the photon energy of the infrared laser and symmetrically disposed on either side of the main electron peak. A further study performed in 1979 [35] examined how the magnitude of these sidebands depended on the momentum of the incident electron. As the kinetic energy of the incident electron increased the number and intensity of these sidebands increased. When the kinetic energy of the electron was relatively low (4.2 eV) they observed the main photo line surrounded by only two sidebands, one on either side of the main photo line corresponding to the absorption/emission of a single infrared laser photon. As the energy of the electron was increased up to 76.4 eV they observed multiple sidebands up to the 4<sup>th</sup> order which indicated that the free electron was emitting and/or absorbing multiple laser photons.

In the work presented here, a similar study was performed, but the electron beam in ref. [35] was substituted by photoelectrons generated by one-photon ionization of atoms using the intense EUV beam from the FEL. In the direct-photoionization of a valence electron by the absorption of an FEL photon by a rare gas atom the ejected electron will have a kinetic energy equal to the difference between the photon energy and the characteristic binding energy of the electron to the core. In the case of helium, a 90.5 eV photon from the FEL (13.7 nm) will directly ionize the He 1s electron, promoting it into the continuum with an excess energy of  $\sim 65$  eV. As seen in the work of Weingartshofer *et al.* [35] the magnitude of the photoelectron sidebands depended on many parameters, one of which was the initial kinetic energy of the dressed electron.

Specifically, the effect of changing the kinetic energy of the photo-ejected electron on the intensity of the sidebands in helium is studied. Unlike in the work of Weingartshofer *et al.* [35] who used a beam of mono-energetic electrons, here the tunable EUV beam of the FEL will be used to vary the kinetic energy of the electrons. Specifically two wavelengths of the FEL were selected, namely 13.7 nm (90.5 eV) and 26 nm (47.7 eV) to produce electrons with different kinetic energies. The intensity of the photoelectron sidebands were recorded for the two settings of the FEL wavelength. Firstly, the soft-photon approximation is used to model the behavior of the sidebands in helium. Later on the predictions from the model will be compared to the experimental data. The data for this section was acquired over two beam-times, in 2007 and again in 2009 and as a result a variety of data-normalization procedures were used to ensure that these two distinct data sets are comparable.

## Computer Simulation

A computer model [40] based on a solution of the soft-photon approximation described in Maquet *et al.* [27] was used to model the magnitude of the sidebands in the two-color above-threshold ionization process. From equation 7.14 one can see that the transferred momentum (magnitude of the  $k$ -vector) of the ejected electron scales with the photon energy of the FEL. An increase in the wavelength of the FEL results in a reduction in the kinetic energy of the ejected electron. The value of the Bessel function 7.15 will decrease rapidly when the value of the argument becomes smaller, therefore it is expected that there will be a reduction in the number of sidebands observed for the lower FLASH photon energy (all other parameters, especially the 800 nm intensity, being equal).

The soft-photon approximation model was run for Helium and for a FEL wavelength range from 10 nm – 30 nm. The total intensity of all the sidebands (both low- and high-energy) was plotted as a function of the wavelength of the FEL (figure 7.5). The simulation shows that as the wavelength increases, the total sideband yield decreases. Simulated photoelectron spectra are shown on the right-hand side of figure 7.5. The x-axis scale in this plot is in units of optical laser quanta ( $h\nu_L = 1.55$  eV). The theoretical prediction reveals that the coupling between the electron and the optical laser field is reduced as the kinetic energy of the electron decreases while the influence of the residual nuclear charge becomes concomitantly greater. Cionga *et al.* [37] commented on this fact in their work on laser-assisted photoionization. They mention that a decrease in the frequency of the photon will give rise to a greater amplitude of the quiver-motion of the electron in the laser field. In terms of the present study it is interesting to examine whether this concept translates to the experimental data.

The simulations shown in figure 7.5 using the computer model assume an ideal case where the focal spot of the optical laser is overlapped fully with that of the FEL beam and that a single intensity defines the entire interaction region. The model ignores the variations in the temporal and spatial overlap encountered in the real experiment. Therefore, before the model can be directly compared to the experimental data a number of normalization procedures must be performed. The procedures used to eliminate the shot-to-shot fluctuations in the intensity of the FEL and optical laser and their spatial and temporal overlap will be discussed in the following section.

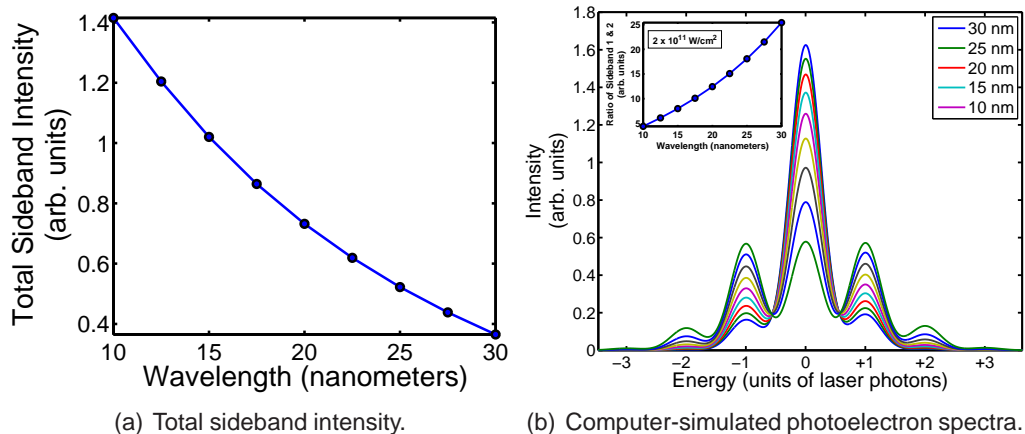


Figure 7.5: (a) Summation of the intensity of all sidebands (both low- and high-energy) in helium as a function of the wavelength of the FEL, determined using the soft-photon approximation where a fixed intensity ( $2 \times 10^{11} \text{ W/cm}^2$ ) of the optical laser was used. Calculated for the case of parallel polarization of both the pump and probe beams. Right-hand panel: Simulated photoelectron spectra using the computer model. Inset: The intensity ratio between the first and second high-energy sidebands as a function of FEL wavelength.

**Normalization Procedure for Experimental Data** Experimental data on two-color ATI in neon for FEL wavelengths of 13.9 nm and 26 nm will be compared to the simulated spectra from the computer model. These experiments were performed on different dates and so the variation in the performance of both FLASH and of the optical laser on each occasion must be accounted for. The average pulse energy of the FEL was  $20 \mu\text{J}$ , but the shot-to-shot energy fluctuated in the region of  $5 \mu\text{J} - 60 \mu\text{J}$ . Therefore, before a comparison of the spectra taken at the two FEL wavelengths can be made it was vital to correct the raw photoelectron spectra for these energy fluctuations. Fortunately, the long-term drift of the centre wavelength of the FEL can be ignored because the separation of sidebands depends only on the the energy of the optical laser photon.

The first procedure was to eliminate the shot-to-shot fluctuations in the energy of the FEL pulse. The energy of each macro-pulse of the FEL was determined from the signal from the gas-monitor detector (GMD) system [41] which is located near to the experimental chamber. Briefly, the intense FEL beam passes through a low-pressure gas cell containing xenon. Photoionization events create electrons and ions which then are detected by two Faraday cups, one for electrons and one for ions. The low gas pressure means that the unit is virtually transparent to the FEL beam and the system can be used continuously without attenuating the beam

intensity reaching the experiment. The system is absolutely-calibrated<sup>1</sup> and the signal from the system is directly proportional to the pulse energy of the FEL. By extracting the area under the curve in the GMD signal it is possible to determine a scaled value of the FEL pulse energy. The signal from the GMD system was used to normalize the corresponding photoelectron spectrum and in this way the shot-to-shot fluctuations in the beam intensity were accounted for.

It is important to note that the one-photon cross-section in equation 7.15 is also dependent on the photon energy of the FEL. Because the electrons are created in the primary ionization step, due to the FEL beam only, one can then deduce that the overall yield of electrons and hence MCP counts should scale with the shot-to-shot energy of the FEL. Therefore, by normalizing the total magnitude of the photoelectron peaks (the summation of the main photoline and the accompanying sidebands) in each spectrum to unity one can eliminate this energy dependence. The total electron yield remains constant between shots regardless of the wavelength or pulse energy of the FEL.

The intensity of the optical laser field which the ejected electron experiences will depend not only on the performance of the optical laser but also on the temporal and spatial overlap between the ionizing and dressing beams. The  $\alpha_0$  component in the argument of the Bessel function in equation 7.15 depends on  $F_{0L}$  which defines the amplitude of the optical dressing field. Firstly, the difference in the temporal overlap between the two lasers can be ignored as the pulse duration of the optical laser for these experiments was set to the 2 to 4 picosecond range which was significantly larger than the temporal jitter between the two sources. However, the variation in the spatial overlap of the two foci was a challenge to normalize. To minimize this effect the intensity of the laser in the most recent beamtime (February 2009) was adjusted so that the photoelectron spectra contained approximately the same number of sidebands as seen in 2007. In our experimental data, the 4<sup>th</sup> sideband was beginning to appear, and the soft-photon approximation predicted this to occur at a dressing field intensity in the region of  $4 - 10 \times 10^{11} \text{ W/cm}^{-2}$  in the case of helium.

Finally, the intensity of the optical laser ( $F_{0L}$ ) is also a critical parameter in the formation of the sidebands. A high intensity optical dressing field (typically  $> 4 \times 10^{11} \text{ W/cm}^2$ ) can produce multiple sidebands in the photoelectron spectrum. Using the ratio of sidebands rather than the overall magnitude of a single sideband results in a

---

<sup>1</sup>Calibrated in the Radiometry Laboratory of the Physikalisch-Technische Bundesanstalt at the electron-storage ring BESSY II in Berlin by Sorokin *et al.* [41].

more accurate determination of the laser field experienced by the electrons. There is only the possibility of one laser intensity for any one particular sideband ratio, hence it is a more accurate way to determine the actual laser intensity experienced by the photo-ejected electrons.

To summarize, before comparing the theoretical results of changing the momentum of the ejected electron ( $k$  in equation 7.15) on the magnitude of the sidebands the other variables in the experiment were normalized. The signal from the GMD system was used to eliminate the fluctuations in the intensity over a number of consecutive shots of the FEL. The one-photon cross-section which is dependent on the wavelength of the FEL has been normalized by ensuring the total electron yield remains equal to unity. And finally, the differences in the optical dressing field between the two data sets was reduced by selecting the ratio between sideband intensities, rather than the intensity of a single sideband. These normalization procedures have been performed on all data used for this comparison. With this in mind, we are now in a position to compare the two data sets, knowing that the only major difference between them will be the kinetic energy of the ejected electron.

**Interpreting the Experimental Results** In figure 7.6 a selection of spectra from neon (a) and xenon (b) are shown for different wavelengths of the FEL. The data has been subjected to the normalization procedures discussed above. The spectra of neon were taken at FEL wavelengths of 13.9 nm and 26 nm and show an increase in the number of sidebands as the wavelength decreases. The same trend can be seen in xenon, the additional spectrum taken at 55nm also follows the trend. In both cases the intensity of the main photoline decreases as the number of sidebands increases as expected. However, on close inspection we find that the intensity of the NIR laser drifted during the course of the experiment. This means that the modulation in the sidebands could be caused by either the change in the wavelength of the FEL, or perhaps by a change in the intensity of the optical dressing field; both of which affect the argument of the Bessel function.

Gaussian profiles were manually fitted to the experimental spectra and the area under each of the photoelectron peaks was recorded. The ratio between the areas of the first and second sidebands were calculated for each of the spectra, see insets in figure 7.6. For a direct comparison between the experimental spectra taken at the different wavelengths of the FEL it is important that the intensity of the optical laser remains fixed for the duration of the experiment. The most accurate way to

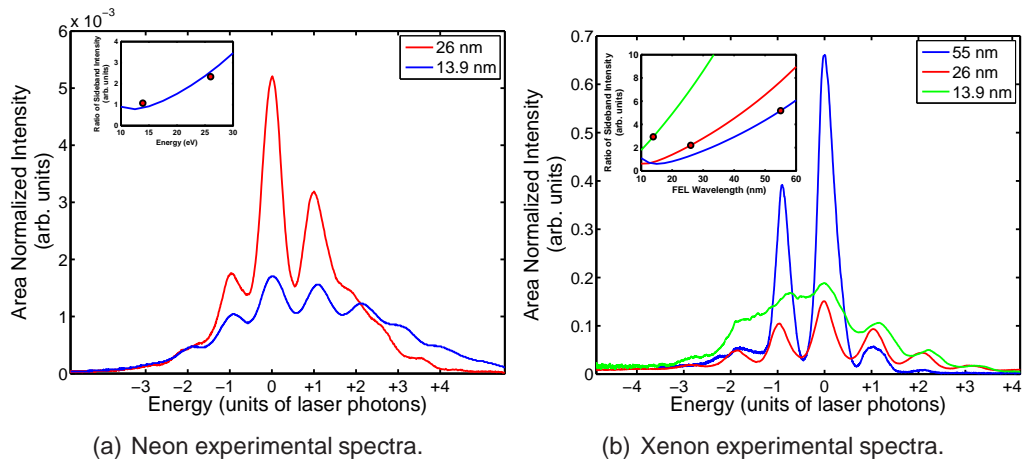


Figure 7.6: Two-color photoionization spectra of neon (a) and xenon (b) taken with different wavelengths of the FEL. Inset: The red markers represent the ratio between the magnitudes of the first and second sidebands for each spectrum and the solid traces represent the sideband intensity ratios calculated using the soft-photon approximation, for different intensities of optical dressing field. In the case of neon, a single laser intensity ( $1.15 \times 10^{12} \text{ W/cm}^2$ ) fits well to the experimental data, meaning that the wavelength of the FEL was the only variable in the experiment. However in the case of xenon, a single intensity does not directly describe the three spectra. The intensity of the NIR laser appears to have drifted between each experiment and as such the analysis of the photoelectron spectra is further complicated. The solid lines in the inset represent results from the computer model for a NIR laser intensity of 0.36 (green trace), 0.93 (red trace) and  $1.34 \times 10^{12}$  (blue trace), respectively.

determine if this is the case is to compare the experimental sideband intensity ratios to that from the computer model. The solid traces in each of the insets in figure 7.6 represents the sideband intensity ratios from the model, calculated for different laser intensities. In the case of neon, figure 7.6 (a), a single laser intensity ( $1.15 \times 10^{12} \text{ W/cm}^2 \pm 10\%$ ) fits well to the experimental sideband ratios for spectra at either FEL wavelength. This means that the two experimental spectra were recorded in much the same conditions, save for the wavelength of the FEL and that we can be confident with comparing the two spectra. On this basis, we find that neon conforms to the theoretical predications and the number of photoelectron sidebands increases as the wavelength of the FEL decreases, i.e., as the argument of the Bessel function increases.

However, this was not the case for xenon. Here, the computer model was not able to replicate the ratios between the sidebands for a single laser intensity. This is clearly seen in the inset in figure 7.6 (b), where there is no correspondence between the experimental data (red markers) and any one of the solid traces. The

computer model reveals that the intensity of the optical laser varied between  $3.5 \times 10^{11}$  W/cm<sup>2</sup> and  $1.3 \times 10^{12}$  W/cm<sup>2</sup>. A direct comparison of the experimental spectra in the case of xenon was not possible, as the drift in the intensity of the laser will act to mask the affect of the change in momentum of the photoelectron.

### 7.2.3.2 Atomic Number of Element

In this section the magnitude of the photoelectron sidebands will be studied as the atomic number of the atom under inspection is changed. The soft-photon approximation predicts that as the sample gas is changed from helium to xenon (and the ionization potential of the atom decreases) the wave vector ( $k$ ) of the dressed electron will increase. The shifted wave-number of the photoelectron is given as

$$k = \sqrt{2(E_{FEL} + E_{IP} + nE_{laser})} \quad (7.21)$$

where  $E_{FEL}$  and  $E_{laser}$  are the photon energies of the FEL and the optical laser respectively,  $n$  is the number of photons absorbed (or emitted) and  $E_{IP}$  is the ionization potential of the atom. In the study presented here, both the energy of the FEL and optical laser remains fixed. As the gas is changed and the ionization potential decreases the argument of the Bessel function in equation 7.15 will increase. Therefore one would expect to observe an increase in the redistribution of the electrons from the main photoline into the sidebands, i.e., as one moves from helium to xenon one would expect to see an increase in the number of sidebands in the photoelectron spectrum.

The computer model was run for the different elements and the intensity of all high and low order sidebands was summed; the results are plotted in figure 7.7 (a). One may see in the figure that the computer simulations do not appear to follow the general trend. In fact the results serve to highlight that the one-photon cross section dominates the number of visible sidebands. More specifically, the asymmetry parameter  $\beta$  appears to dictate the general trend. There is a clear decrease in the total sideband yield in the case of Krypton where the value of the asymmetry parameter for Kr  $4p^{-1}$  is approximately 0.1 [39]. This value is significantly lower than that of either helium ( $\beta = 2$ ) [27], neon ( $\beta = 1.35$ ) [42] or xenon ( $\beta = 1.62$ ) [43]. The simulations were repeated using a fixed value of the  $\beta$  parameter ( $\beta = 2$ ) and are represented by the red diamonds in figure 7.7 (a). In this unphysical scenario the dependence of  $\beta$  in the one-photon yield is ignored and the model predicts a general increase in the total sideband yield.

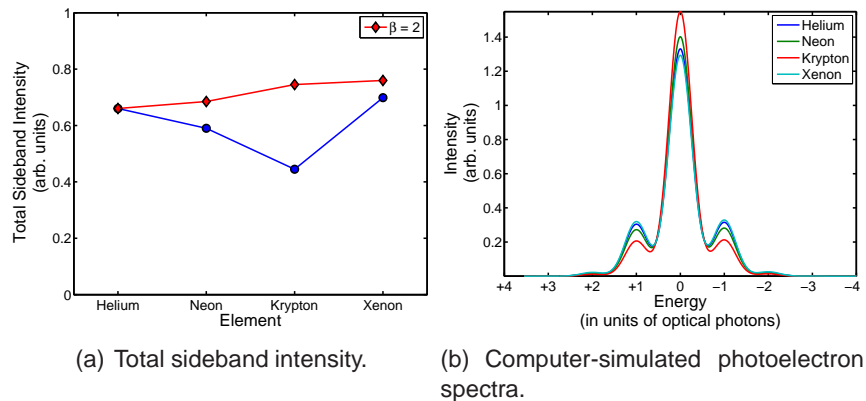


Figure 7.7: Total sideband intensity predicted by the soft-photon approximation for a selection of the rare gas elements. The blue circles indicate a calculation done with the correct value for the asymmetry parameter for each element, while the red diamonds represent a calculation using a beta of 2. The intensity of the optical dressing field was  $5 \times 10^{11}$  W/cm<sup>2</sup>. Right: Simulated photoelectron spectra for the various rare gas elements using the correct beta parameter for the respective element.

Photoelectron spectra were recorded for helium, neon, krypton and xenon at an FEL photon energy of 90.5 eV (13.7 nm) and an optical laser wavelength of 800 nm. The optical laser had a pulse energy of 1.6 mJ and a pulse duration of  $\sim 3$  ps yielding an intensity of  $3 \times 10^{13}$  W/cm<sup>2</sup> at the focus (50  $\mu$ m spot diameter). The temporal delay between the FEL pulse (ionizing the atom) and the optical field was scanned in the range  $\pm 3$  ps and 100-shot averaged photoelectron spectra were recorded. The spectra are shown in figure 7.8.

The intensity of the optical laser was kept relatively constant for the duration of the experiment, ensuring that the  $\alpha_0$  parameter did not mask the results. Furthermore, the area of each spectrum was normalized to unity which ensured that the fluctuations in the energy of the FEL were accounted for. The spectra are shown for a range of time delays between the two laser fields. As the delay was scanned over the range  $\pm 3$  ps the intensity and number of photoelectron sidebands grew as the temporal delay between the two fields (EUV and NIR) approached zero. Examining the spectra taken at the optimum temporal overlap for each gas target one can clearly see that the number and intensity of sidebands scales directly with the atomic number of the element. Helium produces two sidebands, neon produces three, krypton produces two and finally xenon produces four high-energy sidebands. The two exceptions to the general trend appear to be neon and krypton. In the case of Kr it appears that the prediction that the sideband intensities

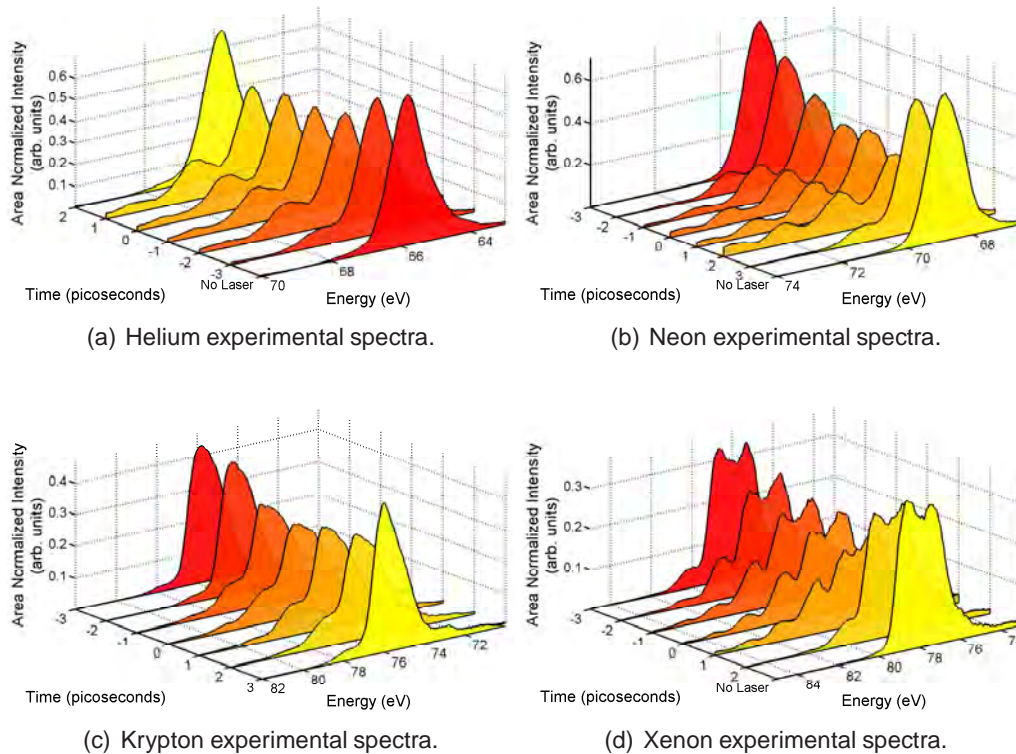


Figure 7.8: Waterfall plot presentation of photoelectron spectra taken during a temporal scan between the pump and probe beams for a selection of rare gas elements. As the delay between the pump and probe beams reaches a minimum a maximum in the number of photoelectron sidebands are observed.

should depart from the generally increasing intensity trend is indeed verified experimentally. In the case of Kr the asymmetry parameter is only 0.1 and is hence less than 10% of the value of the next highest value (Ne at 1.35). This reduction, as was demonstrated using the soft-photon approximation above acts to significantly reduce the one-photon cross section, leading to the reduction in the sideband signal seen here. Ne also departs from the trend by exhibiting three clearly defined sidebands. The observation is still not well understood. However, a preliminary calculation by Hugo van der Hart [44] predicts the existence of resonances around the FEL wavelength which could give rise to a beta parameter significantly different from off-resonance case. So interference from these neighbouring resonances is at present the proposed reason.

The spectra were examined in more detail by extracting the ratio of the sideband magnitudes and comparing these to the soft-photon approximation. The procedure

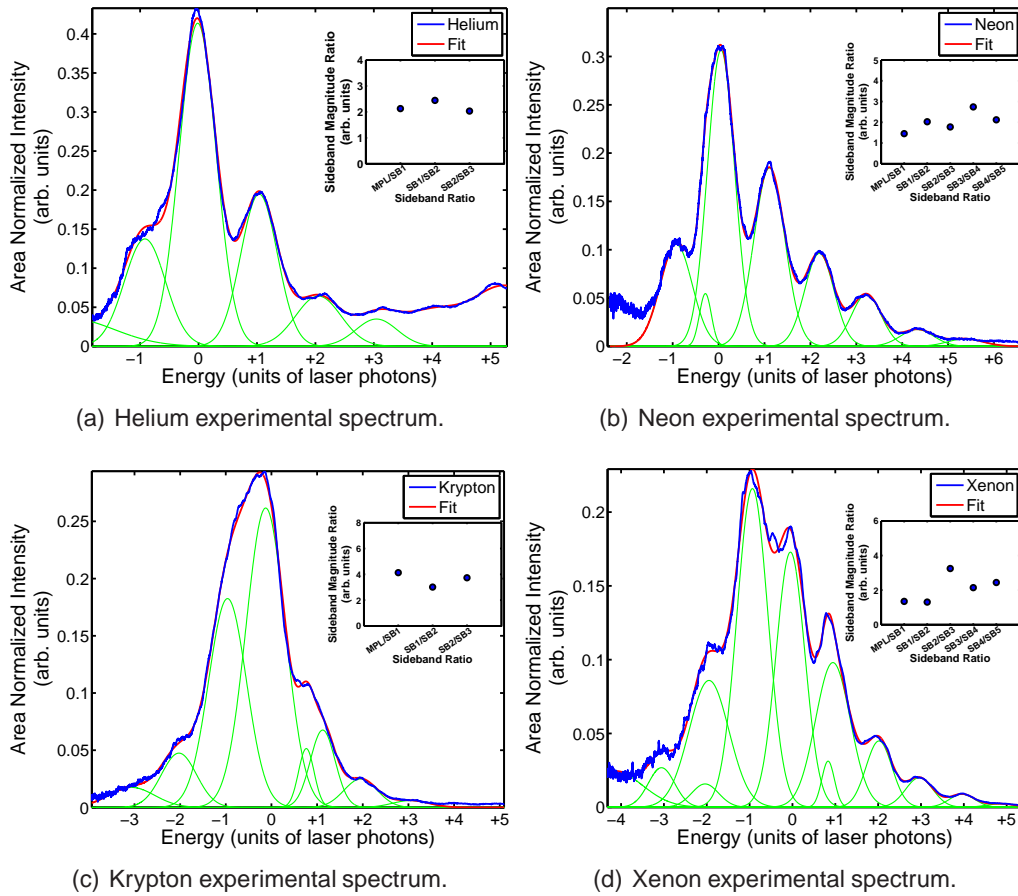


Figure 7.9: Photoelectron spectra for a selection of the rare-gas elements for zero delay between the FEL (pump) and the optical laser (probe) beams. Gaussian fits to the experimental data are represented by the green lines and the combined fit is given by the red line. The area of each spectrum has been normalized to unity. Inset: Ratio of the areas of consecutive sidebands used to determine the intensity of the optical dressing field.

begins with the fitting of multiple Gaussian profiles to the spectra of each target gas,  $\Delta t = 0$  ps. The experimental spectra and the corresponding fits are shown in figure 7.9. The x-axis is in units of optical photon energy (1.55 eV) and the Gaussian fits are represented by the green lines. The area of each fit was extracted and the ratio of consecutive sidebands was plotted (see inset in each figure). These sideband ratios were used to determine a more precise value for the optical laser intensity in the interaction volume by comparing them to the ratios extracted from the computer-simulated spectra.

The computer model was adapted to incorporate a minimization routine whereby an initial estimate of the laser intensity was used to produce a simulated spectrum.

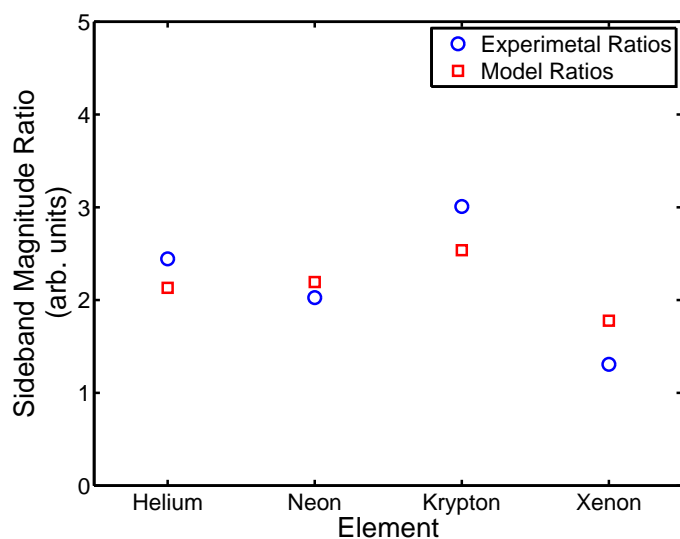


Figure 7.10: Ratio between the magnitude of the first and second high-energy sidebands for a selection of rare gas atoms. A calculation using the soft-photon approximation is shown in red. The output from the model was minimized to the experimental data which resulted in a best fit for an average intensity of  $5.22 \times 10^{11} \text{ W/cm}^2$  for the optical dressing field.

The ratio of the sideband areas in this spectrum were then compared to that of the experimental spectrum. Using the *fminsearch* function in Matlab the value of the laser intensity was then varied until the difference between the simulated and experimental spectra was at a minimum. Figure 7.10 shows the ratio of the first to second sidebands for the different elements. Using this method an intensity of  $5.22 \times 10^{11} \text{ W/cm}^2$  gave the best fit to all the data.

In this section, the soft-photon approximation has been used to model the effect of changing the atomic number of the atom under study. The model revealed that the sideband intensity is dominated by the  $\beta$  parameter contained within the one-photon cross section, rather than the change in the value of the  $k$ -vector of the ejected electron due to the reduction in the ionization potential. Experimentally it was found that the intensity and number of photoelectron sidebands scaled directly with atomic number. Exceptions to this rule were found in the case of neon, where a total of five high-energy sidebands were observed. It was postulated that this is perhaps a result of quantum interference between neighbouring autoionizing resonances which may be present for the energies quoted here. The decrease in the number of sidebands in Krypton was attributed to the substantial reduction in the  $\beta$  parameter for the Kr 4p shell. Finally, the soft-photon approximation was used to

reveal the true laser intensity within the interaction volume which was found to be in the region of  $5 \times 10^{11}$  W/cm<sup>2</sup>.

### 7.2.3.3 Optical Laser Wavelength

In this last section the dependence of the two-color process on the wavelength of the optical laser is examined. The behavior of the photoelectron sidebands with changing optical laser wavelength is modeled with the aid of the soft-photon approximation.

The primary effect of the optical laser in the two-color process is the redistribution of the electrons into the sidebands. Equation 7.15 shows that the effect of the optical laser is entirely contained in the argument of the Bessel function and can be separated into two distinct terms. The first term is the  $k$ -vector of the ejected electron which is given by,

$$k = \sqrt{2(E_{IP} + \omega_x + n\omega_L)} \quad (7.22)$$

where  $E_{IP}$  is the binding energy of the electron and  $\omega_x$  is the angular frequency of the FEL photon. The optical laser effect appears here in the variable  $n\omega_L$ , where  $n$  is the number of optical photons absorbed or emitted and  $\omega_L$  is the angular frequency of an optical photon. It was shown that  $k$ -vector of the outgoing electron becomes quantized into discrete levels called sidebands, the separation of which depends on the value of  $\omega_L$ . The Ti:Sapphire laser used in the experiments at FLASH was operated at both the fundamental (800 nm) and its second harmonic 400 nm. This allowed us to generate and study sidebands separated by either 1.55 eV or 3.1 eV.

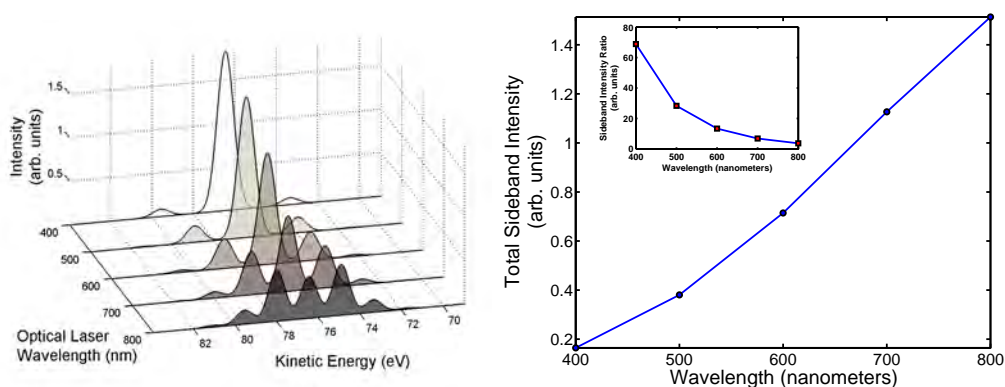
The second and most influential term which involves  $\omega_L$  is of course the  $\alpha_0$  parameter. The value of  $\alpha_0$  depends solely on the optical laser and is given by,

$$\alpha_0 = \vec{F}_{0L}/\omega_L^2 \quad (7.23)$$

where  $\vec{F}_{0L}$  is the intensity of the optical laser. In effect this parameter acts to redistribute electrons from the main-photoline into the sidebands, with the intensity of the optical laser ( $\vec{F}_{0L}$ ) determining the extent of this redistribution. But this equation also shows that  $\alpha_0$  scales with the wavelength of the laser. So, in effect, one would also expect that at a fixed intensity the smaller the frequency the larger than the influence of the laser on the ejected electron [37].

Simulations of the soft-photon approximation for the case of helium irradiated by

superposed EUV and optical laser fields as the wavelength varies from 800 nm to 400 nm are shown in figure 7.11. The spectra show that for a fixed intensity of the optical laser the number of sidebands scales directly with the wavelength of the optical photon. This result is seen more clearly in figure 7.11 (b) where the total sideband yield is plotted as a function of the wavelength of the optical laser. One can see that as the wavelength of the optical laser increases the total sideband yield also increases.



(a) Computer-simulated photoelectron spectra of helium for different optical laser wavelengths.

(b) Total sideband intensity.

Figure 7.11: Photoelectron spectra simulated using the soft-photon approximation for helium as a function of the wavelength of the optical dressing field. (b) Total sideband yield as a function of the wavelength of the optical laser. Inset: Ratio between the magnitudes of the first and second high-energy sidebands in the model which are used to determine the true intensity within the interaction region. The calculation was performed using helium and the target gas, an FEL wavelength of 13.9 nm and an optical laser intensity of  $1 \times 10^{12}$  W/cm<sup>2</sup>.

Comparing this simulation to the experimental data is not straight forward, and caution must be exercised as to how one interprets these results. Due to the low efficiency of the 2<sup>nd</sup> harmonic generation process the average energy of the laser at 400 nm was typically 350  $\mu$ J, while at 800 nm it was 2 mJ. A drop in intensity of the optical laser will no doubt drop the number of sidebands observed (refer to figure 7.3 on page 228). Furthermore, at 800 nm the separation between the sidebands is 1.55 eV, whereas at 400 nm it will be 3.1 eV. In our experiments xenon gas was used as the sample because it produces the strongest sidebands.

Presented in figure 7.12 are spectra of the two-color ionization of xenon plotted as a function of the delay between the FEL and optical laser. On the left-hand side are spectra taken using the 400 nm beam from the optical laser while on the right-hand

side are spectra taken using the 800 nm fundamental beam. The optical laser in this case had a pulse duration of 120 fs meaning that the overlap window is greatly reduced. Consequently the sidebands are only observed over a very small time-delay window of approximately 0.5 ps FWHM, the FWHM of the jitter curve between the two sources. Clearly visible in both waterfall plots is the spin-orbit splitting of the 5p main photoline. The two spin-orbit components are split by approximately 1.3 eV and both produce photoelectron sidebands. In the case of the 400 nm one can see that the sidebands also contain this structure. But in the case of 800 nm case this structure overlaps with the preceding sideband. The spin-orbit splitting of 1.3 eV is on the order of the photon energy of the laser and so the first sideband of the  $5p_{3/2}$  line will overlap with the second sideband of the  $5p_{1/2}$  line, and so forth.

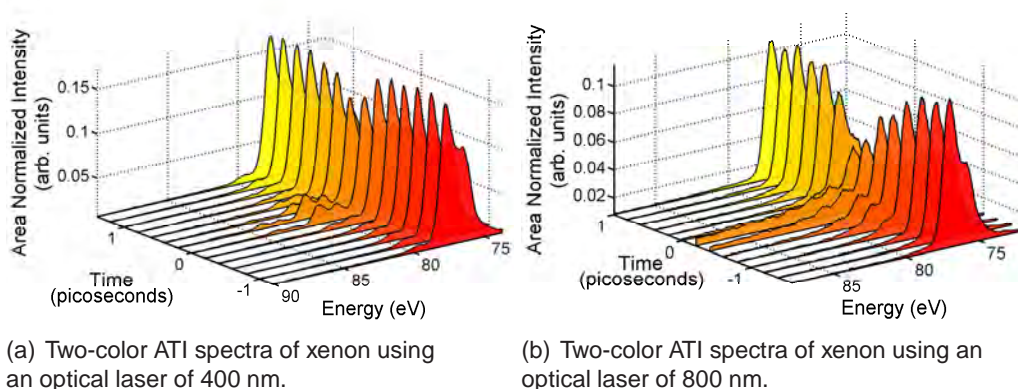


Figure 7.12: Temporally resolved photoelectron spectra of the two-color above-threshold ionization of xenon using a combination of 13.9 nm radiation from the FEL and 400 nm (left) or 800 nm (right) radiation from the optical laser. The main-photoline corresponds to the ionization of the Xe 5p line and lies at approximately 77 eV. The two spin-orbit components (separated by 1.3 eV) are visible in both the main-photoline and in the sidebands. In the case of 800 nm the sidebands of the two components are overlapped and so the spin-orbit structure is not observed.

From the experimental data one can see that as the wavelength of the optical laser increases the number of sidebands also increases. Whether or not the effect of the overlapping sidebands in the case of the 800 nm data is amplifying the signal is difficult to determine. A comparison between the ratio of the sidebands with that from the model may reveal a departure from theory.

Figure 7.13 shows two photoelectron spectra taken using a 400 nm (left) and 800 nm (right) optical laser when the temporal delay between the FEL and optical laser was at a minimum. The green lines in the figure represent Gaussian fits to the

individual peaks from which the areas of the sidebands are extracted (see inset). These spectra clearly show a dramatic increase in the number of sidebands when the wavelength of the optical laser is increased from 400 nm to 800 nm. The data corresponding to the 400 nm laser shows the presence of three sidebands, while for the 800 nm spectrum there are a possible five sidebands visible.

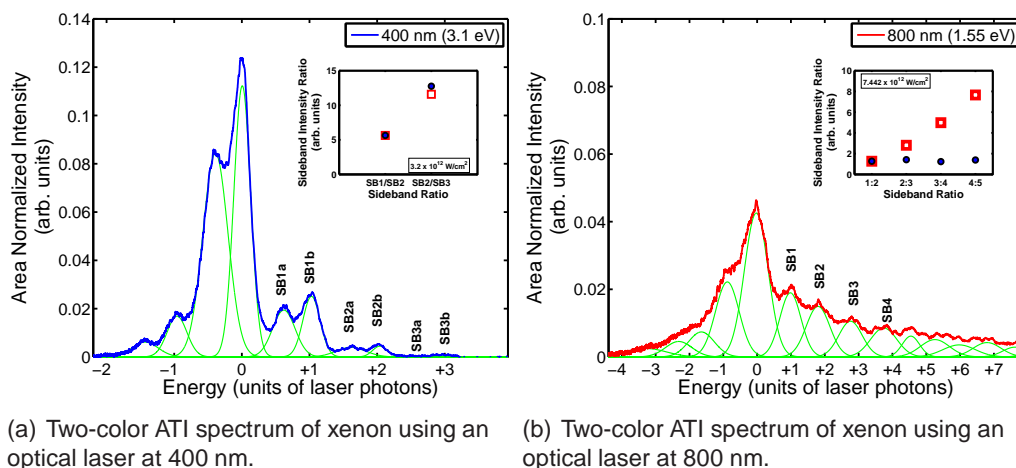


Figure 7.13: Two-color photoelectron spectra of xenon taken for two different wavelengths of the optical laser. Left-hand panel: 400 nm optical laser where the sidebands are separated by 3.1 eV. Right-hand panel: 800 nm optical laser, where the sidebands are separated by 1.55 eV. Gaussian profiles (green lines) have been fitted to each peak in the data and used to determine the area of each sideband. Inset: Ratio between the areas of consecutive sidebands which will be used to highlight a departure from theory.

The spin-orbit splitting of the Xe 5p level is clearly visible in both spectra, and the sidebands in the spectrum corresponding to the 400 nm laser show signs of structure also. This is not the case for the 800 nm data where sidebands from the different spin-orbit components overlap with the alternate sideband from the other component. The inset in each figure shows the ratio of consecutive sidebands (blue) and a fit using the experimental data (red). As can be seen in the 400 nm case the ratio of the first to second sideband gives very good agreement to the model for an intensity of  $\sim 3 \times 10^{12} \text{ W/cm}^2$ . In the case of the ratio of sidebands in the 800 nm case, the data set shows clear signs of a departure from the soft-photon approximation. It appears that the first sideband will fit the model for an intensity of  $7.5 \times 10^{12} \text{ W/cm}^2$  while the ratio of the second to third sideband drifts slightly. The departure from the model at higher sideband ratios is caused by, either a high background signal and/or by mixing between the sidebands of the two spin orbit components.

In this section the concept of two-color above-threshold ionization in rare gases was examined. When an electron is ejected from an atom through photoionization in the presence of an intense laser field it was shown that under certain conditions this ejected electron may exchange one or even an integer number of laser photons with the NIR laser field. The photoelectron spectrum will contain a main photoline corresponding to the one-photon ionization event surrounded by sideband peaks which are separated by the photon energy of the optical laser. The soft-photon approximation was introduced and a computer model was used to help describe the parameters which affect the intensity of the sidebands and the two-color process. While the comparison between the model and experiment was rather qualitative in places, the experimental data did agree with the overall trends predicted by the model. It was shown that the sideband intensity and quantity scaled with FEL wavelength, optical laser wavelength, laser intensity and target ionization potential in a manner well described by the soft-photon approximation.

#### 7.2.4 Polarization Control in Two-color Above-Threshold Ionization

The dependence of the high-energy sidebands on the angle between the polarization vectors of the FEL and optical laser fields will be studied in this section. The specific case of helium, where photoionization originates from the  $s$ -shell and where the electron is promoted to an  $\epsilon p$  state in the helium photoionization continuum will form the primary example in this study. The optical laser will induce further transitions between this  $\epsilon p$  state to either  $\epsilon s$  or  $\epsilon d$  states in the continuum. These are known as free-free transitions. Therefore, a single sideband will be composed of a superposition of electron waves having undergone either  $\epsilon p \rightarrow \epsilon s$  or  $\epsilon p \rightarrow \epsilon d$  transitions. The photoelectron detector used in these experiments captured electrons from  $4\pi$  and was not angle resolving. Hence it was unable to discriminate between electrons with different angular momenta. So in order to map the angular distribution of the photoelectrons and to determine the relative contribution each channel makes to the overall magnitude of the sideband the polarization vector of the optical laser was rotated with respect to the fixed position of the entrance slit of the electron spectrometer. In this way, it was possible to probe the angular distributions of the photoelectrons and determine the relative contribution which the two ionization channels make to the formation of the sidebands.

Studies of this kind have been performed in the past using EUV photons produced from high-order harmonic generation (HOHG or HHG) sources, see refs. [8, 26, 23] and references therein. In these experiments the many harmonics in the source

produced evenly-spaced peaks resulting in a comb of photoelectron lines each due to the one-photon (EUV harmonic) ionization process. The time-synchronized optical dressing laser field introduced even more coherent continuum channel couplings with a concomitant complex interference between the many competing ionization pathways. These experiments while elucidating the underlying physics of the two-color process were complicated by these effects of interference, making the analysis quite challenging. The aim of the work presented here is to study the two-color ATI process using the intense and nearly monochromatic EUV beam from FLASH. The properties of FLASH are ideal for such an experiment and facilitate for the very first time an interference-free study of two-color above-threshold ionization.

Detailed analysis using both a modified version of the soft-photon approximation (carried out by Richard Taïeb and Alfred Maquet for the He case and also with my own simplified code for it and all other targets) and second-order perturbation theory (carried out by Grum-Grzhmailo *et al.* [45]) in helium was restricted to a low-intensity  $\leq 10^{12}$  W/cm<sup>2</sup> optical dressing field, where a single sideband was produced as a result of the two-photon (one EUV photon and one IR photon) process. At higher intensities of the optical laser multiple sidebands are produced due to multiple photon emission/absorption events. The photoelectron sidebands are then composed of electrons which have undergone many transitions in the continuum. In this case the number of angular momentum channels,  $d, f, g, h$ , etc. grows quickly with the order of the sideband and the calculation becomes very complex. The final section of this chapter briefly examines some of the other rare gas targets, namely neon, krypton and xenon. In the case of these elements, the continuum states will have the configuration  $p^5\epsilon l$  where  $\epsilon$  is the photoelectron kinetic energy and  $l$  is the orbital angular momentum. A qualitative comparison between the soft-photon approximation and the experimental data will be made in this case. With this in mind the study of photoionization of rare gases begins with helium as our primary target.

#### 7.2.4.1 Helium

First to be examined is the polarization dependence of the photoelectron sidebands produced in helium in the regime of low optical dressing field. In this case the  $\alpha_0$  parameter describing the laser field strength is quite low resulting in a small value of the argument of the Bessel function in equation 7.15 which in turn leads to the formation of one sideband on both the high- and low-energy sides of the main He

1s photoline. This ionization scheme is illustrated on the left-hand-side of figure 7.14. An EUV photon from the FEL (represented by the blue arrow) promotes a 1s electron into an  $\epsilon p$  state in the helium continuum. This electron may then couple to the time-synchronized optical laser absorbing a photon (red arrows) and undergo a transition to either an  $\epsilon s$  or an  $\epsilon p$  state. At these low intensities the single sideband is composed of electrons having undergone either an  $\epsilon p \rightarrow \epsilon s$  or an  $\epsilon p \rightarrow \epsilon d$  transition, where  $\epsilon$  represents the kinetic energy of the free-electron. It is assumed that the  $k$ -vector of the ejected electron is preferentially aligned parallel to the polarization vector of the FEL beam [46], and, as the two final states have a different orbital symmetry, the ratio of the contribution of these two pathways to the measured photoelectron sideband amplitude will depend on the relative angle between the linear polarization vectors of the FEL and optical laser. By rotating the plane of polarization of the optical laser with respect to the FEL one can directly tune the ratio of contributions from each ionization channel to the overall sideband signal. The dichroism in the two-color process can then be determined by calculating the intensity difference  $I_{\parallel} - I_{\perp}$  for the first sideband.

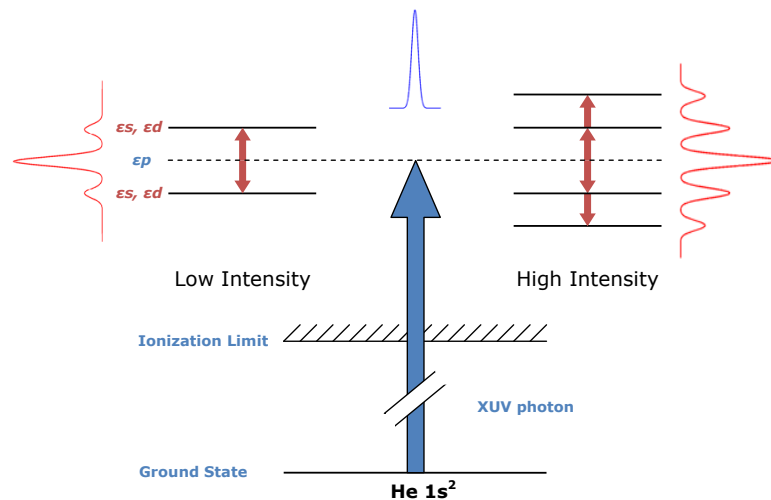


Figure 7.14: Simplified energy level diagram illustrating the two-color above-threshold ionization (ATI) of a helium 1s electron using a combination of 13.7 nm and 800 nm beams from the FEL and optical laser respectively. The scheme for low-intensity ( $10^{10} \text{ W/cm}^2$ ) and high-intensity  $10^{12} \text{ W/cm}^2$  of the optical dressing field are depicted on the left and the right-hand side of the figure respectively [45].

In the second instance, a high-intensity optical laser was used to produce multiple photoelectron sidebands in helium. Using a high intensity optical dressing field there is the possibility of exchanging a number of IR photons with the photoelectron

which results in the formation of multiple sidebands. This is illustrated on the right-hand-side of figure 7.14. One may recall from equation 7.9 on page 225 that the  $\alpha_0$  parameter contained in the Bessel function of the soft-photon approximation depends on  $\vec{F}_{0L}$ , the amplitude of the optical laser field. An increase in  $\vec{F}_{0L}$  will lead to a larger argument in the Bessel function resulting in an increase in the redistribution of the electrons from the main photoline into the sidebands. The multiple sidebands complicate things as each sideband may now be composed of multiple competing pathways with either even (*s, d, g, ...*) or odd (*p, f, h, ...*) symmetries. In this case the precise calculation of the matrix elements for each of the different channels is not easy using second order perturbation theory, however the soft-photon approximation is able to reproduce the general polarization trend for all atoms and for multiple sidebands.

### Low-Intensity Optical Laser

A FEL wavelength of 13.7 nm (90.5 eV) was selected for the one-photon ionization of helium. The binding energy of the 1s electron in helium is 24.6 eV and therefore upon photoionization the ejected electron had a kinetic energy of approximately 66 eV. The Ti:sapphire laser was operated at the fundamental wavelength of 800 nm and had a pulse duration of 4 ps, an average pulse energy of 2 mJ and was focussed to a spot approximately 50  $\mu\text{m}$  in diameter. The intensity of the optical laser was attenuated to  $\sim 8 \times 10^{10}$  W/cm<sup>2</sup> through a combination of pulse lengthening and by passing the beam through an attenuator composed of a polarizer and a half-wave plate. Once the optical laser and FEL beams were overlapped in time and space using the methods described earlier, a series of photoelectron spectra were recorded as the relative angle between the linear polarization vectors of the two lasers was varied. The polarization angle of the optical laser was controlled by rotating a half-wave-plate which was located in the optical path of the 800 nm beam. In this low-field regime a single sideband was observed on the high-energy side of the main photoline resulting from the two-color ATI process.

Figure 7.15 shows a series of typical photoelectron spectra with the helium 1s photoline positioned at ca. 65.5 eV plotted as a function of the angle between the linear polarization vectors of the FEL and optical fields. A slight shift in the energy of the main photoline is due to a combination of the ponderomotive shift (calculated to be 60 meV) and some space-charge effects<sup>2</sup>. The calculated ponderomotive shift

---

<sup>2</sup>Caused by the electrostatic charge on a fiber optic ferrule located in close proximity to the interaction volume.

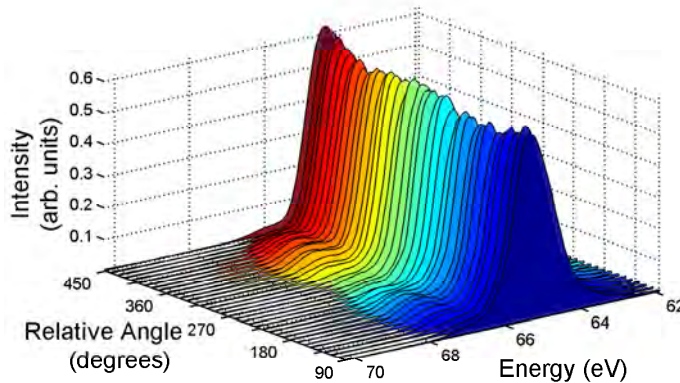


Figure 7.15: Series of photoelectron spectra showing the He 1s photoline and the high energy sidebands for low intensity of the optical dressing field ( $\sim 8 \times 10^{10}$  W/cm<sup>2</sup>). Spectra are shown for incremental values of the polarization angle ( $\phi$ ) between the linear polarization vectors of the EUV and optical lasers. The FEL was operating at a wavelength of 13.7 nm.

was  $\sim 10$  meV. Each individual spectrum is composed of an average of 100 single-shot spectra and so the spectra may become broadened as a result of summing the spectra where the shot-to-shot drift in the wavelength of the FEL is aggregated into an apparent line broadening. A single sideband may be seen on the high kinetic energy side of each photoelectron spectrum. A voltage of -60 V was applied to the retardation grids at the entrance to the MBES in order to improve the resolution of the spectrometer. This has the effect of suppressing the low-energy portion of the spectrum so therefore the low-energy sideband are not observed.

In figure 7.15 one can see that the intensity of the sidebands vary as the polarization angle of the optical laser is changed, with the sidebands reaching a maximum when the polarization vectors of the two fields are parallel i.e., at  $n\pi$  (where  $n = 0, 1, 2, \dots$ ) and a minimum when they are perpendicular. Because the optical laser does not contribute to the primary one-photon ionization process, the total ion yield will remain constant, irrespective of the intensity of the optical laser. The modulation of the intensity of the main-photoline appears to be quite faint in the experimental data. This may be due to the following reasons: The focus of the optical laser may not fully overlap that of the FEL, and so some electrons in the periphery of the interaction volume may experience little or no dressing field of the optical laser. These electrons will add intensity to the main-photoline thus distorting the correct peak intensity ratios. The second and most likely cause is that the MCP detector was saturated (by the main strong photoline only). In this case the number of electrons

impinging on the detector was so high that the electron detector was operating in a non-linear regime.

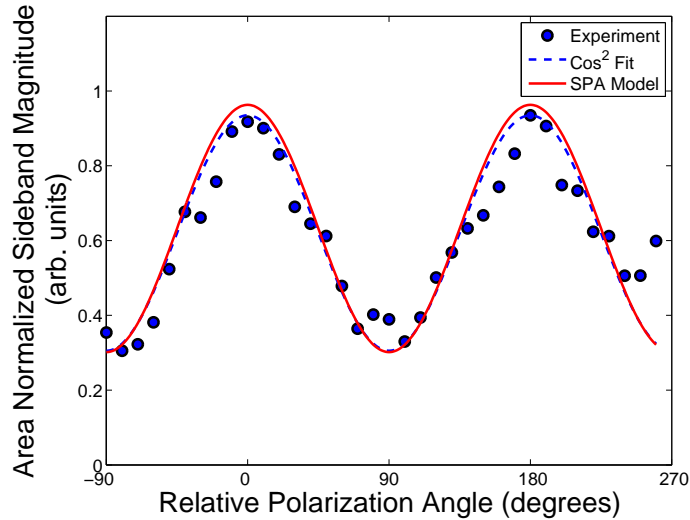


Figure 7.16: Magnitude of the first photoelectron sideband in helium as a function of the relative angle between the linear polarization vectors of the FEL and optical laser for a low-intensity optical dressing field ( $\sim 8 \times 10^{10}$  W/cm<sup>2</sup>). The dashed blue line is a  $\cos^2$  fit to the experimental data and the red line represents the output from the soft-photon approximation model.

The sensitivity of the polarization dependence of the photoelectron sidebands is more clearly illustrated when the integrated intensity of the first sideband is displayed as a function of the relative orientation between the two linear polarization vectors. This is done in figure 7.16. To determine the magnitudes of the sidebands, the first stage was to subtract a background signal from each spectrum. Then Gaussian profiles were fitted to each of the peaks in the spectrum where the area under the curve was taken as a measure of the magnitude of the sideband. As the intensity of the optical dressing field was low ( $\sim 8 \times 10^{10}$  W/cm<sup>2</sup>), only one sideband was observed. In this low-dressing field regime a total of two photons give rise to the formation of the first sideband, a single EUV photon which initially promotes the electron in the 1s shell up to an  $\epsilon p$  state in the continuum; and a second infrared photon (from the optical laser) which is absorbed (or emitted) by this electron, promoting it to either an  $\epsilon s$  or an  $\epsilon d$  state. It is assumed that the  $k$ -vector of the photoelectron will be aligned parallel to the linear polarization vector of the FEL and so the contribution from either an  $\epsilon p \rightarrow \epsilon s$  or an  $\epsilon p \rightarrow \epsilon d$  channel in the formation of the sideband will depend on the relative polarization angle between the two laser fields.

Figure 7.16 shows a  $\cos^2$  dependence of the sideband intensity on the relative angle between the field polarization vectors and is in excellent agreement with the predictions of the soft-photon approximation model (solid red line). It has been shown that when the kinetic energy of the ejected electron is considerably larger than the photon energy of the dressing field (the so called soft-photon limit) then the differential cross section for the absorption of one EUV photon along with the exchange of  $n$  optical photons can be written as [27],

$$\frac{d\sigma^{(n)}}{d\Omega} = J_n^2(\vec{\alpha}_0 \cdot \vec{k}_n) \left( \frac{d\sigma^{(0)}}{d\Omega} \right) \quad (7.24)$$

where  $k_n = \sqrt{2(E + \omega_X + n\omega_L - U_p)}$  is the shifted wave number of the ejected electron,  $\vec{\alpha}_0 = \vec{F}_{0L}/\omega_L^2$  is the classical excursion vector of a free electron embedded in a laser field of amplitude  $\vec{F}_{0L}$ , and  $d\sigma^{(0)}/d\Omega$  is the one-photon cross-section. The cross section  $\sigma^{(n)}$  of the two-color ATI process is obtained by integrating over the electron solid angle  $\Omega \equiv (\eta, \phi)$ . In the simple case of a 1s electron in helium the cross section is given by [27],

$$\sigma^{(n)} \propto a_n + b_n \cos^2 \theta \quad (7.25)$$

where the coefficients  $a_n$  and  $b_n$  are:

$$\left. \begin{array}{l} a_n \\ b_n \end{array} \right\} = \int_0^{\pi} d\eta \sin \eta J_n^2(\alpha_0 k_n \cos \eta) \left\{ \begin{array}{l} \sin^2 \eta \\ (2 - 3 \sin^2 \eta) \end{array} \right. \quad (7.26)$$

and  $\theta$  denotes the angle between the polarization directions of the two laser fields. At low intensity the value of the  $\alpha_0$  parameter in the model is small. The reader is reminded that  $\alpha_0$  parameter represents the classical excursion vector of a free electron in an intense laser field and depends on both the magnitude of  $\vec{F}_{0L}$  and on value of  $\omega_L$ , the amplitude and angular frequency of the optical laser pulse. When  $\alpha_0 \ll 1$  the argument in the Bessel function ( $\alpha_0 \cdot k_n$ ) becomes small and the Bessel function in approximates to

$$J_n(x) = x^n \quad (7.27)$$

and so the Bessel function in equation 7.24 becomes proportional to  $(\alpha_0 k_n \cos \eta)^n$ , where  $\eta$  is the angle between the polarization of the optical laser and the momentum vector of the ejected electron, and  $n$  is the number of photons absorbed or emitted. Equation 7.26 leads to  $b_n/a_n = 2n$  where  $b_n$  represents the amplitude and  $a_n$  represents the offset of the cosine function in equation 7.25. The contrast, which is the ratio between the value at parallel polarization and that at perpendicular po-

larization, is predicted by the model to be:

$$\frac{\sigma_{max}^{(n)}}{\sigma_{min}^{(n)}} = 2n + 1 \quad (7.28)$$

The necessary parameters were extracted from the fits to the experimental data in figure 7.16 and summarized in table 7.1. Using these parameters, the measured contrast which is the ratio of the sideband intensity at parallel and perpendicular polarizations is equal to 3.1, which is in excellent agreement with the theoretical value of 3 ( $2n + 1$ , where  $n = 1$ ).

Parameter	Value	95% Confidence
$a_1$	0.305	(0.26, 0.36)
$b_1$	0.630	(0.56, 0.70)
$\sigma_{max}^{(1)}$	0.935	(0.81, 1.06)
$\sigma_{min}^{(1)}$	0.305	(0.26, 0.36)
$b_n/a_n$	2.062	(1.97, 2.19)
$\sigma_{max}^{(1)}/\sigma_{min}^{(1)}$	3.062	(2.97, 3.19)

Table 7.1: Experimental  $a_n$  and  $b_n$  parameters extracted from the polarization dependence of the sidebands on the He 1s photoline.

The contrast ( $\sigma_{max}^1/\sigma_{min}^1$ ) can be used to determine the relative contribution of the  $\epsilon s$  and  $\epsilon d$  partial waves to the overall magnitude of the sideband. By applying second-order perturbation theory the two-color ionization cross-section for photo-electron emission from a closed shell (neglecting spin-orbit interactions) is given by,

$$W(E_c) = C(3(S_1 + S_2) + (2S_0 - 3S_1 + S_2) \cos^2(\theta)) \quad (7.29)$$

with  $S_i = |T_i|^2$ , where  $T_i (i = 0, 1, 2)$  are the second-order reduced radial integrals associated with the emission of an  $s$ ,  $p$  and  $d$  electron respectively. In the case of helium, the magnitude of the sidebands in the ionization of an  $s$  electron can be described by [47],

$$\sigma(\theta) \propto 3S_2 + (5S_0 + S_2) \cos^2(\theta) \quad (7.30)$$

When the linear polarization vectors of the FEL and optical lasers are aligned parallel ( $\theta = 0$ ), equation 7.30 reduces to  $\sigma(n\pi) = 4S_2 + 5S_0 = \sigma_{max}$ ; and when perpendicular  $\sigma(n\pi/2) = 3S_2 = \sigma_{min}$ . Using the measured contrast, the ratio of the  $s$ -electrons to  $d$ -electrons ( $S_0 : S_2$ ) is equal to 1.04 which is in good agreement

with the value of 1 predicted by the soft-photon approximation.

The results show a stronger than expected contribution of the *s*-electrons to the strength of the sidebands in helium. This result deviates from the propensity rules which predict that upon absorption of a photon, transitions resulting in an increase of angular momentum ( $l \rightarrow l+1$ ) are favored over those which results in a decrease ( $l \rightarrow l-1$ ) [48]. In this case, the ratio differs from the value obtained in studies on the two-color ionization via discrete intermediate states,  $\text{He}^* 1snp \ ^1P$  ( $n = 2, 3$ ), where a more than 10 times higher cross section for *d* than for *s* electrons was determined [49]. For resonant ionization, the overlap between the discrete *np* and continuum *s* or *d* electron wave functions governs the branching ratio. Close to the ionization threshold for He, due to the centrifugal barrier, the first lobe of the *d* wave overlaps considerably the lobe of the *np* ( $n = 2, 3$ ) wave function. In contrast, the first oscillation of the *s*-wave is much closer to the nucleus, leading to compensation of positive and negative contributions to the transition matrix elements. Near the threshold, the *d*-wave dominates the resonant two-color ionization. For the ATI case, the strengths of the  $p \rightarrow s$  and  $p \rightarrow d$  transitions are mainly determined by the overlap of the oscillatory asymptotics of the coupled continuum states, approximately by the squared cosine of their scattering phase difference [50]. This quantity varies smoothly with the energy of the coupled continuum states and accords preference to the *s* channel for He at the FEL wavelength used here.

### High Intensity Optical Laser

When the intensity of the optical laser was increased to  $I_0 \geq 10^{11} \text{ W/cm}^2$  the number and intensity of photoelectron sidebands increased. The probability of the photoelectron absorbing (or emitting) multiple optical photons becomes quite high and so multiple sidebands are seen in the photoelectron spectra. This ionization scheme is illustrated on the right-hand-side of figure 7.14 on page 248 where the red arrows indicate the multiple transitions of the electron. Each sideband is now composed of electrons with either even (*s, d, g, ...*) or odd (*p, f, h, ...*) symmetries, having undergone transitions via many competing pathways.

By increasing the intensity of the optical laser to  $\sim 6 \times 10^{11} \text{ W/cm}^2$  a total of four photoelectron sidebands appeared on either side of the main He 1s photoline. Presented in figure 7.17 are a series of photoelectron spectra of helium plotted as a function of the relative angle between the linear polarization vectors of the FEL and optical laser. Again one can observe that the intensity of the main He 1s photoline decreases as the intensity of the sidebands increases, indicating that the total ion

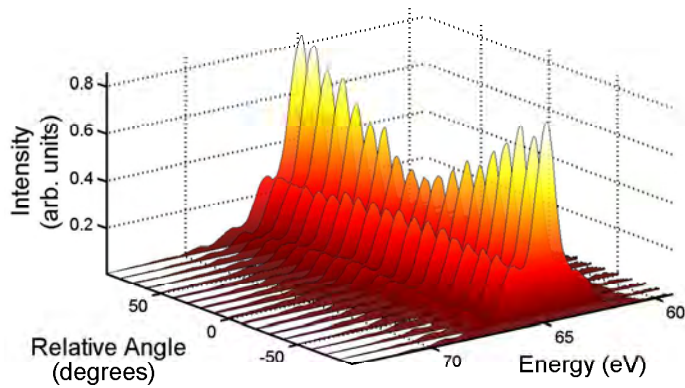


Figure 7.17: Photoelectron spectra showing the He 1s photoline and the high energy sidebands for high intensity of the optical laser. The intensity of the laser was  $\sim 6 \times 10^{11}$  W/cm<sup>2</sup>. Spectra are plotted as a function of relative angle ( $\phi$ ) between the linear polarization vectors of the EUV and optical fields.

yield remains constant.

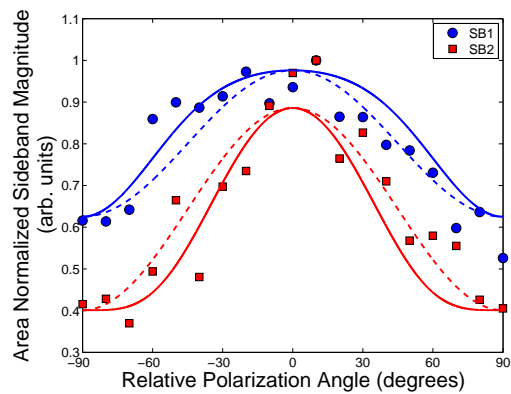


Figure 7.18: Magnitude of the first and second high-energy sidebands as a function of the polarization angle in the case of helium for an optical dressing field of  $\sim 6 \times 10^{11}$  W/cm<sup>2</sup>. The dashed lines represent a fit to the experimental data, while the solid lines represent the results from the soft-photon approximation.

Presented in figure 7.18 are the magnitudes of the first and second sidebands as a function of deviation between the polarization directions of the EUV and NIR fields. A  $\cos^2$  fit to the data for each sideband is represented by the dashed colored line, while the results from the soft-photon approximation are shown as the solid lines. One can immediately observe that the amplitude of the first sideband data is smaller than that of the second sideband. The theoretical value of the con-

trast ( $\sigma_{max}^1/\sigma_{min}^1$ ) of the first sideband is reduced from 3 at low intensity to 1.56 at high intensity according to equation 7.28. However if one examines the second sideband (SB2 in figure 7.18) it is clear that while the contrast is larger than that of the first sideband, (reaching a value of 2.2 in the experiment) it does not reach the theoretical value of  $2n + 1 = 5$  which is predicted by the soft-photon approximation. This discrepancy between theory and experiment can be understood using the following argument. At high intensities, ( $\alpha_0 k_n \geq 1$ ) the value of the Bessel function in equation 7.24 is no longer proportional to  $(\alpha_0 k_n \cos \eta)^n$  when  $n$  is small. Hence there will be a reduction in the ratio of  $b_n/a_n$  as the intensity of the optical laser is increased. This effect impacts the first sideband to a greater extent than the second or consecutive sidebands because of the dependence on the order number ( $n$ ). If the intensity of the optical laser increases further the remaining higher-order sidebands will experience a similar reduction in contrast.

The reduced contrast in the polarization dependence of the sidebands may be as a result of quantum interference between the many competing ionization channels opened up by the two colour fields. Each sideband is now composed of a mixture of electrons which may have undertaken countless absorption/emission events before arriving at the final state. This results in many quantum paths leading to the same final state and the degree of destructive interference between these competing free electron waves becomes the root cause of this attenuation of the low-order sidebands.

## Summary

In this section results from the two-color above-threshold ionization of helium have been presented. The polarization dependence of the photoelectron sidebands produced when the photoelectron undergoes free-free transitions in the continuum induced by the optical laser were examined for both low- and high-intensity of the optical (800 nm) laser. In the first case, a single sideband was observed signifying a transition from an  $\epsilon p$  state to either an  $\epsilon s$  or  $\epsilon d$  state. The ratio between these two ionization channels which contribute to the overall magnitude of the first sideband were studied by changing the polarization of optical laser with respect to the FEL and recording the magnitude of the photoelectron sidebands. The  $\cos^2$  dependence of the sidebands was compared to the soft-photon approximation and it was found that the  $p \rightarrow s$  was equal to the  $p \rightarrow d$  pathway. This result is in stark contrast to the normal propensity rules which state that transitions which gain angular momentum dominate over those which lose angular momentum.

The second part of this section dealt with a high intensity of optical dressing field. In this case multiple sidebands were observed up to the 4<sup>th</sup> order, which signified multiple free-free transitions. With each sideband now composed of an even more complex mixture of ionization channels, interference between the competing pathways was seen in the polarization dependence of the first sideband. The sideband contrast ( $\sigma_{max}^{(1)}/\sigma_{min}^{(1)}$ ) dropped from 3 at low intensity to 1.5 at high intensity. It was concluded that destructive interference was the cause of this observation. Determining the ratio between the  $\epsilon p \rightarrow \epsilon s, \epsilon d$  channels was hampered by the multiple pathways, but the soft-photon approximation was seen to agree well with the experimental results.

In the next section the polarization dependence of the photoelectron sidebands in the other rare-gas elements will be studied. As ionization originates from a  $p$  subshell for these atoms the number of continuum channels increases (from 2 in the case of helium) and the basic multiphoton ionization calculation of Grum-Grzhmailo *et al.* [45] becomes very difficult. Hence, for this case the study relies exclusively on the soft-photon approximation to predict the relative intensities of the sidebands and also to examine qualitatively their polarization dependence.

#### 7.2.4.2 Neon, Krypton & Xenon

The study of the remaining rare gas targets introduces another level of complexity into the analysis of the sideband magnitudes. In this section we will present results on the polarization dependence of sidebands using a high-intensity optical laser ( $6 \times 10^{13} \text{ W/cm}^2$ ) in neon, krypton and xenon. We distinguish these elements from helium because they have a common first step involving the ionization of a  $p$  electron, in contrast to He where an  $s$  electron is ionized in the first step. As stated above, the soft-photon approximation is used to qualitatively study the polarization dependence of the sidebands for photoionization from the  $np$ -shell, where  $n = 2, 4, 5$  for neon, krypton and xenon respectively.

It was shown in simulations presented earlier in section 7.2.3.2 that the experimental data departed from the predictions of the soft-photon approximation in the case of neon, but overall the general trend indicated that the sideband magnitude scales directly with the atomic number of the element.

In the case of the other rare gases the ejected electron originates from the  $np$  valence shell, where  $n = 2, 4, 5$  for neon, krypton and xenon respectively. This ionization scheme is illustrated in figure 7.19 (right-hand panel) where the photo-

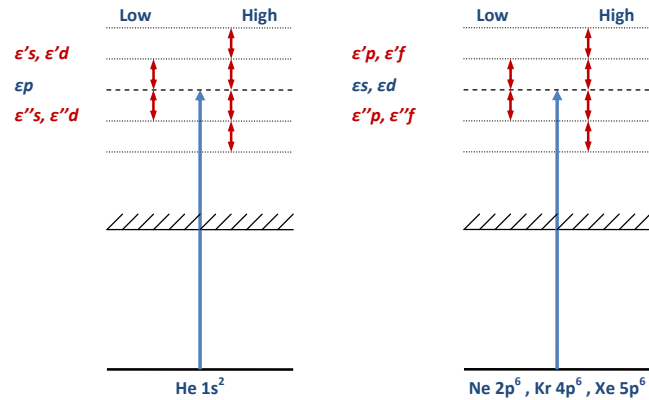


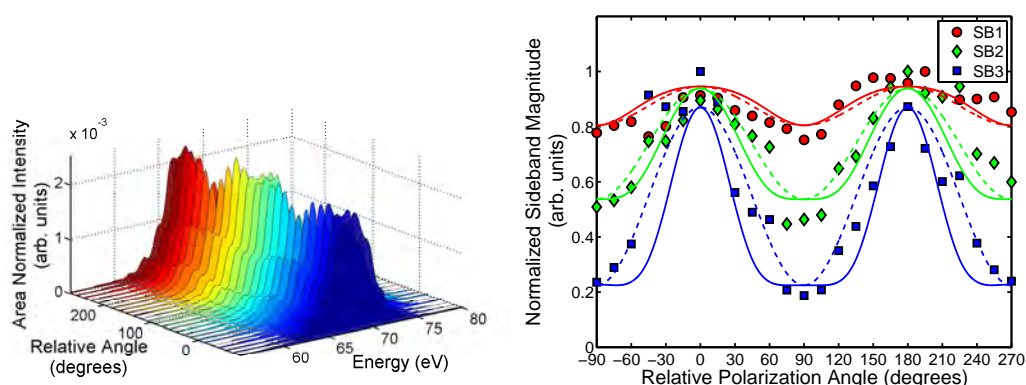
Figure 7.19: Simplified energy level diagram of the two-color above-threshold ionization scheme for helium (left-hand panel) and neon, krypton and xenon (right-hand panel).  $\epsilon'$  refers to an increase in kinetic energy (absorption of a photon), while  $\epsilon''$  refers to a decrease in the kinetic energy of the ejected electron (emission of a photon).

electron sidebands originate from laser-induced transitions involving an  $\epsilon s$  or  $\epsilon d$  initial state in the continuum. The sidebands are now composed of an even more complex mixture of electrons with either even ( $s, d, g, \dots$ ) or odd ( $p, f, h, \dots$ ) symmetries. This situation cannot be treated any longer through the second-order perturbation theory (at least not very easily), while the soft-photon approximation is still appropriate to calculate the strengths of the higher-order sidebands and their polarization dependence.

## Neon

We begin this section with a look at the photoelectron spectrum for the case of neon atoms irradiated with the FEL beam. In this experiment the FEL was operating at a wavelength of 13.7 nm (90.5 eV) with an average pulse energy of 22  $\mu\text{J}$ . This resulted in an average intensity in the region of  $6 \times 10^{13} \text{ W/cm}^2$  assuming a focal spot diameter of 45  $\mu\text{m}$  and an FEL pulse duration of 20 fs. This, as we will see later was sufficiently high to produce doubly ionized species in krypton through the sequential absorption of two EUV photons. The optical laser operated at a wavelength of 800 nm (1.55 eV) with an average pulse energy of 2 mJ before entering the vacuum chamber (loss of  $\sim 50\%$  after focusing optics). The intensity of the optical laser was  $\sim 1.2 \times 10^{13} \text{ W/cm}^2$  assuming a focal spot diameter of 50  $\mu\text{m}$  inside the chamber and a pulse duration of 4 ps. When used with the soft-photon approximation, we found that this intensity was high enough to produce

multiple photoelectron sidebands in neon.



(a) Polarization modulated two-color photoelectron spectra of neon. (b) Magnitude of first, second and third sidebands in neon.

Figure 7.20: Photoelectron spectra showing the Ne photoline at approximately 68.8 eV corresponding to the one-photon ionization of the Ne 2p valence electron by an FEL photon. The main photoline is surrounded on both the high- and low-energy sides by photoelectron sidebands which correspond to two-color (FEL and optical laser) above-threshold ionization of the Ne 2p photoelectron. (b) Magnitudes of the first, second and third photoelectron sidebands with respect to the relative polarization angle between the FEL and optical laser fields. The magnitudes have been normalized to the maximum value in their respective datasets.

In figure 7.20 (a) we present photoelectron spectra of the neon as a function of polarization angle between the FEL and the optical laser. A retardation voltage of 50 V was applied to grids located at the entrance of the MBES to improve the electron energy resolution of the system. Each spectrum in the figure has been somewhat broadened during the averaging of the 100 single shot spectra used to obtain it. The strongest feature in this plot is the feature at an electron kinetic energy of 70 eV, corresponding to the Ne 2p photoline. The two spin orbit components which have binding energies of 21.6 eV and 21.7 eV respectively are not resolvable. The photoline is surrounded by the photoelectron sidebands which are separated by an energy of 1.55 eV, the photon energy of the optical laser.

The spectra are plotted with respect to the polarization angle between the FEL and optical laser fields. During the experiment the polarization of the FEL remained constant and the polarization of the optical laser was rotated with the aid of a half-wave plate. The polarization dependence of neon displays a similar trend to the case of two-color ATI in helium. We observe the maximum number of sidebands when the polarizations of the two lasers is parallel ( $\phi = 0^\circ$ ) and a minimum when perpendicular.

The magnitudes of the photoelectron sidebands in these spectra has been extracted as the area of Gaussian profiles fitted to the experimental data. This magnitude of the first, second and third high-energy sidebands is presented in figure 7.20 (b). Each data set has been normalized to unity by dividing each data point by the corresponding maximum value. One can see that the data agrees well with a  $\cos^2$  fit to the data. We find that the contrast ( $\sigma_{max}^{(n)}/\sigma_{min}^{(n)}$ ) is 1.18, 1.75 and 3.87 for the first, second and third sidebands respectively.

A comparison to the soft-photon approximation model was made, and is shown to agree well with the the first sideband but not for the higher-order sidebands. This was observed earlier in section 7.2.3. Also the response from the model appears to depart from a  $\cos^2$  dependence for the higher sidebands. The adaption of the model to introduce the cosine dependence on the polarization means that for orthogonal polarizations the argument of the Bessel function goes to zero. The model was used to determine the true laser intensity experienced by the electrons and the ratio of the first to second low-energy sideband was 1.75 while the second to third sideband ratio was 3.04. When the ratio of the sidebands in the synthetic photoelectron spectra produced using the model were minimized to these values, an intensity of  $9.5 \times 10^{11}$  W/cm<sup>2</sup> was extracted which is not far from the  $1 \times 10^{12}$  W/cm<sup>2</sup> estimated from the experimental parameters.

## Krypton

We now move to Krypton ( $Z = 36$ ) where we examine photoionization of the 4p electron using the FEL. In figure 7.21 we present a series of photoelectron spectra for krypton which were recorded for optimum temporal and spatial overlap between the FEL and the optical laser (800 nm). The spectra are plotted as a function of the angle between the linear polarization vectors of the FEL and optical laser. The two main features in the figure at 63 eV and 74 eV and correspond respectively to the Kr  $4s^{-1}$  and Kr  $4p^{-1}$  ( $^2P_{3/2,1/2}$ ) photolines. Accompanying these photoelectron peaks are the photoelectron sidebands which are due to the two-color ATI process. The region of the 4s photoline has been magnified and is presented on the right-hand side of the figure. Strong sidebands were observed in the case of both the 4p photoline and the 4s photoline.

The sidebands appear to be strongest for parallel polarizations and weakest for orthogonal polarization of the EUV and NIR fields, which is in keeping with the results from the previous work on helium and neon. In figure 7.22 the magnitudes as a function of polarization angle of the first sideband for the Kr 4s and Kr 4p

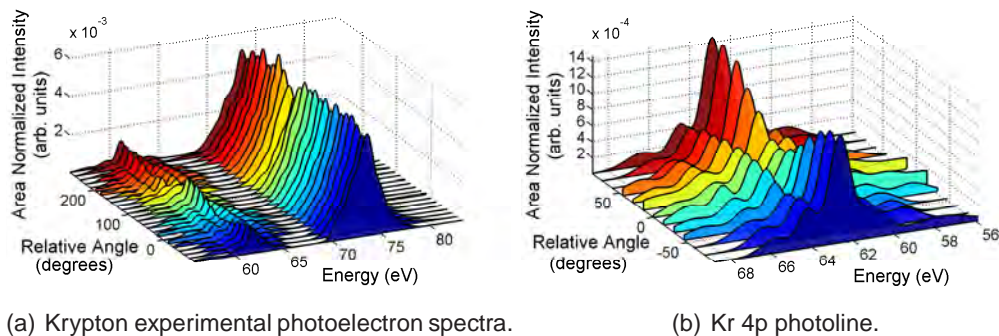


Figure 7.21: (a) Series of photoelectron spectra of krypton plotted as a function of the relative polarization angle between the FEL and optical laser. The Kr  $4p^{-1}$  photoline is visible at approximately 75 eV. The region at 63 eV containing the Kr  $4s^{-1}$  photoline is magnified and shown in (b).

photolines are presented. The presence of the 4s photoline provides a rare and unique opportunity to examine the polarization dependence of an s-electron in a more complex multielectron atom than helium. The results show that the contrast ( $\sigma_{max}^{(n)}/\sigma_{min}^{(n)}$ ) for first sideband of the 4p photoline is approximately 1.4 while for the transition involving the 4s level it is 1.7. One may expect the contrast of the 4s to be larger than that of the 4p, given the possibility for enhanced destructive interference opened up in the 4p case by the increased number of ionization channels. It does not however approach the theoretical value of 3 ( $2n + 1$ , where  $n = 1$ ). This may be due to a number of reasons, one of which may be due in part to the fact that the 4s in krypton is a sub-valence electron and as such may be subject to significant distortions due to the proximity of the 4p orbital.

## Xenon

The final element to be studied was xenon where the magnitude of the sidebands is complicated by mixing between the  $5p_{1/2, 3/2}$  spin-orbit components. Each sideband now contains a mixture of sidebands from each of the spin-orbit components of the  $5p^{-1}$  hole which are separated by approximately 1.3 eV. This value lies close to the photon energy of the optical laser (1.55 eV) and therefore the separation between the sidebands. Illustrated in figure 7.23 are two simulated spectra produced using the computer model of the soft-photon approximation where there is a 1.3 eV separation between the main photolines of both spectra. One may see from the figure that there is mixing between the alternate sidebands of the two spin-orbit components. The first sideband from the  $^2P_{3/2}$  component overlaps with the sec-

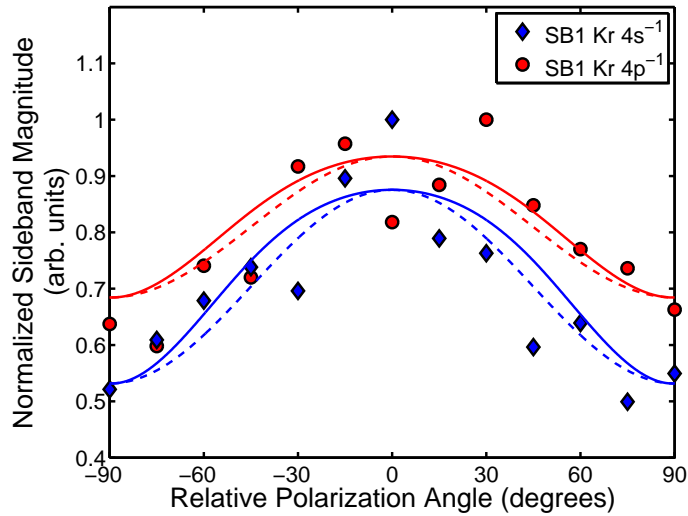


Figure 7.22: Magnitude of photoelectron sidebands of the Kr 4s and 4p photolines as a function of the angle between the FEL and optical laser linear field vectors.

ond sideband from the  ${}^2P_{1/2}$  component. In this case the magnitude of the main photoline and the first sideband will appear to be more intense than predicted from the model. This effect was accounted for in the analysis of the sideband magnitudes by running the code twice for an electron kinetic energy of  $E_k = h\nu_L - E_{IP}$  where  $E_{IP}$  was equal to the individual ionization potentials of the two components (12.13 eV and 13.43 eV respectively). The output from both iterations was summed and the resulting spectrum is shown in figure 7.23 in blue.

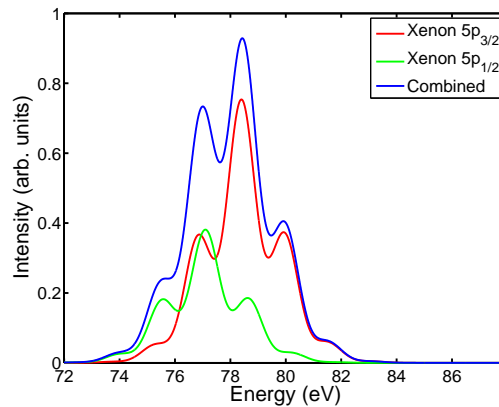


Figure 7.23: Simulated photoelectron spectra from the soft-photon approximation computer model for the 5p ( ${}^2P_{3/2,1/2}$ ) levels in xenon. Each spectrum has been weighted according to the statistical weighting ( $g = 2j+1$ ) of the respective level. The blue line represents a summation of the two simulated spectra.

Figure 7.24 shows experimental photoelectron spectra for both low- (a) and high-intensity (b) of the optical dressing field plotted as a function of the relative polarization angle between the FEL and optical laser. Each spectrum is an average of approximately 100 single shot spectra and the total area has been normalized to unity. One can see a radical difference between the number of sidebands in the low-intensity case compared to the case of high-intensity. At low-intensity only a single photoelectron sideband is observed, the intensity of which reaches a maximum when the polarization field vectors are parallel. In the high-intensity case, figure 7.24 (b) one can clearly observe sidebands up to the 4<sup>th</sup> order. The modulation in the intensity of the main photoline is substantial and follows a sinusoidal dependence with respect to the polarization angle.

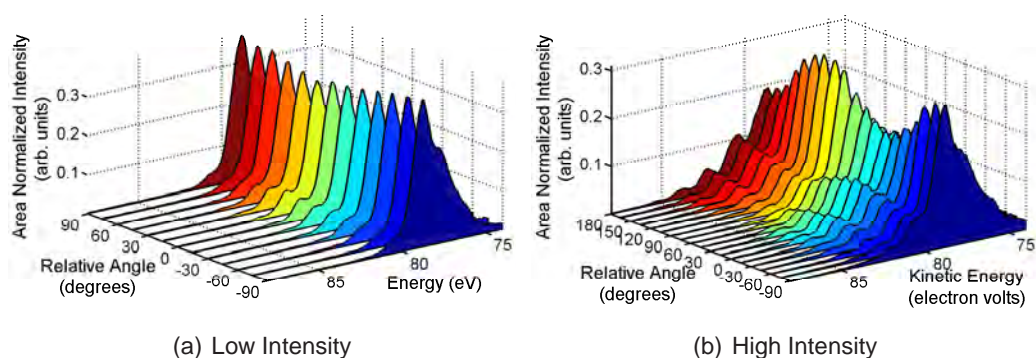


Figure 7.24: Experimental photoelectron spectra showing the Xe 5p photoline and the high energy sidebands for low (left) and high (right) intensity of the optical laser,  $\sim 8 \times 10^{11}$  and  $\sim 4 \times 10^{12}$  W/cm<sup>2</sup> respectively.

Once again the behavior of the sidebands is more clearly observed when the magnitudes are plotted as a function of polarization angle, as is figure 7.25. The markers represent the experimental magnitudes of the first high-energy sideband, the dashed colored lines represent a  $\cos^2$  fit to the data and the solid colored lines represent the soft-photon approximation. The amplitude (contrast) of the low-intensity signal is approximately 1.7 while at high-intensity it reduces to 1.4. The contrast suppression for high-intensity signal may be due to interference between the additional multiple quantum paths. The soft-photon approximation appears to fit the experimental data well, though deviating slightly in the high-intensity case, and were calculated assuming an intensity of  $6 \times 10^{10}$  W/cm<sup>2</sup> and  $2 \times 10^{11}$  W/cm<sup>2</sup> for the low- and high-intensity cases.

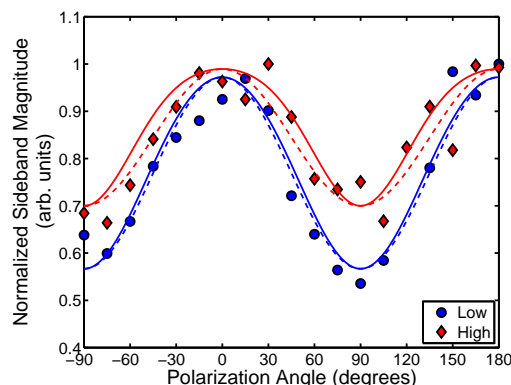


Figure 7.25: Magnitude of the first sideband for both low and high-intensity of the optical dressing field ( $\sim 8 \times 10^{11}$  and  $\sim 4 \times 10^{12}$  W/cm<sup>2</sup>) as a function of the angle ( $\phi$ ) between the polarization vectors of the FEL and optical laser. The dashed coloured lines are simple  $\cos^2$  fits to the experimental data, while the dashed coloured lines represent the results from the soft-photon approximation, calculated with an optical laser intensity of  $6 \times 10^{10}$  W/cm<sup>2</sup> and  $2 \times 10^{11}$  W/cm<sup>2</sup> respectively.

### 7.3 Conclusions

The monochromatic and intense EUV beam provided by FLASH gave the opportunity to perform the first interference-free study of the two-color above-threshold ionization process in rare gas atoms. In order to achieve this ultimate aim it was necessary to firstly characterize the spectral content of the EUV beam from FLASH using a flat-field spectrometer, and secondly determine the temporal and spatial overlap of the pump (EUV) and probe (NIR) beams.

Having achieved the optimum pump-probe setup, the relative contributions of the *s*- and *d*-waves to the two-color process in helium was examined by the polarization method. The results showed that there was a greater contribution from the *s*-electron wave to the two-color signal which was in contrast to the behavior expected by propensity rules. When the intensity of the optical laser was increased multiple photoelectron sidebands were observed. In this case many additional ionization channels were opened up. At a high intensity of the optical dressing field we observed a decrease in the contrast (the ratio of the sideband intensity at parallel and perpendicular polarizations) of the first sideband which indicated that there may be destructive interference occurring between the many competing pathways.

In the case of the other rare gas elements, namely neon, krypton and xenon, as the ionization originates from a *p* subshell for these atoms the number of continuum channels increases (was only 2 in the case of helium) and the basic single active

electron approximation breaks down and information about the relative contributions of the partial electron waves to the magnitude of the sidebands was unattainable. However, the soft-photon approximation was seen to describe the polarization dependence of the sidebands quite well.

# Bibliography

- [1] P. Radcliffe, S. Düsterer, A. Azima, W.B. Li, E. Plönjes, H. Redlin, J. Feldhaus, P. Nicolosi, L. Poletto, J. Dardis, J.P. Gutierrez, P. Hough, K.D. Kavanagh, E.T. Kennedy, H. Luna, P. Yeates, J.T. Costello, A. Delyseries, C.L.S. Lewis, D. Glijer, D. Cubaynes, and M. Meyer. An experiment for two-color photoionization using high intensity extreme-uv free electron and near-ir laser pulses. *Nuclear Instruments and Methods in Physics Research Section A: Accelerators, Spectrometers, Detectors and Associated Equipment*, 583(2-3):516 – 525, 2007.
- [2] W. Ackermann. Operation of a free-electron laser from the extreme ultraviolet to the water window. *Nature Photonics*, 1(6):336, 2007.
- [3] E. L. Saldin, E. A. Schneidmiller, and M. V. Yurkov. Properties of the odd harmonics of the radiation from SASE FEL with a planar undulator. *ArXiv Physics e-prints (arXiv:physics/0509164)*, 2005.
- [4] E. L. Saldin, E. A. Schneidmiller, and M. V. Yurkov. Properties of the third harmonic of the radiation from self-amplified spontaneous emission free electron laser. *Physical Review Special Topics: Accelerators and Beams*, 9(3):030702, 2006.
- [5] J. Feldhaus, J. Arthur, and J. B. Hastings. X-ray free-electron lasers. *Journal of Physics B: Atomic, Molecular and Optical Physics*, 38(9):S799–S819, 2005.
- [6] E. L. Saldin, E. A. Schneidmiller, and M. V. Yurkov. Expected properties of the radiation from VUV-FEL at DESY (femtosecond mode of operation). Technical report, DESY, 2004.
- [7] J. M. Schins, P. Breger, P. Agostini, R. C. Constantinescu, H. G. Muller, A. Bouhal, G. Grillon, A. Antonetti, and A. Mysyrowicz. Cross-correlation measurements of femtosecond extreme-ultraviolet high-order harmonics. *Journal of the Optical Society of America B: Optical Physics*, 13:197–200, 1996.

- [8] T. E. Glover, R. W. Schoenlein, A. H. Chin, and C. V. Shank. Observation of laser assisted photoelectric effect and femtosecond high order harmonic radiation. *Physical Review Letters*, 76(14):2468–2471, 1996.
- [9] A. Bouhal, R. Evans, G. Grillon, A. Mysyrowicz, P. Breger, P. Agostini, R. C. Constantinescu, H. G. Muller, and D. von der Linde. Cross-correlation measurement of femtosecond noncollinear high-order harmonics. *Journal of the Optical Society of America B: Optical Physics*, 14:950–956, 1997.
- [10] E. S. Toma, H. G. Muller, P. M. Paul, P. Breger, M. Cheret, P. Agostini, C. Le Blanc, G. Mullo, and G. Cheriaux. Ponderomotive streaking of the ionization potential as a method for measuring pulse durations in the XUV domain with fs resolution. *Physical Review A*, 62(6):061801, 2000.
- [11] M. Meyer, D. Cubaynes, P. O’Keeffe, H. Luna, P. Yeates, E. T. Kennedy, J. T. Costello, P. Orr, R. Taïeb, A. Maquet, S. Düsterer, P. Radcliffe, H. Redlin, A. Azima, E. Plönjes, and J. Feldhaus. Two-color photoionization in XUV free-electron and visible laser fields. *Physical Review A*, 74(1):011401, 2006.
- [12] P. Radcliffe, S. Dusterer, A. Azima, H. Redlin, J. Feldhaus, J. Dardis, K. Kavanagh, H. Luna, J. Pedregosa Gutierrez, P. Yeates, E. T. Kennedy, J. T. Costello, A. Delserieys, C. L. S. Lewis, R. Taieb, A. Maquet, D. Cubaynes, and M. Meyer. Single-shot characterization of independent femtosecond extreme ultraviolet free electron and infrared laser pulses. *Applied Physics Letters*, 90(13):131108, 2007.
- [13] R. Mitzner, B. Siemer, M. Neeb, T. Noll, F. Siewert, S. Roling, M. Rutkowski, A. A. Sorokin, M. Richter, P. Juranic, K. Tiedtke, J. Feldhaus, W. Eberhardt, and H. Zacharias. Spatio-temporal coherence of free electron laser pulses in the soft X-ray regime. *Optics Express*, (24):19909–19919, 2008.
- [14] S. Cunovic, N. Muller, R. Kalms, M. Krikunova, M. Wieland, M. Drescher, Th. Maltezopoulos, U. Fruhling, H. Redlin, E. Plonjes-Palm, and J. Feldhaus. Time-to-space mapping in a gas medium for the temporal characterization of vacuum-ultraviolet pulses. *Applied Physics Letters*, 90(12):121112, 2007.
- [15] C. Gahl, A. Azima, M. Beye, M. Deppe, K. Doebrich, U. Hasslinger, F. Hennies, A. Melnikov, M. Nagasono, A. Pietzsch, M. Wolf, W. Wurth, and A. Foehlich. A femtosecond X-ray/optical cross-correlator. *Nature Photonics*, 2(3):165–169, 2008.

- [16] A. L. Cavalieri, D. M. Fritz, S. H. Lee, P. H. Bucksbaum, D. A. Reis, J. Rudati, D. M. Mills, P. H. Fuoss, G. B. Stephenson, C. C. Kao, D. P. Siddons, D. P. Lowney, A. G. MacPhee, D. Weinstein, R. W. Falcone, R. Pahl, J. Als-Nielsen, C. Blome, S. Dusterer, R. Ischebeck, H. Schlarb, H. Schulte-Schrepping, T. Tschentscher, J. Schneider, O. Hignette, F. Sette, K. Sokolowski-Tinten, H. N. Chapman, R. W. Lee, T. N. Hansen, O. Synnergren, J. Larsson, S. Techert, J. Sheppard, J. S. Wark, M. Bergh, C. Caleman, G. Huldt, D. van der Spoel, N. Timneanu, J. Hajdu, R. A. Akre, E. Bong, P. Emma, P. Krejcik, J. Arthur, S. Brennan, K. J. Gaffney, A. M. Lindenberg, K. Luening, and J. B. Hastings. Clocking femtosecond X rays. *Physical Review Letters*, 94(11), 2005.
- [17] A. Azima, S. Dusterer, P. Radcliffe, H. Redlin, N. Stojanovic, W. Li, J. Feldhaus, D. Cubaynes, M. Meyer, J. Dardis, P. Hayden, P. Hough, V. Richardson, E. T. Kennedy, and J. T. Costello. Time-resolved pump-probe experiments beyond the jitter limitations at flash. *Applied Physics Letters*, 94(14):144102, 2009.
- [18] S. Düsterer, P. Radcliffe, G. Geloni, U. Jastrow, M. Kuhlmann, E. Plönjes, K. Tiedtke, R. Treusch, J. Feldhaus, P. Nicolosi, L. Poletto, P. Yeates, H. Luna, J. T. Costello, P. Orr, D. Cubaynes, and M. Meyer. Spectroscopic characterization of vacuum ultraviolet free electron laser pulses. *Optics Letters*, 31:1750–1752, 2006.
- [19] L. Poletto, L. Epulandi, P. Nicolosi, M. G. Pelizzo, P. Zambolin, J. Feldhaus, U. Jastrow, U. Hahn, E. Ploenjes, and K. Tiedtke. Grazing-incidence spectrometer for the monitoring of the VUV FEL beam at DESY. volume 5534, pages 37–46, 2004.
- [20] M. Martins, M. Wellhoefer, J. T. Hoeft, W. Wurth, J. Feldhaus, and R. Follath. Monochromator beamline for FLASH. *Review of Scientific Instruments*, 77(11), 2006.
- [21] Deutsches Elektronen-Synchrotron (DESY). Free-electron laser at DESY delivers highest power at shortest wavelengths and reaches water window. Press Release 07092006, 2006.
- [22] Deutsches Elektronen-Synchrotron (DESY). Light of the Future - The European XFEL Facility, <http://xfel.eu/en/documents/>. Technical report, 2006.

- [23] O. Guyetand, M. Gisselbrecht, A. Huetz, P. Agostini, R. Taïeb, V. Véniard, A. Maquet, L. Antonucci, O. Boyko, C. Valentin, and D. Douillet. Multicolour above-threshold ionization of helium: quantum interference effects in angular distributions. *Journal of Physics B: Atomic, Molecular and Optical Physics*, 38(22):L357–L363, 2005.
- [24] O. Guyetand, M. Gisselbrecht, A. Huetz, P. Agostini, R. Taïeb, A. Maquet, B. Carré, P. Breger, O. Gobert, D. Garzella, J. F. Hergott, O. Tcherbakoff, H. Merdji, H. Bougeard, M. Böttcher, Z. Ansari, and P. Antoine. Evolution of angular distributions in two-color, few-photon ionization of helium. *Journal of Physics B: Atomic, Molecular and Optical Physics*, 41(5):051002, 2008.
- [25] V. Véniard, R. Taïeb, and A. Maquet. Two-color multiphoton ionization of atoms using high-order harmonic radiation. *Physical Review Letters*, 74(21):4161–4164, 1995.
- [26] P. O’Keeffe, R. López-Martens, J. Mauritsson, A. Johansson, A. L’Huillier, V. Véniard, R. Taïeb, A. Maquet, and M. Meyer. Polarization effects in two-photon nonresonant ionization of argon with extreme-ultraviolet and infrared femtosecond pulses. *Physical Review A*, 69(5):051401, 2004.
- [27] Maquet A. and Taieb R. Two-colour IR+XUV spectroscopies: the ‘soft-photon approximation’. *Journal of Modern Optics*, 54(13-15):1847–1857, 2007.
- [28] A. Weingartshofer, J. K. Holmes, G. Caudle, E. M. Clarke, and H. Krüger. Direct observation of multiphoton processes in laser-induced free-free transitions. *Physical Review Letters*, 39(5):269–270, 1977.
- [29] L. Rosenberg. Intermediate-and strong-coupling approximations for scattering in a laser field. *Physical Review A*, 23(5):2283–2292, 1981.
- [30] M. H. Mittleman. Potential scattering of charged particles in the field of a low-frequency laser. *Physical Review A*, 19(1):134–138, 1979.
- [31] J. I. Gersten and M. H. Mittleman. Electron scattering from atoms in the presence of a laser field. *Physical Review A*, 13(1):123–130, 1976.
- [32] G. Ferrante and L. L. Cascio. Eikonal theory of charged particle potential scattering in the presence of a low frequency laser field. *Journal of Physics B: Atomic, Molecular and Optical Physics*, 12(14):2319–2324, 1979.
- [33] F. E. Low. Bremsstrahlung of very low-energy quanta in elementary particle collisions. *Physical Review*, 110(4):974–977, 1958.

- [34] N. M. Kroll and K. M. Watson. Charged-particle scattering in the presence of a strong electromagnetic wave. *Physical Review A*, 8(2):804–809, 1973.
- [35] A. Weingartshofer, E. M. Clarke, J. K. Holmes, and C. Jung. Experiments on multiphoton free-free transitions. *Physical Review A*, 19(6):2371–2376, 1979.
- [36] Wolkow D. M. Über eine klasse von lösungen der diracschen gleichung. *Zeitschrift für Physik A: Hadrons and Nuclei*, 94(3):250–260, 1935.
- [37] A. Cionga, V. Florescu, A. Maquet, and R. Taïeb. Target dressing effects in laser-assisted X-ray photoionization. *Physical Review A*, 47(3):1830–1840, 1993.
- [38] M. Jain and N. Tzoar. Compton scattering in the presence of coherent electromagnetic radiation. *Physical Review Letters*, 18(2):538–545, 1978.
- [39] J. W. Cooper and S. T. Manson. Photo-ionization in the soft X-ray range: Angular distributions of photoelectrons and interpretation in terms of subshell structure. *Physical Review*, 177(1):157–163, 1969.
- [40] P. Hayden. Private communication, 2008.
- [41] A. A. Sorokin, S. V. Bobashev, J. Feldhaus, Ch. Gerth, A. Gottwald, U. Hahn, U. Kroth, M. Richter, L. A. Shmaenok, B. Steeg, K. Tiedtke, and R. Treusch. Gas-monitor detector for intense and pulsed VUV/EUV free-electron laser radiation. volume 705, pages 557–560, 2004.
- [42] F. Wuilleumier and M. O. Krause. Photoionization of neon between 100 and 2000 eV: Single and multiple processes, angular distributions, and subshell cross sections. *Physical Review A*, 10(1):242–258, 1974.
- [43] M. O. Krause, T. A. Carlson, and P. R. Woodruff. Angular distribution of photoelectrons of Xe 5*p* spin-orbit components between 20 and 105 eV. *Physical Review A*, 24(3):1374–1379, 1981.
- [44] H. Van Der Hart. Private communication, 2009.
- [45] M. Meyer, D. Cubaynes, D. Glijer, J. Dardis, P. Hayden, P. Hough, V. Richardson, E. T. Kennedy, J. T. Costello, P. Radcliffe, S. Dusterer, A. Azima, W. B. Li, H. Redlin, J. Feldhaus, R. Taïeb, A. Maquet, A. N. Grum-Grzhimailo, E. V. Gryzlova, and S. I. Strakhova. Polarization control in two-color above-threshold ionization of atomic helium. *Physical Review Letters*, 101(19):193002, 2008.

- [46] F. J. Wuilleumier and M. Meyer. Pump probe experiments in atoms involving laser and synchrotron radiation: An overview. *Journal of Physics B: Atomic, Molecular and Optical Physics*, 39:425, 2006.
- [47] R. Taïeb, V. Véniard, A. Maquet, N. L. Manakov, and S. I. Marmo. Circular dichroism from unpolarized atoms in multiphoton multicolor ionization. *Physical Review A*, 62(1):013402, 2000.
- [48] U. Fano. Propensity rules: An analytical approach. *Physical Review A*, 32(1):617–618, 1985.
- [49] A. Johansson, M. K. Raarup, Z. S. Li, V. Likhnygin, D. Descamps, C. Lynga, E. Mevel, J. Larsson, C. G. Wahlstrom, S. Aloise, M. Gisselbrecht, M. Meyer, and A. L’Huillier. Two-color pump-probe experiments in helium using high-order harmonics. *European Physical Journal D: Atomic, Molecular, Optical and Plasma Physics*, 22(1):3–11, 2003.
- [50] T. Mercouris, Y. Komninos, S. Dionissopoulou, and C. A. Nicolaides. Effects on observables of the singularity in the multiphoton free-free dipole matrix elements. *Journal of Physics B: Atomic, Molecular and Optical Physics*, 29(1):L13–L19, 1996.

# Conclusions & Perspectives

The work presented in this thesis was divided into two main themes. The first concerned the interaction of an intense table-top Nd:YAG ( $\lambda = 1064$  nm) laser system with solid metal targets, while the second was based on the interaction of the intense EUV FEL beam at FLASH with dilute targets (gaseous entities such as atomic beams or jets). In the first instance, we used emission imaging and spectroscopy in the soft X-ray and visible spectral regions to study the plasmas produced when the beam from an EKSPLA™ 312p laser system was tightly focused onto a target surface. The laser had a pulse duration of 170 ps which enabled the study of laser-produced plasmas in a temporal region which was relatively unexplored in the literature.

Photon diagnostics in the soft X-ray region, presented in Chapter 3, employed the use of a pinhole camera and a Bragg crystal spectrometer and provided time-integrated images and spectra of single and colliding plasmas respectively. Images revealed that each seed plasma was composed of a small and brightly emitting core region, about  $10 \mu\text{m}$  in diameter. Some have argued [1] that the size of this region is indicative of the dimensions of the focal spot of the laser. If this is true, then the focal spot diameter in these experiments could be within the  $10 - 20 \mu\text{m}$  range. Emission from this plasma region was bright and it was estimated that the duration of the X-ray emission was on the order of a few hundred picoseconds. Soft X-ray spectra revealed that the laser system was capable of producing plasmas which had an initial temperature of a few hundred electron volts and which were composed of highly charged ions. The electron temperature of the plasma was deduced from these spectra using a simple scaling law which relates the plasma temperature to the highest ionization charge state observed. This model [2], predicted a core plasma temperature of between 100 eV and 250 eV.

These studies used an X-ray sensitive back-illuminated CCD camera that accumulated emission within the spectral region below 1 nm (the cutoff of the aluminium

filter) over the entire life-cycle of the plasma. Such time-integrated measurements placed restrictions on the level of information that could be gained from the plasma. Future work into these hot, dense and rapidly expanding plasmas would benefit greatly from the addition of gateable detectors which can operate in the sub-nanosecond temporal regime. This would yield detailed information about the formation and evolution of the X-ray emitting core of these particular laser-produced plasmas. However, at this present time, current CCD-based detector systems which unite sub-nanosecond temporal resolution with sensitivity in the XUV and soft X-ray spectral regions are costly.

In order to fully characterize the plasmas produced by this intense table-top laser system we extended the photon diagnostics into the visible spectral region. Here we had access to gateable detectors which permitted time-resolved imaging and spectroscopic measurements to be made. Images obtained at 10 ns intervals were used to chart the expansion of the plasma plume into vacuum. Interestingly, these images revealed that the plasmas expanded quite rapidly away from the target surface ( $\sim 10^6$  cm/s), within the first 50 ns or so. After this period we saw that the brightest part of the plasma remained localized to a region lying within a few millimeters of the target surface. We concluded that this was a result of the following scenarios: (i) The hot plasma material evaporating from the surface of the target (which continues to occur for a few tens of nanoseconds after the end of the laser pulse) became localized to a small region near the target having been confined by the colder plasma material that had already expanded, cooled and slowed down. (ii) Or, more likely to be the case, emission from the recombination of ions located in this region. As a consequence, the bright region of the plasmas seen in these images appeared to become almost stationary at a time delay of 50 ns. In fact, while this hot region appeared to remain localized to within a few millimeters of the surface of the target, material was being violently ejected from the front end of the plume, similar in appearance to an astrophysical jet, and so overall the plume continued to expand (quite rapidly) up to and beyond 200 ns after the laser pulse had ended. This effect may have an application in the field of pulsed-laser deposition, whereby this laser system and target arrangement could aid in the production of droplet-free thin-films which may lead to more-homogenous mechanical and electrical properties [3]. However, for this to be applicable, the on-target irradiance of the laser system would have to be substantially reduced, in line with current PLD systems [4].

Spectroscopy was performed using a Chromex™ 0.5 visible spectrometer. Analysis

of the spectra so obtained permitted the determination of temporally and spatially resolved electron temperatures and densities. We observed strong self-absorption in the spectral lines of aluminium and calcium corresponding to emission which involved the ground state. Consequently, two distinct analysis methods were used in order to determine the electron density in the high density region close to the target surface, and the low density region beyond approximately 2 mm from the target surface. The first was the conventional method using direct Stark analysis of the widths of spectral lines (for regions  $> 2$  mm from the target surface). The second method employed a computer model which was based on a solution of the one dimensional equation of radiative transfer. The model produces an initial simulated spectrum, generated using estimated plasma parameters, which is then fitted to the experimental spectrum (containing the spectral lines that suffer from opacity) through an iterative parameter minimization process in Matlab™. When the simulated spectra were matched to the experimental spectra an approximate value of the local electron density could be extracted from the model. There was good agreement between the two methods at the overlap region (at  $\approx 2$  mm). The spatially- and temporally-resolved electron temperature of the plasma was determined by comparing the intensities of spectral lines from successive charge states. At long time delays ( $\tau_d \geq 100$  ns) the plasma became iso-thermal, yielding an average temperature along the length of the plume of approximately 2.5 eV (in the case of aluminium).

Colliding plasma systems were also studied during the course of this work. In Chapter 5 the collisionality parameter was introduced which was used to define the boundary between the processes of either stagnation or interpenetration. The study began with diagnostics in the soft X-ray spectral region, where the collisionality of the colliding plasma system was low ( $\xi \approx 1$ ), and where interpenetration was most likely to occur; to the visible spectral region, where the larger plasma separation ( $D = 2$ mm) in conjunction with the smaller ion-ion mean free path ( $\lambda_{ii} \approx 20 \mu\text{m}$ ) yielded a high value of the collisionality parameter. In this regime, where  $\xi \approx 100$ , theory predicted that stagnation was the dominant scenario, which agreed nicely with what was observed in the time-resolved images. A bright, well-defined stagnation layer was formed by the collision of two aluminium seed plasmas. In section 4.3 we proposed that the width of the stagnation layer can lead to a qualitative measure of the degree of plume interpenetration. This hypothesis was investigated by adjusting the collisionality parameter through the use of alternative target configurations and focusing arrangements. Specifically, we used wedge-shaped targets where the two seed plasmas were orientated in a more-opposing

configuration. Here the collisionality of the system was reduced from the flat-target case, because the seed plasmas collided at a higher relative velocity, resulting in an increase in the width of the stagnation layer. We also experimented with other focusing arrangements, whereby a cylindrical lens was used to create a line focus of the laser beam on the surface of the target. In this case, the collision of the two seed plasmas was over an extended front (given by the width of the line focus, 12 mm) and so the stagnation layer resembled a long thin sheet. Results from this study revealed that there was a substantial increase in the width of the layer implying that the two plumes had interpenetrated beyond a distance of 1 mm. The results show that the collisionality parameter was quite low in this case which we concluded was due to a decrease in the average charge state of the plasma (on account of the reduced laser irradiance).

Colliding plasma systems appear to be on the brink of revolutionizing many existing technologies, one of which is pulsed-laser deposition (PLD). Camps *et al.* [5] made one of the first demonstrations of the advantages of combining colliding plasma systems with conventional PLD. Their studies have been key to highlighting the main feature of the colliding plasma PLD (also known as crossed-beam PLD or CBPLD) technique. What they revealed was that during thin-film deposition using colliding plasmas, the silicon substrate showed significantly less amorphism (or damage to the crystal structure). This is mainly caused by the bombardment of high-energy particles such as highly-charged ions, hot electrons or aggregated material such as clusters onto the substrate, which can lead to the sputtering of material from or embedding of material within the top-most surface of the substrate, so-called 'splashing'. In order to understand this new deposition technique it was vital to study both the collision of the two seed plasmas and the subsequent interaction of the resultant stagnation layer with the silicon substrate. The study presented in this thesis went some way to achieving the former. The photon diagnostics in the visible spectral region, presented in Chapter 4, provided information on the mid-life (50 – 500 ns) of the stagnation layer. Recently, some of the first detailed studies into the early stage of the collision between two seed plasmas ( $\tau_d < 50$  ns) obtained using Nomarski interferometry has been reported [6]. The clear advantage of using the stagnation layer as a new source for PLD has renewed interest in this field and has motivated further characterization of the stagnation layer using techniques such as shadowgraphy and Schlieren imaging along with diagnostics of the substrate using electrical and optical techniques, work on which is already underway [7].

The second theme to the work in the thesis concerns the interaction of the intense extreme ultraviolet (EUV) beam from the free-electron laser in Hamburg (FLASH) with atomic gas jets. Specifically, we investigated two-color above-threshold ionization using a combination of EUV and near-infrared (NIR) photons. Work began with the characterization of the pump-probe scheme. Details of the temporal synchronization system used to overlap the EUV FEL beam with the NIR laser beam which was critical to the success of our experiments at FLASH were introduced in Chapter 2. This simple electronic device incorporated XUV sensitive high-speed photodiodes to overlap the pump and probe beams to within a temporal window of  $\pm 25$  ps. This was later refined to  $\sim 250$  fs (rms) through the use of a cross-correlation method, presented in Chapter 7. It is well known that the SASE process in the undulator can lead to the amplification of harmonics of the fundamental FEL radiation, up to the  $\mu\text{J}$  energy level. Their presence in the beam will result in an unwanted background photoionization signal, and so it was important to measure the spectral content of the FEL beam and determine the relative intensities of these higher harmonics. A flat-field spectrometer (supplied by Queen's University, Belfast) which consisted of a Harada grating and a back-illuminated EUV sensitive CCD camera was used for this purpose. In addition to measuring the energy of the 2nd and 3rd harmonics, the 5th harmonic of the fundamental radiation (13.7 nm) which is located inside the so-called 'water-window' was recorded at an energy of  $10 \pm 4$  nJ, a world-record for FEL based light sources. The water window is the wavelength region between 2.3 nm and 4.4 nm where the carbon atoms in organic matter absorb radiation, whereas the water or aqueous environment remains transparent, thus providing the greatest level of contrast for the imaging of biological samples.

The photoionization experiments performed at FLASH were mainly concentrated on the two-color photoionization of rare gas atoms. Introduced in Chapter 5 was the concept of free-free transitions induced by the NIR laser field - two-color photoionization. This results in a modification of the one-photon (EUV only) photoelectron spectrum by the addition of sidebands disposed symmetrically on either side of the one-photon peak. Using helium atoms, where the first photoelectron sideband results from either an  $\epsilon p \rightarrow \epsilon s$  or an  $\epsilon p \rightarrow \epsilon d$  free-free transition, we examined the relative contribution the two pathways made to the overall formation of the sideband. In order to do this with our electron spectrometer, which was not capable of measuring the angular distribution of the outgoing electrons, dichroic effects in the two-color signal were exploited. Specifically, the intensity of the sideband signal as a function of the relative polarization angle between the FEL and

NIR laser was measured and resulted in a  $\cos^2$  dependence. By employing both second order perturbation theory and the soft-photon approximation we were able to determine the relative contribution between  $\epsilon s$  and  $\epsilon d$  partial waves. The study was extended to other rare gas elements, namely neon, krypton and xenon. As the ionization originates from a  $p$ -subshell for these atoms the number of continuum channels increases (from the two,  $s$  and  $d$ , channels in the case of helium). Hence, for this case we relied exclusively on the soft-photon approximation to predict the relative intensities of the sidebands and also to examine qualitatively their polarization dependence.

Improvements to the EUV FEL at FLASH are ongoing. A new infrared (IR) beamline has recently been commissioned at FLASH [8] which provides relatively short pulse (0.3 – 10 ps) radiation in a spectral range of 10  $\mu\text{m}$  – 200  $\mu\text{m}$  (30 THz – 1.5 THz). As the same electron bunch used in the generation of the EUV FEL radiation is passed through a second undulator (undulator gap: 40 mm, period length: 400 mm, number of periods: 9 [9]) both THz and EUV radiation are inherently temporally synchronized to each other. It is envisioned that this beamline will supersede the existing NIR laser (the Ti:Sapphire laser used in this work) by providing a vastly improved temporal jitter between it and the EUV FEL pulse, while also permitting the survey of a far wider spectral range for future pump-probe studies. Work has already begun on transforming the existing EUV FEL at FLASH. The *sFLASH* project aims at producing coherent radiation via the seeding of the current undulators with 30 nm radiation, produced by a high-harmonic generation source. This will have several advantages over the existing SASE beamline [10]: Firstly, there will be an improvement in the shot-to-shot stability of the EUV output. Secondly, the temporal and spectral coherence is expected to be greatly improved. As the conventional SASE process begins with spontaneous emission from the electrons in the bunch, the output radiation is prone to the random fluctuations of this process (i.e., a form of shot-noise). When seeded using an external laser, the SASE process is vastly improved. The laser radiation stimulates the electrons to emit coherently rather like the interaction of the spontaneous undulator radiation which causes micro-bunching in conventional SASE. However, because this emission is “*coherently triggered within the seed pulse length*” the statistical fluctuations in the temporal and spectral profiles should be reduced [11]. Finally, the 30 nm (seeding) radiation can be transmitted to the end-station along with the SASE radiation and so provide users with an alternate pump-probe scheme. Notwithstanding the improvements envisioned for the EUV FEL at FLASH over the next few years, the ground-work has already begun on the building of the X-ray free electron laser or

X-FEL. With an expected completion date of 2014, the XFEL is envisioned to make the FLASH facility a world-leading center for the study of intense EUV laser interactions with matter [12], rivaled only by the LINAC Coherent Light Source (LCLS) in California and the facility at SPRING-8 in Japan [13].

# Bibliography

- [1] L. A. Gizzi, A. Giulietti, O. Willi, and D. Riley. Soft-x-ray emission dynamics in picosecond laser-produced plasmas. *Physical Review E*, 62(2):2721–2727, 2000.
- [2] D. Colombant and G. F. Tonon. X-ray emission in laser-produced plasmas. *Journal of Applied Physics*, 44(8):3524–3537, 1973.
- [3] E. Irissou, F. Vidal, T. Johnston, M. Chaker, D. Guay, and A. N. Ryabinin. Influence of an inert background gas on bimetallic cross-beam pulsed laser deposition. *Journal of Applied Physics*, 99(3), 2006.
- [4] C. McLoughlin, P. Hough, J. Costello, E. McGlynn, and J.P. Mosnier. Growth and field emission properties of zno nanostructures deposited by a novel pulsed laser ablation source on silicon substrates. *Ultramicroscopy*, 109(5):399–402, 2009.
- [5] E. Camps, L. Escobar-Alarcón, E. Haro-Poniatowski, and M. Fernández-Guasti. Spectroscopic studies of two perpendicularly interacting carbon plasmas generated by laser ablation. *Applied Surface Science*, 9(197-198):239–245, 2002.
- [6] P. Hough, C. McLoughlin, T. J. Kelly, P. Hayden, S. S. Harilal, J. P. Mosnier, and J. T. Costello. Electron and ion stagnation at the collision front between two laser produced plasmas. *Journal of Physics D: Applied Physics*, 42(5), 2009.
- [7] P. Hough. Private communication, 2009.
- [8] M. Gensch, L. Bittner, A. Chesnov, H. Delsim-Hashemi, M. Drescher, B. Faatz, J. Feldhaus, U. Fruehling, G. A. Geloni, Ch. Gerth, O. Grimm, U. Hahn, M. Hesse, S. Kapitzki, V. Kocharyan, O. Kozlov, E. Matyushevsky, N. Morozov, D. Petrov, E. Ploenjes, M. Roehling, J. Rossbach, E. L. Saldin, B. Schmidt, P. Schmueser, E. A. Schneidmiller, E. Syresin, A. Willner, and M. V. Yurkov.

New infrared undulator beamline at FLASH. *Infrared Physics & Technology*, 51(5):423 – 425, 2008.

- [9] V. Borisov. Commissioning of the IR beamline at FLASH. In *Proceedings of European Particle Accelerator Conference, 2006*, page 3595, 2006.
- [10] A. Azima, J. Bödewadt, M. Drescher, H. Delsim-Hashemi, S. Khan, T. Maltezopoulos, V. Miltchev, M. Mittenzwey, J. Rossbach, R. Tarkeshian, M. Wieland, H. Schlarb, S. Düsterer, J. Feldhaus, and T. Laarmann. Experimental layout of 30 nm high harmonic laser seeding at FLASH. In *Proceedings of European Particle Accelerator Conference, 2008*, pages 127–129, 2008.
- [11] G. Lambert, T. Hara, D. Garzella, T. Tanikawa, M. Labat, B. Carre, H. Kitamura, T. Shintake, M. Bougeard, S. Inoue, Y. Tanaka, P. Salieres, H. Merdji, O. Chubar, O. Gobert, K. Tahara, and M.-E. Couprie. Injection of harmonics generated in gas in a free-electron laser providing intense and coherent extreme-ultraviolet light. *Nature Physics*, 4:296–300, 2008.
- [12] The European X-ray Free Electron Laser. <http://xfel.eu/>.
- [13] SPRING-8, Japan. <http://www.spring8.or.jp/en/>.

## Appendix A

# Reference Material

### A.1 World Record at FLASH in Hamburg

#### DESY Press Release, September 2006

In the worldwide competition towards the highest laser power at the shortest wavelengths, the FLASH facility at the DESY research center in Hamburg established a new world record. In operation, the free-electron laser generated laser light flashes at wavelengths between 13.5 and 13.8 nm with an average power of 10 mW and record energies of up to 170 mJ per pulse – and this at repetition rates of 150 times per second. Since the pulses have a duration of only around 10 fs, the peak power per pulse can reach 10 GW. These powers are larger than is currently available at even the biggest plasma X-ray laser facilities worldwide. At 2.7 nanometers a specific part of the radiation, the so-called fifth harmonic, enables FLASH to reach deep into the water window – a wavelength range that is crucially important for the investigation of biological samples.

*FLASH is currently the only laser facility in the world to deliver ultra-short high-power laser flashes in the X-ray range with a very high repetition rate,” said DESY Research Director Professor Jochen R. Schneider. “FLASH thus opens up completely new experimental opportunities for researchers from nearly all the natural sciences, even within the so-called water window between 2.3 and 4.4 nm. In this wavelength range, the carbon atoms in organic matter absorb radiation very well, whereas the water environment remains invisible. This enables investigations that have not been feasible so far, for instance single shot holographic imaging of cellular systems in their natural in vitro environments.”*

*The free-electron laser FLASH, which has been available for research since August 2005, currently generates laser radiation with fundamental wavelengths between 13.1 and 40 nm. At wavelengths from 13.5 to 13.8 nm, the average energy per pulse was up to 70 mJ at an unprecedented repetition rate of 150 pulses per second, so that the average power was in excess of 10 mW. Future development of FLASH will see the repetition rate reach the multi-kHz range and the average power concomitantly increase to more than 100 mW. Simultaneously, FLASH also produced coherent radiation at the 3rd and 5th harmonics of the 13.7 nm fundamental wavelength, i.e. at around 4.6 and 2.7 nm with less than 10-femtosecond pulse duration. The corresponding pulse energies approached 1 mJ and 10 nJ per pulse for the 3rd and 5th harmonics, respectively. In 2007, FLASH will undergo an upgrade that will allow it to generate radiation with a fundamental wavelength that is continuously tunable between 6 and 60 nm. At the higher harmonics, FLASH will thus provide ultra-short laser pulses with mJ energies whose wavelengths will be tunable within and across the edges of the water window. This will open up unprecedented opportunities for high-resolution in vitro 2D and 3D imaging and spectroscopy of biological systems.*

*FLASH is the worldwide only free-electron laser facility for extreme ultraviolet and soft X-ray radiation. Around 200 scientists from 60 institutes in 11 countries use the intense laser light at currently four experimental stations for their experiments. Many further projects in various areas of physics, chemistry or molecular biology have already been proposed. The FLASH facility also plays an important pioneering role for future free-electron laser facilities that will generate laser flashes of even shorter wavelengths. Among these will be the 3.4-kilometer-long European X-ray free-electron laser (XFEL), whose realization is currently being prepared at DESY in international cooperation, and which should take up operation in 2013.*

*The FLASH record performance has been achieved by the DESY FLASH team in collaboration with international partners, the characterization of the photon beams was performed in collaboration with re-*

*searchers from LIXAM (CNRS/Université Paris-Sud), the IRCEP (Queen's University Belfast) and the NCPST (Dublin City University).*

DESY press release, September 2006.

## A.2 List of Publications

The following is a list of publications which have arisen from the work in this thesis, presented in chronological order.

J. Dardis, A. Murphy, H. de Luna, E. T. Kennedy, A. Seugnet, P. Orr, J. Greenwood, C. McKenna, C. L. S. Lewis, and J. T. Costello. Progress report on compact system for point projection X-ray absorption spectroscopy and imaging of laser produced plasmas. *Opto-Ireland 2005: Optical Sensing and Spectroscopy. Proceedings of the SPIE*, 5826:363-370, 2005.

H. Luna, J. Dardis, D. Doria, and J.T. Costello. Analysis of time-resolved laser plasma ablation using an imaging spectra technique. *Brazilian Journal of Physics*, 37:1301-1305, 2007.

P. Radcliffe, S. Düsterer, A. Azima, W.B. Li, E. Plönjes, H. Redlin, J. Feldhaus, P. Nicolosi, L. Poletto, J. Dardis, J.P. Gutierrez, P. Hough, K.D. Kavanagh, E.T. Kennedy, H. Luna, P. Yeates, J.T. Costello, A. Delyseries, C.L.S. Lewis, D. Glijer, D. Cubaynes, and M. Meyer. An experiment for two-color photoionization using high intensity extreme-UV free electron and near-IR laser pulses. *Nuclear Instruments and Methods in Physics Research Section A: Accelerators, Spectrometers, Detectors and Associated Equipment*, 583(2-3):516-525, 2007.

P. Radcliffe, S. Dusterer, A. Azima, H. Redlin, J. Feldhaus, J. Dardis, K. Kavanagh, H. Luna, J. Pedregosa Gutierrez, P. Yeates, E. T. Kennedy, J. T. Costello, A. Delserieys, C. L. S. Lewis, R. Taieb, A. Maquet, D. Cubaynes, and M. Meyer. Single-shot characterization of independent femtosecond extreme ultraviolet free electron and infrared laser pulses. *Applied Physics Letters*, 90(13):131108, 2007.

W. Ackermann, ..., J. Dardis, et. al. Operation of a free-electron laser from the extreme ultraviolet to the water window. *Nature Photonics*, 1(6):336, 2007.

M. Meyer, D. Cubaynes, D. Glijer, J. Dardis, P. Hayden, P. Hough, V. Richardson, E. T. Kennedy, J. T. Costello, P. Radcliffe, S. Dusterer, A. Azima, W. B. Li, H. Redlin, J. Feldhaus, R. Taieb, A. Maquet, A. N. Grum-Grzhimailo, E. V. Gryzlova, and S. I. Strakhova. Polarization control in two-color above-threshold ionization of atomic helium. *Physical Review Letters*, 101(19):193002, 2008.

A. Azima, S. Dusterer, P. Radcliffe, H. Redlin, N. Stojanovic, W. Li, J. Feldhaus, D. Cubaynes, M. Meyer, J. Dardis, P. Hayden, P. Hough, V. Richardson, E. T. Kennedy, and J. T. Costello. Time-resolved pump-probe experiments beyond the jitter limitations at flash. *Applied Physics Letters*, 94(14):144102, 2009.